A Frequency-Stabilised Diode Laser and its Application to Atomic Spectroscopy of Caesium

A thesis presented in partial fulfilment
of the requirements for the degree of

PhD in Physics

at

Massey University

Peter Saunders

1993

Massey University Library
Thesis Copyright Form

Title of thesis: A Frequency-Stabilised Diode Laser and its Application to Atomic Spectroscopy of Caesium

1) (a) I give permission for my thesis to be made available to readers in Massey University Library under conditions determined by the Librarian.

(b) I do not wish my thesis to be made available to readers without my written consent for ... months.

(2) (a) I agree that my thesis, or a copy, may be sent to another institution under conditions determined by the Librarian.

(b) I do not wish my thesis, or a copy, to be sent to another institution without my written consent for ... months.

3) (a) I agree that my thesis may be copied for Library use.

(b) I do not wish my thesis to be copied for Library use for ... months.

Signed Rob Saunders

Date 18/2/93

The copyright of this thesis belongs to the author. Readers must sign their name in the space below to show that they recognise this. They are asked to add their permanent address.

NAME AND ADDRESS DATE

Abstract

This thesis examines the hypothesis that a commercially available single-chip AlGaAs diode laser can be rendered suitable for atomic physics research through the addition of external circuitry alone. This circuitry is discussed and the frequency-stabilised laser is applied to some interferometric and spectroscopic studies. These studies also include the development of theoretical models.

The design and construction of an ultra-stable constant current source is discussed, along with an evaluation of its effectiveness. The current source is capable of supplying up to 100-mA dc with the addition of a ramp current of up to 20 mA to allow frequency scanning of the laser, and exhibits short-term fluctuations of ± 8 μA with a drift of less than 2 μA in ten hours. A temperature controller, capable of both heating and cooling the laser, is described. This can maintain temperature stability to ± 1 mdeg. A data acquisition and control unit is designed and constructed to enable the interfacing of both the laser and other measurement apparatus to a micro-computer.

A system for automatically measuring wavelength maps as a function of injection current and laser temperature is developed, utilising the data acquisition and control unit in conjunction with a grating spectrometer. This is applied to four diode lasers. Linearity measurements are made of the frequency scan with injection current. The linewidth of one laser is measured as a function of its output power by heterodyning its output with that of a second laser operated at fixed injection current and temperature, and observing the beat note on a rf spectrum analyser. The linewidth can be reduced to below 10 MHz. The absolute frequency stability of the laser is measured by monitoring the change in absorbed power over time when the laser is tuned to the D_2 transition of caesium. The drift is measured to be 10 kHz/s over five hours, and is attributed largely to temperature drift.

An analysis is presented which allows the spectral linewidth of a light source with a Lorentzian or Gaussian profile to be calculated from the measured fringe visibility of the transmission fringes of a high-finesse scanning Fabry-Perot interferometer when these fringes are not fully resolved. The method is also applied to truncated spectral profiles, which may provide a more appropriate model for the spectral profile of some lasers, and the differences are characterised. The analysis is then extended to interferometers with low finesse and also to include the Voigt profile. An experimental verification of the analysis is made using a diode laser whose spectral profile is demonstrated to be Lorentzian in shape.

The frequency-stabilised diode laser is applied to the study of saturated absorption spectroscopy of the caesium D_2 line at 852.1 nm. Both single-beam and two-beam experiments are performed using an absorption cell containing caesium vapour with no buffer gas. A theoretical model is developed, based on rate equations for the population densities of the 48 sublevels involved in the transition, including a rate for ground state relaxation due to transit of atoms through the laser beam. The model facilitates the analysis of the effects of optical pumping and extent to which the ground state relaxation rate limits the optical pumping. For the medium-resolution single-beam experiments the laser is shown to be a suitable source for resolving the Doppler-broadened transitions, and good agreement is obtained with the model for sufficiently low laser powers. However, for the sub-Doppler two-beam experiments the limited frequency stability is revealed. An analysis of the lock-in detection process for the two-beam experiments is made, emphasising the relationships between the detection frequency, the ground state relaxation rate, and the shape of the detected signal. It is discovered that if the detection frequency is of the order of the ground state relaxation rate then a simple subtraction of the Doppler-broadened background from the probe absorption signal does not adequately model the lock-in detection process. A technique is described to experimentally determine the ground state relaxation rate from the detected signal as a function of the lock-in phase.

Acknowledgements

First and foremost I wish to thank Dr Deborah Kane, my original supervisor, for her enthusiasm and inspiration which motivated me to undertake this project, for her active role as instructor and mentor in the development stage, and for her continued interest in the project despite the many obstacles that have arisen.

I would like to thank Associate Professor Neil Pinder for the unfaltering support and encouragement he has shown, and also Dr Robert O'Driscoll for his helpful advice and support.

I gratefully acknowledge the assistance of the staff of the Electronics and Mechanical Workshops at Massey University in the construction of many pieces of apparatus. In particular, I am indebted to Robin Dykstra for many hours of stimulating discussion and for much advice concerning the electronic content of this thesis.

I thank Professor Wes Sandle for the critical contribution he has made towards the completion of this work, and the other staff, in particular Dr Don Warrington and Dr Rob Ballagh, and graduate students of the Atomic Physics Group at the University of Otago for their assistance and kind hospitality during my several visits to Dunedin. I am grateful to Robin Gledhill for the construction of the caesium cells.

I would like to express much appreciation to Diane Reay for her unfailing encouragement and for her well-informed advice concerning the layout of the thesis.

I wish to thank my parents, Bryan and Denise Saunders, for their constant encouragement throughout this project.

Thanks to the staff and graduate students of the Department of Physics and Biophysics at Massey University for their advice and help when needed, and for maintaining a friendly working environment.

Among the many unaware contributors, I would to like to express thanks to David Bowie for providing much inspiration, and to Roger Waters and *Pink Floyd* for helping to maintain my sanity.

Finally, I am grateful to the former NZ University Grants Committee for providing financial assistance and for the Massey University Vice-Chancellor's PhD study award.

Table of Contents

List of Figures

List of Tables

1. Introduction

> *"But since Maxwell showed that an electromagnetic wave does not differ in any way from a light wave, we must suppose that it carries photons, and we are bound to wonder why this case differs from that of the emission of an isolated photon."* Louis de Broglie†.

The advent of the laser in the early 1960's triggered renewed interest in atomic physics research and prompted the development of many new experimental techniques. Since then, the dye laser has been a dominant source of tunable continuous wave radiation, operating reliably over the wavelength range from about 450 to 720 nm, and has been applied to a wide range of investigations. More recently, the titanium sapphire laser has extended this range into the near infrared from about 700 to 1200 nm. Although the dye and titanium sapphire lasers have proved to be invaluable tools for atomic physics research, they do have certain disadvantages: in comparison with other experimental apparatus they are relatively expensive; these lasers are optically pumped by argon ion lasers which typically require high voltage lines and water cooling; to obtain good output characteristics these lasers require optical elements which are easily misaligned.

For many applications the diode laser has been an attractive alternative to the dye laser or titanium sapphire laser. Although the diode laser was invented before the dye laser, it wasn't until the late 1970's that the diode laser could operate reliably enough at room temperature to begin to have significant impact on atomic physics research. In comparison with the dye laser for example, the diode laser is a fraction of the price, operates on an even smaller fraction of electrical power, and lases at the flick of a switch. On the other hand, the diode laser produces significantly less output power, has a smaller wavelength coverage (restricted largely to the infrared), has a smaller tunability range, and has a larger free-running linewidth. However, over recent years these factors have been steadily improving.

The tunability and spectral characteristics of standard single-chip diode lasers can be improved through optical feedback, by creating an external cavity. This often involves physically modifying the diode laser itself, requiring a reasonable amount of sophistication. Although external-cavity diode lasers are commercially available, they are several orders of magnitude more expensive than the single-chip device. There is at present a large amount of work being carried out with laboratory-made external-cavity diode lasers. However, the specialised techniques required to construct one may be inaccessible to the small laboratory. The aim of the present work is to investigate the

† From *New Perspectives in Physics*, (Edinburgh and London: Oliver & Boyd Ltd, 1962), p. 8.

hypothesis that commercially available single-chip diode lasers can be rendered suitable for atomic physics research by the application solely of simple inexpensive external circuitry. The circuitry used here consists of a purpose-built ultra-stable constant current source and a precision temperature controller.

A review of some of the relevant properties of the double heterostructure AlGaAs diode laser is given in Chapter 2. This begins with a brief account of the invention of the diode laser, emphasising the problems inherent in the early devices which prevented them from making major contributions to atomic physics research. Following this is a description of the single-mode room temperature device that is commercially available today, with discussions on the aspects important to atomic physics, such as tunability and spectral output. A discussion of some of the applications in which diode lasers have been employed is given at the end of the chapter.

Chapter 3 contains a description of the injection current and temperature control circuitry required to drive a diode laser with the appropriate degree of frequency stability and control over output wavelength necessary for its use in spectroscopy. The current source was developed as an integral part of the present research and was designed so that it could provide flexible control over the diode laser output, thus enabling frequency scanning through an atomic transition either manually or by means of computer control. Also described in Chapter 3 is a data acquisition and control unit developed to facilitate the collection and analysis of experimental data concerning the laser properties themselves and resulting from the application of the laser to scientific problems.

The results of measurements of various laser properties are presented in Chapter 4. The data acquisition and control unit was used to generate wavelength maps of four diode lasers, which are invaluable for selecting the appropriate laser for a particular experiment. These maps were also used to determine the rate of frequency change with injection current and temperature. The linearity of frequency scanning by injection current sweep was determined with the aid of a passive Fabry-Perot interferometer (FPI). The spectral profile of a diode laser was recorded by heterodyning two similar lasers and a measurement was made of the change in linewidth with output power. Long term frequency drift was measured by monitoring the change of an atomic absorption signal.

The standard method of measuring linewidth is to use a high finesse FPI with the appropriate free spectral range (FSR). In Chapter 5 a theoretical method is developed

to extract the linewidth of either a Lorentzian or Gaussian spectral profile from the transmitted fringe pattern when the FSR is too small to resolve this linewidth. The theory is extended to include interferometers with a finesse which is insufficiently high to render the instrumental profile of the FPI negligible, and also to include the Voigt profile. Experiments were performed in order to test the theory using a diode laser, and to measure the linewidth versus power relationship for comparison with the result obtained in Chapter 4 using the heterodyne technique.

The laser diode is applied to the study of saturated absorption spectroscopy in caesium vapour in Chapter 6. The caesium D_2 transition at 852.1 nm was examined both theoretically and experimentally. A rate equation model, including all 48 Zeeman sublevels, and the effect of ground state relaxation due to the transit time of atoms through the beam, is developed to describe the influence of the laser field on the populations involved in the transition. The results from this model are compared with experimental spectra obtained from both single-beam and two-beam arrangements. The effects on the two-beam spectra of changing the ground state relaxation rate are examined theoretically, and it is found that for critical values of this rate two of the resonances change sign. A lock-in amplifier was used, in the usual manner, for the experimental two-beam spectra to increase the signal-to-noise ratio and to suppress the Doppler background. This resulted in major discrepancies between theory and experiment. An analysis is made of the relationship between the frequency of the lock-in detection and the ground state relaxation rate, and it is discovered that for chopping frequencies of the order of ground state relaxation rate the spectra are distorted by the detection system. Moreover, this analysis provides a simple experimental technique for measuring the relaxation rate.

2. Review of Diode Laser Properties

2.1. Introduction

This chapter contains a review of the properties of diode lasers pertaining to their use in atomic physics. In Section 2.2 there is a brief discussion on the advent of the diode laser and some of the problems inherent in the early devices which kept them away from main stream atomic physics research for many years. Technological advances have helped to overcome these obstacles and since the early eighties there has been a rapid increase in their application to the field of atomic physics research, as well as to a number of other research and commercial areas. These include infrared atomic and molecular spectroscopy, trapping and cooling of atoms, optical pumping for time and frequency standards, precise metrology, optical communications, laser gyroscopes, and optical disk systems. Diode lasers are also used as a pumping source for other laser systems.

The features that diode lasers have for the above applications are:

(*i*) They are inexpensive in terms of watts per dollar compared to other lasers.

(*ii*) They are tunable over a region of tens of nanometres within which continuous tuning ranges of tens of gigahertz are punctuated by mode hops.

(*iii*) They can lase in an essentially single longitudinal mode within a few megahertz of the desired wavelength as soon as they are turned on. Although the spectral emission is well characterised by a pure Lorentzian, there are in reality many much less intense spectral components hundreds of gigahertz away from the main mode.

(*iv*) They operate in the infrared where many molecular transitions occur, and where fibres used for optical communications have least loss and dispersion.

(*v*) They are capable of rapid modulation.

(*vi*) They are portable and have a low power consumption, and hence can be operated "in the field" using battery power. However, low power consumption implies low output power and this is not always a desirable feature.

The properties of the double heterostructure AlGaAs diode laser are reviewed in Section 2.3 with emphasis placed on those characteristics relevant to atomic spectroscopy. Section 2.4 discusses some of the atomic physics research applications for which the diode laser has been employed. The electronic circuitry (stable current source and temperature controller) used to convert the commercially available laser into a spectroscopic tool is discussed in Chapter 3.

2.2. Early Diode Lasers

Since well before the invention of the diode laser it has been known that photons can be produced by applying electromagnetic fields to solid materials[1]. This phenomenon, known as electroluminescence, is caused by spontaneous emission between energy bands in the material due to electron-hole recombination. The light produced in this manner is, of course, incoherent. In order to observe stimulated emission and laser action several requirements must be fulfilled[2]. First, the electron and hole populations must be large enough that their quasi-Fermi levels are separated by an energy greater than that of the radiation produced. This arises from the requirement that the number of photons emitted is greater than the number absorbed. Secondly, the losses due to absorption by other processes must be smaller than the gain produced by stimulated emission. This implies that some sort of confinement of the stimulated emission is necessary so that it is not lost to regions of the material where there is insufficient population inversion. Lastly, the population inversion must be contained within a cavity which has a resonant frequency in the spectral range for which stimulated emission is possible.

It was discovered that some semiconductor materials were appropriate for fulfilling the above conditions and in November and December 1962 laser action in GaAs at 8420 Å was first reported by three independent groups[3–5]. Lasing in the visible was observed also in $Ga(As_{1-x}P_x)$ alloys at about 6600 Å[6]. All of these diode lasers were made by forming a simple p-n junction and creating an optical cavity by polishing the parallel end faces of the crystal. Because the refractive index is quite high, 3.6 for GaAs, reflection coatings were not needed[2]. The sides were roughened to prevent lasing in the unwanted direction. The diodes in Reference 3 were approximately cubes, 0.4 mm on each edge. In order to create a population inversion between the conduction and valence bands, to allow stimulated emission to occur, the junction was forward biased causing a so-called injection current to flow through the device. Initially, short current pulses of 5 to 20 μs were used. However, improved fabrication techniques soon led to cw operation[7]. The population inversion was built up as the current increased from zero until a threshold current was reached where spontaneous emission gave way to stimulated emission and laser action in a small region near the junction (active region). The threshold level was identified through a rapid increase in light intensity and a sudden narrowing of the spectral distribution as the current density was increased. Above threshold the light was determined to be coherent by the observation of vertical bands on an infrared converter tube due to interference between waves emitted from various points along the edge of the junction. The wavelength of the emitted light was

approximately equal to the bandgap energy, although since impurity levels tend to alter the band structure, it was observed that the wavelength corresponded to an energy slightly less than the bandgap.

Several considerations meant that the early diode lasers had to be operated at reduced temperatures, either liquid nitrogen or liquid helium temperatures[1]. The lifetime of an electron-hole pair prior to recombination was found to be extremely short, about 10^{-9} to 10^{-10} s, therefore a large current was needed to maintain the population inversion. The threshold current is strongly dependent on temperature. Values of about 200 A cm^{-2} below 20 K, rising to 750 A cm^{-2} at 77 K, and up to 50 000 A cm^{-2} at room temperature were measured. The size of the active region was defined by the extent to which electrons and holes diffused across the junction, and was typically about 2 μm wide. Because of this small size, the laser light was highly divergent and spilt over into regions of the semiconductor where the population inversion was insufficient for laser action. This radiation was absorbed by the semiconductor leading to the generation of significant amounts of heat in the device. This problem was enhanced at higher temperatures due to both the increase in threshold current and the decrease in thermal conductivity.

Laser emission was almost always observed to be produced by many modes simultaneously. Only in special cases was single-mode operation obtained, generally at liquid helium temperature. The spectral distribution was rather broad, typically several hundred GHz. Also, due to inhomogeneities in the crystal structure, the spatial pattern of the output beam was highly complicated. For these reasons early semiconductor lasers did not find their way into many atomic physics experiments.

Not long after the discovery of laser action in GaAs, it was found that many different types of semiconductor material could lase (for a list of early materials used see Reference 8). These materials are all direct bandgap semiconductors, that is the maximum energy of the valence band and the minimum energy of the conduction band occur for the same wavevector. It was discovered that laser action is favoured in direct bandgap semiconductors rather than indirect bandgap semiconductors[9]. The principal reason for this is that in indirect bandgap semiconductors electron-hole recombination is accompanied by a change in wavevector. This change must be taken up by some other agent such as a phonon or an impurity. The probability of this second order process is smaller than the first order process of radiative transition that occurs in a direct bandgap semiconductor involving only the electron-hole pair and a photon, hence the former transition is weaker. In addition, the second order process has a relatively long lifetime

(10^{-5} s compared with 10^{-9} s for direct transitions) and so there is more time for non-radiative loss mechanisms, such as free carrier absorption, to operate. This reduces the optical gain making the conditions for lasing less favourable.

2.3. The AlGaAs Double Heterostructure Diode Laser

2.3.1. Introduction

In the past 30 years major advances in semiconductor laser technology have been made. Laser sources from a wide range of semiconductor materials with a range of wavelengths extending from 670 nm to about 30 μm are now commercially available[10]. This wavelength range is by no means complete, the development of new wavelengths being driven somewhat by consumer demand. Thus, for example, lasers based on InGaAsP which operate at 1.3 and 1.5 μm have been developed for the communications industry. For the purpose of atomic spectroscopy there is presently available the AlGaAs diode laser which operates in the near infrared from about 750 to 890 nm. Molecular spectroscopy has been assisted by the lead-salt family of diode lasers which emit in the middle to far infrared.

There have also been major advances in laser construction and complexity. The simple p-n junction laser has been replaced by heterostructure lasers[11] and quantum well lasers[12] to achieve lower thresholds and more efficient operation. In addition, several new geometries including cleaved-coupled-cavity[13], distributed feedback[14], and distributed Bragg reflection[15] devices, and external-cavity lasers have been developed to give single frequency operation with better than 20-dB suppression of the next most intense mode. High output powers (up to 20 W cw) have been achieved through the construction of diode arrays. Since this thesis is concerned with the role of the commercially available single-chip diode lasers in atomic physics research, and due to the fact that the lasers used experimentally in the present research were double heterostructure AlGaAs lasers, the remainder of this chapter discusses those properties of these lasers which bear a consequence on this theme. It also happens that the AlGaAs lasers have the best overall characteristics of all the semiconductor lasers to date[16].

2.3.2. Laser Structure

The problem of confining the stimulated emission within the active region, and thus reducing losses, was overcome with the development of the heterostructure laser. These lasers also made possible single-mode cw operation at room temperature. A typical double heterostructure laser is shown in Figure 2.1. The active region is a layer

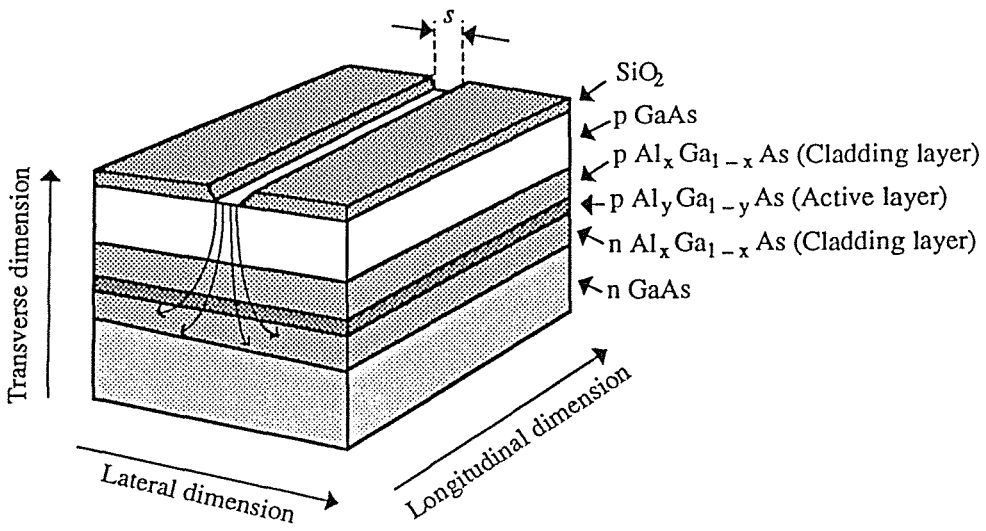

Figure 2.1. Various layers in a double heterostructure AlGaAs diode laser. Current is injected in the transverse direction through the stripe of width s, and the laser radiation emerges from a narrow region of the front plane.

of $Al_yGa_{1-y}As$ and is sandwiched between two cladding layers of $Al_xGa_{1-x}As$. The mole fraction, x, of Al in the cladding layers is greater than that, y, in the active region, and hence the bandgap is higher and the refractive index lower[17] in the cladding layers than the active region. As electrons are injected into the active region, through a stripe of width s, they encounter a potential energy barrier due to the higher bandgap of the cladding impeding their exit and hence are confined to the active region. The photons subsequently produced by electron-hole recombination are also confined in the transverse direction due to the refractive index waveguiding effect of the cladding layers. Both of these properties reduce the threshold current density required for laser action (typically 1000 A cm^{-2} at room temperature). The thickness of the active region is typically less than one micron and this ensures fundamental transverse mode operation. Fundamental lateral mode operation is achieved by building in a spatial variation of the refractive index in this direction.

2.3.3. Spatial Output Characteristics

Transverse and lateral dimensions of the active region are around 0.1 μm and 0.3 μm, respectively. Because the lasing wavelength (850 nm) is of a similar magnitude to the physical size of the active region the laser emission diverges rapidly. Divergence angles (full width at half intensity) are commonly 30° in the transverse direction and 10°

in the lateral direction. The beam can be collimated using a lens with a small f number resulting in an elliptical beam.

The typical transverse mode that lases is a TE mode polarised linearly in the lateral direction. Although the degree of linear polarisation is quite high, more complex polarisations have been observed resulting from anisotropies in the crystal axes[18].

2.3.4. Output Power

Single-mode output powers range from about 5 to 30 mW for lasers with cleaved facets, and this can be increased up to about 200 mW with the addition of a high-reflectance coating on the back facet and a reduced reflectance coating on the output facet[19]. The output power of an individual laser is a function of both the injection current and temperature, although the injection current dependence is far stronger. This is illustrated qualitatively in Figure 2.2. The sharp rise in power above a certain value of injection current signifies the onset of stimulated emission and laser action. Although the turn-on is not infinitely sharp, the threshold current is usually defined by

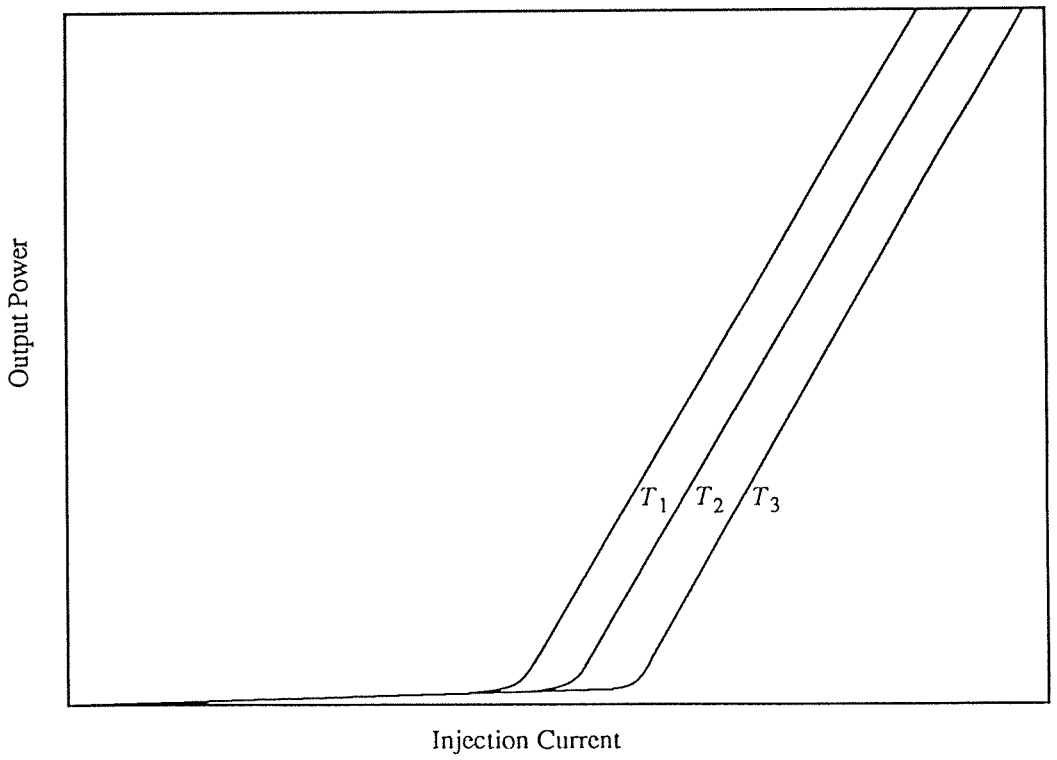

Figure 2.2. Typical form of output power versus injection current curves as a function of temperature for an AlGaAs diode laser. $T_1 < T_2 < T_3$.

extrapolating the steeper linear part of the power versus injection current characteristic down to zero power.

Above threshold the power can be expressed as[17]

$$P = \eta_{ex} \frac{h\nu}{e} (I - I_{th}), \tag{2.1}$$

where η_{ex} is the differential external quantum efficiency, defined as the change in laser photon output rate per unit change of current above threshold, and I_{th} is the threshold current. η_{ex} describes both the generation of a lasing photon by radiative recombination, and its subsequent escape from the cavity. The temperature dependence of the output power comes about principally through the variation of threshold current with temperature. This latter variation differs between lasers but is found in general to increase with temperature.

2.3.5. Laser Tuning

One of the most important properties of the diode laser for use in atomic physics is its tunability. Commercially available lasers are individually tunable over a range of about 20 nm. The wavelength about which lasing occurs is to a large extent determined by the bandgap of the semiconductor material, although this can be altered by varying the doping levels. Tuning of the wavelength can be achieved by altering either the laser's temperature, the amount of injection current, its ambient pressure, or the strength of an applied magnetic field. A combination of temperature and injection current tuning is by far the easiest method to implement and control.

Temperature tuning occurs due to the temperature dependence of both the refractive index of the active region and the bandgap energy. The gain curve has the same temperature dependence as the bandgap, which is given by[20]:

$$E_g(T) = E_g(0) - \frac{\alpha T^2}{T + \beta}, \tag{2.2}$$

where α and β are constants for a particular semiconductor and are both positive for GaAs. Thus, the gain curve shifts to longer wavelengths as the temperature is increased. The lasing wavelength corresponds to the Fabry-Perot mode nearest the centre of the gain curve. The wavelength of this mode is given by

$$\lambda(T) = \frac{2Ln(T)}{m}, \tag{2.3}$$

where L is the cavity length, $n(T)$ the temperature-dependent active region refractive index, and m an integer. Thus, the wavelength of the lasing mode has the same temperature dependence as the refractive index (the thermal expansivity of the active region is negligible[2]). This is given by[17]

$$n(T) = n(0) + pT, \tag{2.4}$$

where p is a constant. Hence, the lasing mode, like the gain curve, shifts to a longer wavelength with an increase in temperature. However, the latter shifts at a faster rate and the lasing mode gets out of step with the gain curve. When the gain is no longer sufficient for this mode to lase the lasing wavelength jumps to the next mode with sufficient gain. Thus, temperature tuning is characterised by continuous regions of linearly increasing wavelength punctuated by discontinuous mode-hops to larger wavelengths.

Injection current tuning occurs in two ways. Increasing the injection current leads to a rise in the temperature of the active region due to Joule heating, and causes a decrease in refractive index due to the greater carrier density[21]. However, this latter effect only occurs for operation below threshold. By driving lasers with short pulse-width small duty-cycle current pulses, thereby minimising Joule heating, Chambliss and Johnson[22] have observed no change in output wavelength above threshold with an increase in current magnitude, indicating that the carrier density is clamped above threshold. Thus, injection current tuning operates in the same manner as described above for temperature tuning. The advantage of injection current tuning is that it allows a more precise control over the output wavelength. For this reason it is usual to adjust the laser temperature for gross control over the wavelength and to use injection current tuning for fine adjustments and frequency scanning.

Although the above discussion gives a qualitative description of tuning, it is impossible to infer from this the tuning characteristics of an individual laser. In fact, no two diode lasers behave in exactly the same fashion. Each laser has its own unique wavelength map, which must be experimentally determined. In addition, lasers are observed to display anomalous behaviour to that described above. This includes mode hops to shorter wavelengths and hysteresis effects in the mode hopping behaviour[23]. The tuning rates also vary from laser to laser, but for AlGaAs diode lasers are typically in the ranges –20 to –30 GHz/°C and –3 to –7 GHz/mA for temperature and injection current changes, respectively.

2.3.6. Spectral Output

For many applications, including atomic physics experiments, the spectral output of the laser is extremely important. There are two natural scales over which the spectral content of the output can be examined. The largest of these corresponds to the spacing of the longitudinal modes. As given by equation (2.3), this is determined by the length of the laser cavity and the refractive index of the active region, and is typically of the order of 100 GHz. The relative intensities of the output modes vary with output power. Below and slightly above threshold the mode intensities are of similar magnitude, giving a multi-mode output. As the power is increased the gain is channelled into a single mode. Although this is referred to as single-mode operation, there is still a small amount of power in the nearby longitudinal modes. Nakamura *et al.*[23] have observed that the intensities of these "non-lasing" modes decrease with increasing power due to spectral hole burning in the gain profile near the main lasing mode. As well as at low powers, multi-mode behaviour can be observed at the onset of mode hopping.

The other spectral scale corresponds to the width and shape of a single longitudinal mode. High resolution studies[24] have revealed the shape of this mode to be Lorentzian, as expected by conventional laser theory. However, examination under lower resolution[25] found that some lasers emit lines having sub-structure consisting of small peaks separated by 1 to 2 GHz from the main peak. These are due to relaxation oscillations of the optical field caused by spontaneous emission events. An intuitive calculation of this effect has been made by Henry[26] and can be summarised as follows. Each spontaneous emission event adds a new component to the field with a random phase. This gives rise to an instantaneous change in the phase and intensity of the field. Due to coupling of the field with the population inversion, the laser undergoes damped relaxation oscillations, with a period of the order of 1 ns, to restore the field intensity to its steady-state value. This produces a further time dependent change in the phase of the field. The power spectrum of the lasing mode is given by the Fourier transform of the exponential of minus one-half of the mean square phase change. Thus, the instantaneous phase change due to spontaneous emission gives rise to a Lorentzian profile and the subsequent relaxation oscillations produce small resonances 1 to 2 GHz away.

For a long time the width of the main Lorentzian mode was thought to be given by the modified Schawlow-Townes linewidth[27, 28]:

$$\Gamma_{ST} = \frac{\pi h \nu \Delta \nu_c^2}{P}, \tag{2.5}$$

where $\Delta\nu_c$ is the linewidth of the passive cavity resonator and P is the power in the mode. However, detailed measurements of the linewidth of an AlGaAs diode laser by Fleming and Mooradian[24] showed equation (2.5) to be too small by a factor of about 50. This discrepancy was explained by Henry[29] to arise from two sources. The first comes from the fact that in semiconductor lasers the population inversion is not complete. The valence levels are not empty and so photons are absorbed which can subsequently decay via spontaneous emission adding further fluctuations to the field intensity. Thus, the modified Schawlow-Townes linewidth is broadened by the temperature-dependent spontaneous emission factor, n_{sp}, which is the ratio of the spontaneous emission per mode to the stimulated emission per laser photon. At room temperature n_{sp} is about 2.5 and becomes unity at 77 K[30]. Further broadening arises from the coupling between phase and intensity fluctuations discussed above. During the relaxation oscillations both the real and imaginary parts of the refractive index are altered in response to the change in electron population density. The broadening factor is given by $1 + \alpha^2$, where α is the ratio of the change in the real part to the change in the imaginary part of the refractive index. Thus, the laser linewidth is given by

$$\Gamma = \Gamma_{ST} n_{sp}(1 + \alpha^2). \tag{2.6}$$

Typical values of α for AlGaAs range from 4.6 to 6.2[29] giving a broadening factor ranging from about 22 to 39.

2.4. Applications to Atomic Physics

2.4.1. Previous Applications

Since the early 1980's diode lasers have found increasing utility in atomic physics. The important characteristics of narrow single-mode linewidth and ease of tunability, together with its low cost, have meant that the diode laser has become an attractive alternative to the traditional dye laser or titanium sapphire laser for many applications, particularly for multi-laser experiments. The review articles by Camparo[17] and Wieman and Hollberg[16] discuss many of these applications and have extensive lists of references. These include spectroscopic experiments in which the diode laser is used to probe an atomic species without perturbing the system, and optical pumping experiments where the diode laser interacts with an atomic system influencing the atomic characteristics. Spectroscopic studies have been carried out on many atomic systems with transitions occurring in the infrared (see Reference 17 for a list of atomic transitions).

The first report of an atomic spectroscopy experiment using a diode laser was made by Siahatger and Hochuli[31]. They used a current pulse to sweep the frequency of a cw GaAs laser operating at 77 K through the caesium D_2 transition at 852.1 nm, thus resolving the hyperfine splitting of the $6^2S_{1/2}$ ground state. They also used fluorescence spectra to estimate the lifetime of the $6^2P_{3/2}$ excited state. Hirano[32] resolved, for the first time, the hyperfine structure of the $6^2P_{3/2}$ excited state using the technique of saturated absorption spectroscopy with a room temperature AlGaAs diode laser. Here, frequency scanning was achieved by slowly sweeping the temperature of the laser. Other applications in the "passive laser" category utilising a standard AlGaAs diode laser include: the measurement of hyperfine structure and isotope splitting in a rubidium atomic beam[33] using a single laser beam and monitoring the fluorescence spectrum as the laser frequency was temperature-tuned; the accurate determination of the wavelengths of several water vapour absorption lines near 820 nm[34] by locking the diode laser frequency to the third derivative of each of these lines and measuring the laser wavelength in comparison with a Lamb-dip-stabilised helium-neon laser, using the coincidence method; the measurement of collisional broadening and shifts of spectral lines in argon[35] at 810.4, 811.5, and 840.8 nm, as a function of argon number density, by comparing absorption profiles from a reference (fixed density) discharge tube and a test discharge tube, scanning the laser frequency by means of a sawtooth injection current pulse; and atomic parity violation in bismuth[36] in which the rotation of the plane of polarisation of the laser output was measured upon passing the

beam through a bismuth vapour cell and injection-current-tuning the wavelength through the 875.7-nm absorption line.

One of the first optical pumping experiments performed with a diode laser was made by Singh *et al.*[37] They observed population inversion between the $F = 3$ and $F = 4$ hyperfine components of the caesium $6^2S_{1/2}$ ground state, and suggested the possibility of optically pumping caesium vapour for the purpose of obtaining a portable frequency standard. Arditi and Picqué[38] later made preliminary tests of the operation of a caesium atomic clock, based on the usual field insensitive $F = 3, M_F = 0 \leftrightarrow F = 4, M_F = 0$ microwave transition (at 9 192 631 770 Hz by definition), pumping an atomic beam with a single GaAs diode laser. They have also studied light shifts[39] of this transition induced by the pumping radiation. More recently[40, 41], work has been carried out towards improving the signal-to-noise ratio of the microwave transition by using two AlGaAs diode lasers to pump almost all the atoms into the $F = 4, M_F = 0$ sublevel of the ground state. Non-velocity-selective optical pumping was observed by Klimcak and Camparo[42], where two beams from a single AlGaAs diode laser were used to pump and probe a rubidium atomic beam in spatially separated regions. Here, the laser linewidth was much broader than the residual Doppler width due to the angular separation of the pump and probe, resulting in optical pumping dips in a homogeneously-broadened line.

With the use of external cavities very narrow linewidths are obtainable. This allows high sensitivity experiments to be performed. Tanner and Wieman[43] have made precise measurements of the caesium $6^2P_{3/2}$ excited state hyperfine splittings by locking the laser frequency to one component in an absorption cell, then splitting off a second beam and frequency-shifting it using an acousto-optic modulator. The modular frequency was adjusted to bring this beam into resonance with the other hyperfine components in a caesium atomic beam thus determining the frequency separations. An example of a multi-laser experiment for which the diode laser's low cost renders it a prime contender is the trapping and cooling of atoms. This has been carried out in a caesium beam by Sesko *et al.*[44] using an optical molasses of six intersecting narrow-linewidth diode laser beams tuned slightly below the $F = 4$ to $F' = 5$ hyperfine transition of the caesium D_2 line. Additional lasers were required to initially slow the atoms and to prevent atoms building up in the non-resonant $F = 3$ ground state level. Gibble and Gallagher[45] have used two external-cavity diode lasers to study the effects of ground-state velocity-changing collisions between rubidium atoms and those of several noble gases. They used velocity-selective optical pumping to extract single-collision kernels over the full thermal range of velocity changes.

Recently Yabuzaki *et al.*[46] have used a diode laser to perform a new type of high-resolution spectroscopy on caesium and rubidium vapour in which the laser was neither frequency scanned nor modulated. In this experiment they detected the intensity fluctuations of the transmitted light when the laser was tuned near a Doppler-broadened transition. The power spectrum of the intensity fluctuations was examined with a radio-frequency spectrum analyser and was found to contain information concerning both Zeeman and hyperfine splittings. This experiment was possible because of the diode laser's stable output intensity but relatively large frequency fluctuations extending into the wings several gigahertz from line centre. Thus, the spectra were due to the response of the atoms to these random frequency fluctuations.

2.4.2. Application in this Thesis

The experiments presented in Chapter 6 of this thesis involve saturated absorption measurements of the caesium D_2 line. In these experiments the laser frequency is scanned using an injection current ramp. The experimental results are compared to a theoretical model which describes the effects of saturation and optical pumping. The influence of the $6^2S_{1/2}$ ground state relaxation rate on the spectra is also examined.

3. Diode Laser Electronics

3.1. Introduction

As discussed in Chapter 1, a key feature of the work in this thesis involves the careful stabilisation and control of the frequency of a standard commercial AlGaAs diode laser operating at the 852.1-nm D_2 resonance in caesium. The electronic circuitry used for these purposes, consisting of an ultra-stable constant current source and a precision temperature control unit, is described in this chapter.

The value of using highly stabilised, but optically unmodified, diode lasers has been recognised by other workers. Bradley *et al.*[47] and Cafferty and Thompson[48] have recently reported designs for diode laser current supplies stable to ±1 μA at 150 mA and ±40 μA at 1.3 A, respectively. The latter supply is designed for high current operation of lead-salt diode lasers and features cut-off protection circuitry for a range of undesirable conditions, but has no provision for ramping the current. The supply of Bradley *et al.* contains three analogue voltage inputs which are added together to set the output current. Two of these, the coarse and fine adjustments, are derived from an internal precision voltage reference using potentiometers. The third voltage input, the sweep input, is obtained from an external source upon which its stability depends.

The present work, which was started before these designs appeared, follows a somewhat different philosophy. It employs digital circuitry for contol over the laser injection current and uses a single precision voltage reference for current stability during tuning and scanning. The temperature controller provides coarse frequency tuning of the laser while the current source enables fine tuning and frequency scanning to be performed.

A microprocessor-based computer interface is also described in this chapter. This interface was designed to allow the laser circuitry to be easily controlled remotely via computer and also to enable automatic acquisition of data in digital form.

3.2. Current Source

3.2.1. Design Criteria

The current source design was based on the following criteria: (*i*) the need for a high precision source capable of supplying up to 100-mA dc (bias current); (*ii*) an additional current (ramp current), up to 20 mA, to be added to the bias current in the form of a current ramp; (*iii*) the necessity to avoid any voltage spikes and transients which could easily destroy the device; (*iv*) provision of a means of interfacing the current source to a computer to allow flexibility and greater precision in the way the laser can be controlled in a particular experiment; and (*v*) the current source had to be inexpensive and relatively easy to construct, due to resource limitations.

The bias current is required, in conjunction with temperature control, to be able to select a particular diode laser wavelength, that is to grossly tune the laser near to an atomic transition. The ramp current provides fine tuning of the frequency and a means of performing a frequency scan through the desired atomic transition.

The design has built-in digital circuitry in order to meet the requirements listed above. The digital circuitry also allows the current source to be interfaced without loss of stability to a computer which can both set the bias current and perform a current scan at a desired rate. Ultra-stable components have been selected to ensure long-term current stability and immunity to ambient temperature changes. Finally, the present circuit is simple, reliable, and effective: the stability of the voltage inputs (bias and ramp) is determined only by that of the D/A converters as there are no potentiometers, and no additional circuitry is required to ramp the current.

3.2.2. Design Implementation

Figure 3.1 shows the circuit used. It is based on a constant current supply for a SQUID[49] which has been modified to fulfil the above criteria. The operational amplifiers labelled A1 to A5 were chosen for their low offset voltage drifts ($< 0.5\ \mu$V per °C) and low noise. The resistors are metal foil resistors which have a temperature coefficient of 0.3 ppm per °C and a tolerance of ±0.005%. The current amplifier has an offset voltage temperature coefficient of 8 μV per °C and has a larger

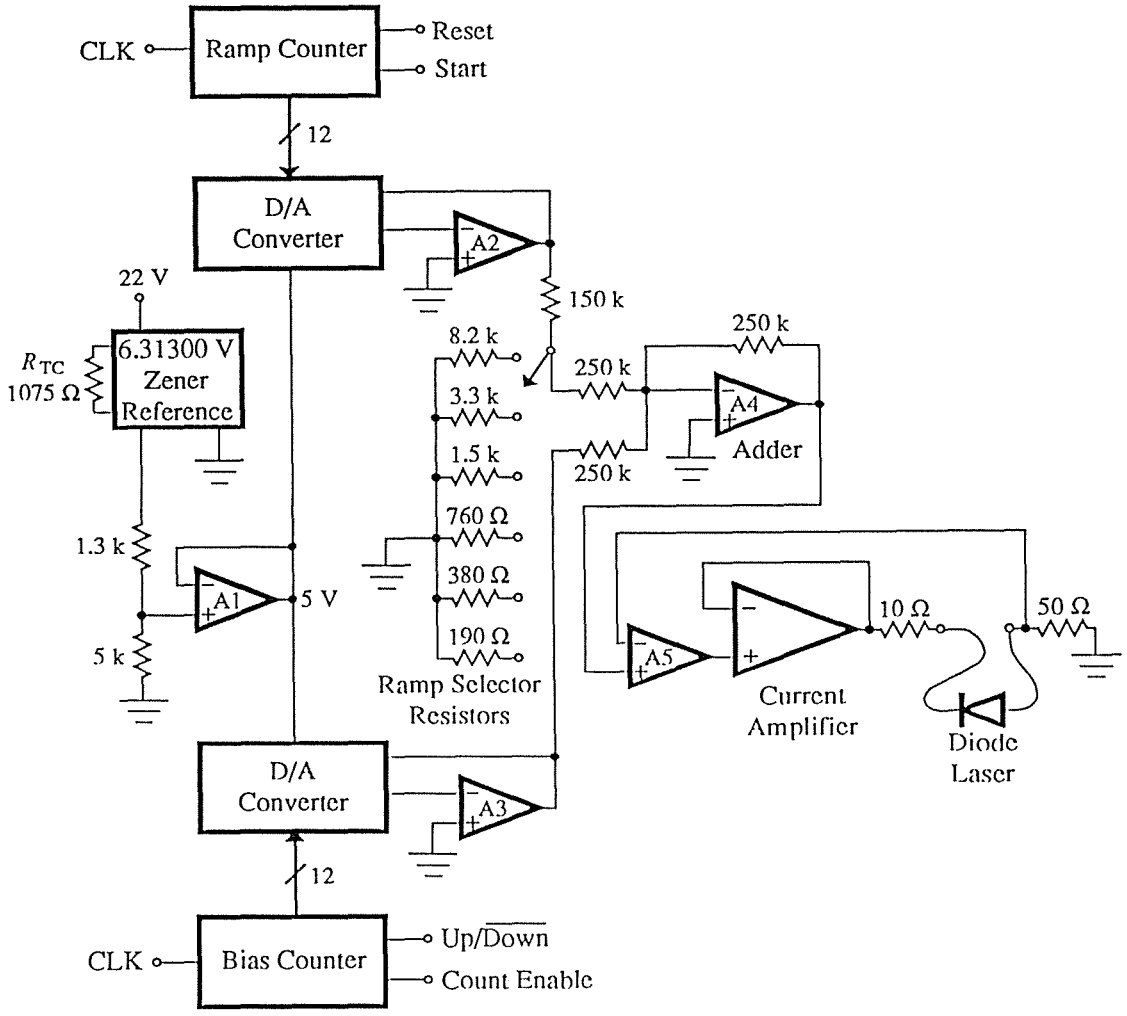

Figure 3.1. Current source for diode laser, capable of up to 100-mA constant current plus up to 20-mA ramped current. The 12 digital inputs to the D/A converters come from counter circuits which can be internally clocked at variable speeds or clocked by computer. The components are as follows—Op. amps A1 to A5: AD510; D/A converters: AD563; Current amplifier: AD3554; Zener reference: ZVR-506; Diode laser: Hitachi HL8314E; Resistors: Vishay metal foil.

noise figure than the amplifiers A1 to A5, but although it is wideband it was the most appropriate amplifier available at the time of construction. A cadmium/tin low thermal solder was used to minimise thermal effects at component contact points. Two digital counters are used to control the current through the laser, one for slowly setting the bias current and the other to produce a current ramp in addition. The bias counter circuit consists of three 4029B 4-bit synchronous up/down counters, operated in BCD mode, and three 74C85 4-bit magnitude comparators (see Appendix *A*). This provides digital counts from 000 to 999. The desired value is set using three thumb switches. Under normal operation the up/down counters are clocked by an internal variable speed clock. For remote operation this internal clock is disabled and the clock pulses are sent directly

from a computer. The scan counter circuit is similar in design to the bias counter, however the scan counter always counts directly from 000 to 999 where upon it can be reset back to 000. The scan direction can be reversed by adding some logic to the output which converts 000 to 999, 001 to 998, etc (this was not present in the original design, hence the add-on logic). The digital outputs from the counter circuits are converted to analogue via the 12-bit D/A converters in Figure 3.1. These have true 12-bit accuracy with a maximum error of ±0.5 LSB at 25 °C, and have a maximum zero drift of 2 ppm of full scale per °C. The reference voltage for the D/A converters is taken from a Zener reference with a rated output voltage of 6.31300 V, which is divided down to 5 V and buffered. The 50-Ω resistor between the laser and ground limits the bias current to 100 mA for a full scale setting on the bias D/A converter. The ramp voltage is divided down with the ramp selector resistors to obtain the desired tunability range, and is added to the bias voltage before being converted into a constant current. The current amplifier is configured as a unity voltage gain buffer and, together with the laser, is enclosed in a constant current feedback loop. It is important that the leads to the laser itself are inside a shielded cable. Without this precaution the laser current was observed to oscillate at near 100 MHz due to the pick-up of a local radio station.

The digital values on the D/A converters are shown on digital displays connected directly to the counter circuits. Once calibrated, this provides a "non-invasive" reading of the current through the laser without disruption and with no effect on its stability.

The bias current is ramped up slowly when initially turned on, and is reduced to zero before disconnecting the mains power supply to avoid sudden changes in injection current. Decoupling capacitors on the power supply lines to the operational amplifiers are the only safety features included to eliminate voltage spikes and transients. (To date, not a single laser has been destroyed!)

The current can be ramped over ranges of 0.12 up to 20 mA, each range consisting of 999 steps. This corresponds to frequency scan ranges of about 0.5 up to 80 GHz for the AlGaAs lasers used. These ranges can be readily varied by changing the selector resistors. However, the sizes of the continuous tuning ranges are influenced by mode hopping, the occurrence of which depends on the particular diode laser being used. Uninterrupted scans of more than 20 GHz have been achieved with the lasers used here.

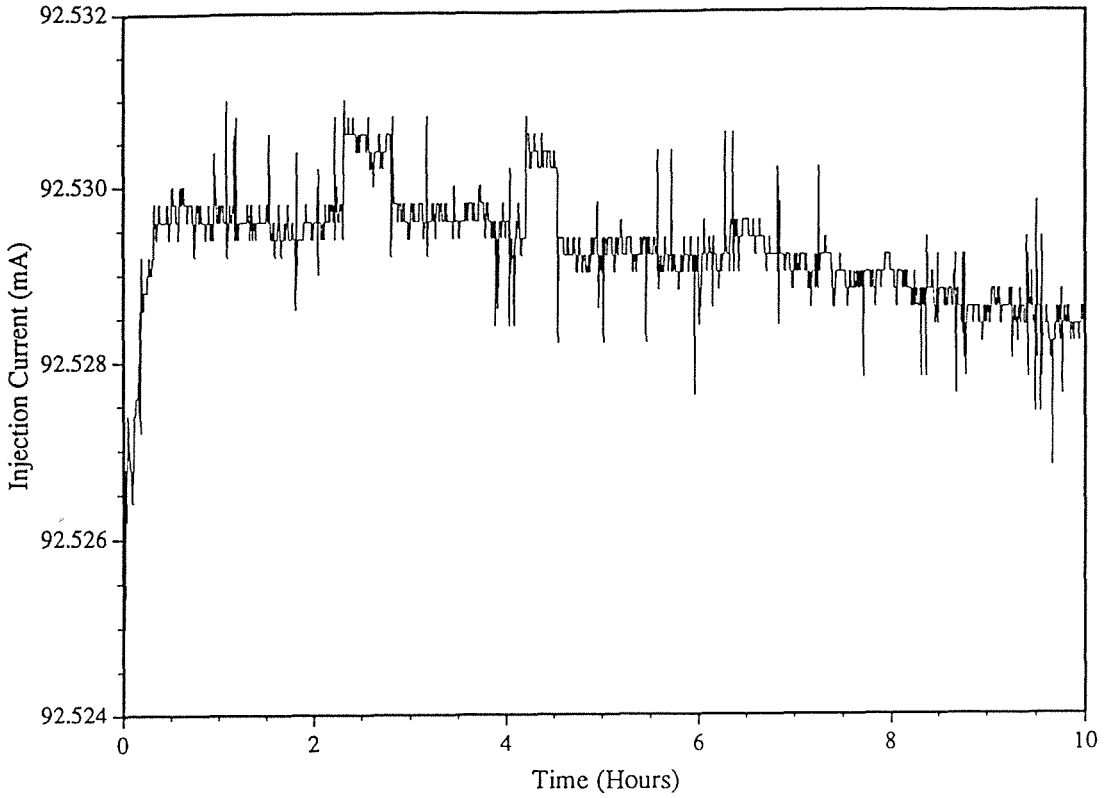

Figure 3.2. Injection current variation over a 10-hour period.

Figure 3.2 illustrates the current stability. The voltage across the 50-Ω resistor was monitored using a Philips PM2535 System Multimeter (with a 20-ms averaging time) while the laser was operating near 92 mA. Following a 20-minute warm up period, during which the current increased by 5 μA, the current remained stable to within ± 1 μA and drifted by only 1.2 μA in over 10 hours. The accuracy of the multimeter is ± 0.1 mV, giving a current accuracy of ± 2 μA. Hence, the values plotted in Figure 3.2 reflect the resolution limit of the meter. The short-term stability up to 20 ms, measured using an oscilloscope, was found to be about 8 μA peak-to-peak. The maximum error of the 12-bit D/A converters (± 0.5 LSB) implies a maximum contribution to this current noise of ± 12 μA. This would be reduced to less than ± 1 μA by using 16-bit D/A converters, but at increased cost. Any remaining noise is due to the current amplifier, and could possibly be reduced by replacing this component by a less noisy one, such as a single transistor, should such a component become available.

The linearity of the current ramp was also measured with the Philips multimeter for each range, again with the bias current set near 92 mA. The result with the 8.2-kΩ ramp resistor selected is shown in Figure 3.3. The upper line shows the change in current as the ramp counter was swept and has a slope of

$(5.0560 \pm 0.0002) \times 10^{-3}$ mA per count, indicating good linearity. The residuals resulting from subtraction of the measured values from the best-fit straight line are shown in the lower curve. The other scan ranges also produce similar accuracy for the slopes. The linearity of the laser frequency scan will be discussed in Section 4.6.

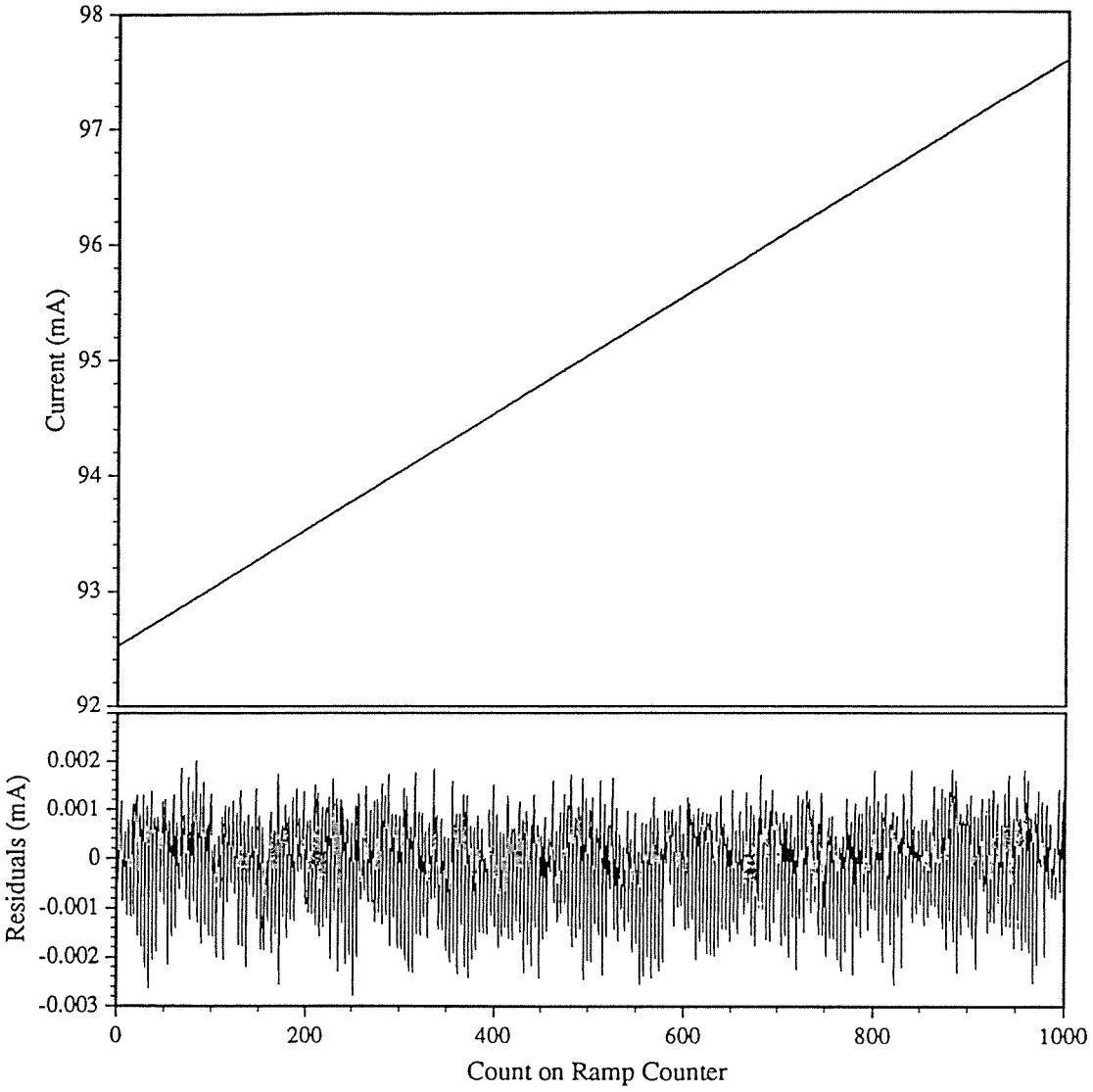

Figure 3.3. Linearity of current ramp for the 8.2-kΩ ramp resistor. The upper line gives the change in current as the ramp counter is scanned and the bottom curve corresponds to the difference between the measured current values and the best-fit straight line.

3.3. Temperature Controller

A standard heater/cooler circuit is used as a temperature controller. This is shown in Figure 3.4. The circuit uses a thermistor to sense the laser's temperature and a peltier element to heat or cool the laser in response to a change in temperature. A constant current (0.2 mA) is fed through the thermistor to ground producing a voltage drop proportional to the resistance of the thermistor. Once calibrated, the temperature of the thermistor can be obtained through a measurement of this voltage drop (V_{th}). The temperature is set by varying the voltage at the temperature-set point (V_{TS}), either internally through a 10-turn 20-kΩ potentiometer or by applying an external voltage. This causes the temperature to oscillate about the set point with decreasing amplitude. These oscillations typically die out in less than 10 minutes.

A schematic of the laser mount is illustrated in Figure 3.5. The laser is electrically isolated from its aluminium mounting plate by a thin sheet of mica. A collimating lens can be positioned in front of the laser by sliding it inside a perspex cylindrical sleeve attached directly to this plate. The thermistor is mounted inside a drilled hole as close as possible to the laser. The peltier element is sandwiched between the mounting plate and an aluminium heat sink. All other contact with the mounting plate is made through thermally insulating material. The whole assembly is placed inside a metal box with an opening in the side from which the heat sink fins protrude, and can be tilted relative to the box for alignment. The box helps to isolate the laser from ambient disturbances.

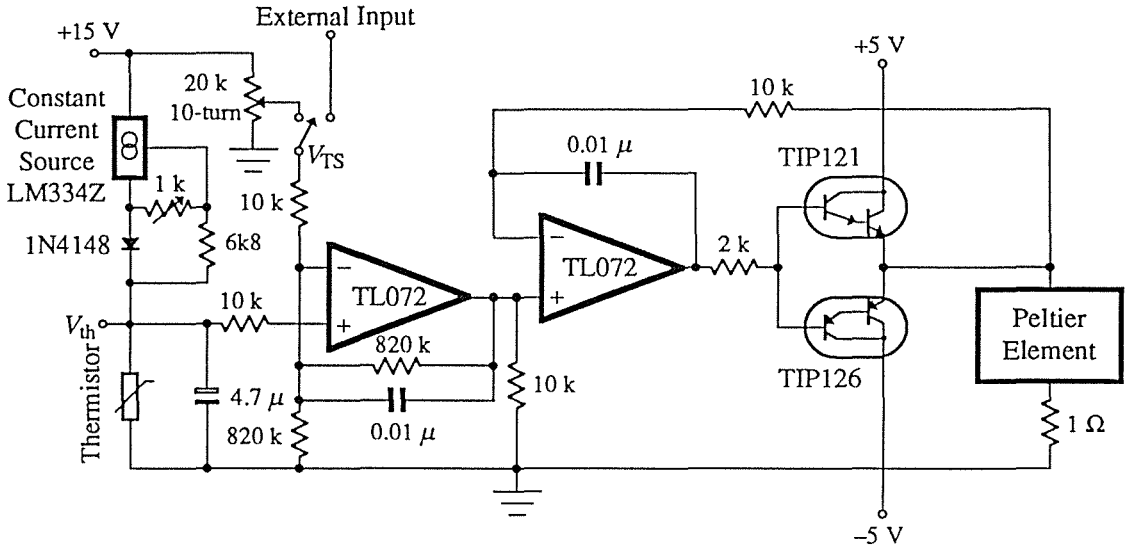

Figure 3.4. Temperature controller for diode laser.

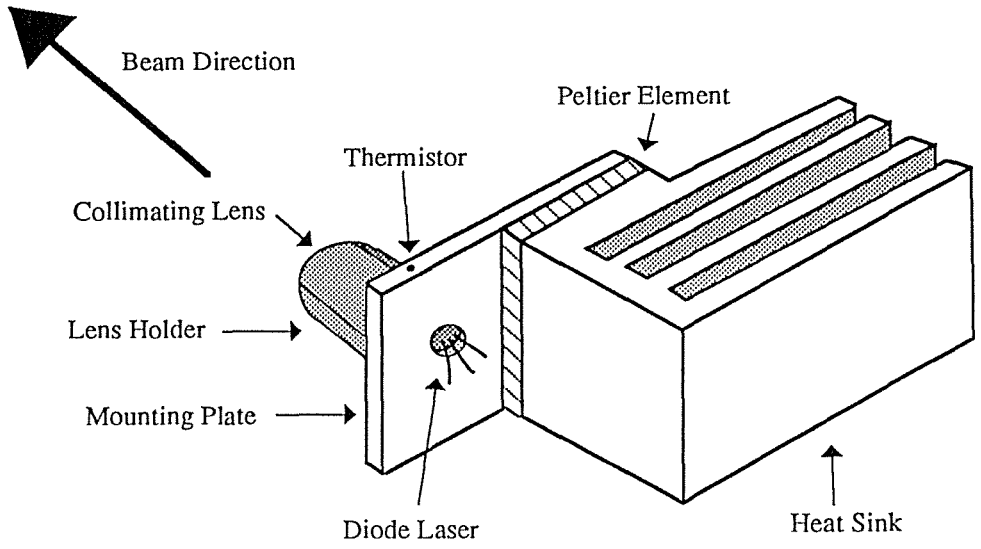

Figure 3.5. Schematic of laser mount.

The unit is capable of a short-term stability of ±1 millidegree when the laser is operating (Figure 3.6(*a*)), although over a long time period the temperature drifts in accordance with room temperature changes (Figure 3.6(*b*)). Over a 10-hour period the laser temperature was observed to change by 10 millidegrees at 32 °C while the room temperature varied by 1.5 °C. However, during the course of a typical spectroscopy experiment (about 1 minute) the room temperature would not be expected to fluctuate by more than about 0.02 °C. Other, more complex, circuits have been constructed[50–52, 47] which can achieve stabilities of ±10, 15, 100, and 300 microdegrees, respectively.

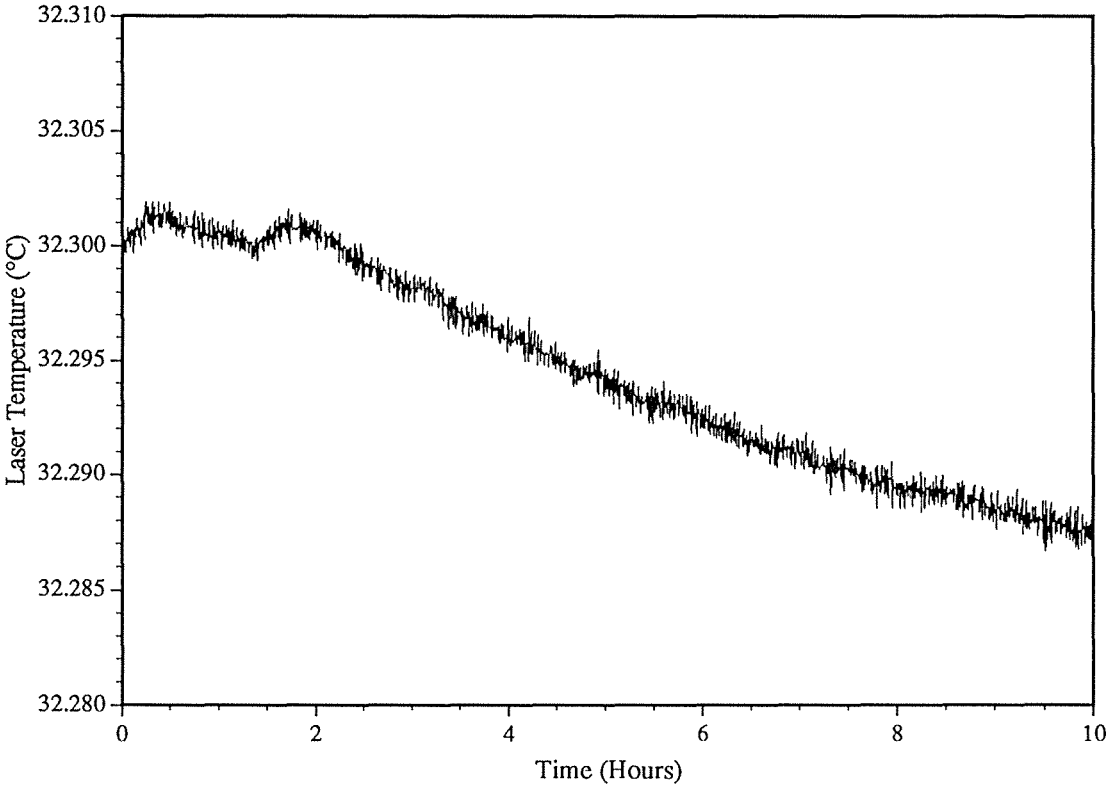

Figure 3.6(*a*). Variation in laser temperature over a 10-hour period. Short term fluctuations were within ±1 mdeg and the long-term drift of 10 mdeg is due to a drift in ambient temperature of 1.5 °C (see below).

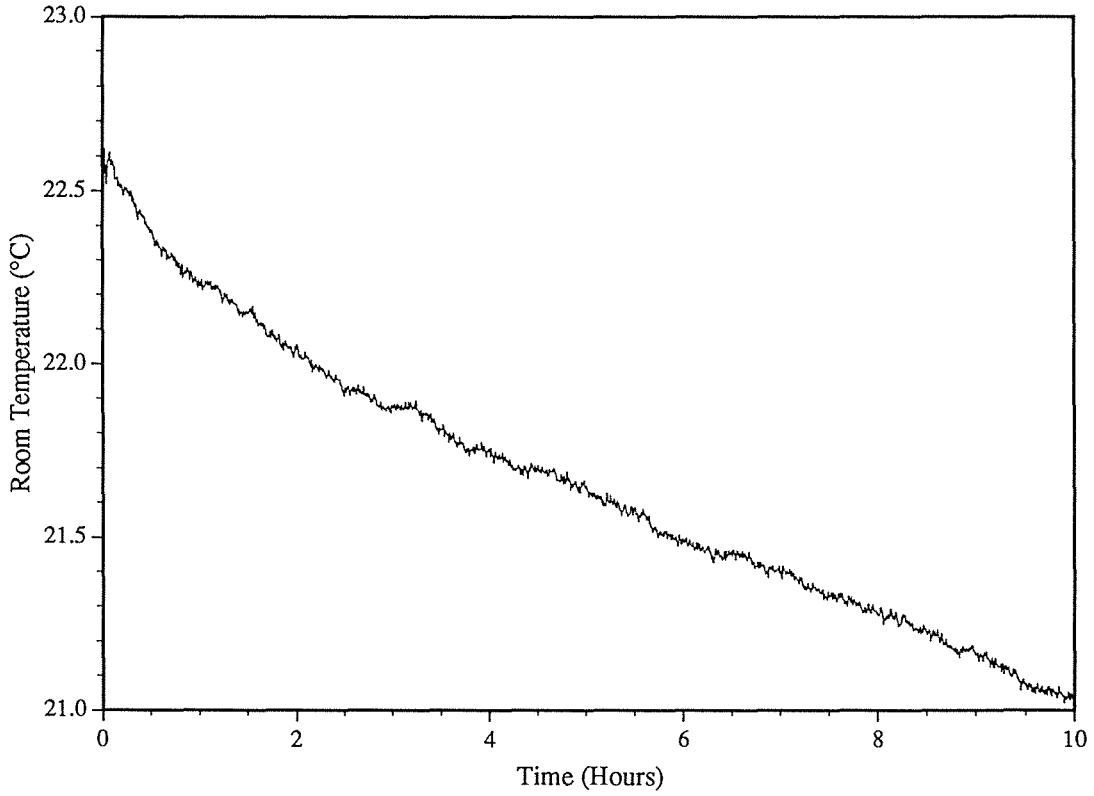

Figure 3.6(*b*). Drift in ambient temperature over the 10-hour period for which the laser temperature was monitored.

3.4. Data Acquisition and Control Unit

3.4.1. Introduction

This section describes a multipurpose data acquisition and control unit which acts as an interface between various pieces of experimental apparatus and a micro-computer. The interface was built around a Motorola MC6809 8-bit microprocessor and provides:

(*i*) eight multiplexed analogue input channels using a 12-bit A/D converter (–4 to 4 V range);
(*ii*) one analogue output channel using a 12-bit D/A converter (0 to 10 V range);
(*iii*) four TTL output lines;
(*iv*) three TTL input lines;
(*v*) one bi-directional asynchronous RS232 communication channel.

All commands to the interface are input via a second bi-directional RS232 channel, which in most situations would be connected to a computer. Output from the interface is available only via this channel.

The motivation for developing this unit was derived from the need to fulfil two main requirements. The first was to obtain wavelength maps of several diode lasers in order to select the temperature and injection current values needed for operation at the desired wavelengths. This involved automatically setting both the temperature and injection current, and scanning a spectrometer to determine the peak wavelength for the settings. The second purpose for the interface was to produce atomic spectra by automatically scanning the laser injection current while simultaneously recording the laser signal from a photodiode. These methods will be discussed in later sections, as well as other experiments performed with the aid of the interface.

3.4.2. Operation of the Interface

The interface responds to a set of commands sent to it via the RS232 communication channel with the capability of performing particular tasks and sending data back along this channel. Each command consists of a control character (*A* to *R*) followed by a number of data characters and/or optional characters. These are all listed and explained in Appendix *B*.

3.4.3. Design of the Interface

A block diagram of the interface is shown in Figure 3.7. Its operation is controlled by software stored in ROM on the processor board via the MC6809 microprocessor chip. This board also accommodates the serial and parallel input/output ports for communication with peripheral devices external to the microprocessor.

The parallel lines are responsible for getting information to and from the A/D and D/A converters, and provide a direct link with the TTL lines. The processor board has only one serial port which needs to provide access to two RS232 ports, one for communication with a computer (in this case a Macintosh Plus) and the second for communication with an external device (in this case a SPEX Compudrive which drives a SPEX 1870 Spectrograph). It is never necessary to access both ports simultaneously, but rather to switch between them. This is accomplished by the switching circuit in Figure 3.7, which is a logic switch controlled by a binary switching signal determined by the microprocessor and sent out via the parallel port. When the

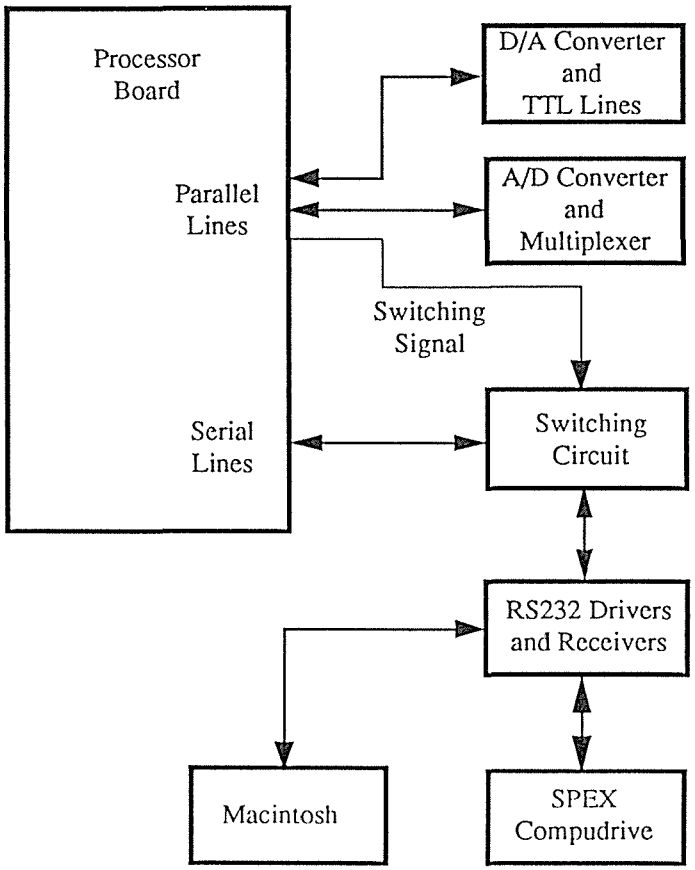

Figure 3.7. Block diagram of the interface.

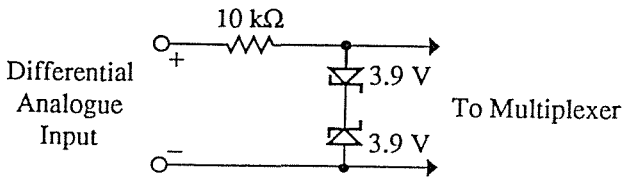

Figure 3.8. Input protection for eight-channel multiplexer.

interface is first turned on, the RS232 port connected to the computer is enabled, as is also the case at the end of a command sequence. The RS232 drivers and receivers are responsible for converting RS232 signal levels to TTL levels and vice versa.

Detailed information describing each block in Figure 3.7 is given in Appendix *C*, and the software controlling the internal operation of the interface can be found in Appendix *H*.

However, there is one block which merits some attention here: the A/D converter and multiplexer. The multiplexer allows a single A/D converter to serve eight separate analogue input channels. A problem arises if the differential input to the multiplexer exceeds the 5 V supply voltage. To protect the multiplexer from overload voltages two 3.9 V Zener diodes were added to each input, as illustrated in Figure 3.8. For differential inputs with absolute values greater than 2 V the diodes introduce a non-linearity which must be corrected to obtain meaningful readings. A plot of the input voltage versus the output of the A/D converter is given in Figure 3.9. The solid line is a three-piece fit to the curve. For the region of measured values between –2 V and +2 V a linear fit was used, and on either side of this region fifth order polynomials were employed. Since the digital data must be processed by a computer in order to obtain a voltage reading, this correction can be readily applied at the same time. An improvement to the circuit would be to use a larger supply voltage (say 15 V) for the multiplexer. This would permit the use of larger-voltage Zener diodes for protection, thus increasing the linear range beyond the required ±4 V.

The A/D converter (ICL7109) is an integrating converter which performs conversions at a rate determined by an external oscillator. Internal circuitry divides the oscillator frequency by 58 to provide an internal clock. Each conversion involves integration of

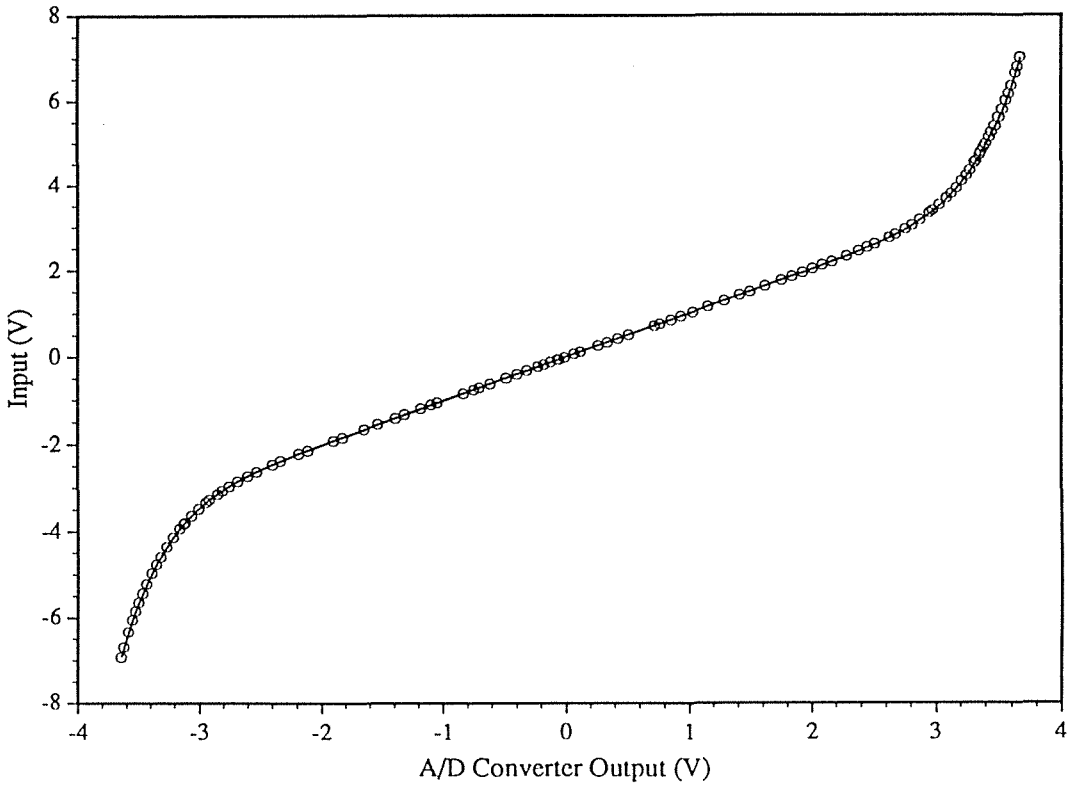

Figure 3.9. Non-linearity introduced by input Zener diodes (circles) with a three-piece polynomial fit (solid line).

the input signal over a fixed time of 2048 clock periods. By choosing the oscillator frequency carefully one can achieve optimal 50-Hz rejection. With f_{osc} = 5.9392 MHz, the integration time is

$$T = (2048 \text{ clock periods})\left(\frac{58}{5.9392 \text{ MHz}}\right) = 20 \text{ ms.} \qquad (3.1)$$

Therefore, any 50-Hz signal present at the input will be integrated out. The maximum total time for one conversion is 8192 clock periods, or 80 ms (corresponding to a full scale reading). Therefore, with a 5.9392 MHz crystal, the ICL7109 can perform a minimum of 12.5 conversions per second. The maximum rate (zero reading) is twice this rate. Thus, the calculation to correct the diode distortion does not slow down the operation of the interface as the A/D converter is relatively slow.

4. Experimental Determination of Diode Laser Properties

4.1. Introduction

In this chapter the particular properties of an actual AlGaAs diode laser are examined and measurements are made of the operating characteristics needed in subsequent experiments.

In Section 4.2 a procedure is described which uses the electronics discussed in Chapter 3 to obtain wavelength maps of several diode lasers in which the injection current and laser temperature are parameters. These wavelength maps facilitate the choice of an appropriate laser for a specific spectroscopic experiment.

Following this, measurements are presented of the tunability of the output frequency with both temperature and injection current, the change in output power with injection current, the temperature dependence of the threshold current, the spatial beam profile, and the linearity of the frequency scan with injection current.

Frequency stability measurements are reported in Sections 4.7 and 4.8. These involve measuring the spectral linewidth using a heterodyne technique and the absolute frequency stability by monitoring an atomic absorption signal. Not only are these measurements pertinent to the saturated absorption experiments of Chapter 6, but they also help to evaluate the effectiveness of the injection current and temperature control circuits.

4.2. Automated Diode Laser Wavelength Measurement System

4.2.1. Introduction

It is essential to know the available lasing wavelengths of a diode laser in order to be able to utilise it in atomic spectroscopy. As discussed in Section 2.3.5, diode laser wavelengths are strongly dependent on both temperature and injection current, with the wavelength predicted to increase approximately linearly with increase of either of these parameters. These continuous tuning ranges are punctuated by mode hops which occur at unpredictable values of temperature and injection current for a given laser. Furthermore, due to the manufacturing process, no two diode lasers have identical wavelength characteristics. The experimenter must examine each laser individually in order to determine its suitability for a particular experiment. This involves changing both the temperature and injection current in a systematic way and measuring the wavelength with, for example, a spectrometer (or wavemeter) for each different setting. To obtain a reasonably high resolution wavelength map manually is an extremely tedious task. This section describes a system designed to carry out this procedure automatically.

4.2.2. Procedure

A block diagram of the wavelength measurement system is shown in Figure 4.1. A micro-computer (Macintosh Plus) was used both to control the entire process and to store the results of the wavelength characterisation. All instructions issued by the computer were passed through the data acquisition and control unit (interface) described in Section 3.4, as were the data received by the computer.

The laser temperature was set by sending a voltage to the analogue output channel of the interface which was connected to the external input of the temperature-set point on the temperature control circuit for the laser (see Section 3.3). Initially, this caused the temperature to fluctuate about the set point. The damping of these fluctuations was monitored by reading the voltage across the thermistor of the temperature controller via one of the eight analogue input channels.

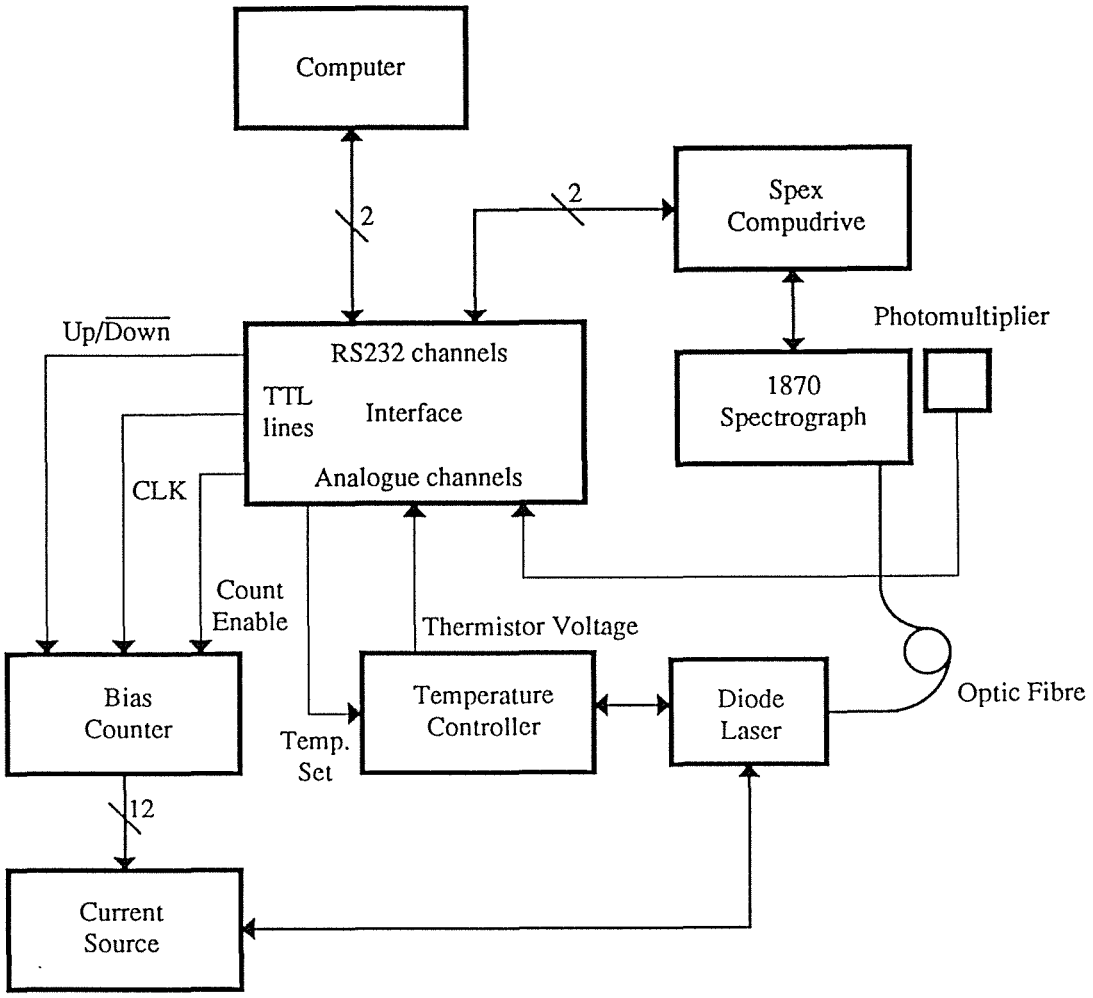

Figure 4.1. Block diagram of wavelength measurement system.

The laser injection current was controlled through three of the TTL output lines of the interface. One line was used to externally clock the bias counter of the laser current source, the second to set the count direction ('high' for up), and the third to enable the counter (active 'low').

The laser wavelength was measured using a Spex 1870 Spectrograph. This is a grating spectrometer (1200 lines per mm) with a wavelength accuracy of ±1.3 Å (over a range of 11 000 Å), a resettability of ±0.3 Å (over the same range), and a step resolution of 0.02 Å. The laser beam entered the spectrometer via a length of optic fibre which allowed the laser to be placed at any position relative to the spectrometer without the need for realigning the beam. Scanning of the spectrometer was performed using a Spex CD2A Compudrive unit. Scanning can be done either directly through the unit's keyboard or remotely via its RS232 communication port. The latter method was used

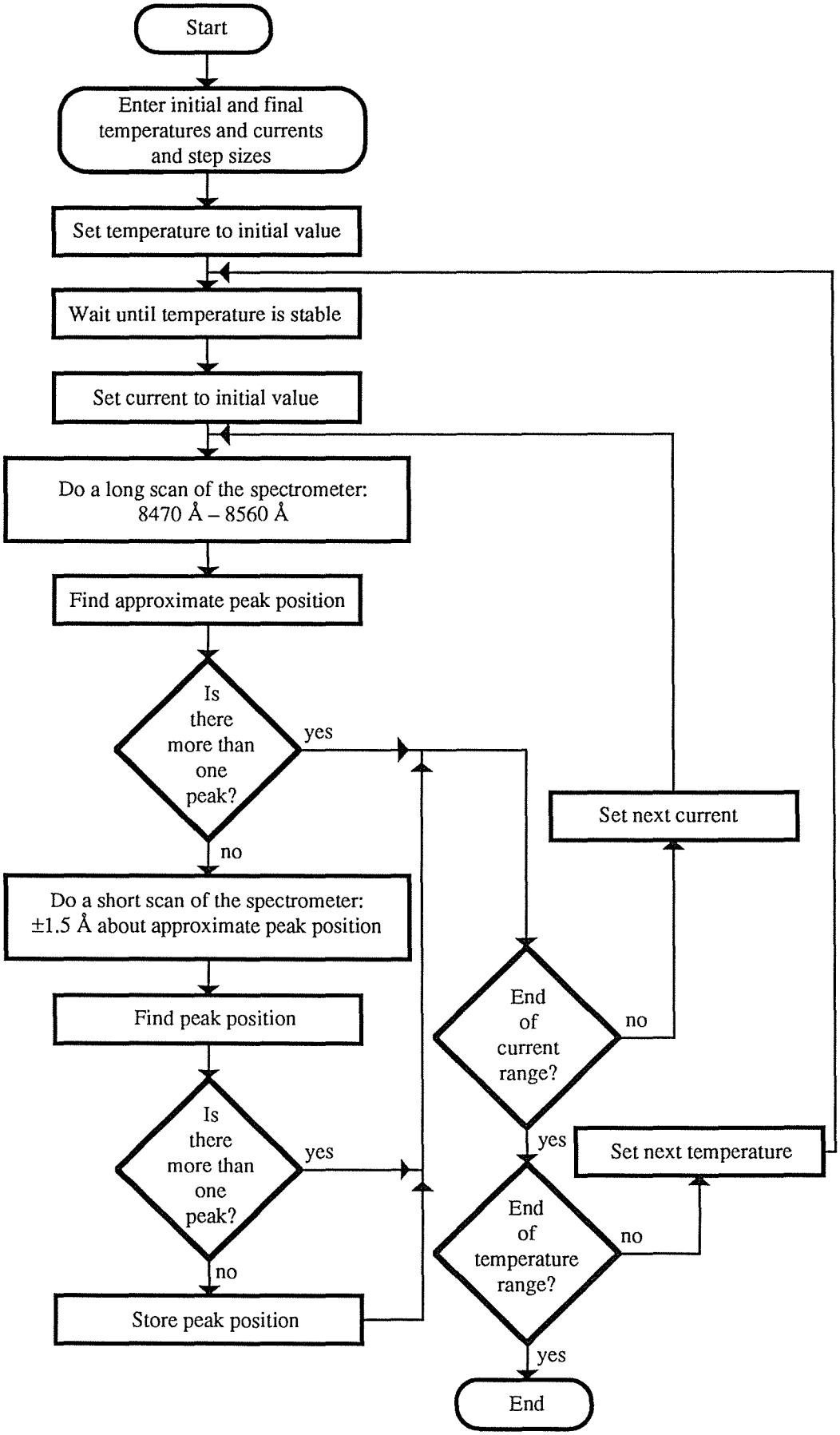

Figure 4.2. Flow chart for wavelength characterisation procedure.

in this application with the computer sending scan information to the Compudrive (start position, end position, scan rate, and when to scan), and the Compudrive sending back the spectrometer's current wavelength position each time it was updated (minimum change of 0.02 Å). The output from the spectrometer was detected by a photomultiplier and read by the computer through a second of the analogue input channels of the interface.

A flow chart of the wavelength characterisation is shown in Figure 4.2. The procedure cycles through two nested loops. For a given temperature the injection current is stepped up through each of its assigned values, then reset by counting down the required number of steps. This is repeated for each temperature. For each combination of the temperature and injection current parameters the spectrometer is scanned twice. The first scan is a coarse scan from 8470 Å to 8560 Å (this is the gross tuning range of the lasers used) at a rate of 1 Å per second. This scan is used to locate the approximate laser wavelength. The second scan is a fine scan of length 3 Å about the approximate wavelength position at a rate of 0.02 Å per second (maximum resolution rate). During these scans the computer stores each wavelength position and corresponding photomultiplier reading. These data are analysed to determine the peak wavelength and whether there exists more than one peak. This situation can occur either for critical parameters leading to the onset of mode hopping or for multi-mode operation. The former situation arises because at a given temperature and injection current the output can be bi-stable between two modes. Because of the relatively long time required to perform a complete scan, a peak can be detected at the wavelengths of both modes. An arbitrary criterion was chosen to determine the presence of a second peak. Namely, any peak with an intensity greater than 10% of the highest peak was defined as a second peak.

4.2.3. Wavelength Maps

Wavelength maps of four Hitachi HL8314E diode lasers were obtained using the above procedure. These lasers had been wavelength-selected for 852 nm (corresponding to the caesium D_2 transition). The wavelength emitted by each laser was measured for injection current values from ranging 70 mA to 120 mA in steps of 0.5 mA, and for temperatures between 20 °C and 30 °C in steps of about 0.4 °C. This gave about 2500 values for each laser. From the scan rates mentioned above, the scan time required for each reading is 4 minutes. Including the dwell time necessary for thermal equilibrium and the time needed for additional processing, each reading required on average

5.6 minutes. Hence, 2500 readings took the somewhat excessive time of 9.7 days to complete, and this was for each laser! However, because of the entirely automated nature of the process, it could be performed during those hours of the day which are devoted to more social or essential activities, and temporarily halted when the apparatus was required for more pressing functions. Thus, the wavelength map of each laser was slowly built up until a complete picture was obtained. Of course, the results could be achieved in a shorter time if one were interested only in a more limited range of wavelengths, thus reducing the coarse scan time.

The results of the wavelength characterisation for each of the four lasers are shown in Figure 4.3. The lightly shaded regions indicate continuously tunable ranges with single-mode operation, and are numbered arbitrarily such that different numbers for a given laser correspond to different modes. Heavy shading corresponds to regions in which two or three modes can lase simultaneously. These regions are those where mode hopping occurs. Unshaded regions appear where the characterisation process failed to select a unique wavelength for the corresponding injection current and temperature parameters. These regions can also correspond to mode hopping. It should be noted that the region boundaries have been drawn only approximately. Within a single-mode region the wavelength varies approximately linearly along directions with constant injection current or temperature.

Mode hopping normally occurs in one of two forms. One of these includes hysteresis[23] and the other is accompanied by mode-competition noise[53] (and its associated power dropout[54]) between two modes. Either one or the other of these two types of mode hopping was found to occur distinctly for various combinations of temperature and injection current settings for individual transverse-junction-stripe AlGaAs diode lasers in a study by Hori *et al.*[55] The hysteresis phenomenon was observed to occur more prominently at lower temperatures (over the range 5 °C to 30 °C) and higher injection currents (from threshold up to about four times threshold), while mode-competition noise was more prominent towards the other extremes.

The hysteresis phenomenon allows lasing at two (or more) distinct wavelengths for the same values of injection current and temperature, according to whether these values were approached from above or below. The output wavelength is always stable in these regions and there exists a sharply defined mode hopping point. Mode hopping with hysteresis occurs for some parts of the heavily shaded regions in Figure 4.3.

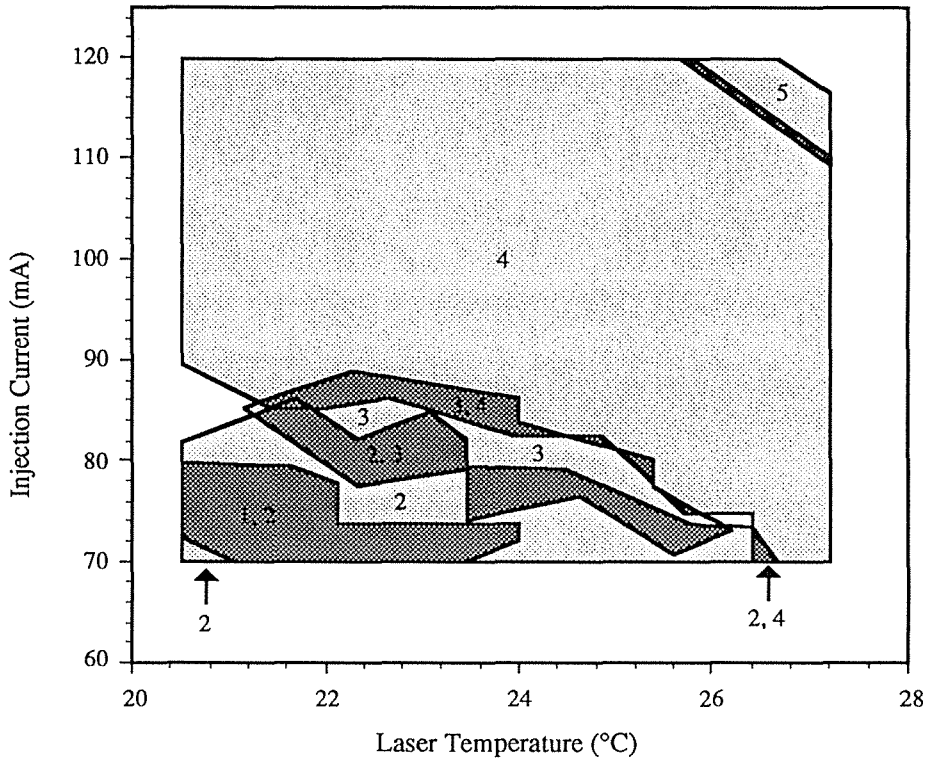

Figure 4.3(*a*). Wavelength map for laser 1. Light shading represents stable single-mode operation, while heavy shading indicates two-mode and three-mode operation (mode hopping). Areas with no shading correspond to failure of the system to find a unique wavelength. The modes have been numbered arbitrarily, and are centred about the following wavelengths—1: 847.151 nm; 2: 848.293 nm; 3: 849.931 nm; 4: 850.654 nm; 5: 851.109 nm.

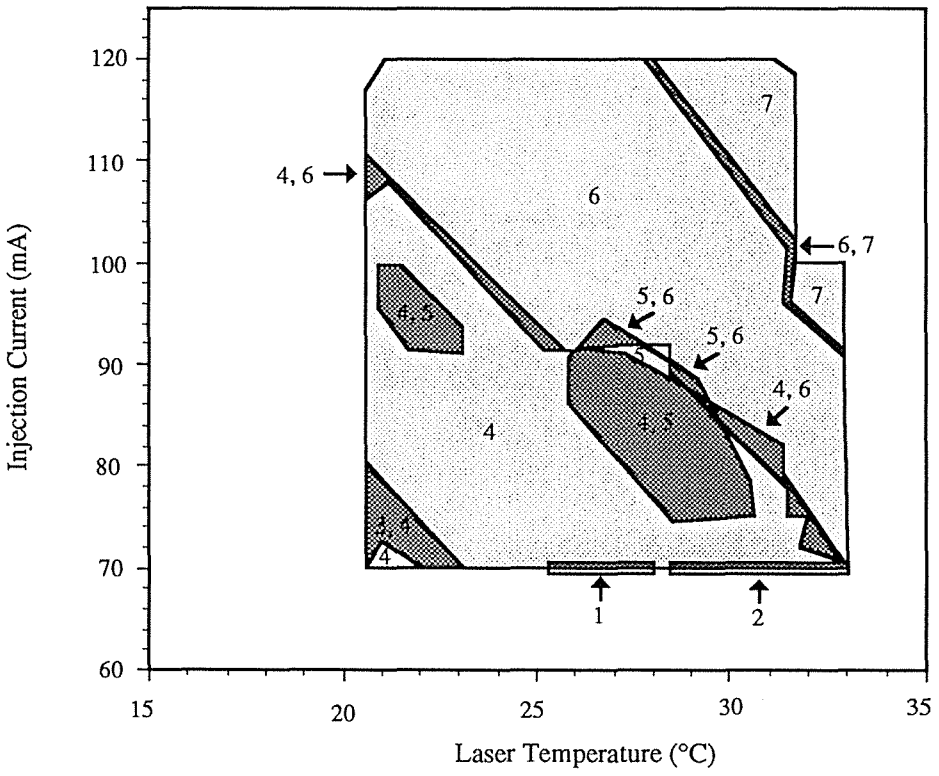

Figure 4.3(*b*). Wavelength map for laser 2. The numbered modes are centred about—1: 845.883 nm; 2: 848.980 nm; 3: 849.261 nm; 4: 849.863 nm; 5: 850.652 nm; 6: 851.840 nm; 7: 853.399 nm.

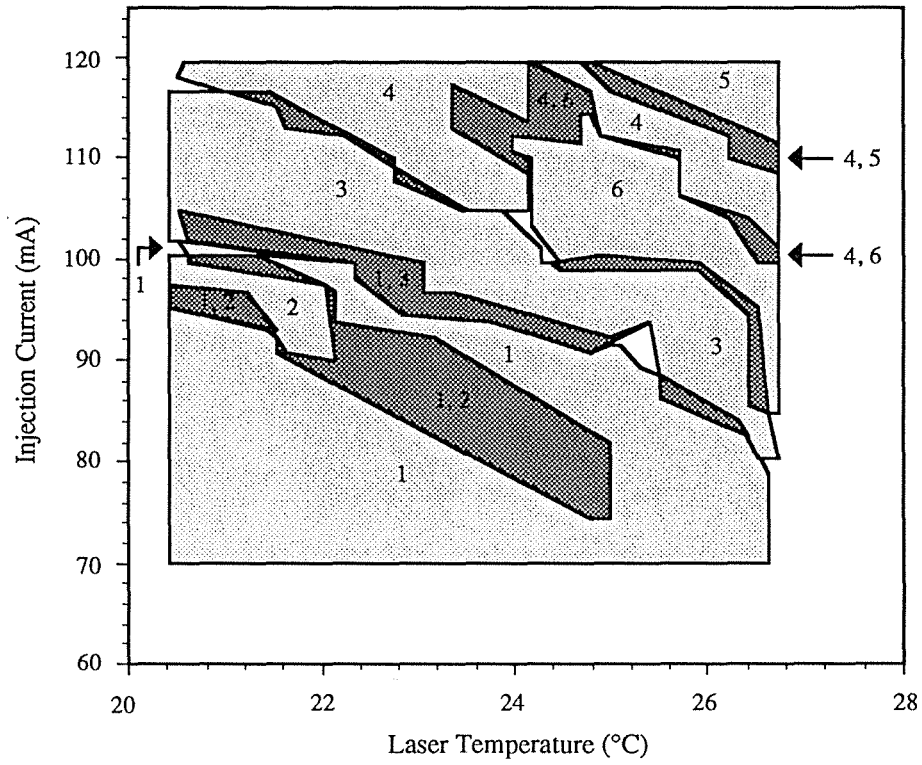

Figure 4.3(*c*). Wavelength map for laser 3. The numbered modes are centred about—1: 848.028 nm; 2: 849.648 nm; 3: 850.255 nm; 4: 850.714 nm; 5: 851.212 nm; 6: 853.032 nm.

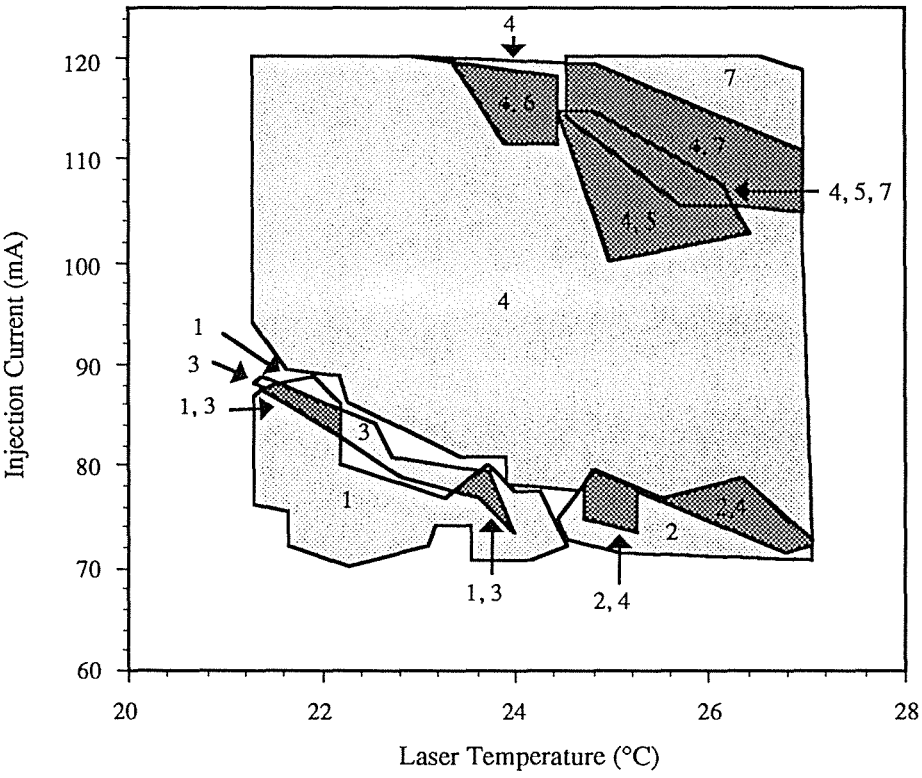

Figure 4.3(*d*). Wavelength map for laser 4. The numbered modes are centred about—1: 849.173 nm; 2: 849.469 nm; 3: 850.212nm; 4: 850.789 nm; 5: 851.353 nm; 6: 851.664 nm; 7: 852.533 nm.

However, these regions do not correspond exclusively to mode hopping with hysteresis because the temperature was always increased and the injection current was only decreased at the end of its range.

Mode-competition noise occurs where the lasing wavelength randomly fluctuates between two modes. The rate of fluctuation varies over several orders of magnitude as the temperature and injection current are changed. Mode-competition noise is illustrated in Figure 4.4(*a*), while Figure 4.4(*b*) shows power dropout where there is a transient increase in a side mode power at the expense of the main lasing mode power. These plots show the simultaneous power in two modes of laser 2 in Figure 4.3(*b*) over an interval of time. They were obtained by spatially separating the modes with a diffraction grating and monitoring the power in each with separate photodiodes. The signals were recorded with a two-channel storage oscilloscope. Note the exclusivity of the two signals. The transition from Figure 4.4(*a*) to Figure 4.4(*b*) occurred through a change in injection current of 1.36 mA at a fixed temperature of 25.8 °C. Since the mode switching can occur quite slowly (Hori *et al.*[55] have observed switching intervals up to 240 s), parts of the heavily shaded regions in Figure 4.3 also correspond to this type of mode hopping.

It follows from this discussion that the wavelength maps on their own cannot be used as a study of mode hopping. However, they do indicate regions of stable single-mode operation, and by perusing the wavelength tables from which the plots in Figure 4.3 were constructed, the appropriate operating conditions for a given experiment can be determined.

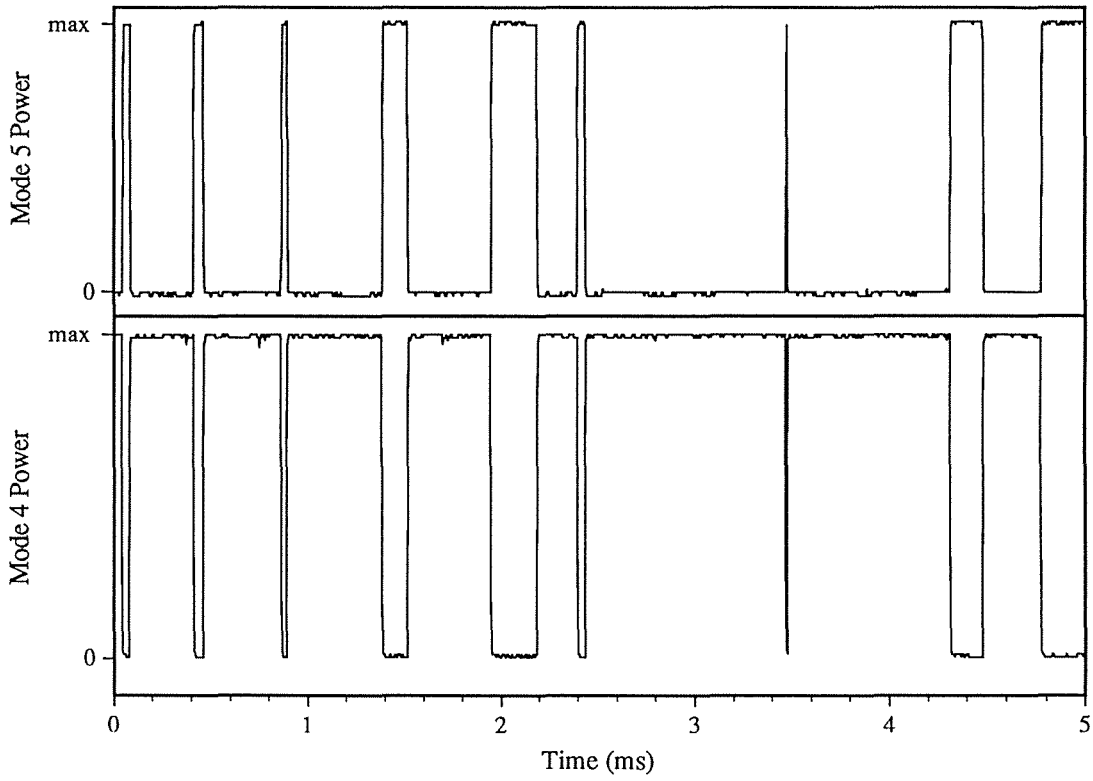

Figure 4.4(*a*). Mode-switching between modes 4 and 5 of laser 2 over a typical time interval of 5 ms, for an injection current of 77.09 mA at 28.7 °C.

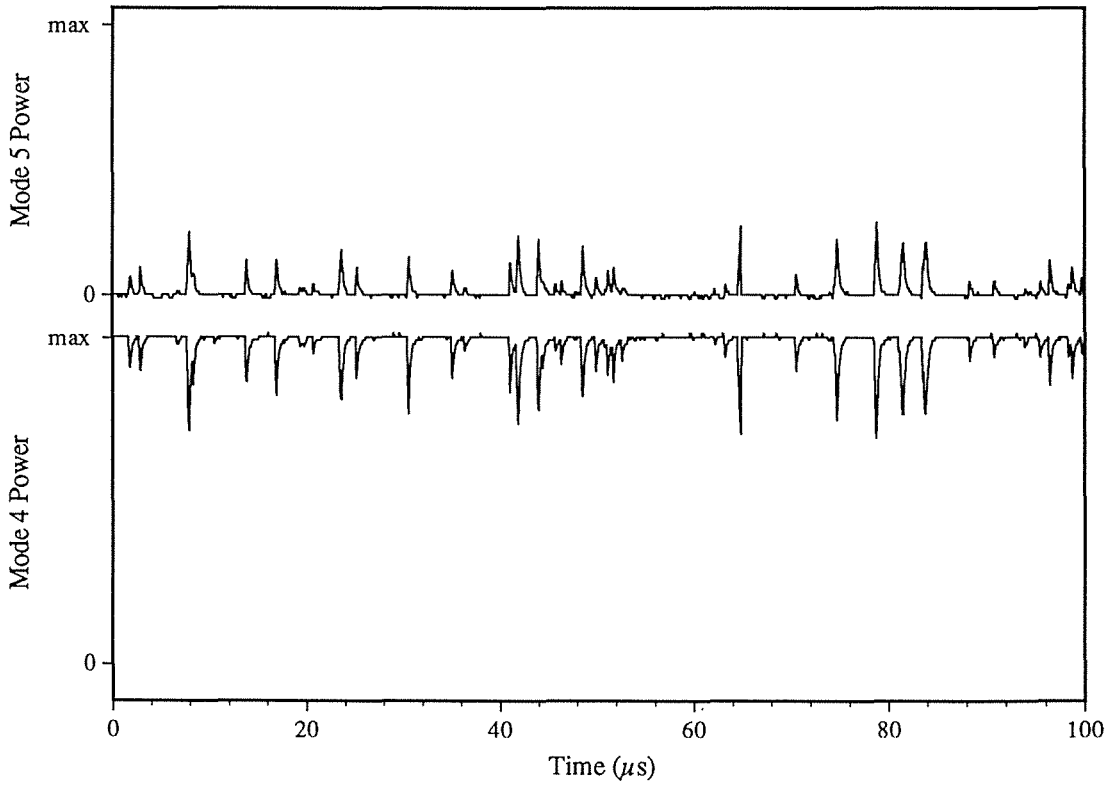

Figure 4.4(*b*). Power dropout from mode 4 into mode 5 for laser 2 over a typical time interval of 100 μs, for an injection current of 75.73 mA at 28.7 °C.

4.3. Injection Current and Temperature Tunability

The data obtained from the wavelength characterisation of a laser described in the previous section can be used to calculate the frequency tunability with injection current and temperature within a given mode for that laser. One of the aims of this research was to stabilise the frequency of a diode laser so that it could be used as a tool for saturated absorption measurements in caesium. A major requirement on the laser is that it be tunable through the 852.1-nm wavelength. Fortunately, one of the four lasers (laser 2 in Figure 4.3(*b*)) has a mode which lases at this wavelength (but unfortunately, the other three do not). Data for this mode will be examined in the following.

Plots of frequency versus injection current and heat sink temperature are shown in Figure 4.5. As expected, both these plots are approximately linear. The variations in the measured values about the best-fit line are principally due to the resettability of the spectrometer (±0.3 Å). Each adjacent measurement on the injection current plot corresponds to consecutive spectrometer scans, while those on the temperature plot were separated by many scans (see Figure 4.2). Hence the greater variation on the latter plot. The slopes give the tuning rates:

$$\frac{\Delta \nu}{\Delta I} = -3.74 \pm 0.05 \text{ GHz/mA} \tag{4.1}$$

and

$$\frac{\Delta \nu}{\Delta T} = -24 \pm 1 \text{ GHz/°C}, \tag{4.2}$$

where $\Delta\nu$ is the frequency change corresponding to changes in injection current, ΔI, or heat sink temperature, ΔT. A more accurate estimate of the rate of change of frequency with injection current will be obtained in Section 4.6 with the aid of a Fabry-Perot interferometer.

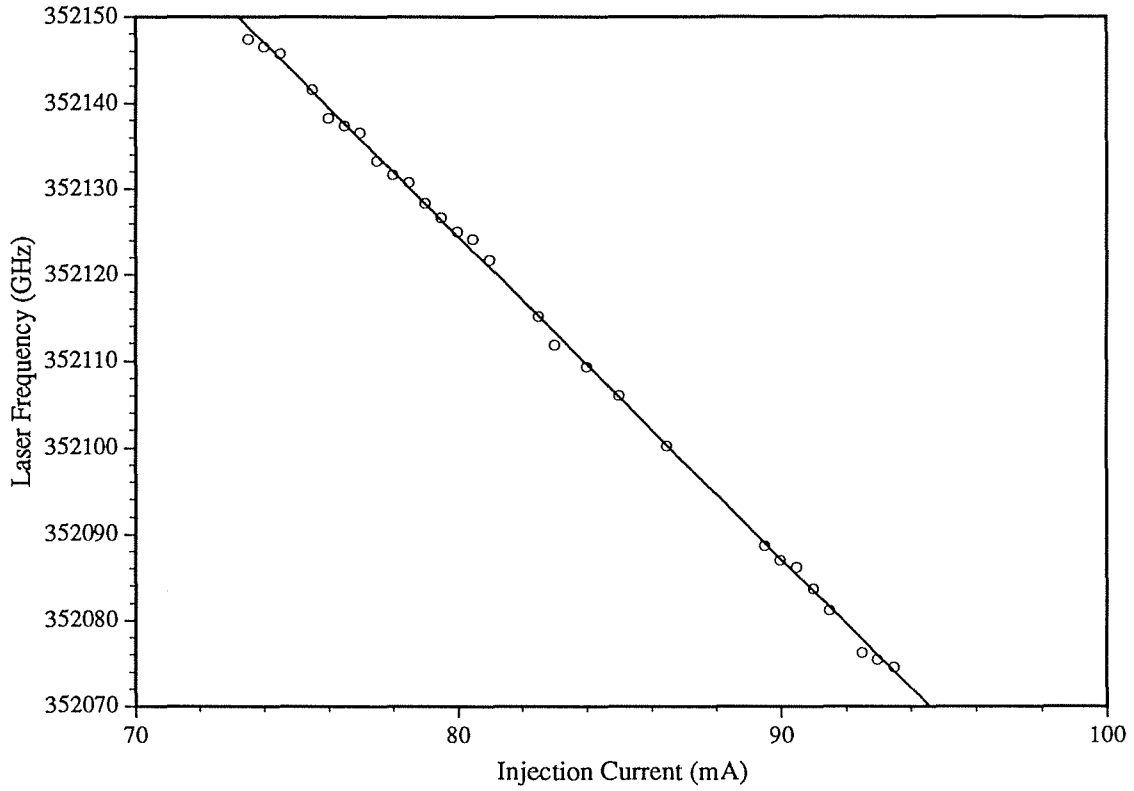

Figure 4.5(*a*). Variation of laser frequency with injection current for a fixed heat sink temperature of 32.2 °C.

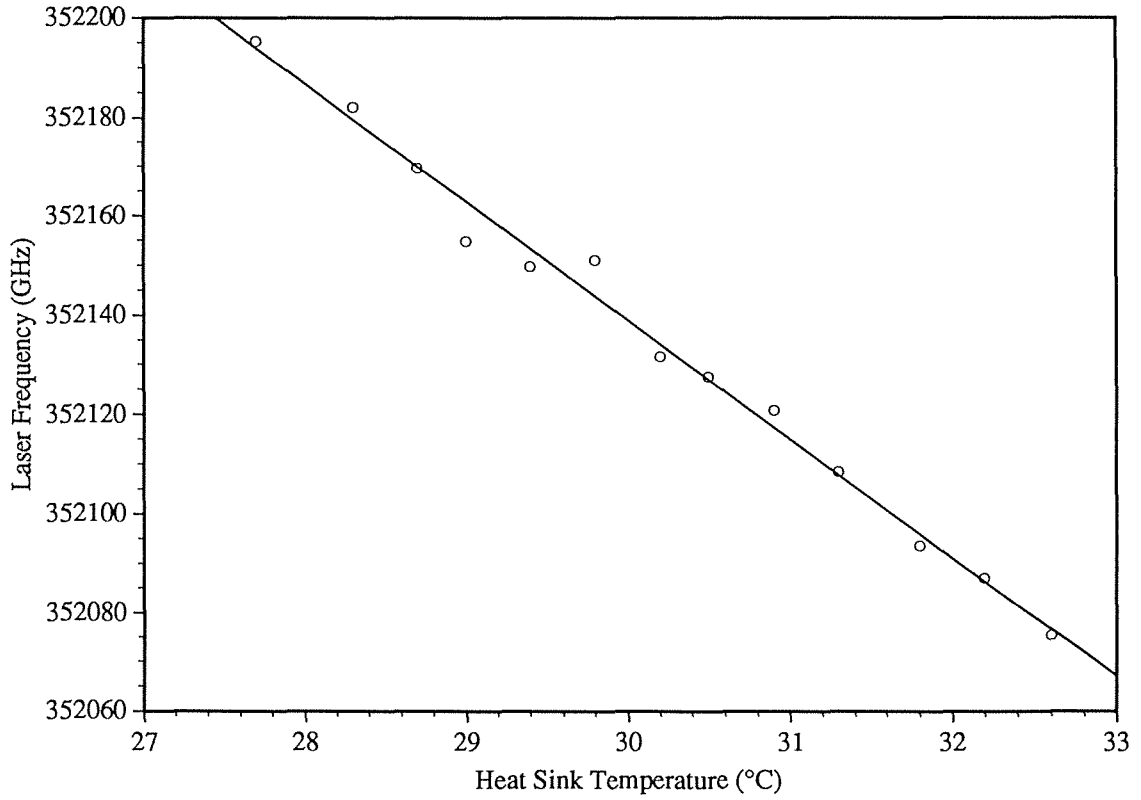

Figure 4.5(*b*). Variation of laser frequency with heat sink temperature for a fixed injection current of 90 mA.

4.4. Output Power versus Injection Current

A typical plot of output power, as measured by a Spectra Physics Model 404 power meter, versus injection current at a fixed heat sink temperature is given in Figure 4.6. The curve was obtained automatically with the aid of the data acquisition and control unit by simply clocking the bias counter from 000 to 999 and recording the power meter reading at each setting. The curve shows the onset of laser action at around 54 mA followed by near-linear increase in power above this threshold current. However, the linear region shows two glitches, one at about 77 mA and the other at about 98 mA, as indicated by the arrows in Figure 4.6. These currents both correspond to mode hopping by more than 10 Å to larger wavelengths and were observed to shift with temperature. As discussed in Section 2.3.4, two competing processes operate to determine the output power as the injection current increases:

$$P = \eta_{ex}(h\nu/e)(I - I_{th}). \tag{2.1}$$

The power is increased due to the greater rate of carrier injection, but is decreased due to the subsequent injection current tuning producing a reduced photon energy. Within single-mode operation the former dominates leading to the linear regions in Figure 4.6,

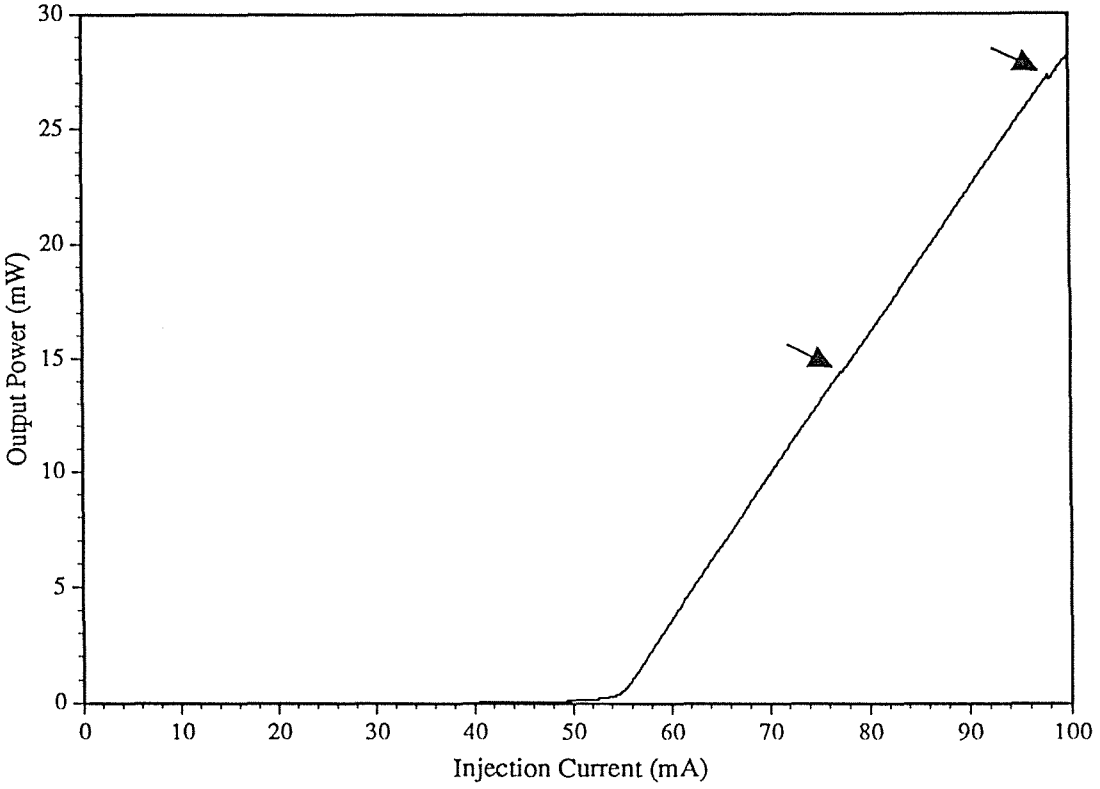

Figure 4.6. Output power versus injection current for laser operating at 32.2 °C. The arrows indicate glitches.

whereas at a mode hop the latter can prevail resulting in the glitches.

The region between the two glitches in Figure 4.6 contains the 852.1-nm wavelength. Fitting a straight line to this section gives

$$P = (0.6261 \pm 0.0009)[I - (54.4 \pm 0.1)], \tag{4.3}$$

where the errors give a 95% confidence interval on the fitted values.

Several sets of data of the type shown in Figure 4.6 were recorded at different heat sink temperatures. From these the threshold current was obtained by extrapolation of the linear region down to zero power. The result is drawn in Figure 4.7. This shows regions of linearly increasing threshold current with temperature and, like Figure 4.6, reflects the mode hopping phenomenon.

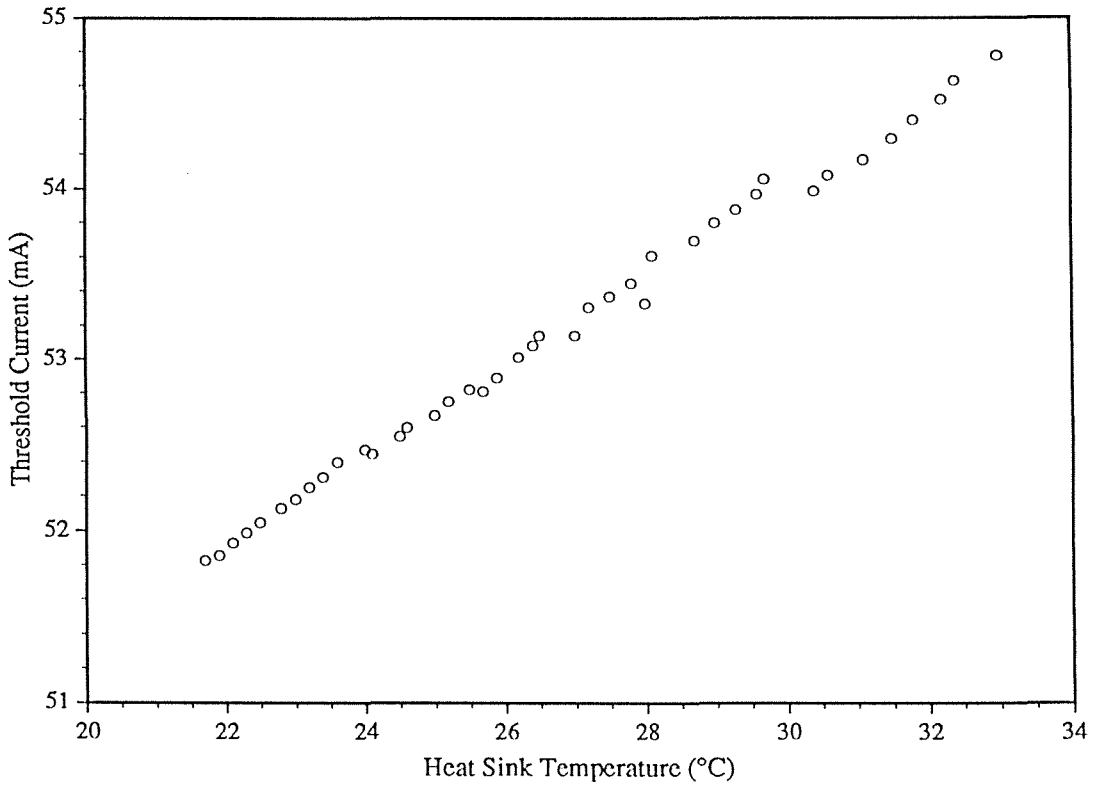

Figure 4.7. Threshold current versus temperature for an AlGaAs diode laser.

4.5. Spatial Beam Profile

Certain experimental studies require detailed knowledge of the spatial laser beam profile and the beam width: in the spectroscopic experiments (Chapter 6) the beam-atom interaction time and the laser field strength are quantities which are strongly affected. The former is determined by the beam width, while for a non-rectangular beam profile, the latter depends also upon the position of the atom in the beam.

The spatial profile was measured by reflecting the beam from a mirror, mounted at the centre of a rotating table, to a power meter positioned directly behind a 25-μm-diameter pinhole. The mirror was rotated in half-minute steps so that the beam was swept across the pinhole. The mirror-to-pinhole spacing was 0.16 m giving a spatial step resolution of 23 μm. The laser was mounted with the junction plane first perpendicular then parallel to the axis of mirror rotation. Two typical profiles are shown in Figure 4.8. The fitted line for each profile is a Gaussian. The experimental profiles were shaped by the collimating lens and mirrors and show some deviation from a pure Gaussian. There is also a side-lobe present in the profiles. However, since the profiles are approximately Gaussian, the fits were used to extract the beam width for each orientation. This produced a width of 430 μm for the junction plane perpendicular to the axis of mirror rotation (Figure 4.8(a)) and 390 μm for the parallel direction (Figure 4.8(b)). These widths correspond to the half width at the e^{-2} point of the Gaussian intensity profile. Letalick and Renhorn[56] have given correction factors for the measured width due to the instrumental effects of a pinhole. For the ratio of pinhole diameter to measured width obtained here, the correction factor is 0.999, and thus is negligible.

The profiles in Figure 4.8 were measured at the position where the caesium cell was to be inserted for the absorption experiments in Chapter 6. Profiles were also measured at different distances from the laser in the absence of all optical elements except the collimating lens. There was no evidence of side-lobes in these profiles. The divergence angle of the beam was on the order of 100 μrad for both orientations.

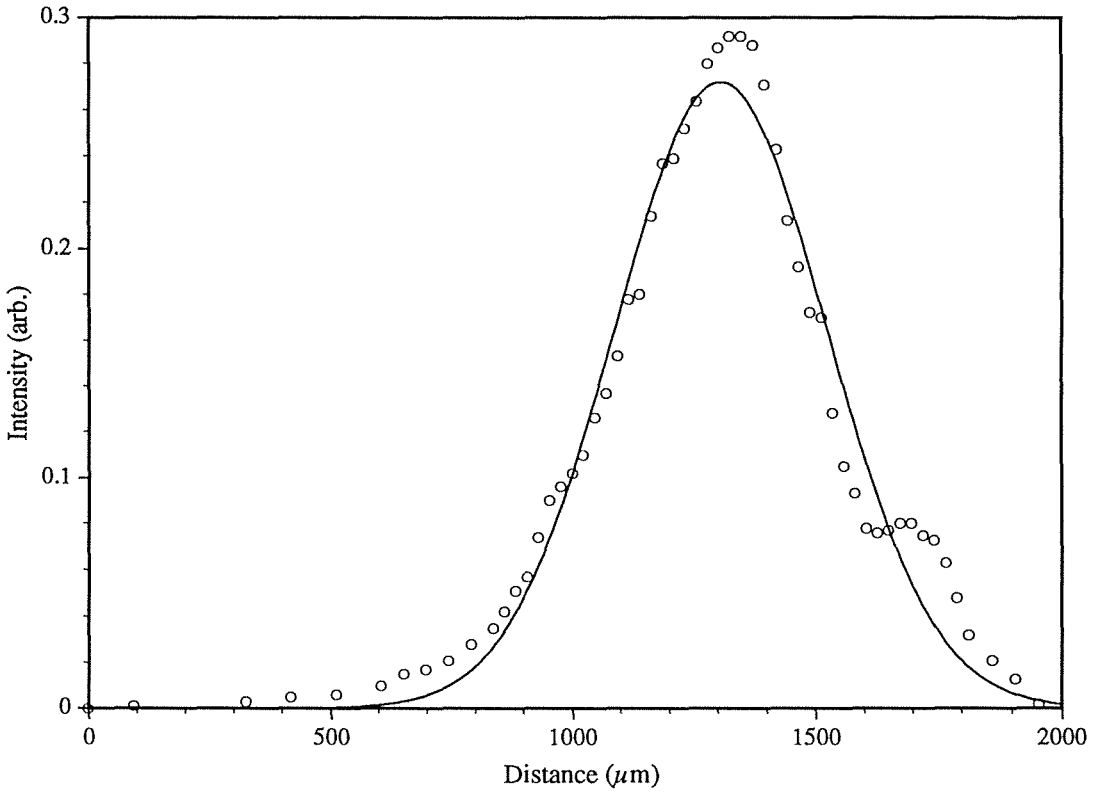

Figure 4.8(*a*). Spatial beam profile (circles) with junction plane perpendicular to the axis of mirror rotation. The solid line is a Gaussian fit.

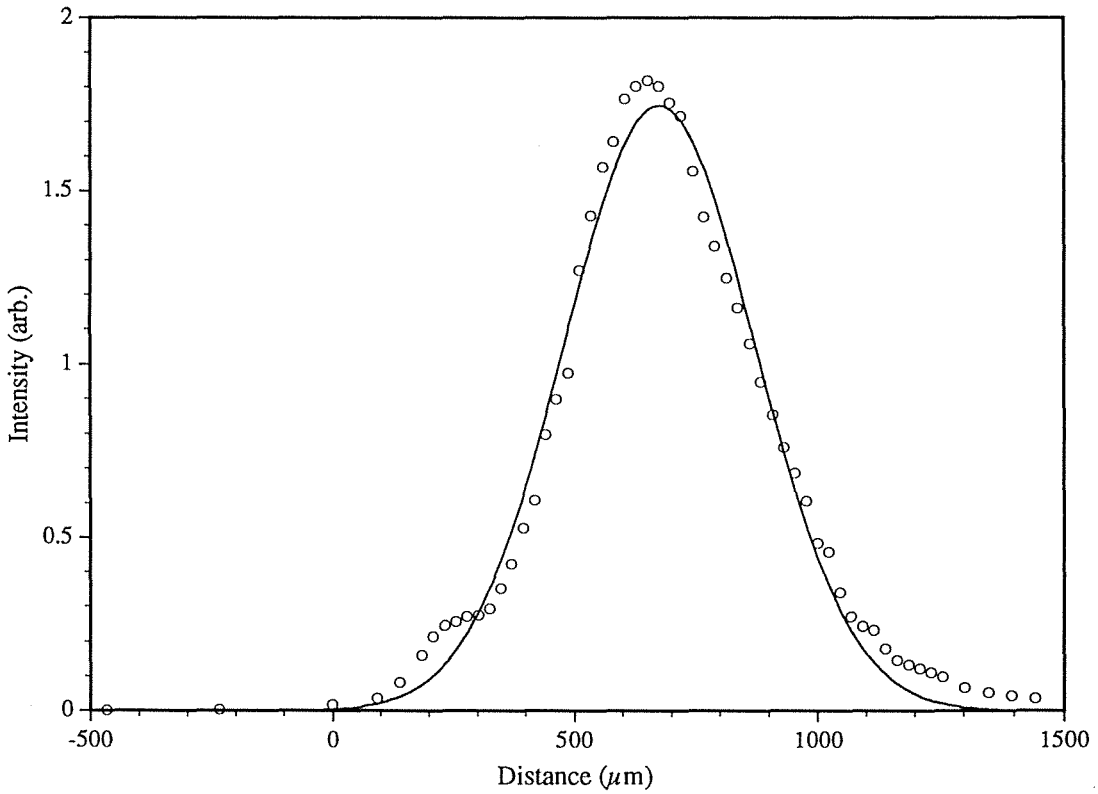

Figure 4.8(*b*). Spatial beam profile (circles) with junction plane parallel to the axis of mirror rotation. The solid line is a Gaussian fit.

4.6. Linearity of Laser Frequency Scan

It was shown in Figure 3.3 that the current increases linearly as the ramp counter is scanned. It is expected that the laser wavelength (and therefore frequency over a small interval) is linear with injection current. A "low resolution" confirmation of this was made in Section 4.3 based on data from the wavelength maps obtained using a spectrometer. However, this was subject to various systematic errors, in particular the limited resettability of the spectrometer. In this section a plane-plane Fabry-Perot interferometer (FPI) is used to make a more accurate measurement of the linearity.

The experiment simply involved passing the laser beam through the FPI, scanning the ramp counter, and recording the resulting fringes detected by a photodiode at the output of the FPI. The beam was slightly misaligned to avoid optical feedback into the laser cavity. The scan duration was approximately 45 s. A typical fringe pattern for the 8.2-kΩ ramp resistor is shown in Figure 4.9. This scan range corresponds to a sweep through the two ground state hyperfine components of the caesium D_2 line (*i.e.* about 10 GHz). The growth in fringe intensity is due to the increase in output power with injection current. There was a slight modulation superimposed on the fringe intensity, possibly due to the presence of other weak "non-lasing" modes in the output spectrum of the laser. The discontinuity at a count of around 800 arose from a mode hop.

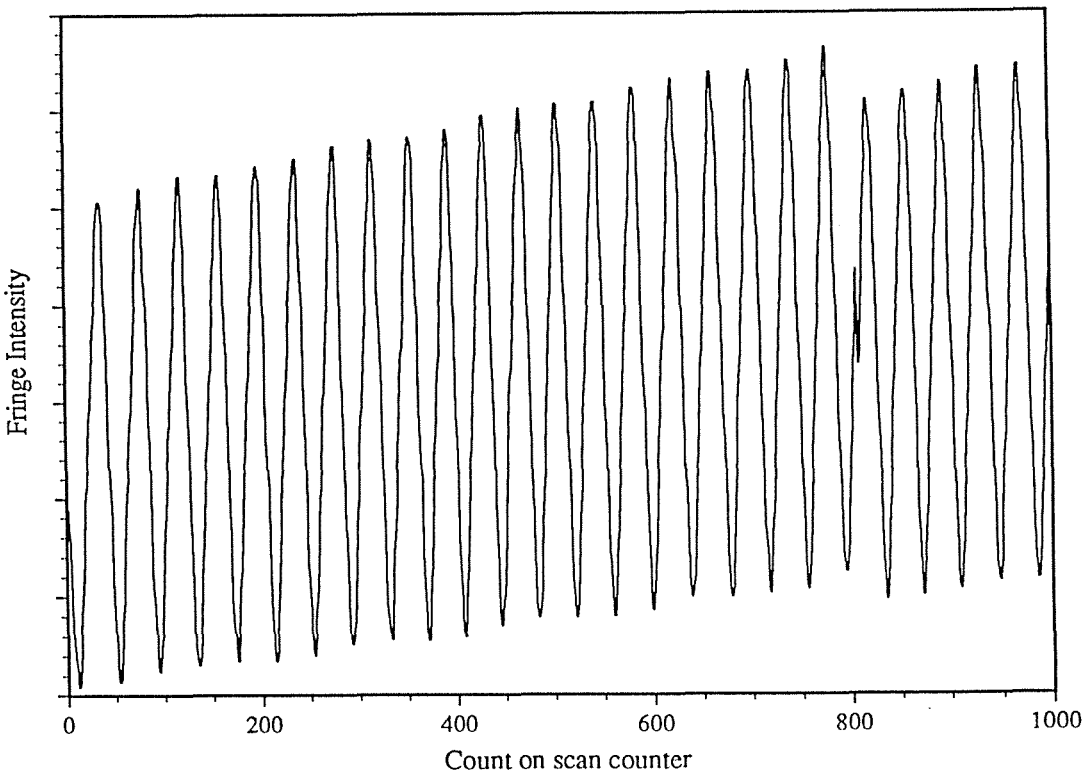

Figure 4.9. Fringe pattern from FPI for 8.2-kΩ ramp resistor.

The free spectral range (FSR) of the FPI was calculated from the mirror separation to be 780.2 ± 0.4 MHz. This determines the frequency scale of the horizontal axis in Figure 4.9. A plot of the peak position against FSR number is given in Figure 4.10, showing good linearity of the frequency scan. Several sets of data were taken resulting in an average count rate of 39.1 ± 0.3 counts/FSR. Using the result from Figure 3.3 for the current change per count, this corresponds to the tuning rate:

$$\frac{\Delta \nu}{\Delta I} = -3.95 \pm 0.03 \text{ GHz/mA}. \tag{4.4}$$

This differs by about 5% from the value obtained from the wavelength maps (equation (4.1)), implying that the latter "low resolution" result gives a reasonable indication of the true value. The residuals in Figure 4.10 imply that the frequency deviation per FSR is about 40 MHz. This is in agreement with equation (4.2) given the short-term laser temperature fluctuations shown in Figure 3.6(*a*).

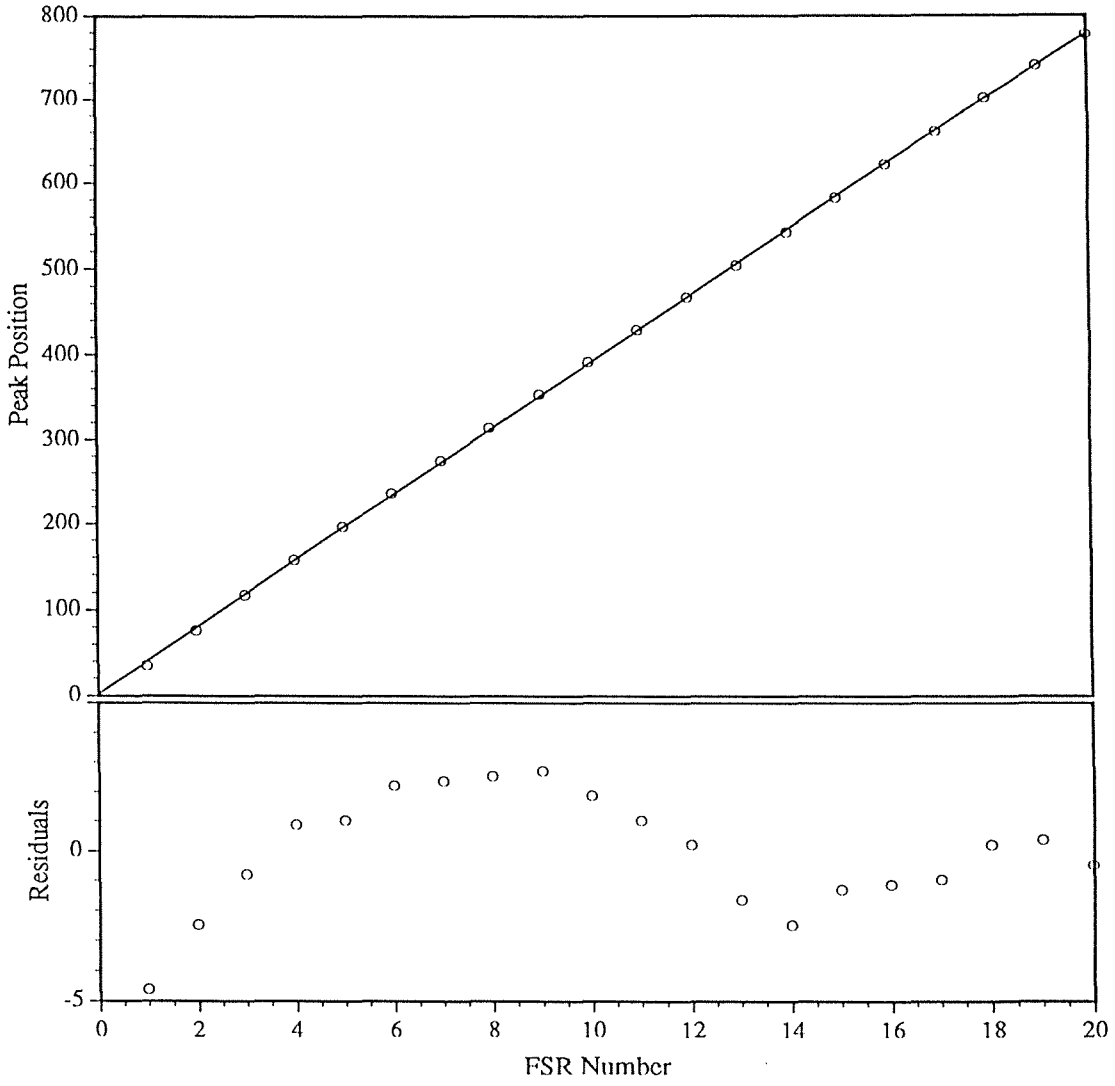

Figure 4.10. Linearity of frequency scan. The upper graph shows the scan counter values for maximum transmission of the FPI (circles), and the lower graph gives the residuals from the linear fit.

4.7. Heterodyne Measurement of Laser Linewidth

4.7.1. Introduction

One of the most important characteristics of the diode laser in both atomic physics research and communications is its spectral lineshape. In performing spectroscopic experiments, for example, it is necessary to know how the laser frequency distribution affects the shape of the measured spectrum. It is fairly well established that the shape of a single longitudinal mode of a diode laser is well approximated by a Lorentzian profile[24]. However, the linewidth of this Lorentzian is strongly dependent upon output power and hence injection current. As discussed in Section 2.3.6, the fundamental linewidth limit of a free-running laser (*i.e.* without optical feedback) is predicted to increase linearly with inverse power, with the proportionality factor dependent on temperature. However, this fundamental limit, due to spontaneous emission into the lasing mode, may not be reached under typical operating conditions mainly due to fluctuations in injection current. Therefore, it is necessary to determine the way in which the lineshape and, particularly, the linewidth vary with output power under the operating conditions appropriate to a particular experiment.

The standard technique of measuring laser lineshapes is to use a scanning Fabry-Perot interferometer (FPI). There are two requirements for this method. First, the finesse of the FPI must be sufficiently high that the instrumental width has a negligible effect on the transmitted fringe shape due to the laser itself, and secondly, the free spectral range (FSR) of the FPI must be appropriate to allow measurement of the lineshape with sufficient resolution over the range of possible linewidths. If this range covers several orders of magnitude, a FPI with an adjustable FSR may be required to obtain fully resolved fringes.

No FPI satisfying these criteria was available, so instead a heterodyne technique was used to measure the laser lineshape. This experiment is described in this section. In Chapter 5, a technique is developed for extracting the linewidth using a FPI for which the conditions discussed above do not hold, thus extending the applicability of the instrument. The results of the present section, as well as being important in their own right, serve as a test for this alternative technique.

4.7.2. Experiment

The measurement of a heterodyne signal has long been used to measure short term frequency fluctuations of lasers[57]. Ideally one beats a laser having an unknown lineshape against a second stabilised laser whose frequency characteristics are well known and whose linewidth is much narrower than that of the laser under scrutiny. This was not possible for the experiment to be described here, so two similar diode lasers operating at nearly the same wavelength were used. One laser (laser *A*) was operated at a fixed temperature of 25.5 °C and a fixed injection current of 76 mA (output power of 14.6 mW), and hence had a constant lineshape within the limits of its stability. The temperature and injection current of the second laser (laser *B*) was varied in a systematic way so that its wavelength remained close to that of laser *A* for a range of output powers.

The experimental arrangement is shown in Figure 4.11. The beams from the two lasers, with the same polarisation, were aligned, using a beam splitter, to fall collinearly onto a high-speed Hewlett Packard 5082-4220 PIN photodiode. It was important to avoid optical feedback into the lasers since this was observed to cause dramatic narrowing of the beat signal. The only offending surface was the input window of the photodiode and this was tilted to steer the reflected light away from the lasers. The photodiode produced a current proportional to the square of the sum of the amplitudes of the two lasers. The response time of the photodiode was about 1 ns. Therefore, the current consisted of a dc component and an ac component at the difference frequency of the two lasers when they were within 1 GHz of each other. This signal was ac coupled to an Anritsu MS68A spectrum analyser, from which the signal was downloaded to a

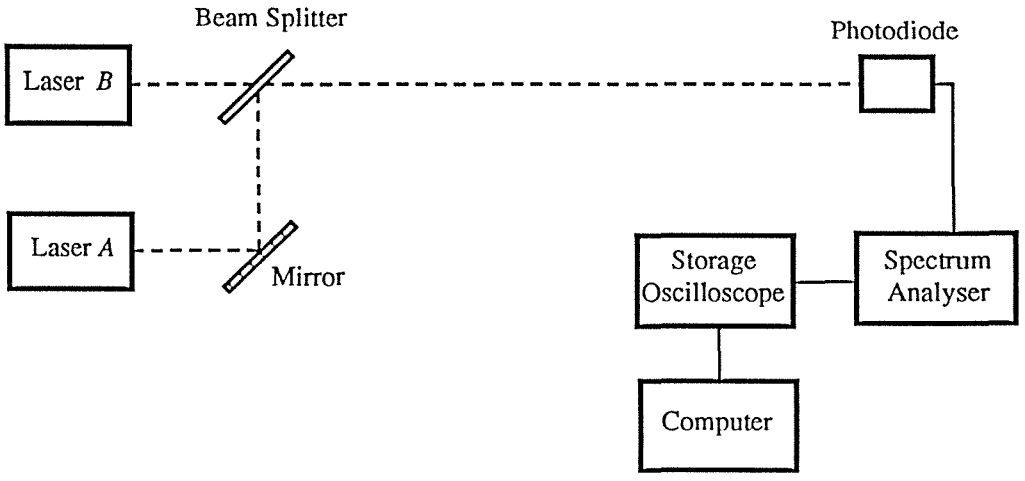

Figure 4.11. Experimental arrangement for heterodyne experiment.

Macintosh Plus computer via a storage oscilloscope and an IEEE interface board (designed and built by R.C. O'Driscoll and R. Dykstra, Massey University). The resolution bandwidth of the spectrum analyser was set to 300 kHz; hence instrumental effects were negligible in the recorded signal.

Several recordings of the beat signal were made for each temperature and current setting. These signals were fitted with Lorentzian profiles: in all cases the data were quite well approximated by Lorentzians—a result that was expected since the convolution of two Lorentzian functions gives a Lorentzian with a width equal to the sum of the two individual widths (see Appendix *D*). A typical fit is shown in Figure 4.12. The fitted parameters are centre frequency, maximum intensity, FWHM, and also the base line (since the signal was arbitrarily positioned on the oscilloscope). Oscillation sidebands, about 2 GHz away from the main lasing mode, and other longitudinal modes, more than 100 GHz away, did not influence the shape of the beat signal since they were well outside the frequency response of the photodiode. A plot of the average total FWHM against inverse power of laser *B* is shown in Figure 4.13. Note that the abscissa does not correspond to the inverse of the *total* output power of laser *B* but rather to the inverse power of the *mode* which was heterodyned. This was

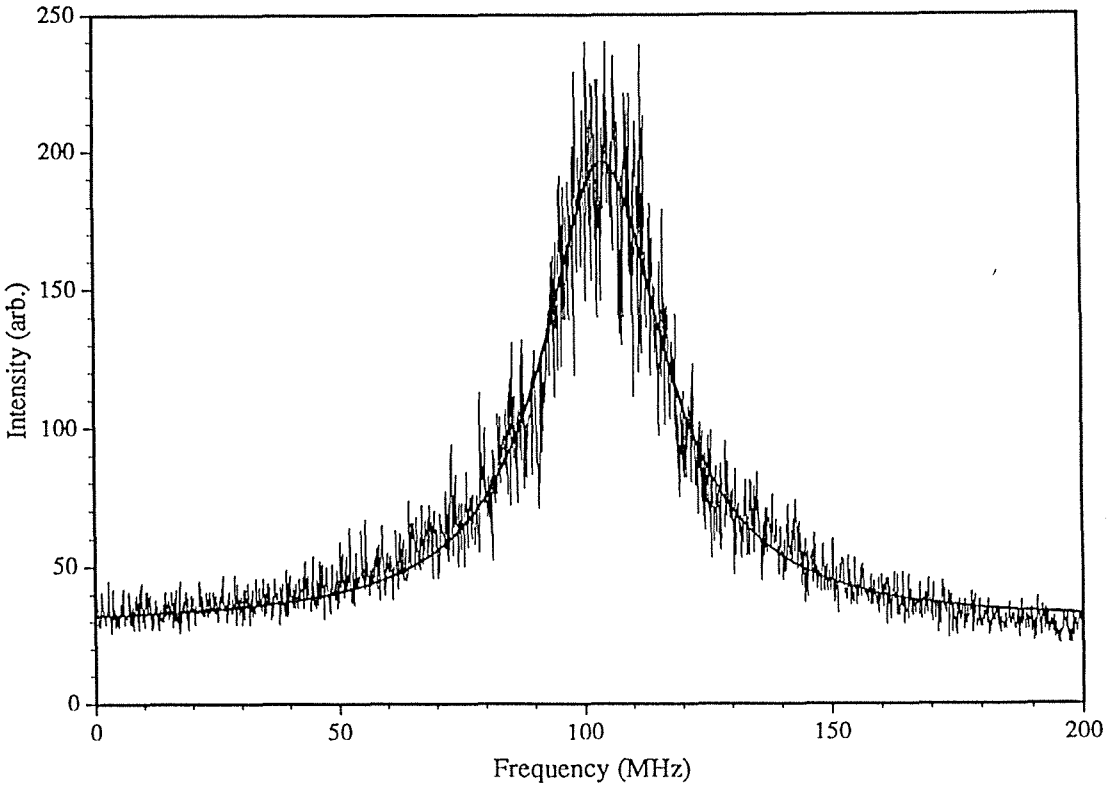

Figure 4.12. Heterodyne signal (jagged line) with fitted Lorentzian profile (smooth line) for laser *B* operating at 76.4 mA and 27.0 °C (14.7 mW). The FWHM of the fitted profile is 30.0 ± 0.1 MHz.

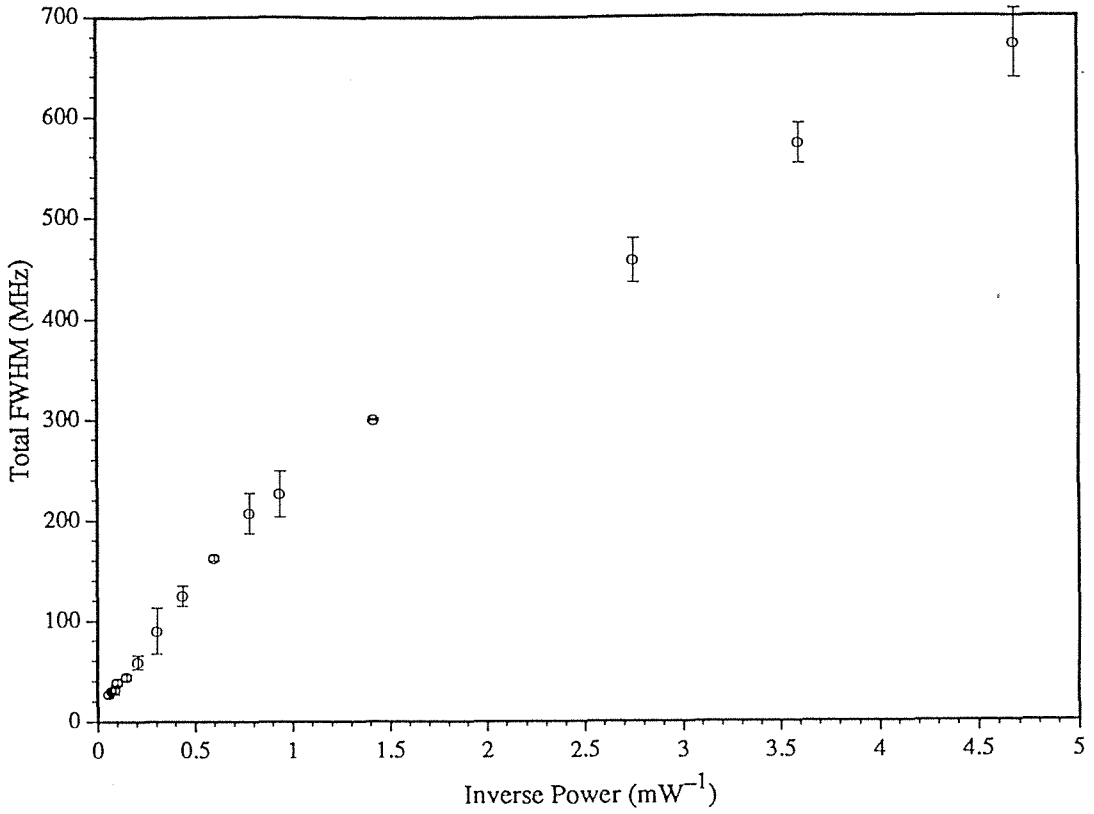

Figure 4.13. Total FWHM (circles) of the heterodyne signal as a function of inverse power.

determined by using a diffraction grating to spatially separate the modes and measuring the fraction of total power in the appropriate mode. The error bars represent a 95% confidence interval on the fitted widths. The upper and lower laser power limits for which linewidth measurements could be made were determined by the extent to which laser *B* remained in the same mode for different temperatures and injection currents. However, the signal-to-noise ratio reduces as the power decreases towards the shot noise limit[58], making linewidth measurements more difficult as the injection current approached threshold.

The data in Figure 4.13 show two distinct linear regions separated by a "knee" at an inverse power of about 0.8 mW^{-1}. Ohtsu and Kotajima[59] have also observed a knee in similar measurements for an InGaAsP diode laser, using the delayed self-heterodyne technique[60]. Fitting straight lines to the data in Figure 4.13 gives

$$\text{FWHM} = (10 \pm 3) + (254 \pm 8)P^{-1} \text{ for } P^{-1} < 0.8, \qquad (4.5a)$$

and

$$\text{FWHM} = (120 \pm 30) + (120 \pm 9)P^{-1} \text{ for } 0.8 < P^{-1} < 5, \qquad (4.5b)$$

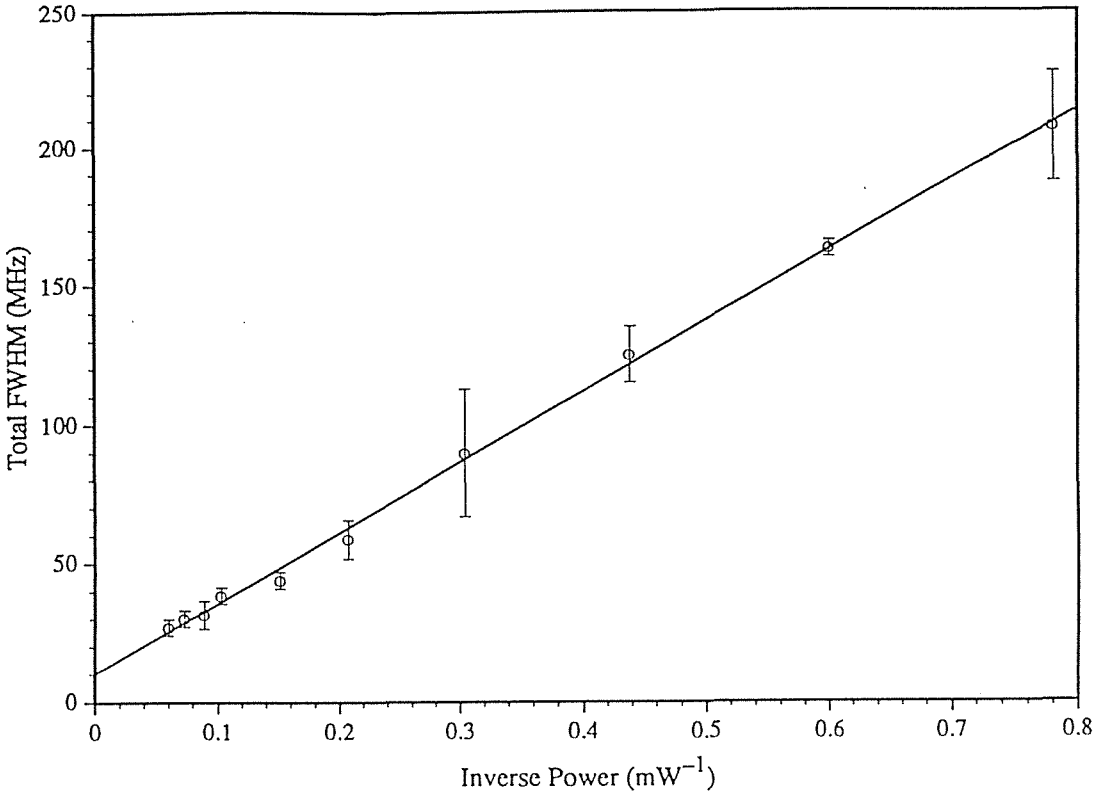

Figure 4.14. Expanded view of Figure 4.13 for the region below the knee.

where the FWHM is given in MHz for the mode power, P, in mW. The region below the knee is expanded in Figure 4.14.

One should be reminded that the FWHM in equations (4.5) refers to the sum of the individual widths of lasers A and B. The experimental conditions on laser A were not varied so it would be natural to assign the quantity 10 ± 3 MHz to its width. However, Welford and Mooradian[61] have observed power-independent contributions to individual AlGaAs diode lasers. They attributed this to refractive index fluctuations resulting from statistical fluctuations in the number of conduction electrons in the small active volume of the laser. This contribution increases with decreasing laser temperature, and at room temperature is about 1 MHz. On the other hand, Ohtsu and Kotajima[59] have reported no power-independent contribution in their measurements on an InGaAsP diode laser. The temperature variation of laser B in the present experiment was sufficiently small (26.2 °C to 29.6 °C) that the temperature dependence of the power-independent linewidth contribution and of the rate of change of linewidth with inverse power[62] are not expected to influence the results. Moreover, it is not possible to infer the existence of a power-independent contribution to the linewidth of the laser under study since the error in the intercept in Figure 4.14 is larger than the probable size of this contribution (~ 1 MHz), should it exist.

4.8. Absolute Frequency Stability

The drift of the laser frequency was measured by passing the beam through a pyrex cell, 10 cm in length, containing caesium vapour, exciting the caesium D_2 transition at 852.1 nm. The absorption of the beam was monitored by a photodiode. The cell was placed inside an insulated enclosure and left at room temperature. The slope of the absorption signal was used to relate a change in the output of the photodiode to a change in laser frequency. The hyperfine transition with $F = 4$ in the ground state was used rather than $F = 3$ because of the greater absorption on the former (see Figure 4.15). Chapter 6 contains detailed discussions concerning the hyperfine structure of the caesium D_2 line. The laser was tuned to the lower wavelength side of the $F = 4$ peak and the photodiode signal was recorded by the data acquisition and control unit at regular intervals for a period exceeding 5 hours. This signal is dependent not only on changes in laser frequency, but also on intensity fluctuations of the laser output itself, and on changes in the caesium number density which is determined by the cell temperature (see Section 6.5.1 for the relationship between temperature and number density). Laser intensity fluctuations were measured to be

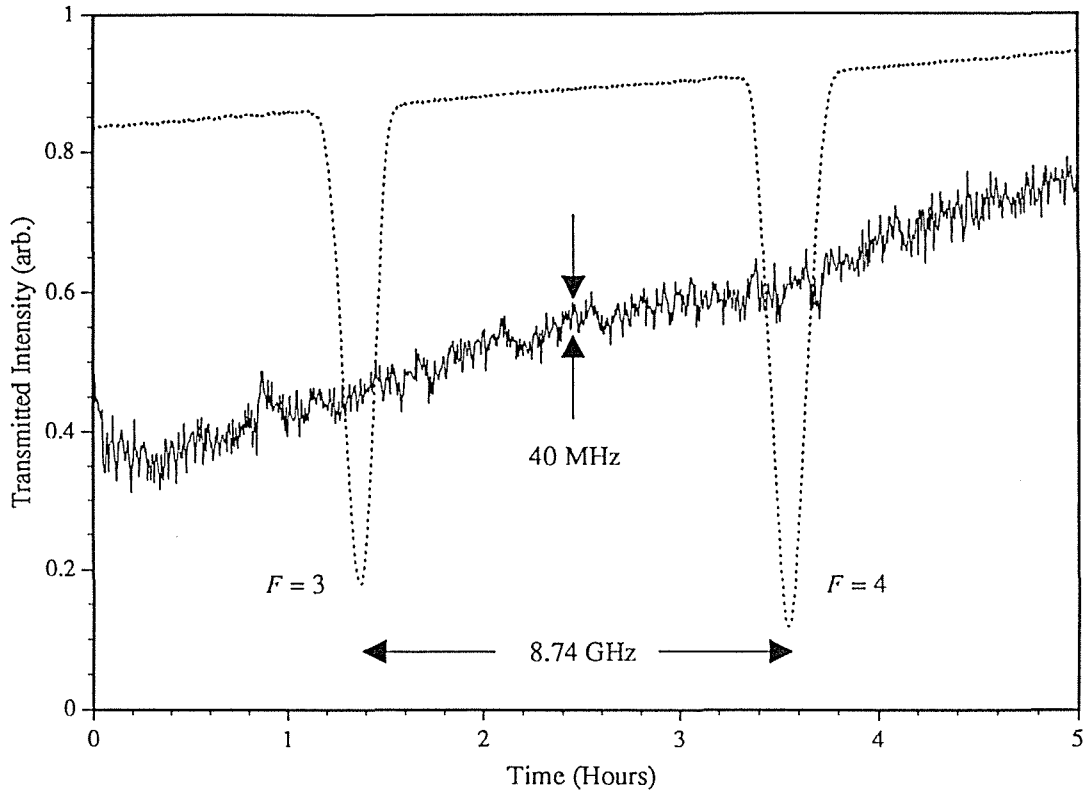

Figure 4.15. Frequency stability of an AlGaAs diode laser (solid line), overlaid on the absorption spectrum (dotted line) due to caesium vapour. The solid line shows the drift of the transmitted intensity (corresponding to a frequency drift) over a period of 5 h. The horizontal scale for the dotted line is indicated by the 8.74 GHz spacing of the two peaks.

smaller than ±1% of the initial intensity with no significant drift over the time scale depicted in Figure 4.15. These fluctuations account for 4% of the total fluctuations. The temperature of the caesium cell drifted by no more than 0.5 °C, giving an intensity drift of 4% of the initial intensity over 5 hours, that is only 7% of the total drift shown in Figure 4.15. The remaining intensity fluctuations and drift were due to laser frequency changes. Frequency fluctuations were within ±20 MHz and there was an overall drift of about 10 kHz per second.

The typical injection current and temperature drifts were 3.3×10^{-5} μA/s (Figure 3.2) and 4.2×10^{-7} °C/s (Figure 3.6(*a*)), respectively. Using these values and the tuning rates given in equations (4.4) and (4.2), the individual contributions to the overall frequency drift arising from injection current and temperature instabilities can be calculated. These are 0.1 and 10 kHz/s, respectively. Hence, the long-term stability of the temperature controller would need to be improved in order to reduce the long-term frequency drift. This could be achieved by placing the circuit in a constant temperature enclosure, although the extra effort and cost involved may not be warranted since, for the purpose of spectroscopy, the frequency drift over the duration of a scan through a transition (< 1 minute) would not be significantly improved. Short-term temperature variations could be improved by using a more sophisticated circuit, such as that in Reference 47, which uses PID gain stages and optimised time constants.

5. Relationship Between Fabry-Perot Fringe Visibility and Spectral Linewidth

5.1. Introduction

A large amount of research has been carried out on the use of the Fabry-Perot interferometer (FPI) to resolve atomic emission line spectra for such applications as hyperfine splitting measurements and isotope shift, and the investigation of line broadening processes. In general, this involves deconvolution of the instrumental (Airy) line function to obtain the Voigt profile under study. In some cases, it is possible to approximate the Voigt profile by a Lorentzian or a Gaussian profile. The former approximation is valid if natural or pressure broadening is the dominant broadening process, and the latter if Doppler broadening is dominant. In all these cases it is important that the spacing of the FPI is such that its free spectral range (FSR) is significantly larger than the linewidth of the spectral line being investigated. In this chapter, an analysis is presented of the case in which the Lorentzian or Gaussian spectral width to be measured is of the order of the FSR of the interferometer, and it is shown that the linewidth can be calculated from the measured fringe visibility when the profile is not fully resolved.

The first part of the chapter examines the following cases:

(*i*) Full Lorentzian and Gaussian profiles with negligible instrumental width.

(*ii*) Truncated Lorentzian and Gaussian profiles with negligible instrumental width.

(*iii*) Full Lorentzian, Gaussian and Voigt profiles with non-negligible instrumental width.

In all cases the linewidth is expressed as a multiple of the FSR of the interferometer, and therefore, the analysis is applicable to any interferometer. Case (*ii*) is included because the mode envelope of a laser light source may be observed to be better modelled by a truncated Lorentzian or Gaussian due to the finite number of modes that lase, corresponding to the laser cavity modes. There are significant and unexpected differences in the results for the full and truncated cases, which will allow truncated profiles to be easily identified in practical lasers if they occur.

The analysis may be applied to spectral emission lines which are well approximated by a single Lorentzian or Gaussian lineshape and to some lasers. The intensities of the modes of a mode-locked laser, for example, are predicted to have a Gaussian frequency

distribution[63]. This is well supported by fitting the mode intensities of practical mode-locked lasers to a Gaussian profile (see Appendix *E*). For the analysis to apply to such mode-locked lasers, it is also necessary that the longitudinal modes are numerous and closely spaced in frequency relative to the FSR of the interferometer, so that they provide an essentially continuous frequency distribution. Single-mode lasers may be approximated by a Lorentzian lineshape (*e.g.* diode laser). So too can multi-mode homogeneously broadened lasers which satisfy the condition for number and spacing of longitudinal modes stated above for mode-locked lasers[64].

The second part of the chapter sets out experimental tests of the analysis for the case of a Lorentzian profile, using an 850-nm AlGaAs diode laser. This is done by examining fringe visibility (*i*) as a function of the FSR of a plane-plane FPI, and (*ii*) as a direct function of linewidth. The measurement of linewidth as a function of inverse power made using the heterodyne technique, described in Section 4.7, serves as a test for the validity of the latter experiment. It is found that for sufficiently low output powers the multi-mode nature of the diode laser output invalidates the assumptions made for the fringe visibility analysis to hold.

5.2. Calculation for Negligible Instrumental Width

5.2.1. Fringes

The fringe visibility is defined as

$$V = \frac{I_{max} - I_{min}}{I_{max} + I_{min}}, \tag{5.1}$$

where I_{max} and I_{min} are the maximum and minimum intensities transmitted by the FPI, respectively. The transmitted intensity of the FPI is monitored, using a linear photodetector, while the interferometer is piezo-electrically or pressure scanned. This intensity is a superposition of an infinite number of transmission peaks (fringes), each shifted by one FSR with respect to the adjacent fringe (Figure 5.1). The lineshape of the transmission fringes will be determined to good accuracy by the spectral distribution of the light source and the degree of overlap of the fringes assuming the interferometer has a sufficiently high resolving power. Interferometers with a finesse in excess of 20 000 are available[65], so that for practical values of the FSR, such an assumption is not unrealistic.

In order to determine the resulting fringes, the intensity, rather than the amplitude, of the light transmitted in each order is summed, for a given FPI spacing. This is illustrated in Figure 5.1 and is justified as follows. Light that is different in frequency by multiples of the FSR is transmitted in different orders for a given spacing. If the light is incoherent, there is no interference between the different frequencies and the total transmitted intensity is obtained by adding the individual intensities. If the light is coherent then interference fringes at the mean of any two frequencies, modulated by beating at half the difference frequency, will occur. In this case it is the amplitudes which must be added. When many frequencies are present, the interference and beating effects will tend to be averaged out. Also, as all the frequencies are derived from a single light source, the light is only partially coherent and only partial interference will be observed. When the transmitted light of the FPI is being monitored, a photodetector with a response time which is very long compared with the beat period and interference period is used. Thus, it is the average intensity which is measured, and the average intensity is the sum of the individual intensities.

The following two sub-sections describe the response of the FPI to full Lorentzian and Gaussian profiles, respectively. In both these cases the maximum intensity always occurs at the position of a transmission peak, for any FSR, and the minimum intensity always occurs midway between adjacent transmission peaks.

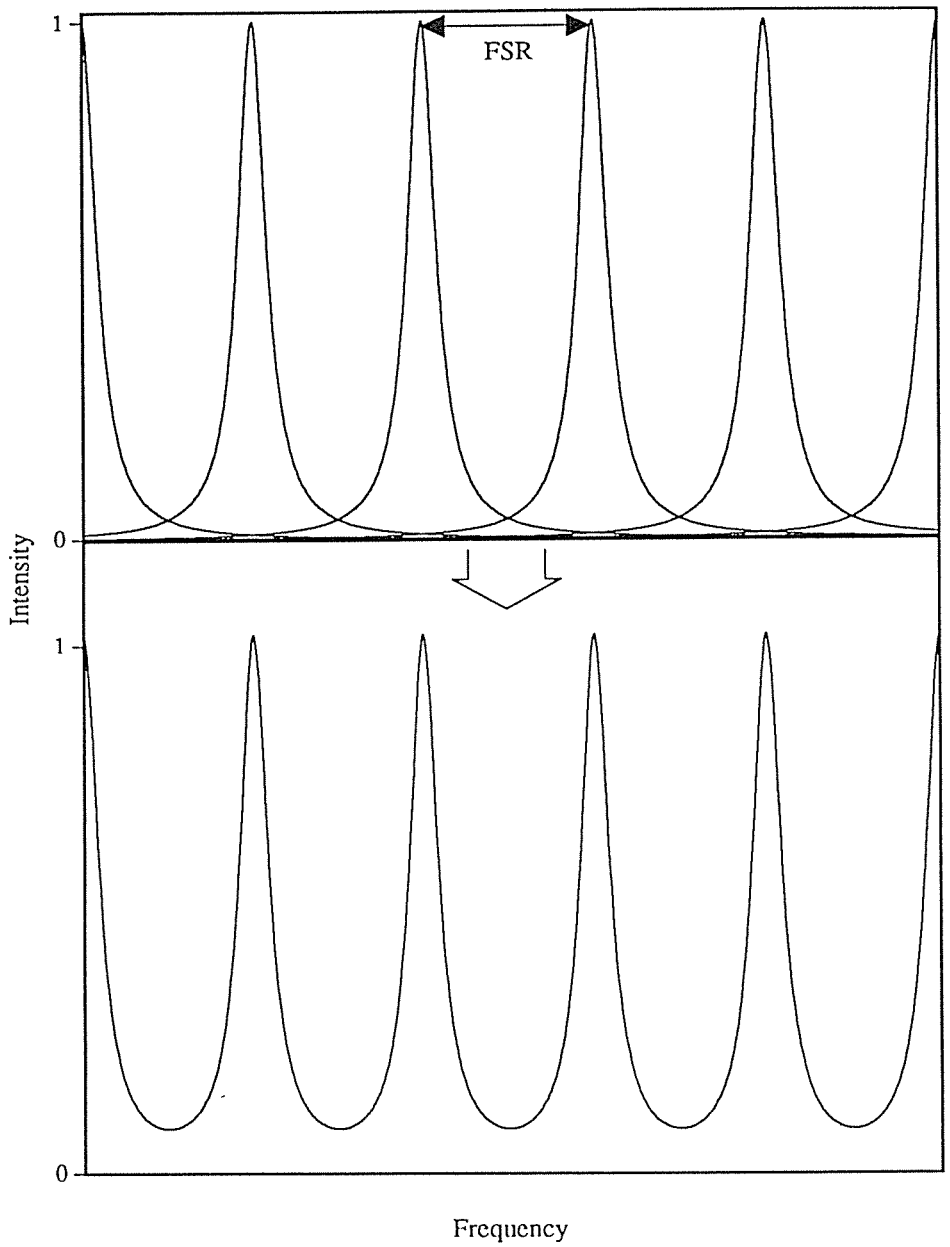

Figure 5.1. Superposition of fringes. The top curve shows the intensities of adjacent orders of a Lorentzian profile transmitted through a FPI of high finesse. The bottom curve is the resulting fringe pattern produced by a superposition of the orders.

5.2.2. Full Lorentzian Profile

The frequency dependence of a Lorentzian profile, normalised to unit peak intensity, is given by

$$I(\Delta\nu) = \frac{(\Gamma/2)^2}{(\Delta\nu)^2 + (\Gamma/2)^2}, \tag{5.2}$$

where Γ is the full width at half maximum (FWHM) and $\Delta\nu$ is the frequency offset from the line centre. In this analysis the linewidth Γ will be written as a multiple of the FSR of the interferometer:

$$\Gamma = p_L \times \mathrm{FSR}, \tag{5.3}$$

where p_L is a positive real number representing a normalised linewidth. The maximum fringe intensity, $I_{\max}$, is a sum of expressions like equation (5.2) with each $\Delta\nu$ an integer multiple of the FSR:

$$\begin{aligned} I_{\max} &= \sum_{k=-\infty}^{\infty} \frac{(p_L \times \mathrm{FSR}/2)^2}{(k \times \mathrm{FSR})^2 + (p_L \times \mathrm{FSR}/2)^2} \\ &= \sum_{k=-\infty}^{\infty} \frac{(p_L/2)^2}{k^2 + (p_L/2)^2} \\ &= \sum_{k\ \mathrm{even}} \frac{{p_L}^2}{k^2 + {p_L}^2}. \end{aligned} \tag{5.4}$$

This is independent of the FSR of the interferometer and hence is valid for any interferometer. Similarly, $I_{\min}$ is obtained from equation (5.2) with each $\Delta\nu$ a half odd integer multiple of the FSR:

$$\begin{aligned} I_{\min} &= \sum_{k=-\infty}^{\infty} \frac{(p_L/2)^2}{(k - 1/2)^2 + (p_L/2)^2} \\ &= \sum_{k\ \mathrm{odd}} \frac{{p_L}^2}{k^2 + {p_L}^2}. \end{aligned} \tag{5.5}$$

The infinite series

$$\sum_{k=-\infty}^{\infty} \frac{{p_L}^2}{k^2 + {p_L}^2} \tag{5.6}$$

may be summed with the aid of Poisson's summation formula[66] which relates the sum of a function ϕ to the sum of its Fourier transform $\hat{\phi}$:

$$\sum_{k=-\infty}^{\infty} \phi(k\lambda) = \frac{1}{|\lambda|} \sum_{n=-\infty}^{\infty} \hat{\phi}\left(\frac{2\pi n}{\lambda}\right). \tag{5.7}$$

If one considers the function

$$\phi(k\lambda) = \frac{1}{1 + (k\lambda)^2}, \tag{5.8}$$

and puts $\lambda = 1/p_L$, then the series on the left-hand side of equation (5.7) becomes the series of equation (5.6), and the series on the right-hand side is a geometric series. This gives

$$\sum_{k=-\infty}^{\infty} \frac{{p_L}^2}{k^2 + {p_L}^2} = \pi p_L \sum_{n=-\infty}^{\infty} e^{-2\pi p_L |n|}$$

$$= \pi p_L \coth(\pi p_L), \tag{5.9}$$

and hence,

$$I_{\max} = \frac{\pi p_L}{2} \coth\left(\frac{\pi p_L}{2}\right). \tag{5.10}$$

$I_{\min}$ is obtained from the fact that

$$\sum_{k=-\infty}^{\infty} \frac{{p_L}^2}{k^2 + {p_L}^2} = \sum_{k \text{ even}} \frac{{p_L}^2}{k^2 + {p_L}^2} + \sum_{k \text{ odd}} \frac{{p_L}^2}{k^2 + {p_L}^2}. \tag{5.11}$$

Thus,

$$I_{\min} = \pi p_L \coth(\pi p_L) - \frac{\pi p_L}{2} \coth\left(\frac{\pi p_L}{2}\right), \tag{5.12}$$

and hence,

$$V = \frac{I_{\max} - I_{\min}}{I_{\max} + I_{\min}} = \operatorname{sech}(\pi p_L). \tag{5.13}$$

5.2.3. Full Gaussian Profile

A Gaussian profile normalised to unit peak intensity has the form

$$I(\Delta\nu) = \exp\left\{\frac{-4\ln 2(\Delta\nu)^2}{\delta\nu_D{}^2}\right\} = 2^{-4(\Delta\nu)^2/\delta\nu_D{}^2}, \tag{5.14}$$

where $\delta\nu_D$ is the FWHM, which is written in terms of a normalised linewidth p_G as

$$\delta\nu_D = p_G \times \mathrm{FSR}. \tag{5.15}$$

The maximum and minimum intensities obtained from equation (5.14) are

$$I_{\max} = \sum_{k=-\infty}^{\infty} \exp\left[-4\ln 2(k^2/p_G{}^2)\right] = 1 + 2\sum_{k=1}^{\infty} 2^{-4k^2/p_G{}^2}, \tag{5.16}$$

and

$$I_{\min} = \sum_{k=-\infty}^{\infty} \exp\left[-4\ln 2(k - 1/2)^2/p_G{}^2\right] = 2\sum_{k=1}^{\infty} 2^{-4(k - 1/2)^2/p_G{}^2}. \tag{5.17}$$

These two infinite series occur frequently enough in mathematics to form part of a set of special functions called theta functions[67]. There are four such functions, each of which is defined as a function of a variable z and a parameter q, where $|q| < 1$. The two theta functions of interest here are

$$\theta_2(z, q) = \sum_{n=-\infty}^{\infty} q^{(n + 1/2)^2} \exp[(2n + 1)iz], \tag{5.18}$$

and

$$\theta_3(z, q) = \sum_{n=-\infty}^{\infty} q^{n^2} \exp(2niz). \tag{5.19}$$

From these one obtains

$$I_{\max} = \theta_3(0, q), \tag{5.20}$$

and

$$I_{\min} = \theta_2(0, q), \tag{5.21}$$

where $q = 2^{-4/p_G{}^2}$. Therefore,

$$
\begin{aligned}
V &= \frac{I_{max} - I_{min}}{I_{max} + I_{min}} \\
&= \frac{\theta_3 - \theta_2}{\theta_3 + \theta_2} \\
&= \frac{1 - 2(y - y^4 + y^9 - y^{16} + y^{25} - \ldots)}{1 + 2(y + y^4 + y^9 + y^{16} + y^{25} + \ldots)},
\end{aligned}
\tag{5.22}
$$

where $y = 2^{-1/p_G{}^2}$. Note, however, that the 2^{-n^2} terms cause the numerator and denominator of equation (5.22) to converge very rapidly, so that taking terms up to y^{16} gives the visibility accurate to better than 0.1% for the whole range of p_G values between 0 and 1.5.

5.2.4. Visibility Curves

Figure 5.2 shows a plot of fringe visibility against normalised linewidth for both the Lorentzian and Gaussian cases. When the visibility is unity, the linewidth may be measured directly from the interferometer transmission fringe width. For smaller

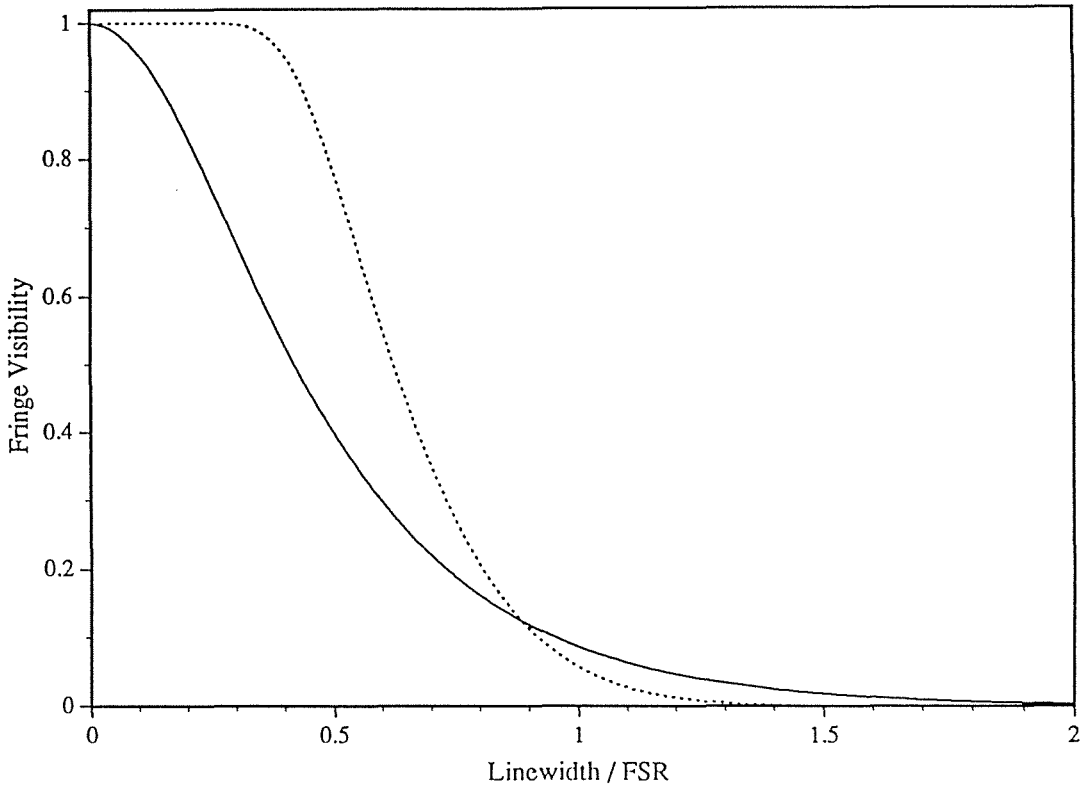

Figure 5.2. Fringe visibility as a function of the linewidth expressed in multiples of the FSR of an interferometer for Lorentzian (solid line) and Gaussian (dotted line) profiles.

visibilities, the curves in Figure 5.2 can be used to obtain the linewidth as a multiple of the FSR of the interferometer using the measured fringe visibility. It can be seen that for Lorentzian profiles, the linewidth can be obtained directly, without correction, only when it is small compared to the FSR (less than about 0.04 × FSR). Hence, the calculation of Section 5.2.2 is particularly useful. For the Gaussian case the visibility remains unity for linewidths up to about 0.33 × FSR and then decreases rapidly for larger linewidths. Using the visibility curves, the range of linewidths which can be measured for a given FSR is extended to about 2 × FSR for Lorentzian profiles and about 1.3 × FSR for Gaussian profiles. Of course, in practice these calculations are subject to uncertainties in the visibility measurements. By calculating the slopes of the curves in Figure 5.2 it can be determined that the uncertainty in the calculated linewidth will be less than that in the visibility measurement for values of p_L in the range 0.1 to 0.6, and p_G in the range 0.4 to 0.85.

5.2.5. Truncated Lorentzian and Gaussian Profiles

This sub-section analyses the situation in which the spectral profile is better modelled as either a truncated Lorentzian or truncated Gaussian lineshape, and demonstrates the differences which occur in comparison with the full profiles. In order to quantify the degree of truncation, a truncation index, t, is defined, which takes a value between 0 and 1 setting a new baseline to the original normalised profile. Cutting off a Lorentzian or Gaussian profile at a truncation index t has the effect of reducing the linewidth, as indicated in Figure 5.3. The reduced linewidth, p'_L, for a Lorentzian profile is given by

$$p'_L = p_L\left(\frac{1-t}{1+t}\right)^{1/2}, \tag{5.23}$$

while the Gaussian reduced linewidth, p'_G, is given by

$$p'_G = p_G\left(\frac{-\ln[(1+t)/2]}{\ln 2}\right)^{1/2}. \tag{5.24}$$

In analysing these lineshapes to determine the resulting fringes, the infinite series for the maximum and minimum intensities obtained previously must be replaced by finite series due to the limited frequency range of the profiles. A direct mathematical analysis of these finite series is very complex since the number of terms in each series varies

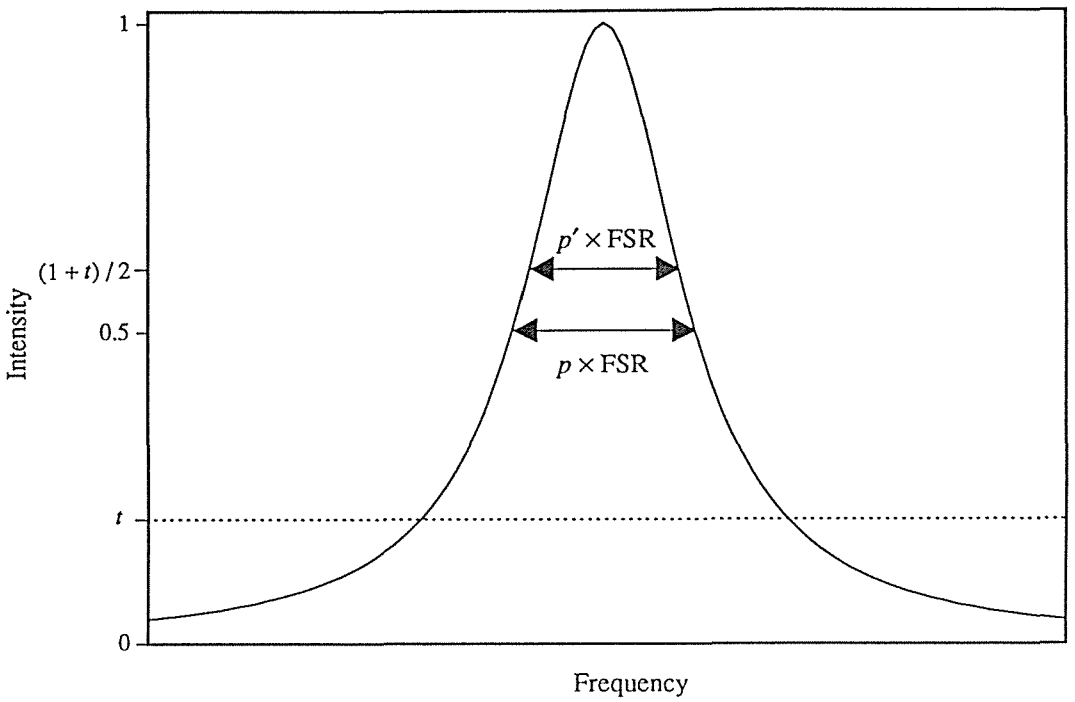

Figure 5.3. Lorentzian or Gaussian profile showing the full linewidth $p \times$ FSR and the reduced linewidth $p' \times$ FSR for a truncation index of t.

with both the linewidth and the truncation index. A simpler approach is to generate these series on a computer for different values of p'_L, p'_G and t. The following analysis describes such a procedure.

The fringe pattern for both Lorentzian and Gaussian profiles is similar and follows a definite pattern as the linewidth increases. In the following, reference is made to a reduced linewidth, p', which stands for that of either a Lorentzian or Gaussian profile. For small values of p', the fringes are of a similar shape to those for the full profiles (Figure 5.4(a)), thus reflecting the lineshape exactly, since this is the region where no overlap of fringes occurs. (Note, the intensity scales of the curves in Figure 5.4 have been chosen to display only the 'ac' components of the fringe pattern. The curves are plotted for a truncation index of $t = 0.2$ for a Gaussian profile.) As p' increases, the fringes begin to overlap in the wings, and thus the bases of the resulting fringe pattern increase leaving the peaks undisturbed. This causes the slope of the lower part of the pattern to decrease as shown in Figure 5.4(b). The fringes first overlap at

$$p'_L = \left(\frac{t}{1 + t}\right)^{1/2} \tag{5.25}$$

for Lorentzian lineshapes, and

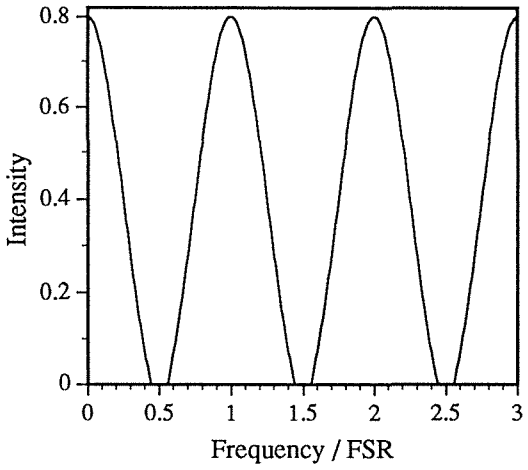

(*a*) $p' = 0.5$.

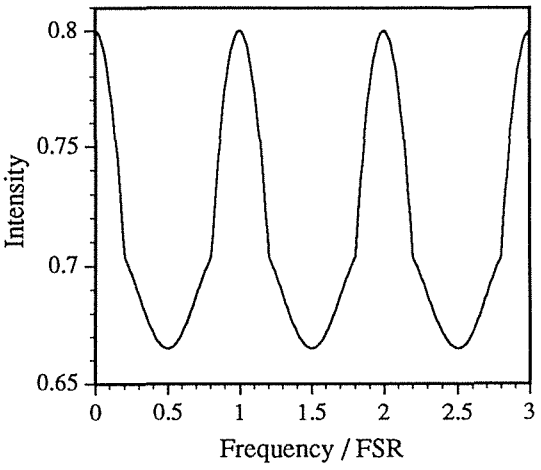

(*b*) $p' = 0.9$.

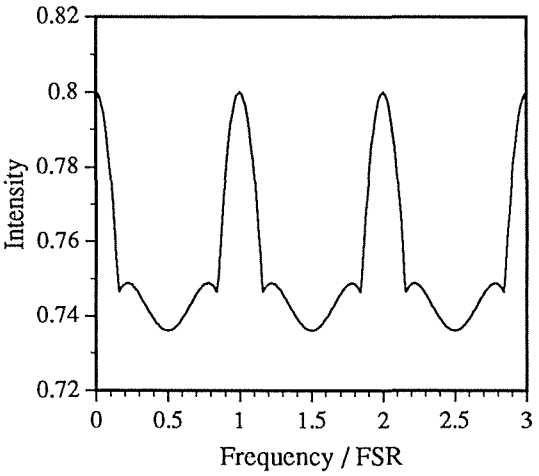

(*c*) $p' = 0.95$.

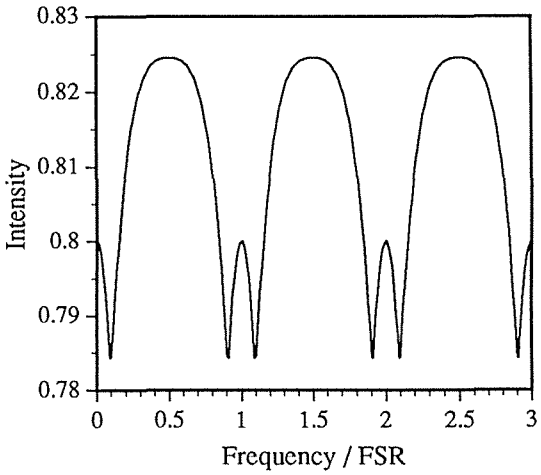

(*d*) $p' = 1.02$.

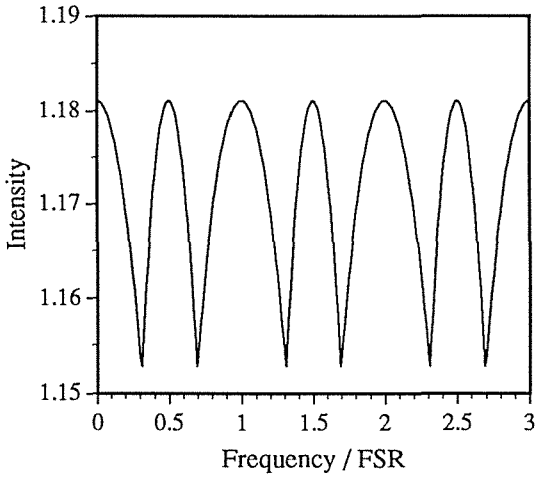

(*e*) $p' = 1.4735$.

Figure 5.4. 'a.c.' components of the fringe pattern calculated for a Gaussian profile with a truncation index of $t = 0.2$. The reduced linewidths are indicated below each figure.

$$p'_G = \left(\frac{\ln[(1+t)/2]}{\ln t}\right)^{1/2} \tag{5.26}$$

for Gaussian lineshapes.

As p' increases further, the number of lineshapes contributing to the fringe pattern differs across one FSR. At any point, this number will increase by one as the successive lineshape orders become non-zero at that point. However, at the peaks corresponding to the transmission maxima of the interferometer, and midway between these peaks, the number of contributing lineshapes periodically increases by two due to the symmetry of these points. The resulting fringe pattern reflects this non-uniformity by a correspondingly non-uniform growth. Two peaks develop on the sides of the main peak, at about $p'_L = 1.6$ for the Lorentzian case and just over $p'_G = 0.9$ for the Gaussian case, for a truncation index of $t = 0.2$ (Figure 5.4(*c*)). These peaks increase in intensity relative to the main peak and also shift closer together. The relative amplitude of these two new peaks in comparison with the 'transmission maxima' peaks is greater for Lorentzian than Gaussian profiles. However, the absolute amplitude, in both cases, is very small and it may be difficult to observe these peaks in practice because of noise. The appearance of these additional peaks is due solely to the way in which the truncated lineshapes superpose. Increasing p' further causes these two peaks to appear to merge, leaving a single peak midway between each successive pair of 'transmission maxima' peaks (Figure 5.4(*d*)). From this point on, as p' increases, the 'transmission maxima' and 'transmission minima' peaks oscillate in amplitude, '180° out of phase' with each other. This oscillation occurs due to the increase of the two contributing lineshapes at these points, as mentioned above. This increase takes place alternately between the transmission maxima and transmission minima positions. Because of the different symmetry of the two positions, each position alternately has one more contributing lineshape than the other, hence the oscillation. This 'anomalous' behaviour is more prominent for higher values of t. When the two peaks are of equal intensity, one could mistakenly identify the intermediate peak as a transmission maximum of the interferometer and conclude that the linewidth is larger by a factor of two than it actually is. However, Figure 5.4(*e*) shows that in this case the widths of the two peaks are not equal.

The visibility curves for the truncated profiles are shown in Figure 5.5 for a truncation index of 0.2. The curve for the truncated Gaussian profile (Figure 5.5(*a*)) is similar to the curve for the full Gaussian profile up to a linewidth of one FSR (this holds for all values of t). For larger linewidths, small bumps noticeably appear for about $t \geq 0.02$

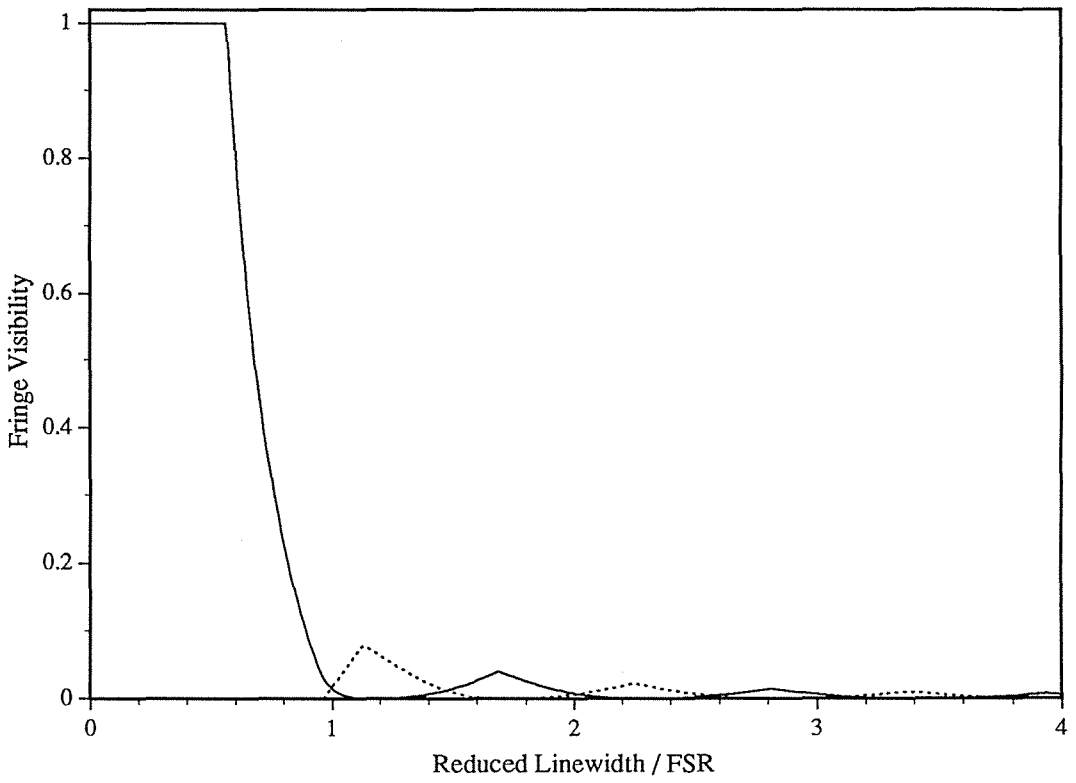

Figure 5.5(*a*). Fringe visibility, for a truncation index of t = 0.2, as a function of the reduced linewidth for a Gaussian profile. The solid line gives the 'transmission maximum' visibility, while the dotted line gives the 'transmission minimum' visibility.

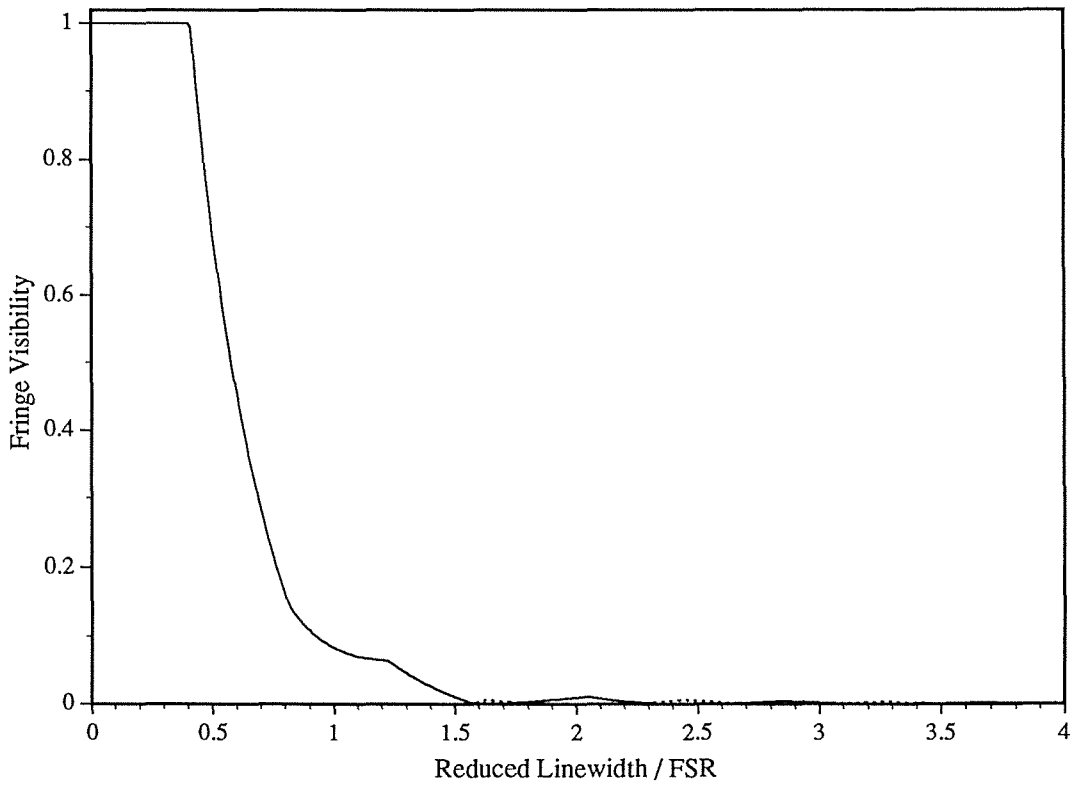

Figure 5.5(*b*). As for (*a*) but for a Lorentzian profile.

due to the oscillating 'transmission maxima' and 'transmission minima' peaks. The solid line in Figure 5.5(*a*) is the fringe visibility with I_{max} taken to be the intensity of the peaks corresponding to the transmission maxima of the interferometer. This value is not necessarily the maximum intensity, as indicated in Figure 5.4. The 'transmission minimum' fringe visibility, where I_{max} is taken to be the intensity of the intermediate peak, is given by the dotted line in Figure 5.5(*a*). The two curves demonstrate the oscillatory nature of the fringes.

The visibility curve for the truncated Lorentzian profile is shown in Figure 5.5(*b*), again for a truncation index of 0.2. The curve has a flat portion with a visibility of unity for small linewidths where the adjacent orders don't overlap, which increases in length with increasing t. This is consistent with the observation that a truncated Lorentzian resembles a Gaussian. The visibility curve drops to zero at approximately the same linewidth as the curve for the full profiles, but at a faster rate for a larger truncation index (as does the Gaussian curve). The visibility begins to oscillate noticeably at about $t = 0.1$. The 'transmission minimum' fringe visibility for the truncated Lorentzian profile is considerably less than that for the Gaussian profile. Note that for both profiles the fringe shape is similar to that shown in Figure 5.4(*e*) when the 'transmission maximum' and 'transmission minimum' visibility curves intersect.

5.3. Calculation for Profiles Including Instrumental Lineshape

5.3.1. The Airy Function

The analysis presented so far in this chapter has been subject to the assumption that the finesse of the interferometer is sufficiently high for the instrumental lineshape to be neglected. Under experimental conditions the finesse of a plane-plane FPI will be degraded due to less than 100% reflectivity of the mirrors, flatness deviations of the mirror surfaces, and imperfect parallelism of the mirrors. The total finesse $\mathcal{F}_t$ can be defined by[68a]

$$\frac{1}{\mathcal{F}_t} = \sqrt{\sum_i \frac{1}{\mathcal{F}_i^2}}, \tag{5.27}$$

where the $\mathcal{F}_i$'s give the individual contributions to the finesse. Since the finesse is defined as the ratio of the FSR to the instrumental width[69], a small finesse implies a large instrumental width, and hence the instrumental function becomes important.

For the case where the total finesse is limited by the mirror reflectivity, the transmitted intensity for a purely monochromatic incident beam of unit peak intensity is given by the well-known Airy function:

$$I(\phi) = \frac{1}{1 + F\sin^2(\phi/2)}, \tag{5.28}$$

where ϕ is the round-trip phase difference given by

$$\phi = \frac{2\pi\Delta\nu}{\mathrm{FSR}}, \tag{5.29}$$

and

$$F = \frac{4R}{(1-R)^2} \tag{5.30}$$

is the "coefficient of finesse" determined by the mirror reflectance, R (mirrors taken to be identical). Defining a damping factor γ_A by[70]

$$\gamma_A = -\ln R, \tag{5.31}$$

one can write equation (5.28) as

$$I(\phi) = \frac{\sinh^2(\gamma_A/2)}{\sin^2(\phi/2) + \sinh^2(\gamma_A/2)}. \tag{5.32}$$

The FWHM of the Airy function of equation (5.32) is defined through the equation:

$$\sin(\phi_1/2) = \sinh(\gamma_A/2), \tag{5.33}$$

where ϕ_1 is the phase for which the intensity is half the peak intensity. Since the right-hand side of equation (5.33) is equal to $F^{-1/2}$, which will be small for moderately large F, the sine function can be replaced by its argument. Expanding the exponentials of the hyperbolic sine function into a power series and retaining terms up to order γ_A (γ_A is small for R approaching unity), equation (5.33) reduces to

$$\phi_1 = \gamma_A. \tag{5.34}$$

Using equation (5.29), the normalised width is

$$p_A = \frac{\text{FWHM}}{\text{FSR}} = \frac{\gamma_A}{\pi}. \tag{5.35}$$

This quantity is just the inverse of the finesse, and will be much less than unity in most practical situations. If this doesn't hold, equation (5.33) must be used to determine the Airy width, and in this case the resolving power of the interferometer will be too small to permit its use in determining spectral linewidths. It is worth noting, however, that for $\gamma_A > 1.76$, p_A is not defined. This can be readily observed from equation (5.33).

The visibility of pure Airy fringes can be easily calculated from equation (5.32) by noting that

$$I_{\max} = 1, \tag{5.36a}$$

and

$$I_{\min} = \frac{\sinh^2(\gamma_A/2)}{1 + \sinh^2(\gamma_A/2)}. \tag{5.36b}$$

These values give

$$V = \frac{I_{\max} - I_{\min}}{I_{\max} + I_{\min}} = \operatorname{sech}(\gamma_A). \tag{5.37}$$

For small values of γ_A, equation (5.35) can be used to give

$$V = \operatorname{sech}(\pi p_A), \tag{5.38}$$

which is identical to equation (5.13) for the Lorentzian profile with the normalised Lorentzian width replaced by that of the Airy function. This is expected. If the Airy function is expanded into a Fourier series, it can be shown (see Appendix *F*) to be represented by a sum of resonance profiles:

$$I(\phi) = \frac{\tanh(\gamma_A/2)}{\gamma_A/2} \sum_{n=-\infty}^{\infty} \frac{\gamma_A^2}{(\phi - 2\pi n)^2 + \gamma_A^2} . \tag{5.39}$$

This is a sum of Lorentzians, each offset by one FSR from the adjacent one, the case which was analysed in Section 5.2.2. Furthermore, when the normalised Airy width is small,

$$\sinh^2(\gamma_A/2) \approx (\gamma_A/2)^2, \tag{5.40a}$$

and

$$\sin^2(\phi/2) \approx \left(\frac{\pi\Delta\nu}{\mathrm{FSR}}\right)^2 . \tag{5.40b}$$

Hence equation (5.32) for the Airy function reduces to the Lorentzian

$$I(\Delta\nu) = \frac{(\mathrm{FWHM}/2)^2}{(\Delta\nu)^2 + (\mathrm{FWHM}/2)^2} . \tag{5.41}$$

5.3.2. Convolution with Lorenztian Profile

The situation to be considered in this sub-section is the investigation of a full Lorentzian profile with an interferometer with a non-negligible Airy function. The resultant profile is equal to the convolution of these two lineshapes. This convolution is most easily determined by considering the Airy function to be of the form given by equation (5.39) (which is exact for any value of γ_A). The result of a convolution of two Lorentzians of widths γ_1 and γ_2 centred about ν_1 and ν_2, respectively, is a Lorentzian of width $\gamma_1 + \gamma_2$ centred about $\nu_1 + \nu_2$ (see Appendix *D*). Thus, the convolution of equation (5.2) with equation (5.39) produces a sum of Lorentzians, each of normalised width $\gamma_L + \gamma_A$, shifted by one FSR from the adjacent one, where

$$\gamma_L = \pi p_L \tag{5.42}$$

has been introduced to represent the normalised Lorentzian width. The visibility curve is thus identical to the pure Lorentzian case with the Lorentzian width replaced by the sum $\gamma_L + \gamma_A$:

$$V = \operatorname{sech}(\gamma_L + \gamma_A). \tag{5.43}$$

If a Lorentzian profile normalised to have unit area, rather than unit peak intensity, is used, then the fringe intensity profile is given explicitly by

$$I(\phi) = \frac{\tanh(\gamma_A/2)}{(\gamma_A + \gamma_L)/2} \sum_{n=-\infty}^{\infty} \frac{(\gamma_A + \gamma_L)^2}{(\phi - 2\pi n)^2 + (\gamma_A + \gamma_L)^2}. \tag{5.44}$$

The normalised width, p_R, of this resultant Airy profile is given, according to equation (5.33), by

$$\sin(\pi p_R/2) = \sinh[(\gamma_L + \gamma_A)/2]. \tag{5.45}$$

For small degrees of fringe overlap, the Lorentzian linewidth can be calculated directly from a measurement of the resultant linewidth with the aid of equation (5.45). However, experimentally the visibility is the more accessible quantity to measure accurately, hence equation (5.43) would give a more precise determination of the Lorentzian linewidth. For large degrees of fringe overlap, the width p_R is not defined (as pointed out following equation (5.35)) and equation (5.43) must be used. However, with slightly more effort, one can perform a non-linear fit of an Airy function, of the form given by equation (5.28), to the resultant profile and obtain a value for F. From this, $\gamma_L + \gamma_A$ can be estimated through the relationship

$$\frac{1}{F} = \sinh^2\left(\frac{\gamma_L + \gamma_A}{2}\right). \tag{5.46}$$

No matter which method is used to determine the Lorentzian width γ_L, it is still necessary to know the Airy width γ_A. This can be obtained from the mirror reflectivity when this is the limiting factor for the finesse, or by direct measurement when the FSR is large enough to render the Lorentzian linewidth negligible.

5.3.3. Convolution with Gaussian Profile

The fringe pattern produced for a full Gaussian profile, including the instrumental function, is obtained by the convolution of a version of equation (5.14) which has been normalised to have unit area with an appropriate expression for the Airy function. In order to make this convolution mathematically tractable, the Fourier expansion of the Airy function (see Appendix *F*) is used:

$$I(\phi) = \tanh(\gamma_A/2)\left(1 + 2\sum_{n=1}^{\infty} e^{-n\gamma_A}\cos(n\phi)\right). \tag{5.47}$$

The convolution can be performed using the standard integral[71a]

$$\int_0^{\infty} e^{-a^2x^2}\cos bx\, dx = \frac{\sqrt{\pi}}{2a}\exp\left(\frac{-b^2}{4a^2}\right) \qquad (ab \neq 0). \tag{5.48}$$

Note that for $b = 0$ equation (5.48) also holds if $a > 0$. The resulting fringe intensity is

$$I(\phi) = \tanh(\gamma_A/2)\left(1 + 2\sum_{n=1}^{\infty} e^{-n\gamma_A}\, e^{-n^2\gamma_G{}^2/4\ln 2}\cos n\phi\right), \tag{5.49}$$

where $\gamma_G = \pi p_G$. The maximum intensity clearly occurs at $\phi = 0$ and the minimum at $\phi = \pi$. Thus, the visibility is

$$V = \frac{2\left(e^{-\gamma_A} z + e^{-3\gamma_A} z^9 + e^{-5\gamma_A} z^{25} + \ldots\right)}{1 + 2\left(e^{-2\gamma_A} z^4 + e^{-4\gamma_A} z^{16} + e^{-6\gamma_A} z^{36} + \ldots\right)}, \tag{5.50}$$

where $z = e^{-\gamma_G{}^2/4\ln 2}$. When the Airy width γ_A is zero, this reduces to

$$V = \frac{2\left(z + z^9 + z^{25} + \ldots\right)}{1 + 2\left(z^4 + z^{16} + z^{36} + \ldots\right)}. \tag{5.51}$$

This must be identical to the expression derived in Section 5.2.3 (equation (5.22)), and indeed this is confirmed by comparing plots of the two functions. Note, however, that equation (5.22) is expanded in terms of $e^{-1/p_G{}^2}$ while equation (5.51) is expanded in terms of $e^{-p_G{}^2}$. This means that for small values of p_G equation (5.22) converges more rapidly than equation (5.51) and for large values of p_G the converse is true. For $p_G \leq 0.55$ equation (5.22) can be reduced to

$$V = \frac{1 - 2y}{1 + 2y}, \tag{5.22a}$$

where $y = e^{-\ln 2/p_G{}^2}$, and for $p_G \geq 0.55$ equation (5.51) can be reduced to

$$V = \frac{2z}{1+2z^4}. \tag{5.51a}$$

In both cases the error in using these equations rather than the full expansions is less than 0.03%.

5.3.4. Convolution with Voigt Profile

The fringe intensity for a Voigt profile incident on the interferometer is obtained by the convolution of a Lorentzian, a Gaussian and an Airy function. This can be written down immediately from the corresponding results for the Lorentzian and Gaussian profiles (equations (5.44) and (5.49), respectively):

$$I(\phi) = \tanh(\gamma_A/2)\left(1 + 2\sum_{n=1}^{\infty} e^{-n(\gamma_A + \gamma_L)}\, e^{-n^2\gamma_G{}^2/4\ln 2}\cos n\phi\right). \qquad (5.52)$$

Thus, the visibility is

$$V = \frac{2\left(e^{-(\gamma_A + \gamma_L)}\, z + e^{-3(\gamma_A + \gamma_L)}\, z^9 + e^{-5(\gamma_A + \gamma_L)}\, z^{25} + \ldots\right)}{1 + 2\left(e^{-2(\gamma_A + \gamma_L)}\, z^4 + e^{-4(\gamma_A + \gamma_L)}\, z^{16} + e^{-6(\gamma_A + \gamma_L)}\, z^{36} + \ldots\right)}, \qquad (5.53)$$

where $z = e^{-\gamma_G{}^2/4\ln 2}$, as before.

5.4. Experiments to Determine Diode Laser Linewidth from Fringe Visibility

5.4.1. Introduction

Two experiments were performed to test the theoretically predicted visibility curve for the case of a full Lorentzian profile. These are described in this section. For both of these experiments a diode laser was used as the light source, the profile of which is approximately Lorentzian, as was shown in Section 4.7.2. A scanning plane-plane Fabry-Perot interferometer with adjustable mirror separation was used to produce the fringes. In the first experiment the laser linewidth was kept fixed by maintaining the same injection current and laser temperature throughout the entire experiment. The ratio of linewidth to FSR was changed by adjusting the mirror spacing of the FPI. In the second experiment a fixed FSR of the FPI was used and the ratio of linewidth to FSR was changed by adjusting the laser power, thereby altering the linewidth. As a test of this result, a comparison is made with the linewidth-inverse power relationship found in Section 4.7.

The arrangement used for both experiments is shown in Figure 5.6. The laser beam was passed normally through the parallel mirrors of the FPI. These 2-inch-diameter mirrors are coated for 98 ± 1% reflectance at 830 nm with anti-reflection coatings on the back sides. The input mirror was mounted on a piezo-electric transducer which was driven by a high voltage ramp. The variation in intensity was detected by a BPX 65 PIN photodiode (peak spectral response at 850 nm) and was displayed on a storage oscilloscope. The oscilloscope was connected to a computer via an IEEE interface board allowing the digitised fringe data to be directly stored to disc.

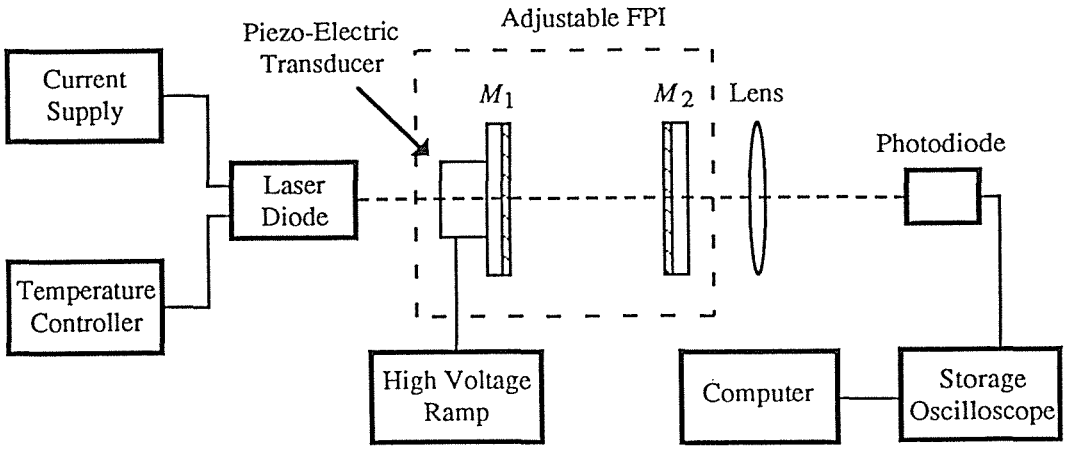

Figure 5.6. Experimental arrangement for recording fringes. M_1 and M_2 are the input and output mirrors of the FPI, respectively.

5.4.2. Experiment with Fixed Linewidth and Variable FSR

For this experiment the laser was operated at a fixed temperature of 24.8 °C and with a fixed injection current of 75 mA. The mirror spacing of the FPI was adjusted from about 1 mm to about 340 mm and was measured using a travelling microscope. The maximum mirror spacing, determined by the physical dimensions of the interferometer, gave a FSR of around 450 MHz. The laser linewidth must be of the same magnitude as the FSR so as to be able to check the visibility curve up to at least $p_L = 1$. Using the stabilised current supply resulted in a linewidth an order of magnitude smaller than this, so a general purpose "noisy" current supply was used to increase the linewidth. For each mirror spacing correct beam alignment was achieved by first ensuring that the back-reflected light from the input mirror returned as closely as possible along the approach path while avoiding optical feedback into the laser cavity. There was a large spacing (about 2 m) between the laser and the FPI. Secondly, the output mirror was tilted to produce the sharpest fringes on the detector.

The fringe visibility was measured for several different mirror spacings. In order to determine how well these data fit equation (5.43), they were converted into a linear relationship in terms of the experimental parameters, from which both the Lorentzian FWHM and the normalised instrumental width, γ_A, could be determined. From equation (5.43), $\gamma_L + \gamma_A$ is given by

$$\gamma_L + \gamma_A = \cosh^{-1}\left(\frac{1}{V}\right). \tag{5.54}$$

Due to the fact that it was necessary to physically alter the mirror spacing, there were variations in finesse arising from differences in mirror alignment. However, these variations were kept small by always ensuring that the sharpest fringes were obtained. Hence, the assumption was made that γ_A remained constant for the entire range of mirror spacings. Thus, equation (5.54) becomes

$$\frac{\pi\Gamma}{\mathrm{FSR}} + \gamma_A = \cosh^{-1}\left(\frac{1}{V}\right), \tag{5.55}$$

where Γ is the Lorentzian FWHM. A plot of $\cosh^{-1}(1/V)$ against 1/FSR is shown in Figure 5.7. Linear regression gives $\Gamma = 580 \pm 20$ MHz and $\gamma_A = 0.07 \pm 0.09$. The large percentage error in γ_A is due to the fact that this quantity is very much smaller than γ_L for almost all of the mirror spacings used. The value of Γ is consistent with the value 560 ± 70 MHz which was obtained by a direct measurement of the fully resolved fringes for two of the mirror spacings.

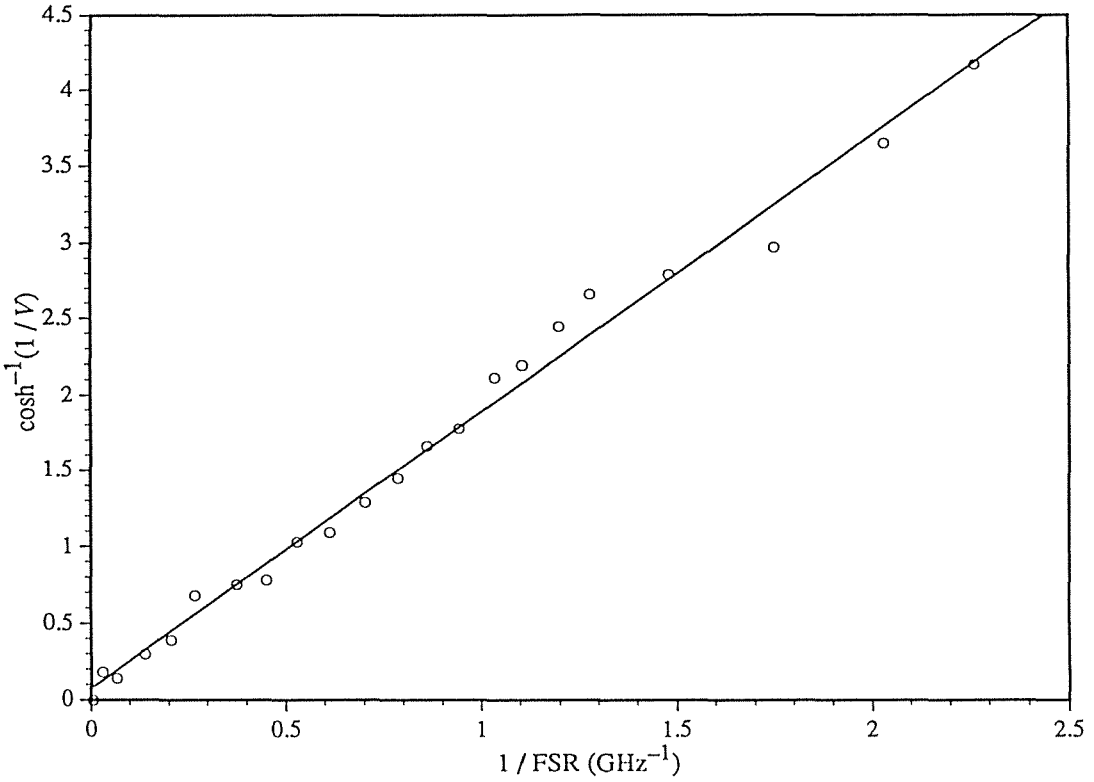

Figure 5.7. A fit of the measured visibility (circles) to equation (5.55) yielding $\Gamma = 580 \pm 20$ MHz and $\gamma_A = 0.07 \pm 0.09$.

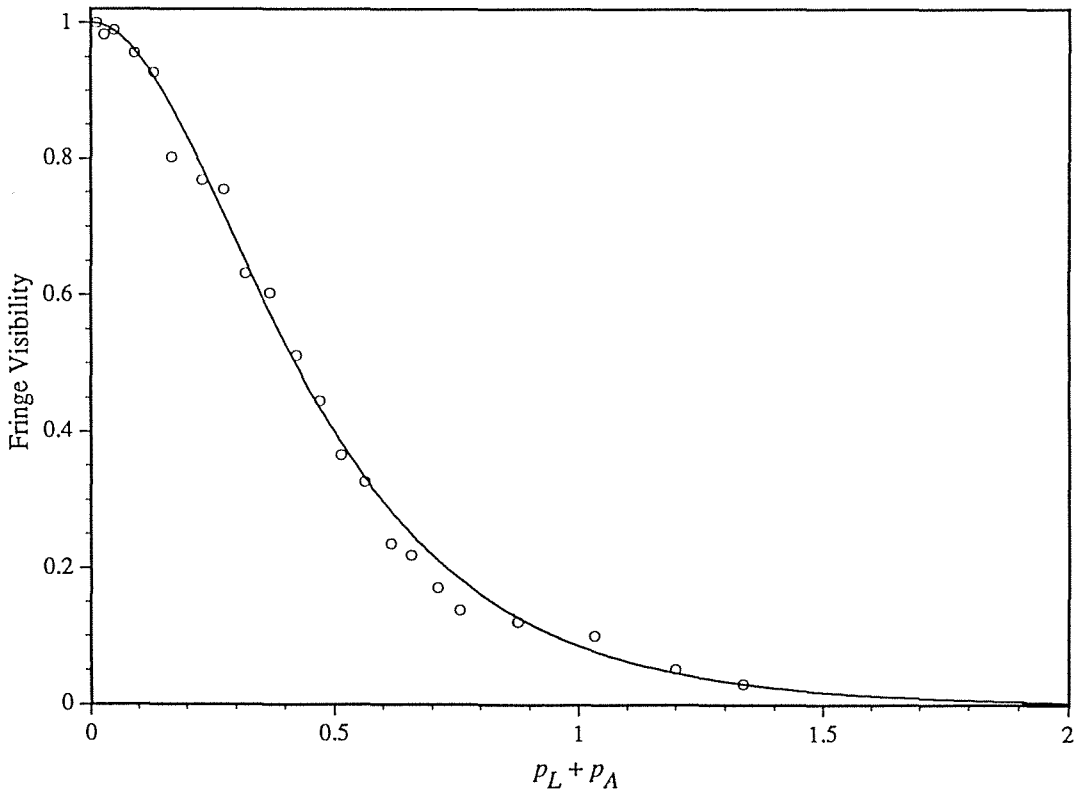

Figure 5.8. Visibility curve for fixed linewidth and variable FSR. The solid line is the theoretical curve from equation (5.43) and the circles are the experimental values.

An Airy function was fitted to each of the fringe patterns. From these fits the visibility was calculated by noting from equation (5.28) that

$$V = \frac{F}{2 + F}. \tag{5.56}$$

These values were within 10% of the directly measured values, supporting the expectation that the fringes were well approximated by Airy functions.

The experimental visibility curve is plotted in Figure 5.8 overlaid on the theoretical curve given by equation (5.43). This shows good agreement, confirming the validity of the result of Section 5.3.2.

5.4.3. Experiment with Fixed FSR and Variable Linewidth

In this experiment the linewidth of the laser was directly changed by altering the injection current while operating the laser at a fixed temperature (32.3 °C in this case). The stabilised current supply was used here to provide accurate control over the injection current. By fixing the FSR of the interferometer (823.3 ± 0.5 MHz) the quantity p_L was varied by a change in injection current. The shape of the theoretical visibility curve was used to determine the functional form of the linewidth dependence on output power.

The resultant fringes were recorded for several different injection current values. Again these were fitted to Airy functions with good agreement. A sample fit is shown in Figure 5.9. The power in the strongest lasing mode was determined for each injection current setting in the same manner as for the heterodyne experiment in Section 4.7. In this case equation (5.43) is written as

$$\frac{\pi}{\mathrm{FSR}} f\left(\frac{1}{P}\right) + \gamma_A = \cosh^{-1}\left(\frac{1}{V}\right), \tag{5.57}$$

where $f(1/P)$ is the functional form of the linewidth variation with inverse power. Here γ_A can be truly considered constant because the alignment of the FPI was not altered throughout the experiment. A plot of $\cosh^{-1}(1/V)$ versus $1/P$ is shown in Figure 5.10. As for the heterodyne experiment, there is a distinct change in behaviour at about $P^{-1} = 0.8$ mW^{-1}. The region below $P^{-1} = 0.8$ mW^{-1} will be looked at in more detail so that a comparison can be made between the results of the visibility experiment and the heterodyne experiment . The region above this will be discussed afterwards.

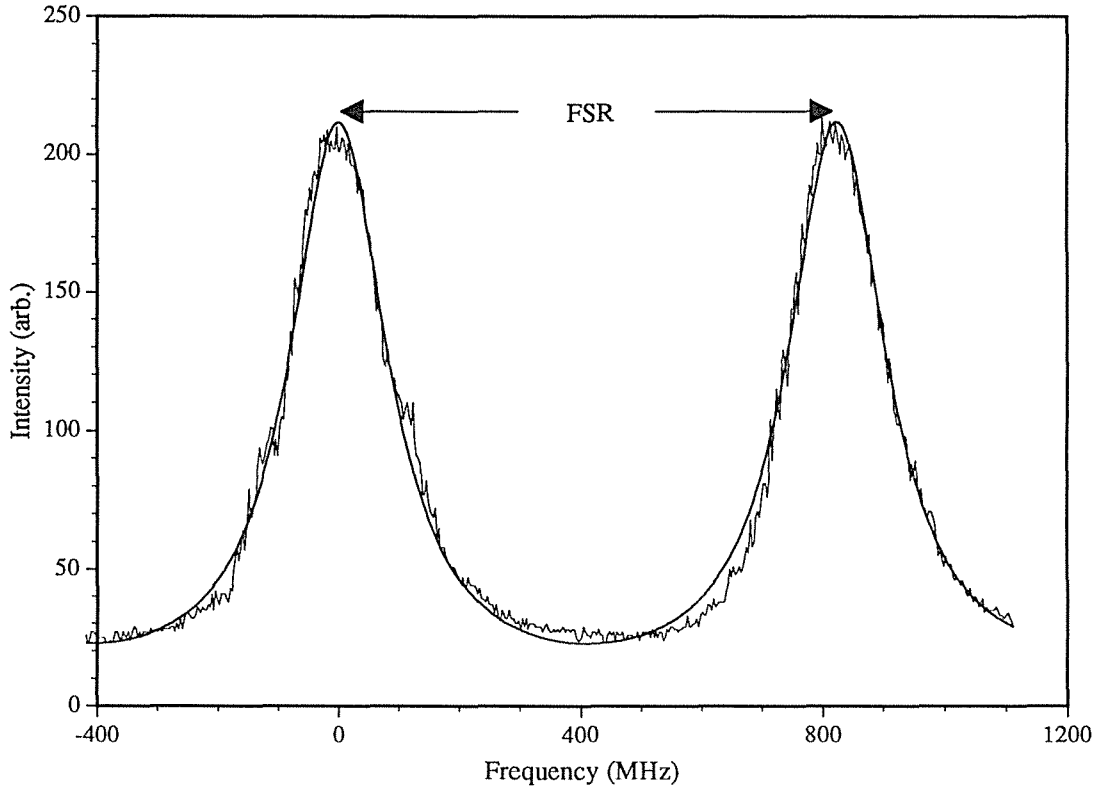

Figure 5.9. Experimental fringes (jagged line) with fitted Airy function (smooth line) for an injection current of 61 mA and FSR of 823.3 MHz.

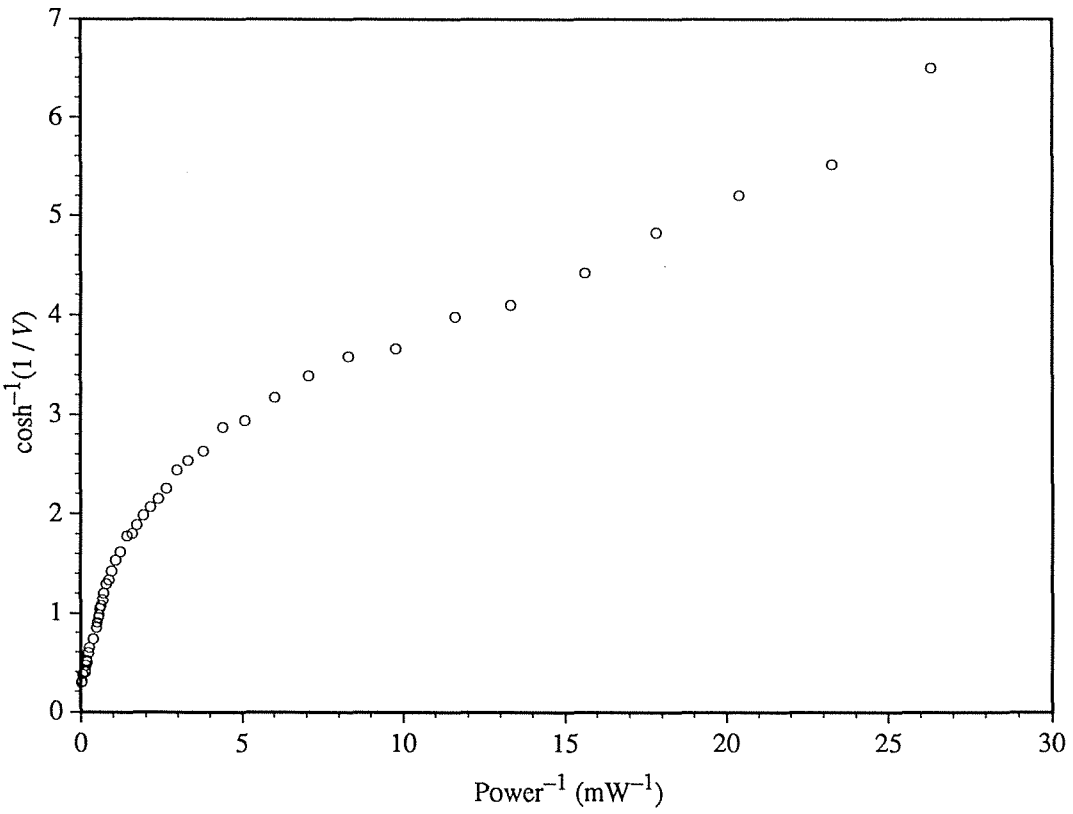

Figure 5.10. Visibility data for fixed FSR and variable linewidth.

An expansion of the visibility data below $P^{-1} = 0.8$ mW^{-1} (Figure 5.11) indicates that the functional form for the linewidth variation with inverse power in this region be taken as linear:

$$f\left(\frac{1}{P}\right) = k\frac{1}{P}. \tag{5.58}$$

Thus, a straight-line fit to the data gives a slope of 1.29 ± 0.05 with an intercept of 0.24 ± 0.02. Combining equations (5.57) and (5.58), gives the rate of change of linewidth with inverse power as 340 ± 10 MHz/mW. The intercept contains information concerning both the instrumental width of the FPI and any power-independent contribution to linewidth. Without a precise measurement of the instrumental width, it is not possible to deduce the value of a power-independent contribution. A simple determination could be obtained by using an ultra-narrow-linewidth laser operating at the same wavelength, such as an external-cavity diode laser, as a probe for the instrumental width. However, such a laser was not available.

There is a fairly large discrepancy for the rate of linewidth change with inverse power between the present value of 340 ± 10 MHz/mW and the value of 254 ± 8 MHz/mW

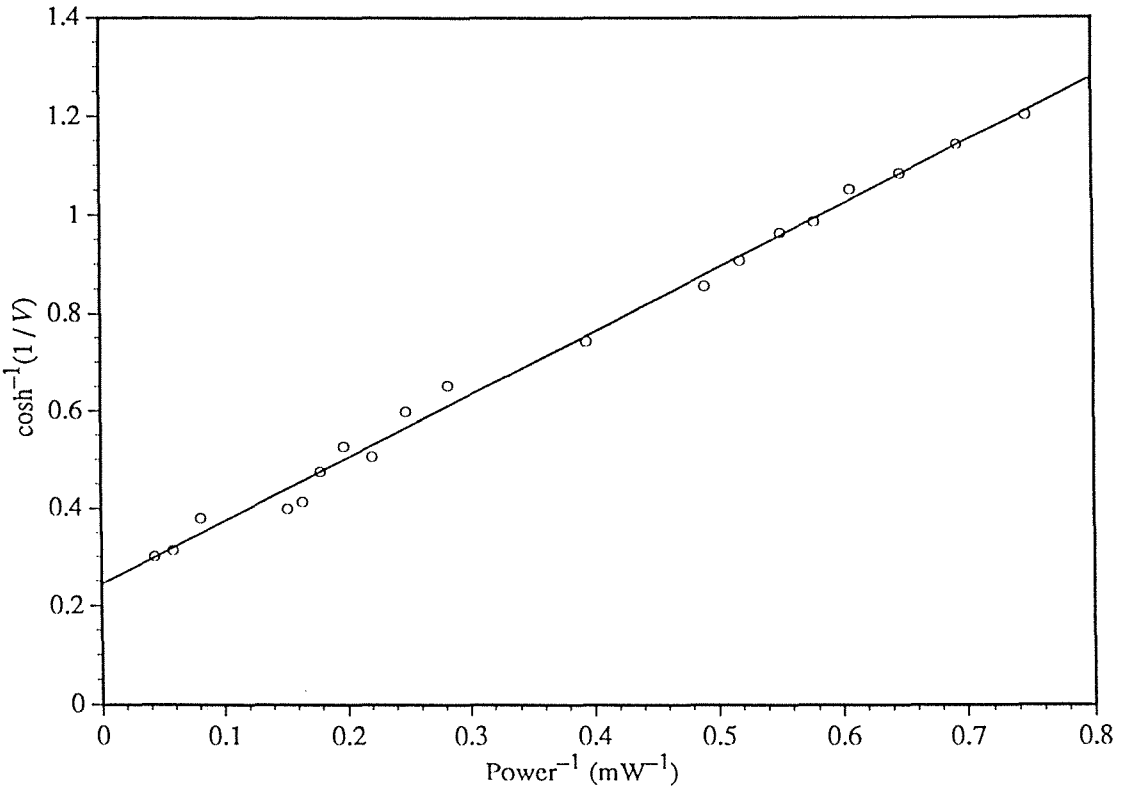

Figure 5.11. Expansion of Figure 5.10 for data below $P^{-1} = 0.8$ mW^{-1} (circles). The solid line is a linear fit to the data.

from the heterodyne experiment. This is most likely due to the presence of additional longitudinal modes in the output spectrum of the laser. A spectrometer was used to observe the relative intensities of the various modes present for the different injection current settings. As the injection current was decreased from well above threshold the additional modes became larger relative to the main lasing mode, while very close to threshold a single main mode could not be identified. The spacing of the modes was 136 GHz. This was too large to have any effect on the heterodyne result, however these modes were folded into the fringe pattern of the FPI, thus reducing the visibility. If these extra modes were not present the ordinate values on the curve in Figure 5.11 would be decreased, producing better agreement with the heterodyne experiment.

The region above $P^{-1} = 0.8$ mW^{-1} on Figure 5.10 corresponds to multi-mode behaviour of the laser output. The side modes increased in relative amplitude in an unpredictable fashion as the injection current was decreased. At currents approaching threshold, the visibility decreased at a faster rate than expected due to the fact that there were many modes with approximately the same intensity tending to smear out the fringe pattern.

The multi-mode behaviour of the diode laser renders invalid a basic assumption of the theoretical analysis of Section 5.3. Thus, the experiment presented here does not produce results in good agreement with those from the heterodyne measurement. However, it is believed that the method itself remains valid when the spectral profile can be taken as single-mode, as evidenced in the fixed linewidth experiment described in Section 5.4.2.

6. Saturated Absorption Spectroscopy

6.1. Introduction

The purpose of this chapter is first to describe theoretically the propagation of a laser beam through a cell containing caesium vapour in the absence of any buffer gas. The laser frequency is tuned through the hyperfine structure of the caesium D_2 line at 852.1 nm and the population densities of each of the 48 hyperfine sublevels are determined as a result of the atomic interaction with the radiation field of the laser. The laser intensity is assumed low enough, and its spectral distribution broad enough, that significant coherences are not built up and thus a rate equation approach is used to determine the populations. From these populations a Doppler-broadened absorption coefficient is calculated. These computations are performed in the régime of low caesium vapour density so that atom-atom collisions can be neglected. The only relaxation mechanisms considered are spontaneous emission of the upper states and beam transit time effects.

Following this theoretical description, experimental results are given. These were obtained using a single 850-nm AlGaAs diode laser stabilised in the manner described in Chapter 3. First, simple single-beam absorption experiments were performed as a "low resolution" test of the theoretical results. Here Doppler broadening masks out the hyperfine structure of the excited-state $6^2P_{3/2}$ level of the transition and the laser is narrow-band with respect to the resolvable features.

Next, the theory is extended to include a strong pump beam and a weak counter-propagating probe beam. Experiments were performed using two beams split from the same laser. These resolve the hyperfine structure and demonstrate the limitations of the stabilisation technique employed here with respect to minimum obtainable laser linewidth and maximum obtainable absolute frequency stability. However, the limitation of linewidth can be considered advantageous in the respect that the laser fills an experimental niche where it is considered sufficiently broad-band that a full density matrix formalism is not necessary to describe its interaction with the atomic system. In particular, this facilitates the analysis of the effects of optical pumping on the atomic populations and the extent to which optical pumping is influenced by ground state relaxation. Finally, an experimental technique is described to determine the ground state relaxation rate from measurements with a lock-in amplifier.

6.2. Interaction of Atoms with a Radiation Field

This section gives a brief review of the interaction of an atomic system with a monochromatic radiation field. The induced population transfer rates are given, followed by a description of the spherical basis used subsequently in specific calculations for the caesium D_2 line.

6.2.1. Population Transfer Rates

It is necessary to calculate the probability of transitions between the various atomic states to determine the effect on the atomic populations of the interaction with the laser radiation field. Assuming that the amplitude of the radiation field is small, this interaction is small compared to the Hamiltonian of the system in the absence of a field. Thus, the transition probabilities may be determined with the aid of perturbation theory. With the field represented by

$$\mathbf{E} = \mathbf{E}_0 \exp i(\mathbf{k} \cdot \mathbf{r} - \omega t) + \text{c.c}, \tag{6.1}$$

where c.c denotes the complex conjugate, the atom will experience a perturbation[72]

$$V = -\mathbf{D} \cdot \mathbf{E}, \tag{6.2}$$

where $\mathbf{D}$ is the electric dipole moment operator of an atom. Happer[73] has shown that the radiation field induces transitions between an initial state $|i\rangle$ and a final state $|f\rangle$ at a rate

$$R_{fi} = \frac{2\pi}{\hbar^2} |\mathbf{D}_{fi} \cdot \mathbf{E}_0|^2 g(\omega - \omega_{fi})$$

$$= \frac{1}{\hbar^2} \frac{|\mathbf{D}_{fi} \cdot \mathbf{E}_0|^2 \Gamma}{(\omega - \omega_{fi})^2 + (\Gamma/2)^2}, \tag{6.3a}$$

where the quantity $g(\omega - \omega_{fi})$ is the normalised atomic frequency response, which for the case of natural broadening only is given by

$$g(\omega - \omega_{fi}) = \frac{1}{2\pi} \frac{\Gamma}{(\omega - \omega_{fi})^2 + (\Gamma/2)^2}, \tag{6.4}$$

and $\Gamma = 1/\tau$ is the spontaneous emission rate of the excited state, where τ is the natural lifetime.

6.2.2. Absorption and Emission

The rate R_{fi} gives the probability per unit time that, under the influence of a radiation field, an atom undergoes a transition from state $|i\rangle$ to state $|f\rangle$. If the initial state $|i\rangle$ has a lower energy eigenvalue, E_i, than the final state $|f\rangle$ with eigenvalue E_f, then this transition is accompanied by the absorption of a quantum of energy at the frequency $\omega_{fi} = (E_f - E_i)/\hbar$. Alternatively, if $E_i > E_f$ then ω_{fi} is negative. In this case the transition rate is given by

$$R_{fi} = \frac{1}{\hbar^2} \frac{\left| \mathbf{D}_{fi} \cdot \mathbf{E}_0^* \right|^2 \Gamma}{\left(\omega + \omega_{fi}\right)^2 + \left(\Gamma/2\right)^2}, \tag{6.3b}$$

where $\mathbf{E}_0^*$ is the complex conjugate of $\mathbf{E}_0$. This situation corresponds to a downward transition with the emission of a photon at $-\omega_{fi}$.

6.2.3. The Electric Dipole Matrix

As shown by equations (6.3*a*) and (6.3*b*), the transition rates for stimulated absorption and emission are determined by the matrix elements of the electric dipole operator. Hence, these will be looked at in some detail. Because electric dipole transitions can't occur between two identical states, the diagonal matrix elements are all zero. The matrix **D** then can be naturally separated into two parts, representing absorption and emission respectively. To see this, **D** is written in the form

$$\mathbf{D} = \mathbf{1D1}, \tag{6.5}$$

where **1** is the identity operator satisfying the closure relation

$$\mathbf{1} = \sum_k |k\rangle \langle k| . \tag{6.6}$$

The set of eigenvectors $|k\rangle$ forms an orthonormal basis of the state space. Thus,

$$\mathbf{D} = \sum_k |k\rangle \langle k| \mathbf{D} \sum_m |m\rangle \langle m|$$

$$= \sum_k \sum_m |k\rangle \langle k| \mathbf{D} |m\rangle \langle m| . \tag{6.7}$$

As stated above, $\langle k| \mathbf{D} |m\rangle = 0$ for $k = m$, and with the definition $\langle k| \mathbf{D} |m\rangle = \mathbf{D}_{km}$ for $k \neq m$ one has

$$\mathbf{D} = \sum_k \sum_{m \neq k} |k\rangle \mathbf{D}_{km} \langle m|$$

$$= \mathbf{D}^+ + \mathbf{D}^-,$$

where

$$\mathbf{D}^+ = \sum_m \sum_{k<m} \mathbf{D}_{mk} |m\rangle \langle k| , \tag{6.8a}$$

and

$$\mathbf{D}^- = \sum_k \sum_{m>k} \mathbf{D}_{km} |k\rangle \langle m| . \tag{6.8b}$$

$\mathbf{D}^+$ takes an atom from a lower energy eigenstate to a higher one, accompanied by the absorption of a photon to satisfy conservation of energy, while $\mathbf{D}^-$ does the reverse with the emission of a photon. Thus, all the information concerning both absorption and emission of radiation is contained in the electric dipole matrix.

6.2.4. Spherical Basis

Symmetry considerations lead to the use of a spherical basis for the representation of both the field amplitude $\mathbf{E}_0$ and the electric dipole operator $\mathbf{D}$. In such a basis

$$\mathbf{E}_0 = \sum_q E_q \hat{\mathbf{e}}_q^* \tag{6.9a}$$

and

$$\mathbf{E}_0^* = \sum_q E_q^* \hat{\mathbf{e}}_q , \tag{6.9b}$$

where $q = -1, 0, 1$, and $\hat{\mathbf{e}}_q$ are the unit basis vectors satisfying

$$\hat{\mathbf{e}}_q \cdot \hat{\mathbf{e}}_{q'}^* = \delta_{qq'} \tag{6.10a}$$

and

$$\hat{\mathbf{e}}_q^* = (-1)^q \hat{\mathbf{e}}_{-q} . \tag{6.10b}$$

The relationships between these spherical basis vectors and the standard Cartesian unit vectors $\hat{\mathbf{i}}$, $\hat{\mathbf{j}}$, and $\hat{\mathbf{k}}$ are

$$\hat{\mathbf{e}}_0 = \hat{\mathbf{k}}, \tag{6.11a}$$

$$\hat{\mathbf{e}}_1 = -\frac{1}{\sqrt{2}} (\hat{\mathbf{i}} + i\,\hat{\mathbf{j}}), \tag{6.11b}$$

$$\hat{\mathbf{e}}_{-1} = \frac{1}{\sqrt{2}} (\hat{\mathbf{i}} - i\,\hat{\mathbf{j}}) . \tag{6.11c}$$

If $\mathbf{D}$ is also written in a spherical basis then, for absorption, the product $\mathbf{D} \cdot \mathbf{E}_0$ becomes

$$\begin{aligned} \mathbf{D} \cdot \mathbf{E}_0 &= \sum_q D_q \hat{\mathbf{e}}_q^* \cdot \sum_{q'} E_{q'} \hat{\mathbf{e}}_{q'}^* \\ &= \sum_q D_q (-1)^q \hat{\mathbf{e}}_{-q} \cdot \sum_{q'} E_{q'} \hat{\mathbf{e}}_{q'}^* \\ &= \sum_q (-1)^q D_{-q} E_q , \end{aligned} \tag{6.12a}$$

where equations (6.10*a*) and (6.10*b*) have been used. Similarly, for emission

$$\begin{aligned} \mathbf{D} \cdot \mathbf{E}_0^* &= \sum_q D_q \hat{\mathbf{e}}_q^* \cdot \sum_{q'} E_{q'}^* \hat{\mathbf{e}}_{q'} \\ &= \sum_q D_q E_q^* . \end{aligned} \tag{6.12b}$$

6.2.5. Polarisation of Radiation Field

The expansion of the vector $\mathbf{E}_0$ in a spherical basis represents a sum over three polarisation components. $q = 0$ represents linear polarisation (π), $q = +1$ left circular polarisation (σ^+), and $q = -1$ right circular polarisation (σ^-). By choosing two of these components to be zero and the third non-zero, the polarisation of the radiation field is

specified to be either pure π, pure σ^+, or pure σ^-. Table 6.1 shows the resulting non-zero $\mathbf{D} \cdot \mathbf{E}_0$ term for absorption and $\mathbf{D} \cdot \mathbf{E}_0^*$ term for emission for these three types of polarisation.

Polarisation	π	σ^+	σ^-
Absorption	$D_0 E_0$	$D_{-1} E_1$	$D_1 E_{-1}$
Emission	$D_0 E_0^*$	$D_1 E_1^*$	$D_{-1} E_{-1}^*$

Table 6.1. Non-zero components of $\mathbf{D} \cdot \mathbf{E}_0$ for linear and circular polarisations.

6.3. Hyperfine Structure

This section briefly reviews the theory of hyperfine structure in order to describe the configuration of the various hyperfine levels involved in the caesium D_2 transition. The hyperfine structure of spectral lines is attributed largely to the interaction between the nuclear magnetic moment $\boldsymbol{\mu}_I$ and the magnetic field $\mathbf{B}_{el}(0)$ produced at the nucleus by the valence electrons. This interaction is small in comparison with the electrostatic and fine structure interactions (described by the Hamiltonian $\mathbf{H}_0$) and can be treated independently. The magnetic moment of a nucleus with spin $\mathbf{I}$ is directed along $\mathbf{I}$ and is equal to $g_I\mathbf{I}$, where g_I is the gyromagnetic ratio in units of the nuclear magneton $e\hbar/2m_pc$, where m_p is the proton mass. The Hamiltonian describing the interaction between $\boldsymbol{\mu}_I$ and $\mathbf{B}_{el}(0)$ can be written as

$$\begin{aligned}\mathbf{H}_1 &= -\boldsymbol{\mu}_I \cdot \mathbf{B}_{el}(0) \\ &= A_J \mathbf{I} \cdot \mathbf{J} \end{aligned} \tag{6.13}$$

since the mean value of $\mathbf{B}_{el}(0)$ in a state with a given value of $\mathbf{J}$ is directed along $\mathbf{J}$. The constant A_J is called the magnetic hyperfine structure constant and can be determined directly from measurement.

The magnetic interaction described above gives by far the most important contribution to the observed hyperfine structure. The next largest contribution arises from the electric quadrupole interaction which exists due to the finite extent of the nuclear charge distribution. It can be shown[74a] that the Hamiltonian describing this interaction has the form

$$\mathbf{H}_2 = \frac{B_J\left[3(\mathbf{I}\cdot\mathbf{J})^2 + \frac{3}{2}(\mathbf{I}\cdot\mathbf{J}) - I(I+1)J(J+1)\right]}{2I(2I-1)J(2J-1)}, \tag{6.14}$$

where the constant B_J is called the quadrupole interaction constant which, like A_J, can be determined experimentally. If $I = 0$ or $\frac{1}{2}$ then the nuclear charge distribution is spherically symmetric and B_J is zero. Likewise if $J = 0$ or $\frac{1}{2}$ the electron charge distribution is spherically symmetric and B_J is again zero.

The total angular momentum is written as

$$\mathbf{F} = \mathbf{I} + \mathbf{J}, \tag{6.15}$$

and the total angular momentum quantum number F can take values

$$F = I+J, I+J-1, ..., |I-J|. \tag{6.16}$$

Writing the hyperfine structure Hamiltonian as

$$\mathbf{H}_{\mathrm{HFS}} = \mathbf{H}_1 + \mathbf{H}_2, \tag{6.17}$$

one can express the energy of a particular hyperfine level as

$$E_F = \langle J\, I\, F\, M_F | \mathbf{H}_0 + \mathbf{H}_{\mathrm{HFS}} | J\, I\, F\, M_F \rangle,$$

where M_F is the projection of **F** onto the quantisation axis. This leads to[75]

$$E_F = E_J + \tfrac{1}{2} A_J K_F + \frac{B_J \left[3K_F(K_F+1) - 4I(I+1)J(J+1)\right]}{8I(2I-1)J(2J-1)}, \tag{6.18}$$

where E_J is the energy, in frequency units, of the fine structure multiplet with total electronic angular momentum quantum number J, and $K_F = F(F+1) - I(I+1) - J(J+1)$.

The hyperfine structure of the caesium D_2 line at 852.1 nm is shown in Figure 6.1. The lower states ($6^2S_{1/2}$) will be labelled $|\, l\, F\, M_F\rangle$ and the upper states ($6^2P_{3/2}$) $|\, u\, F'\, M_F'\rangle$. The $6^2S_{1/2}$ level is the ground state. Caesium has only one stable isotope, ^{133}Cs, with $I = \frac{7}{2}$. The hyperfine splittings shown in Figure 6.1 have been calculated using experimental values of A_J and B_J. There is some discrepancy concerning the exact values of these quantities, but the review article by Arimondo *et al.*[75] gives the recommended values of $A_{1/2} = 2298.1579425$ MHz, $A_{3/2} = 50.34 \pm 0.06$ MHz and $B_{3/2} = -0.38 \pm 0.18$ MHz. The latter two values are the averages of the quantities determined by Buck *et al.*[76], Svanberg *et al.*[77], Violino[78], and Svanberg *et al.*[79] using several different techniques. Since $J = \frac{1}{2}$ for the lower states $B_{1/2} = 0$ and the lower splitting is determined solely by the magnetic interaction and conforms to the Landé interval rule:

$$\begin{aligned} \Delta E_F &= E_F - E_{F-1} = \tfrac{1}{2} A_{1/2}\left(K_F - K_{F-1}\right) \\ &= F A_{1/2}. \end{aligned} \tag{6.19}$$

Therefore, $\Delta E_4 = 4A_{1/2} = 9192.631770$ MHz (precisely, by agreement).

For the $6^2P_{3/2}$ level, $B_{3/2} \neq 0$ and equation (6.18) becomes

$$E_{F'} = E_{3/2} + \tfrac{1}{2} A_{3/2} K_{F'} + \frac{B_{3/2}\left[3K_{F'}(K_{F'}+1) - 236.25\right]}{504}.$$

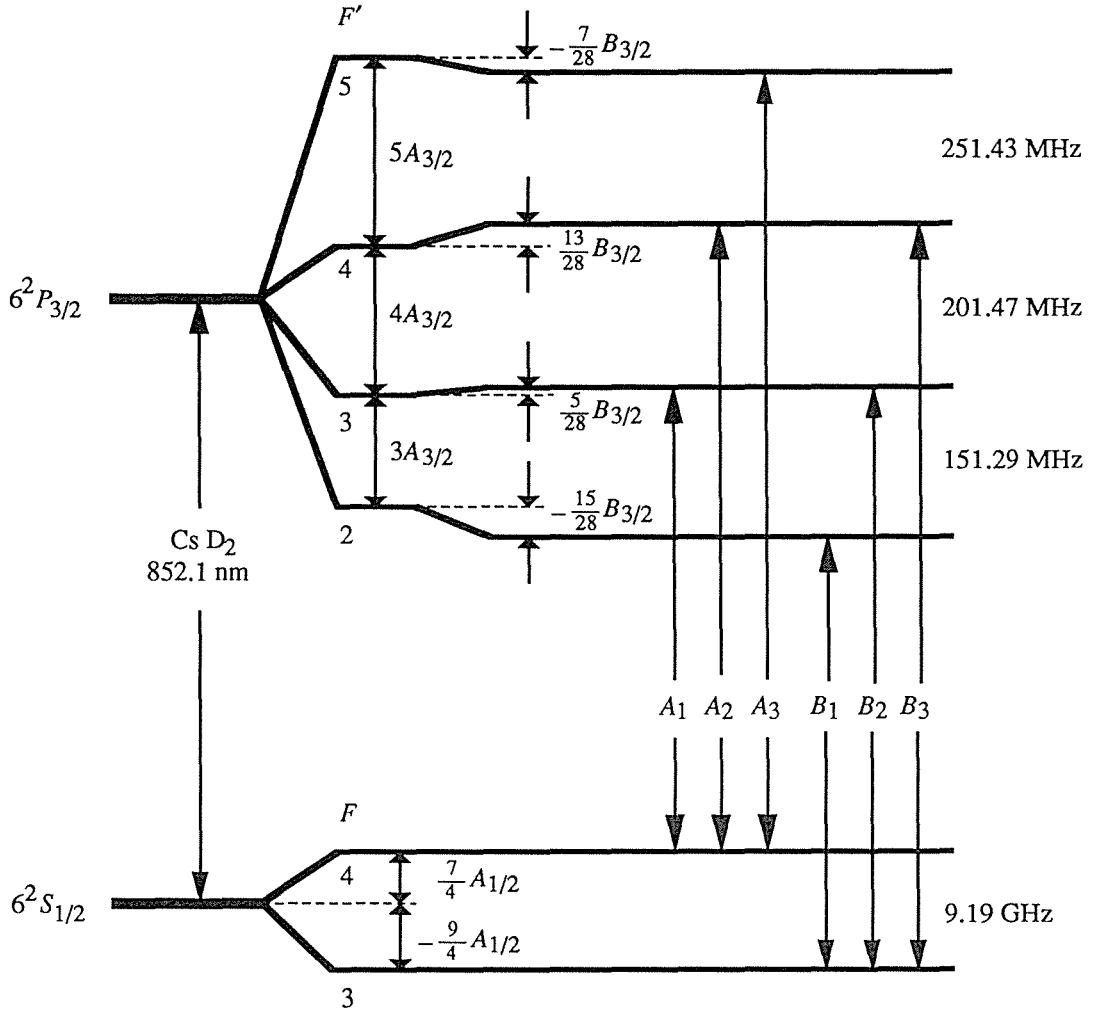

Allowed Transitions

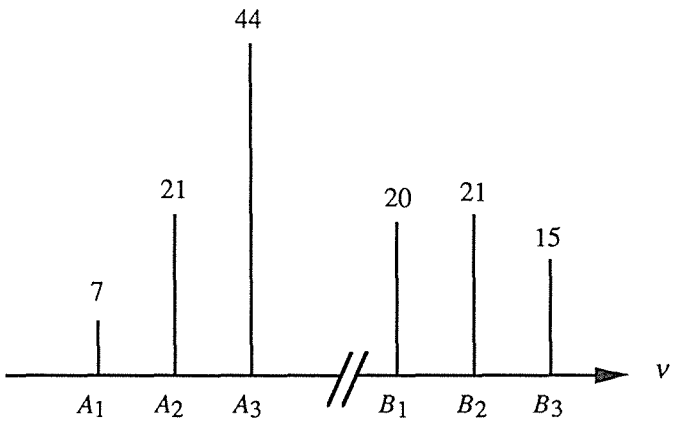

Relative Strengths

Figure 6.1. Energy level diagram for the caesium D_2 transition showing the allowed transitions and relative strengths. The diagram is not draw to scale.

Therefore,

$$\Delta E_{F'} = F'A_{3/2} + \frac{F'B_{3/2}\,(F'^2 - 19)}{42}\,. \tag{6.20}$$

This level is split into $2J'+1 = 4$ hyperfine levels, and the three energy splittings are determined from the above values of $A_{3/2}$ and $B_{3/2}$ (assuming only the magnetic dipole and electric quadrupole interactions). These values can be used to compare the relative contributions to these splittings from the magnetic dipole and electric quadrupole interactions respectively:

$$\begin{aligned} E_3 - E_2 &= 151.02 + 0.27 = 151.29 \text{ MHz}, \\ E_4 - E_3 &= 201.36 + 0.11 = 201.47 \text{ MHz}, \\ E_5 - E_4 &= 251.70 - 0.27 = 251.43 \text{ MHz}. \end{aligned}$$

These values are shown on Figure 6.1.

6.4. Calculation of Transfer Rates for Caesium D_2 Line

This section looks in some detail at the electric dipole matrix elements. Their direct relationship to selection rules is applied to the caesium D_2 line to obtain the allowed transitions, and a calculation is made of each non-zero element. This allows evaluation of the stimulated and spontaneous transfer rates for each allowed transition.

6.4.1. Selection Rules for Electric Dipole Transitions

The allowed electric dipole transitions are those for which the electric dipole matrix elements connecting two states are non-zero. The components of **D**, when expanded in a spherical basis, are spherical tensors of rank 1. These are denoted D_q^k where $k = 1$ (rank) and $q = -1, 0, 1$ (component). According to the Wigner-Eckart Theorem[80a] the matrix elements of a spherical tensor T_q^k can be written

$$\langle \alpha_1 j_1 m_1 | T_q^k | \alpha_2 j_2 m_2 \rangle = (-1)^{j_1 - m_1} \begin{pmatrix} j_1 & k & j_2 \\ -m_1 & q & m_2 \end{pmatrix} \langle \alpha_1 j_1 \| T^k \| \alpha_2 j_2 \rangle, \quad (6.21)$$

where $\begin{pmatrix} j_1 & k & j_2 \\ -m_1 & q & m_2 \end{pmatrix}$ is a 3-j symbol and $\langle \alpha_1 j_1 \| T^k \| \alpha_2 j_2 \rangle$ is the reduced matrix element of T^k, which is independent of m_1, m_2, and q. The matrix elements of **D** are therefore

$$\langle u F' M_F' | D_q | l F M_F \rangle = (-1)^{F - M_F} \begin{pmatrix} F' & 1 & F \\ -M_F' & q & M_F \end{pmatrix} \langle u F' \| D \| l F \rangle, \quad (6.22)$$

where the superscript 1 has been dropped from D. The selection rules can be obtained directly from the definition of the 3-j symbols[81]. The symbol $\begin{pmatrix} j_1 & j_2 & j_3 \\ m_1 & m_2 & m_3 \end{pmatrix}$ is identically zero unless both $m_1 + m_2 + m_3 = 0$ and the vectors $\mathbf{j}_1 + \mathbf{j}_2 + \mathbf{j}_3 = \mathbf{0}$. The latter equality implies the triangle condition on j_1, j_2, and j_3:

$$j_3 = j_1 + j_2, j_1 + j_2 - 1, \ldots, |j_1 - j_2|. \quad (6.23)$$

With these properties, $\langle u F' M_F' | D_q | l F M_F \rangle$ is zero unless $M_F' - M_F = q$ and $F' = F + 1, F, F - 1$. These can be written

$$\Delta M_F = q \quad (6.24a)$$

and

$$\Delta F = 0, \pm 1, \quad (6.24b)$$

where $\Delta M_F = M_F' - M_F$ and $\Delta F = F' - F$. Note that the matrix element $\langle u F' M_F' | D_q | l F M_F \rangle$ describes a transition from a lower state to an upper state. For

downward transitions u and l are interchanged, as are the primed and unprimed quantities in equation (6.22). The effect this has on the selection rules is that in this case $\Delta M_F = -q$. As discussed in Section 6.2.5, for a linearly polarised radiation field only the component D_0 is involved, for left circular polarisation D_{-1} for absorption and D_1 for emission, and for right circular polarisation D_1 for absorption and D_{-1} for emission. Hence, the same states are involved for both absorption and emission for a given polarisation, as one would expect.

6.4.2. Calculation of the Matrix Elements of D

Since the equation for the transition probability between two states contains the square of the matrix elements of **D**, the $(-1)^n$ factors can be ignored:

$$\left|\langle u\,F'\,M_F'|D_q|l\,F\,M_F\rangle\right|^2 = \begin{pmatrix} F' & 1 & F \\ -M_F' & q & M_F \end{pmatrix}^2 \left|\langle u\,F'\|D\|l\;F\rangle\right|^2. \tag{6.25}$$

The selection rule $\Delta F = 0, \pm 1$ determines that there are six non-zero quantities $\left|\langle u\,F'\|D\|l\;F\rangle\right|^2$ for the caesium D_2 transition. These quantities are called the transition line strengths and are denoted $S(u\,F';\,l\,F)$[82a]. The orthogonality property of the 3-j symbols[81]:

$$\sum_{m_1,\,m_2} \begin{pmatrix} j_1 & j_2 & j_3 \\ m_1 & m_2 & m_3 \end{pmatrix} \begin{pmatrix} j_1 & j_2 & j_3' \\ m_1 & m_2 & m_3' \end{pmatrix} = \frac{\delta(j_3, j_3')\delta(m_3, m_3')}{2j_3 + 1} \tag{6.26}$$

implies

$$\sum_{M_F,\,M_F'} \begin{pmatrix} F' & 1 & F \\ -M_F' & q & M_F \end{pmatrix}^2 = \frac{1}{3}. \tag{6.27}$$

Therefore,

$$\sum_{q,\,M_F,\,M_F'} \left|\langle u\;F'\;M_F'\,|D_q|\,l\,F\,M_F\rangle\right|^2$$

$$= \sum_{M_F,\,M_F'} \left|\langle u\;F'\;M_F'\,|\,\mathbf{D}\,|\,l\,F\,M_F\rangle\right|^2 = S(u\;F';\;l\;F). \tag{6.28}$$

Also, since D is Hermitian, $\left|\langle l\,F\|D\|u\,F'\rangle\right|^2 = \left|\langle u\,F'\|D\|l\,F\rangle\right|^2$[82b]; therefore,

$$S(l\,F;\,u\,F') = S(u\,F';\,l\,F). \tag{6.29}$$

The values of the relative line strengths for the caesium D_2 line are shown on Figure 6.1.

Each of the line strengths $S(u\,F';\,l\,F)$ can be related to a single overall line strength $S(u;\,l) = \left|\langle u \,\|D\|\, l\rangle\right|^2$ for the D_2 transition via the expression[80b]

$$\langle J_1\,J_2\,J \,\|\, T^k \,\|\, J_1'\,J_2\,J'\rangle = (-1)^{J_1+J_2+J'+k}\sqrt{(2J+1)(2J'+1)}\begin{Bmatrix} J_1 & J & J_2 \\ J' & J_1' & k \end{Bmatrix}\langle J_1 \,\|\, T^k \,\|\, J_1'\rangle, \quad (6.30)$$

where $\begin{Bmatrix} J_1 & J & J_2 \\ J' & J_1' & k \end{Bmatrix}$ is a 6-j symbol[81]. Equation (6.30) is only valid if T^k commutes with J_2. Thus, for the caesium D_2 line

$$\left|\langle J'\,I\,F' \|D\|\, J\,I\,F\rangle\right|^2 = (2F'+1)(2F+1)\begin{Bmatrix} J' & F' & I \\ F & J & 1 \end{Bmatrix}^2 \left|\langle J' \|D\|\, J\rangle\right|^2,$$

or

$$S(u\,F';\,l\,F) = (2F'+1)(2F+1)\begin{Bmatrix} \frac{3}{2} & F' & \frac{7}{2} \\ F & \frac{1}{2} & 1 \end{Bmatrix}^2 S(u;\,l). \quad (6.31)$$

The 6-j symbol in equation (6.31) contains all the information concerning the allowed values of F and F' in the hyperfine structure of the transition. Symmetry properties of the 6-j symbol[81] imply that the symbol remains invariant under interchange of columns, and also against interchange of any *two* numbers in the bottom row with the *corresponding* numbers in the top row. Furthermore, the 6-j symbol $\begin{Bmatrix} j_1 & j_2 & j_3 \\ l_1 & l_2 & l_3 \end{Bmatrix}$ is identically zero unless, for example, j_1, j_2, and j_3 satisfy the triangle condition $j_3 = j_1 + j_2, j_1 + j_2 - 1, \ldots, |j_1 - j_2|$. Symmetry gives

$$\begin{Bmatrix} \frac{3}{2} & F' & \frac{7}{2} \\ F & \frac{1}{2} & 1 \end{Bmatrix} = \begin{Bmatrix} \frac{3}{2} & \frac{7}{2} & F' \\ F & 1 & \frac{1}{2} \end{Bmatrix} = \begin{Bmatrix} \frac{1}{2} & \frac{7}{2} & F \\ F' & 1 & \frac{3}{2} \end{Bmatrix} = \begin{Bmatrix} F' & 1 & F \\ \frac{1}{2} & \frac{7}{2} & \frac{3}{2} \end{Bmatrix}. \quad (6.32)$$

Applying the triangle condition to the last three of these 6-j symbols gives, respectively, $F' = 5,\ 4,\ 3,\ 2$, $F = 4,\ 3$, and $F' - F = \Delta F = 0, \pm 1$.

The squares of the matrix elements of $\mathbf{D}$ in terms of the single line strength $S(u;\,l)$ are obtained by substitution of equation (6.31) into equation (6.25):

$$\left|\langle u\,F'\,M_F'|D_q|l\,F\,M_F\rangle\right|^2 = (2F'+1)(2F+1)\begin{pmatrix} F' & 1 & F \\ -M_F' & q & M_F \end{pmatrix}^2 \begin{Bmatrix} F' & 1 & F \\ \frac{1}{2} & \frac{7}{2} & \frac{3}{2} \end{Bmatrix}^2 S(u;\,l)$$

$$= \frac{1}{4}\,a_{F'M_F',FM_F} S(u;\,l), \quad (6.33)$$

where

$$a_{F'M_F',FM_F} = 4(2F'+1)(2F+1)\begin{pmatrix} F' & 1 & F \\ -M_F' & q & M_F \end{pmatrix}^2 \begin{Bmatrix} F' & 1 & F \\ \frac{1}{2} & \frac{7}{2} & \frac{3}{2} \end{Bmatrix}^2 \qquad (6.34)$$

is the transfer coefficient between states $|u\,F'\,M_F'\rangle$ and $|l\,F\,M_F\rangle$. Note that the factor of 4 in the transfer coefficients is the multiplicity $2J' + 1$ of the upper $6^2P_{3/2}$ level. These coefficients have been calculated and are shown in Figure 6.2 for each of the allowed transitions.

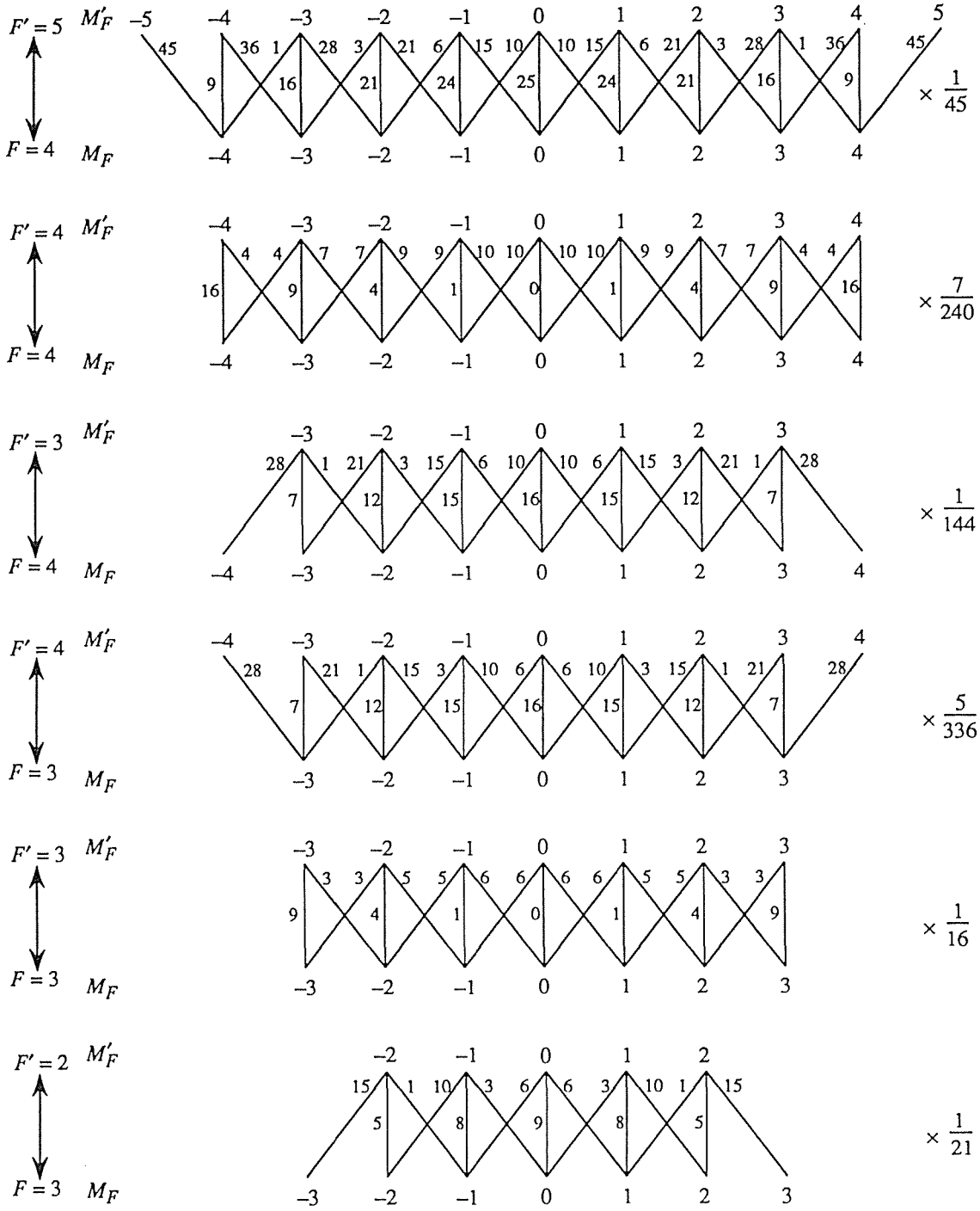

Figure 6.2. Transfer coefficients for the caesium D_2 transition.

6.4.3. Spontaneous Emission

As shown in the previous sub-section, in order to calculate the matrix elements of **D** one must know the line strength $S(u; l)$. This quantity is related to the lifetime of the upper $6^2P_{3/2}$ level, as follows. The spontaneous emission probability from an upper state $|u\,F'\,M_F'\rangle$ to a lower state $|l\,F\,M_F\rangle$ is related to the dipole matrix element, and is given by[83]

$$A_{FM_F,F'M_F'} = \frac{\omega_{lu}^3}{3\pi\varepsilon_0\hbar c^3} \left|\langle l\,F\,M_F|\mathbf{D}|u\,F'\,M_F'\rangle\right|^2, \tag{6.35}$$

where ω_{lu} is the frequency of the D_2 transition. Now

$$\left|\langle l\,F\,M_F|\mathbf{D}|u\,F'\,M_F'\rangle\right|^2 = \sum_q \left|\langle l\,F\,M_F|D_q|u\,F'\,M_F'\rangle\right|^2,$$

where $q = 0, \pm 1$. Therefore, from equation (6.33)

$$A_{FM_F,F'M_F'} = \frac{\omega_{lu}^3}{3\pi\varepsilon_0\hbar c^3} \sum_q (2F+1)(2F'+1) \begin{pmatrix} F & 1 & F' \\ -M_F & q & M_F' \end{pmatrix}^2 \begin{Bmatrix} F & 1 & F' \\ \frac{3}{2} & \frac{7}{2} & \frac{1}{2} \end{Bmatrix}^2 S(l; u). \tag{6.36}$$

If the Zeeman structure is not resolved, equation (6.36) must be summed over the lower M_F states and averaged over the upper M_F' states:

$$A_{F,F'} = \frac{\omega_{lu}^3}{3\pi\varepsilon_0\hbar c^3} \frac{1}{2F'+1} \sum_{q,M_F,M_F'} (2F+1)(2F'+1) \begin{pmatrix} F & 1 & F' \\ -M_F & q & M_F' \end{pmatrix}^2 \begin{Bmatrix} F & 1 & F' \\ \frac{3}{2} & \frac{7}{2} & \frac{1}{2} \end{Bmatrix}^2 S(l; u)$$

$$= \frac{\omega_{lu}^3}{3\pi\varepsilon_0\hbar c^3} (2F+1) \begin{Bmatrix} F & 1 & F' \\ \frac{3}{2} & \frac{7}{2} & \frac{1}{2} \end{Bmatrix}^2 S(l; u), \tag{6.37}$$

where equation (6.27) has been used. Similarly, if the hyperfine structure is not resolved, equation (6.37) must be summed over the lower F levels and averaged over the upper F' levels:

$$A_{lu} = \frac{\omega_{lu}^3}{3\pi\varepsilon_0\hbar c^3} \frac{1}{2J'+1} \sum_{F,F'} (2F+1) \begin{Bmatrix} F & 1 & F' \\ \frac{3}{2} & \frac{7}{2} & \frac{1}{2} \end{Bmatrix}^2 S(l; u). \tag{6.38}$$

From the orthogonality relationship of the 6-j symbol[81]:

$$\sum_{l} (2l+1)(2j''+1) \begin{Bmatrix} j_1 & j_2 & j' \\ l_1 & l_2 & l \end{Bmatrix} \begin{Bmatrix} j_1 & j_2 & j'' \\ l_1 & l_2 & l \end{Bmatrix} = \delta(j',j''), \tag{6.39}$$

equation (6.38) becomes

$$\begin{aligned} A_{lu} &= \frac{\omega_{lu}^3}{3\pi\varepsilon_0\hbar c^3} \frac{1}{4} \sum_{F'} \frac{1}{2J'+1} S(l;u) \\ &= \frac{\omega_{lu}^3}{3\pi\varepsilon_0\hbar c^3} \frac{1}{4} S(l;u) = \frac{1}{\tau} = \Gamma, \end{aligned} \tag{6.40}$$

where τ is the lifetime of the $6^2P_{3/2}$ level and is equal to 32.7 ns[84]. Hence, the line strength $S(u; l)$ is given by

$$S(u;l) = S(l;u) = \frac{3\pi\varepsilon_0\hbar c^3}{\omega_{lu}^3} 4\Gamma. \tag{6.41}$$

Thus, the matrix elements of **D** are, from equation (6.33),

$$\left| \langle u\, F'\, M_F' \left| D_q \right| l\, F\, M_F \rangle \right|^2 = \frac{3\pi\varepsilon_0\hbar c^3}{\omega_{ul}^3} a_{F'M_F',FM_F}\, \Gamma, \tag{6.42}$$

and, from equation (6.35),

$$A_{FM_F,F'M_F'} = a_{FM_F,F'M_F'}\, \Gamma \tag{6.43}$$

are the spontaneous emission rates.

6.5. Calculation of Transmitted Intensity

This section describes the method of calculation used to obtain the transmitted intensity of the laser beam after interaction with the caesium atoms. A rate equation model is first discussed from which an absorption coefficient can be calculated. Finally, the attenuation of the beam as a result of absorption is derived as the beam propagates through the cell.

6.5.1. Rate Equations

A phenomenological approach, which considers the rate equations describing the populations of the various states involved, is used to determine the steady-state populations. The rate equation solution can be considered valid when the laser field is sufficiently weak and broad-band that the time between optical transitions is too short for the build-up of coherences. This can be quantified by defining a pumping time T_p for transfer between states i and j[85]:

$$\frac{1}{T_p} = \frac{2}{\hbar^2 \varepsilon_0 c \Gamma_L} \frac{P}{S} |\mathbf{D}_{ij}|^2, \tag{6.44}$$

where P is the laser power, S the beam cross-section, and Γ_L the laser linewidth. The rate equation approximation will hold for those intensities such that $\tau_L \ll Tp$, where $\tau_L = 1/\Gamma_L$ is the laser coherence time. With a laser linewidth of 10 MHz this restricts the considered intensities to much less than about 300 mW/cm^2 for the weakest transition and 16 mW/cm^2 for the strongest, which convert to 1.5 mW and 0.08 mW, respectively, with the beam radius of 400 μm used in the subsequent experiments. Tremblay and Jacques[41] have shown, however, that when the laser linewidth is larger than the natural linewidth the coherences quickly disappear, particularly when using linearly polarised light. Hence, the above restriction need not be rigidly applied. In addition to the low power requirement, the number density of caesium atoms will be considered small enough that velocity-changing collisions[45] can be neglected. This means that the mean free path of a caesium atom must be large enough that the time between collisions is much longer than the excited-state lifetime. An elementary calculation of the collision cross-section[86] yields an upper limit to the number density of about 10^{22} m^{-3} for hard-sphere collisions. To totally eliminate weak velocity-changing collisions, where atoms interact via long-range forces, will require a much lower density limit.

The rate equation approach has been previously applied to the caesium D_2 transition by several researchers. Hirano[87] has considered four-level and six-level schemes and has obtained exact analytic solutions to the rate equations. This approach neglects the effects of Zeeman pumping. Nakayama[88, 89] has also used a four-level scheme and calculated the relative intensities of the Doppler-free signals for both the caesium and rubidium D_2 lines. These calculations neglected ground state relaxation. A rate equation calculation which considered Zeeman sublevels of a monokinetic caesium atomic beam but not neighbouring hyperfine levels of the upper state was made by de Clerq *et al.*[83], for the purpose of efficiently creating a large population difference between the $M_F = 0$ sublevels of the ground state. Avila *et al.*[40] have done a similar calculation including neighbouring transitions. This hyperfine transition ("clock transition") is important for atomic frequency standards, and is defined as 9.192631770 GHz exactly. Arditi and Picqué[38] have demonstrated the possibility of replacing the magnetic state selection method[90], in which an inhomogeneous magnetic field is used to deflect caesium atoms in a beam, by state selection using optical pumping with a diode laser. The population difference of the "clock transition" should be maximised in order to increase the signal-to-noise ratio of the resonance signal, leading to a more stable frequency standard. A full density matrix calculation including all Zeeman sublevels was performed by Tremblay and Jacques[41], again for the purpose of obtaining efficient optical pumping for the "clock transition". These latter three calculations all neglected ground state relaxation.

The rate equation approach here considers all Zeeman sublevels and includes ground state relaxation. In order to simplify the notation, the population of the state labelled by F and M_F, that is ρ_{FM_F}, will be simply referred to as ρ_i, where i is an integer from 1 to 48. The numbering of the populations is illustrated in Table 6.2. The ρ_i's are

$F' = 5$	ρ_{38}	ρ_{39}	ρ_{40}	ρ_{41}	ρ_{42}	ρ_{43}	ρ_{44}	ρ_{45}	ρ_{46}	ρ_{47}	ρ_{48}
$F' = 4$		ρ_{29}	ρ_{30}	ρ_{31}	ρ_{32}	ρ_{33}	ρ_{34}	ρ_{35}	ρ_{36}	ρ_{37}	
$F' = 3$			ρ_{22}	ρ_{23}	ρ_{24}	ρ_{25}	ρ_{26}	ρ_{27}	ρ_{28}		
$F' = 2$				ρ_{17}	ρ_{18}	ρ_{19}	ρ_{20}	ρ_{21}			
$F = 4$		ρ_8	ρ_9	ρ_{10}	ρ_{11}	ρ_{12}	ρ_{13}	ρ_{14}	ρ_{15}	ρ_{16}	
$F = 3$			ρ_1	ρ_2	ρ_3	ρ_4	ρ_5	ρ_6	ρ_7		
M_F, M_F'	−5	−4	−3	−2	−1	0	1	2	3	4	5

Table 6.2. Numbering of the hyperfine sublevel population densities.

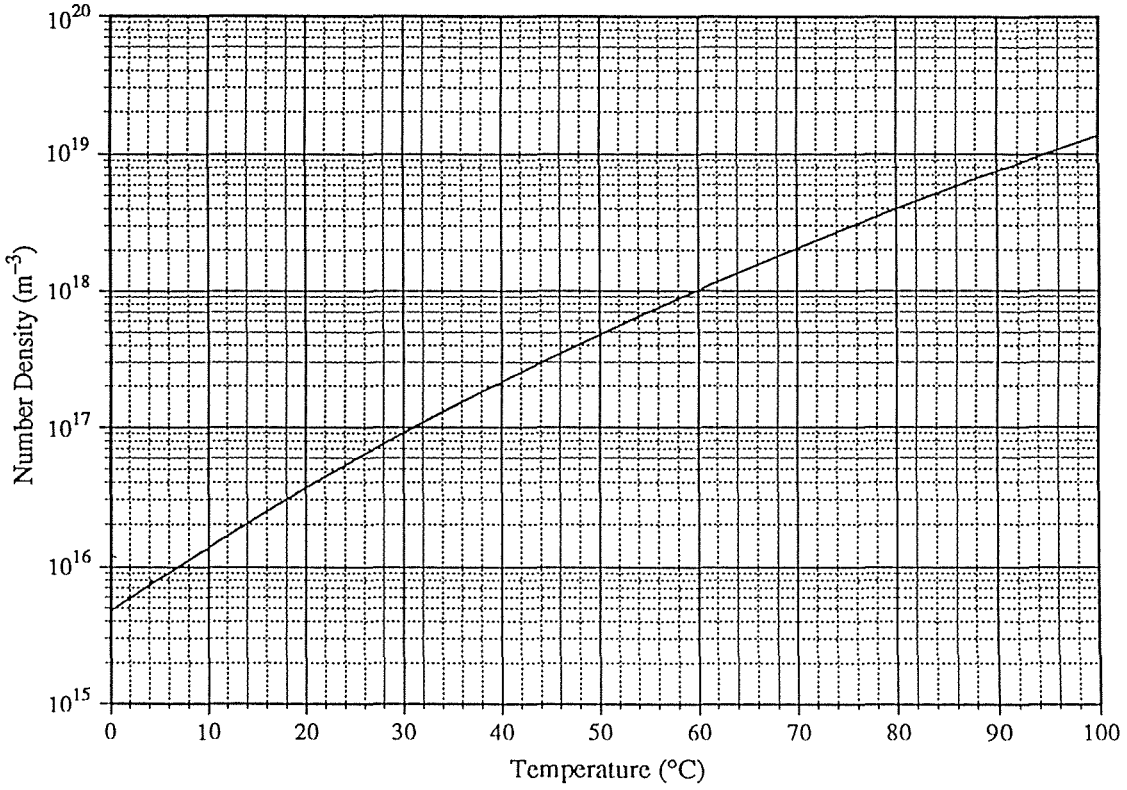

Figure 6.3. Caesium number density as a function of temperature as given by equation (6.46).

normalised such that

$$\sum_{i=1}^{48} \rho_i = 1. \tag{6.45}$$

The actual population densities are obtained by the multiplication of each ρ_i by the caesium atomic number density. Belov *et al.*[91] have experimentally determined this over the temperature range from 304 to 364 K using the magnetic scanning method. Their result is

$$n(T) = \frac{10^{31.508 - 3657.7/T}}{T}, \tag{6.46}$$

where $n(T)$ is the number density, in units of m^{-3}, as a function of the temperature T measured in Kelvin. This result has an accuracy of 10%. Equation (6.46) is graphed in Figure 6.3.

The rate equations form a set of 48 equations of the form:

$$\frac{\partial \rho_i}{\partial t} = \sum_{j=1}^{48} R_{ij}\rho_j - \sum_{j=1}^{48} R_{ji}\rho_i + \sum_{j=1}^{48} A_{ij}\rho_j - \sum_{j=1}^{48} A_{ji}\rho_i + R\left(\rho_{i(0)} - \rho_i\right). \tag{6.47}$$

The first and second terms on the right hand side are due to absorption and stimulated emission. Equations (6.3) and (6.33) show that $R_{ij} = R_{ji}$. The third and fourth terms in equation (6.47) represent spontaneous emission. Since the $6^2S_{1/2}$ level (states 1 to 16) is the ground state, $A_{ij} = 0$ for $j \leq 16$ and $i \geq 17$. The final term in equation (6.47) describes ground state relaxation. The rate R is due to the transit time of the atoms through the laser beam. After leaving the beam the atoms travel to the cell walls where, because the walls are uncoated, almost every collision destroys the atom's polarisation[73]. The population $\rho_{i(0)}$ is the zero-field value of ρ_i. In the absence of the beam the atoms are randomly distributed throughout the lower states, that is $\rho_{i(0)} = \frac{1}{16}$ for $1 \leq i \leq 16$, and $\rho_{i(0)} = 0$ for i ≥ 17 (upper states empty). Atoms enter the beam in the ground state and interact with the radiation field for a duration of $1/R$. This time period is long compared to the lifetime of the upper states, hence the beam transit effect is greater for the lower states than the excited states (spontaneous emission usually dominates the excited state populations). The ground state relaxation rate, R, is not determined by the time between wall collisions, but rather by the beam transit time because this gives the effective rate of destruction of polarisation. Each atom travels at a different velocity with respect to the beam propagation; however, a first approximation is to assume that a single effective relaxation rate applies to the system as a whole, determined by the average atomic speed $v_p = \sqrt{2kT/m}$:

$$R = \frac{v_p}{2a}, \tag{6.48}$$

where a is the beam radius. The validity of this approximation will be examined in Section 6.9.

To obtain the steady-state solution to the set of coupled first order differential equations (6.47), the left hand sides are set to zero. This reduces the problem to solving the following set of linear equations:

$$\begin{aligned} &\sum_{j=17}^{48} R_{ij}(\rho_j - \rho_i) + \sum_{j=17}^{48} A_{ij}\rho_j + R\left(\frac{1}{16} - \rho_i\right) = 0 \text{ for } 1 \leq i \leq 16, \\ &\sum_{j=1}^{16} R_{ij}(\rho_j - \rho_i) - \sum_{j=1}^{16} A_{ji}\rho_i - R\rho_i = 0 \text{ for } 17 \leq i \leq 48. \end{aligned} \tag{6.49}$$

These equations can be rearranged to give:

$$-\rho_i\left(\sum_{j=17}^{48} R_{ij} + R\right) + \sum_{j=17}^{48} \rho_j(R_{ij} + A_{ij}) = -\frac{R}{16} \text{ for } 1 \le i \le 16,$$

$$-\rho_i\left[\sum_{j=1}^{16}(R_{ij} + A_{ji}) + R\right] + \sum_{j=1}^{16} R_{ij}\rho_j = 0 \text{ for } 17 \le i \le 48. \tag{6.50}$$

The first term in each of equations (6.50) represents the rate of loss of population from state i, while the second term gives the rate of gain of population from each of the other coupled states. Equations (6.50) can be written in the form

$$M\rho = \mathbf{b}, \tag{6.51}$$

where the components of the vector ρ are the populations ρ_i, the 48×48 dimensional matrix M describes the coefficients in equations (6.50), and the vector $\mathbf{b}$ corresponds to the right hand sides of equations (6.50). Inversion of M yields the steady-state populations.

6.5.2. Inclusion of Laser Linewidth

The effect of the finite laser linewidth is to distribute the laser power through a range of frequencies thus reducing the pump intensity at any one frequency. To incorporate this into the rate equations the pumping rates are convolved over the spectral profile of the laser light. Since these profiles are both Lorentzian in shape, this convolution results simply in the substitution of the natural width in equation (6.3) by the sum of the natural width and the laser width (see Appendix *D*).

6.5.3. Absorption Coefficient

The absorption coefficient for a two level system is defined by[74b]

$$\alpha(\omega) = \frac{\pi^2 c^2}{\omega_{ik}^2} A_{ik}\left(\frac{g_k}{g_i} N_i - N_k\right) g(\omega - \omega_{ik}), \tag{6.52}$$

where N_i and N_k are the population densities of the lower and upper levels respectively (proportional to ρ_i and ρ_k), g_i and g_k are their respective multiplicities, and $g(\omega - \omega_{ik})$ is the atomic frequency response defined by equation (6.4).

For the multi-level system of the caesium D_2 line equation (6.52) is modified to become a sum over the allowed transitions:

$$\alpha(\omega) = \frac{\pi^2 c^2}{\omega^2} \sum_{i,k} A_{ik} \, (N_i - N_k) \, g(\omega - \omega_{ik}). \tag{6.53}$$

Here the multiplicities are all unity, and ω_{ik} outside the summation is taken to be ω, the $6^2P_{3/2} \rightarrow 6^2S_{1/2}$ frequency.

6.5.4. Doppler Broadening

Due to the thermal motion of the caesium atoms in the absorption cell, the profile of the absorption coefficient in equation (6.53) is considerably broadened. (In fact, equation (6.53) holds only for atoms with zero velocity in the direction of beam propagation.) At thermal equilibrium the atoms follow a Maxwellian velocity distribution[68b]:

$$N_i(v_z) \, dv_z = \frac{N_i}{v_p \sqrt{\pi}} \exp\left[-\left(\frac{v_z}{v_p}\right)^2\right] dv_z, \tag{6.54}$$

where the laser propagation is assumed to be in the z direction, and $v_p = \sqrt{2kT/m}$ is the most probable magnitude of the component of the atomic velocity along z at the temperature T. The Doppler-broadened absorption coefficient is obtained by integrating equation (6.53) over this velocity profile:

$$\alpha_D(\omega, T) = \frac{\pi^{3/2} c^3}{v_p \omega^3} \int \sum_{i,k} A_{ik} \, (N_i - N_k) \, g(\omega' - \omega_{ik}) \times \exp\left\{-\left[\frac{c}{v_p}\left(\frac{\omega' - \omega}{\omega}\right)\right]^2\right\} d\omega'. \tag{6.55}$$

6.5.5. Beam Propagation

The propagation of the beam through the absorption cell is determined by the absorption coefficient of equation (6.55). The intensity $I(z)$ of the beam as a function of distance z travelled through the cell is attenuated according to

$$dI = -\alpha_D I dz. \tag{6.56}$$

The Doppler-broadened absorption coefficient, α_D, is, through the population densities, a non-linear function of intensity. The solution to equation (6.56) is then

$$I(L) = I(0) \exp\left(-\int_0^L \alpha_D(z)\, dz\right), \tag{6.57}$$

where L is the length of the cell and $I(0)$ is the incident intensity. The integral of α_D over the cell length is an integral over intensity since, as the beam propagates, the intensity decreases due to absorption which in turn affects the absorption coefficient. The value of $I(L)$ is calculated in practice by considering the cell to be divided into a number of finite intervals of length Δz_n, with the assumption that the atomic population densities are unchanged by the beam interaction over a distance of one interval. That is to say the medium is optically thin over an interval Δz_n. Then equation (6.57) can be solved iteratively:

$$I(z_{n+1}) = I(z_n)\, e^{-\alpha_D(z_n)\Delta z_n}, \tag{6.58}$$

where
$$\begin{aligned} n &= 0, 1, 2, \ldots, N, \\ z_n &= \Delta z_0 + \Delta z_1 + \ldots + \Delta z_{n-1} \text{ for } n > 0, \\ z_0 &= 0, \text{ and} \\ z_N &= L. \end{aligned} \tag{6.59}$$

The optical thickness $\tau(z)$ is defined as[74c]

$$\tau(z) = \int_0^z \alpha_D(z')\, dz', \tag{6.60}$$

which reduces to

$$\tau(\Delta z) = \alpha_D \Delta z \tag{6.61}$$

if, as assumed above, α_D is constant over the length Δz. The medium is said to be optically thin over Δz if $\tau(\Delta z) \ll 1$, or, from equation (6.61), if $\Delta z \ll 1/\alpha_D$. This gives a practical means of determining each of the Δz_n since the absorption coefficient can be calculated at the start of each interval. The convergence of equation (6.59) is guaranteed for some finite N since the absorption coefficient attains a maximum value for zero laser intensity.

6.6. Single-Beam Experiments

6.6.1. Introduction

A simple absorption experiment was performed as a first test of the utility of the stabilised laser as a spectroscopic source. The experimental arrangement is shown in Figure 6.4. The collimated laser beam was first passed through a Glan-Taylor prism to ensure linear polarisation. Neutral density filters were next inserted to reduce the intensity to the desired level. The beam was then passed through the absorption cell, and the transmitted light was focussed with a 5-cm-focal-length lens onto a PIN photodiode (BPX 65).

The absorption cell used was a pyrex re-entrant cell 2.8 cm in length (constructed by Robin Gledhill, University of Otago, Dunedin), as illustrated in Figure 6.5. This was evacuated to a pressure of about 10^{-6} Torr and filled with a small amount of atomic ^{133}Cs. The windows of the cell are 15 mm in diameter and are misaligned by an angle of 1 degree so as to avoid multiple reflections inside the cell. The cell was placed inside an oven which was constructed from a pyrex cylinder enclosed in a coil of nichrome heating wire. This in turn was placed inside a wooden enclosure padded with an insulating cladding. By passing a current through the heating coil the temperature of the cell could be raised to greater than 100 °C. There was no means for actively stabilising the temperature; rather, the insulating cladding maintained adequate temperature stability while the heating current was switched off. The temperature of the

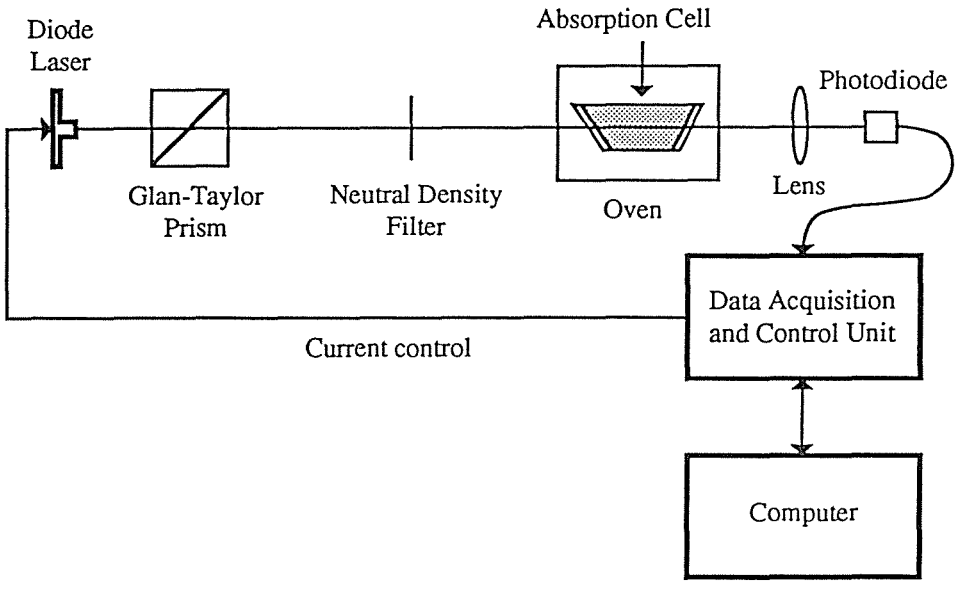

Figure 6.4. Experimental arrangement for obtaining single-beam absorption spectra.

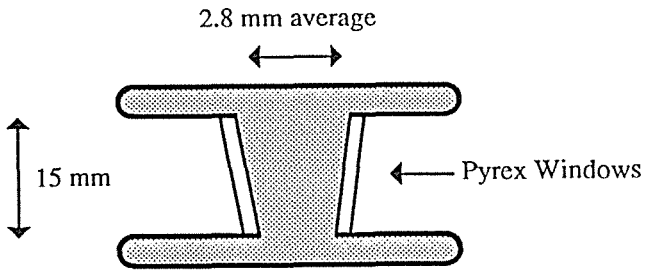

Figure 6.5. Schematic of re-entrant absorption cell containing caesium vapour.

cell was monitored with a Fluke 80TK thermocouple module. The thermocouple probe was placed inside the oven in contact with the outside of the cell.

To estimate the power inside the cell off-resonant light was passed through it, and the incident and transmitted powers, P_i and P_t respectively, were measured. Assuming that the loss coefficient, β, (reflection and absorption) at each window is the same, one has

$$P_t = (1-\beta)P_0 = (1-\beta)^2 P_i, \tag{6.62}$$

where P_0 is the power within the cell. Hence,

$$P_0 = \sqrt{P_i P_t}\,. \tag{6.63}$$

Measurements over a range of incident and transmitted powers gave a value of $\beta = 16.3 \pm 0.6$ %.

The spectra were obtained by directly recording the photodiode signal on computer via the data acquisition and control unit described in Chapter 3. This unit also controlled the laser frequency scan and monitored the temperature of the cell. The scan range was set to 20 GHz so as to be able to sweep through the 9.19-GHz hyperfine splitting of the caesium $6^2S_{1/2}$ ground state. Spectra were recorded for several different intensities over a range of temperatures from 30 °C to 100 °C. This was done by first manually adjusting the intensity with neutral density filters and measuring the beam power with a power meter. Next the cell was heated to above 100 °C, then the heating coil was switched off so that the spectra were recorded in the absence of any magnetic field produced by the coil, leaving only the earth's small field†. The cell then slowly cooled and spectra were automatically taken at 10-°C intervals under computer control.

† The Zeeman splittings are given by the Larmor precession frequency $\omega_L = g_J H/\hbar$[82c], where $g_{1/2} = 2$ and $g_{3/2} = 1.3$ are the Landé g-factors[75] in units of the Bohr magneton, $\mu_B = e\hbar/2mc$. The earth's field is 56 μT, leading to $\omega_L = 2.6 \times 10^4$ s^{-1} for the $6^2S_{1/2}$ state, which is much smaller than the expected ground state relaxation rate given by equation (6.48) (see also Section 6.6.3).

6.6.2. Experimental Results

Some typical spectra are shown in Figures 6.6 and 6.7, for the transitions with (*a*) $F = 4$ and (*b*) $F = 3$ in the ground state. Zero detuning is defined as the lowest-frequency resonance, that is the $F = 4$ to $F' = 3$ resonance. Table 6.3 shows the detunings for each transition. The spectra in Figure 6.6 correspond to low laser intensity (linear absorption régime) over a range of temperatures, while those in Figure 6.7 were taken at different intensities and a fixed temperature. The spectra are complicated slightly by the change in output power of the laser with the change in injection current required to sweep the frequency. The absorption coefficient for each resonance consists of the sum of three overlapping Voigt profiles resulting in the observed asymmetries. At sufficiently high temperature (dependent on beam intensity) there was 100% absorption. However, it was observed (*e.g.* Figure 6.6 at 100 °C) that under these conditions the photodiode signal was not reduced to zero, whereas physically blocking the beam did give a zero signal. This indicates the presence of other modes in the laser output spectrum. Fortunately, these modes are sufficiently spaced from the main lasing mode (~ 130 GHz) that they merely add a background to the detected signal. This background has been subtracted for the spectra in Figure 6.7.

These spectra show significant amounts of noise at resonance for increasing intensity. This corresponds to non-linearity of the laser scan as the frequency was swept through resonance. Optical feedback into the laser cavity of spontaneous emission photons is a possible cause of this, the effect being greater at higher intensities. Indeed, broad-band frequency noise was observed at resonance when analysing the transmitted signal with a rf spectrum analyser, whereas the signal was flat off-resonance. This is illustrated in Figure 6.8. The problem of optical feedback can be avoided to a large extent by using an optical isolator. However, no such device was available for the experiments presented here. Also apparent upon analysing a number of similar spectra is the

Transition	Detuning (GHz)
$F = 4$ to $F' = 3$	0.00
$F = 4$ to $F' = 4$	0.20
$F = 4$ to $F' = 5$	0.45
$F = 3$ to $F' = 2$	9.04
$F = 3$ to $F' = 3$	9.19
$F = 3$ to $F' = 4$	9.39

Table 6.3. Defined detunings for each transition of the caesium D_2 line.

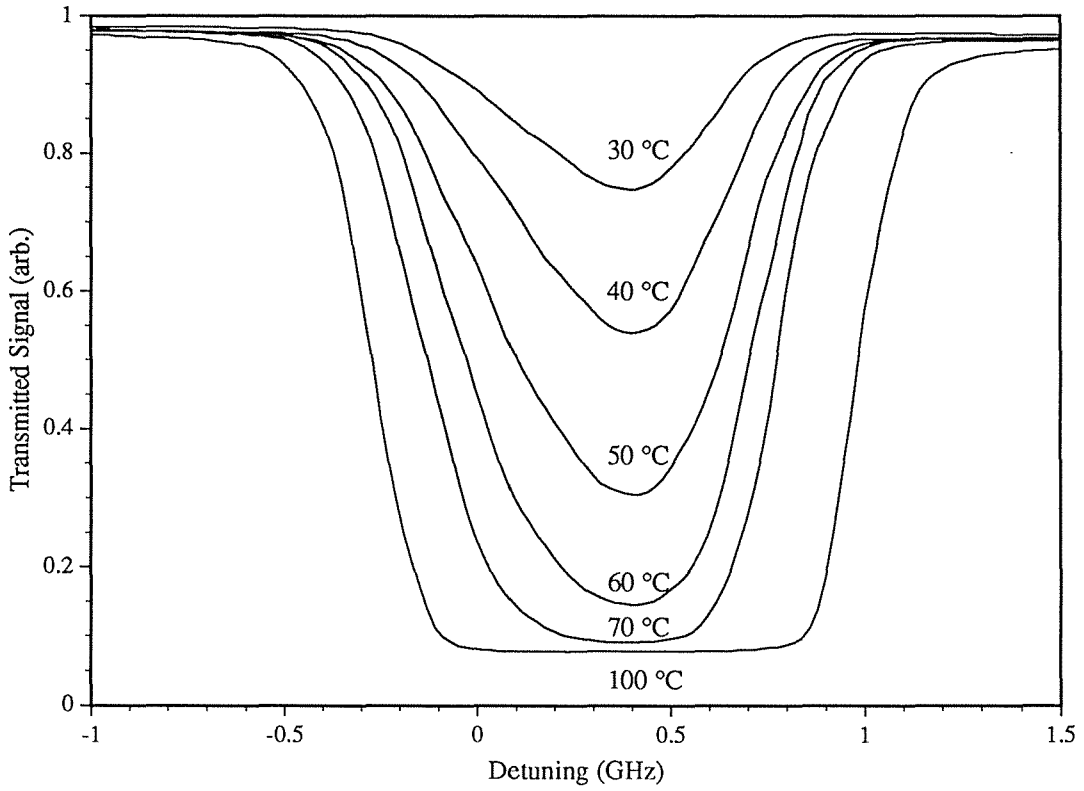

Figure 6.6(*a*). Experimental single-beam spectra with $F = 4$ in the ground state for $P = 0.0011$ mW over a range of cell temperatures. Each signal has been normalised to unity at a common arbitrary frequency.

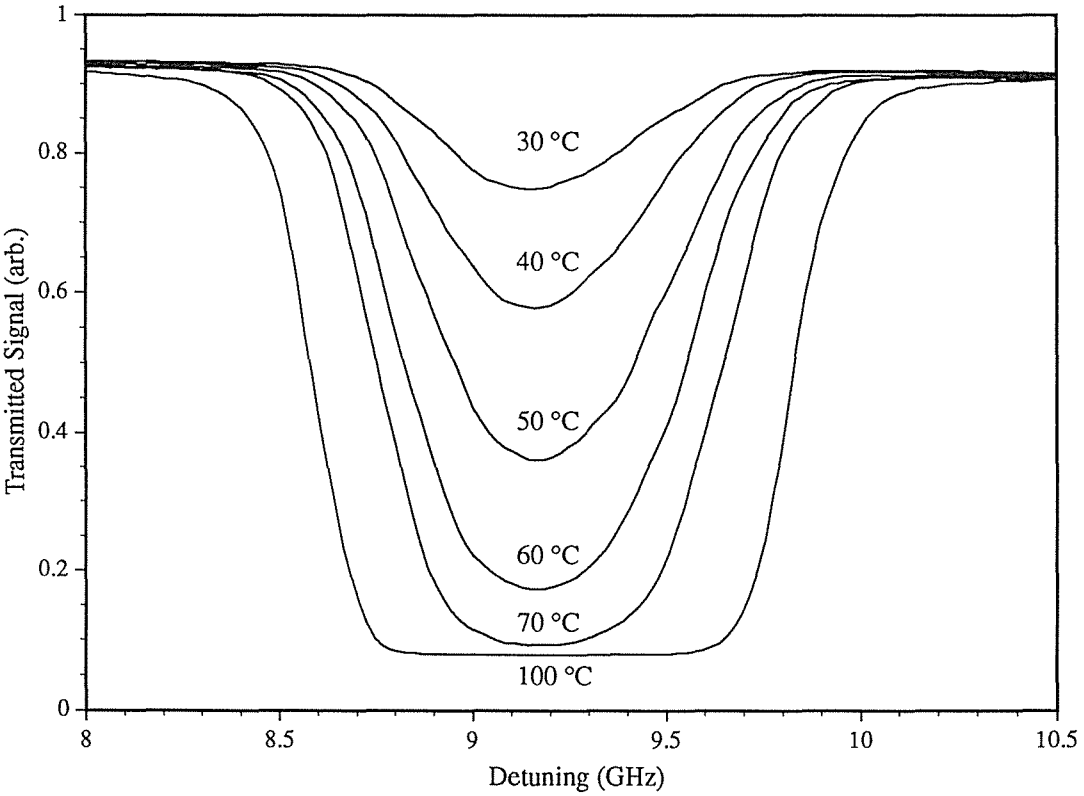

Figure 6.6(*b*). As for (*a*) but with $F = 3$ in the ground state.

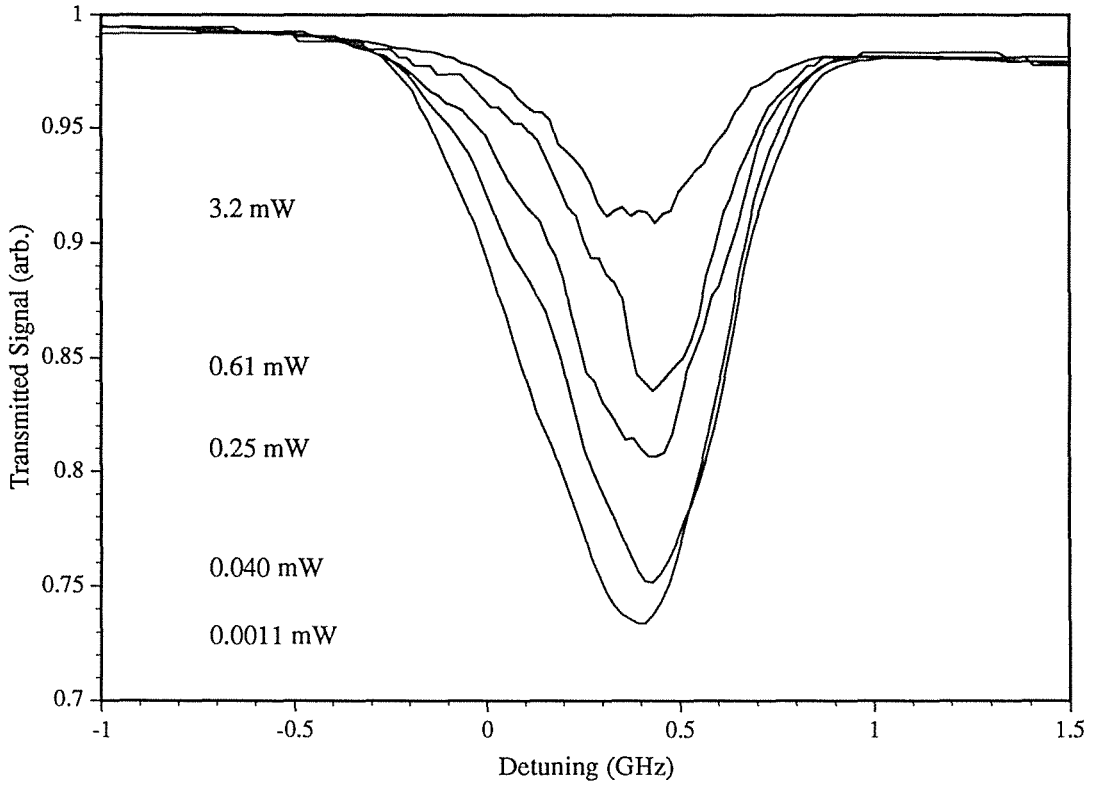

Figure 6.7(*a*). Experimental single-beam spectra with $F = 4$ in the ground state for $T = 30$ °C over a range of laser powers. Each signal has been normalised to unity at a common arbitrary frequency.

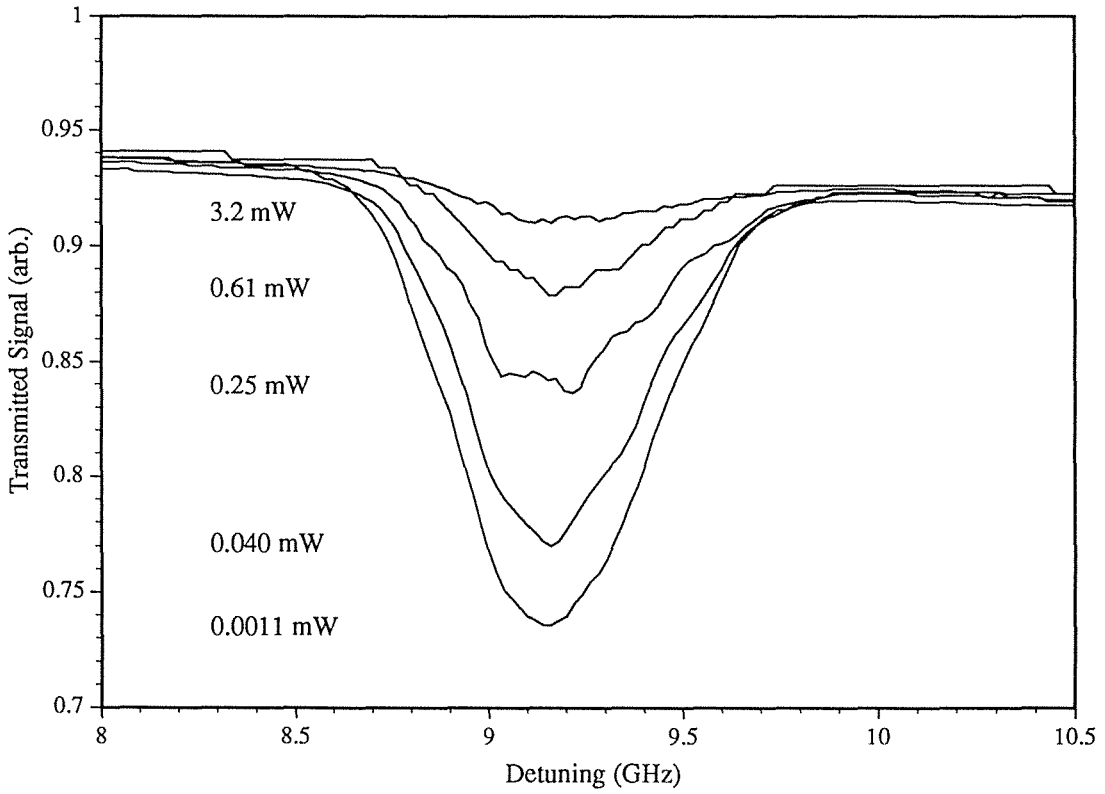

Figure 6.7(*b*). As for (*a*) but with $F = 3$ in the ground state.

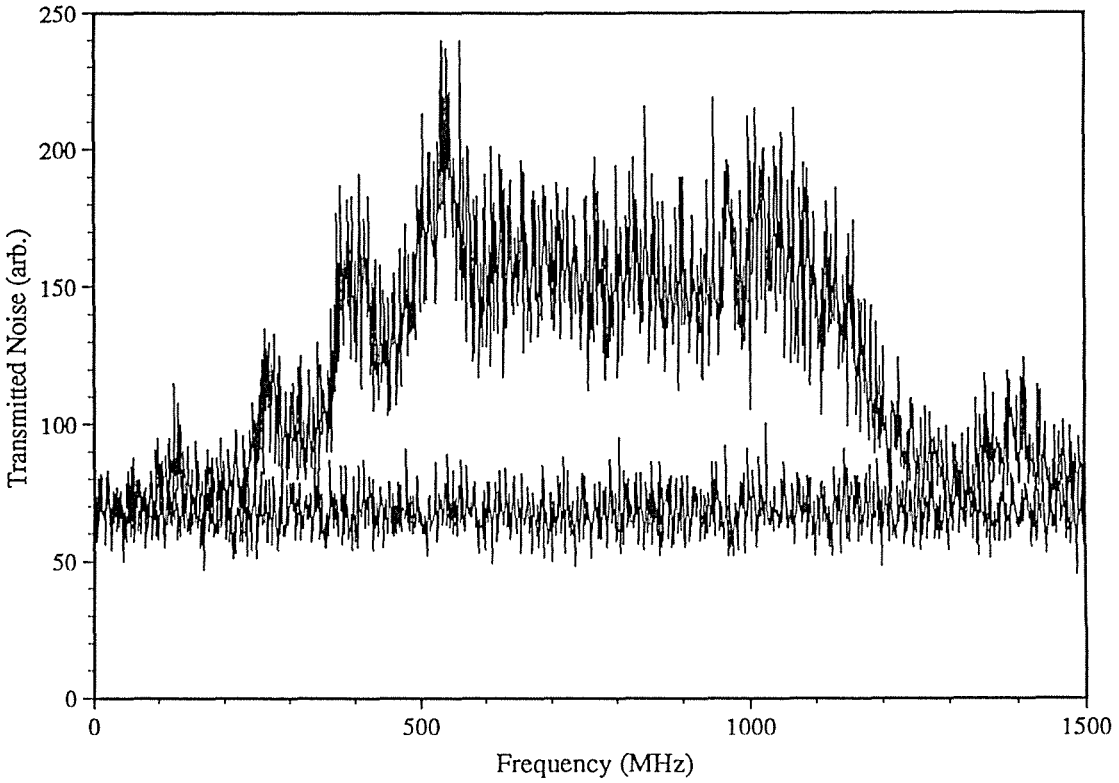

Figure 6.8. rf spectra of transmitted signal on-resonance (top trace) and off-resonance (bottom trace).

presence of weak "fringes" superimposed on some of the spectra, which are better resolved at higher powers. The spacing of these fringes is close to 190 MHz in all cases, corresponding to an extended cavity of length about 80 cm. The only components separated by this distance were the cell and the photodiode. A further feature of the fringes is that they appear in a very frequency-dependent manner, more clearly on the low frequency side of line centre for the lower frequency ($F = 4$) component and on the high frequency side for the higher frequency ($F = 3$) component. Such a frequency-dependent effect is hard to understand unless the fringes arise in some way from the (frequency-dependent) resonant interaction with the atomic system.

Saturation causes the absorption coefficient to decrease with increasing beam intensity. Optical pumping enhances the saturation effect by transferring atoms from the absorbing ground state hyperfine level to the non-absorbing level. These atoms are then slowly redistributed among the ground states through beam transit effects (ground state relaxation) until a steady-state is reached. For a ground state relaxation rate much smaller than the spontaneous emission rate, this process decreases the saturation intensity as compared to a system with no optical pumping. It has been shown by

	$F = 3$		$F = 4$	
T (°C)	α_0 (m^{-1})	P_1 (mW)	α_0 (m^{-1})	P_1 (mW)
30	86.2(8)	0.059(2)	105.8(7)	0.252(8)
40	192.0(8)	0.054(1)	234.3(7)	0.242(4)
50	404.9(8)	0.0538(5)	486.8(7)	0.209(2)
60	818.4(8)	0.0526(2)	943.4(7)	0.2163(8)
70	1580.6(8)	0.0612(1)	1757.4(7)	0.2065(5)

Table 6.4. Small-signal absorption coefficient and saturation power for the transitions with $F = 3$ and $F = 4$ in the ground state.

Pappas *et al.*[92] that for a three-level (Λ) system with optical pumping the on-resonance Doppler-broadened absorption coefficient is given by

$$\alpha_D = \frac{\alpha_0}{\sqrt{1 + I/I_1}}, \tag{6.64}$$

where α_0 is the small-signal absorption coefficient and I_1 is the optical pumping saturation intensity. Equation (6.64) holds extremely well when applied to the caesium D_2 transition. Table 6.4 shows values of α_0 and P_1 obtained from a fit of equation (6.64) to the experimental data for the transitions from the ground-state $F = 3$ and $F = 4$ levels for five different temperatures. Here P_1 is the saturation power equal to I_1 multiplied by the beam cross-section (beam radius 400 μm). The numbers in brackets indicate a 95% confidence interval for the fitted parameters. There appears to be no systematic variation of P_1 over the range of temperatures given in Table 6.4, thus averaging these values gives $P_1 = 0.056 \pm 0.003$ mW for the $F = 3$ transition and $P_1 = 0.22 \pm 0.02$ mW for the $F = 4$ transition. The saturation intensity for the $F = 4$ transition is larger than that for $F = 3$ due to the intense $F = 4$ to $F' = 5$ component of the former (see Figure 6.1). This is a cycling transition and hence is not affected by hyperfine pumping which, as mentioned above, decreases the saturation intensity. Conversely the $F = 3$ to $F' = 2$ cycling transition is weak and does not dominate the Doppler-broadened $F = 3$ transition. The degree of optical pumping that occurs on either transition is also influenced by ground state relaxation since a particular atom interacts with the beam for only a finite length of time. Thus, it would be expected that the Doppler-broadened absorption coefficient for the $F = 3$ transition be more sensitive to the magnitude of the ground state relaxation rate than the $F = 4$ transition.

6.6.3. Comparison with Theory

The theoretical calculations were performed on a Macintosh IIci computer. The rate equations for the zero-velocity group of atoms were solved repeatedly over the range of frequencies of the transitions to simulate the laser scan. The intensity was varied linearly through the simulated scan at a rate determined experimentally. This introduced some error when calculating the Doppler-broadened absorption coefficient since the non-zero-velocity atoms (corresponding to detuned solutions) "experienced" a different intensity. This procedure was used rather than treating each velocity class separately so that the calculations could be performed within a sensible time span. Nevertheless, the variation in intensity was less than 1% over each Doppler-broadened transition. This becomes important only at high intensities where some distortion to the shape of the absorption profile is introduced.

The measured power must be related to the field amplitude since it is this quantity which appears in the induced transfer rates. For a laser field with a Gaussian intensity distribution, the power and amplitude are related by

$$P = \pi a^2 c \varepsilon_0 E_m^2, \tag{6.65}$$

where a is the e^{-1} half-width of the amplitude distribution and E_m is the maximum amplitude of the profile. The computational disadvantage of using a Gaussian beam is that the rate equations must be solved repeatedly for different sections of the beam, greatly increasing the time of the calculation. A first approximation to a Gaussian profile is a rectangular box. However, to obtain the same power in the beam for a given radius the maximum intensity must be halved. It turns out that this is a good approximation at low powers since spectra calculated this way produced only minor differences to those using a Gaussian beam. In fact, better agreement with experiment was obtained using the rectangular approximation in calculations above 0.040 mW than was observed with a Gaussian beam.

The ground state relaxation rate, R, was treated as a parameter in the calculations. A first approximation to its magnitude is the inverse of the mean transit time, given by equation (6.48). However, it is difficult to define this since each atom moves with a different speed in a different direction with respect to the beam. In fact, most atoms traverse the beam away from its centre and thus experience a shorter transit time than an atom going through the centre. On the other hand, atoms with a component of velocity along the beam tend to spend a longer time under its influence. Because of this

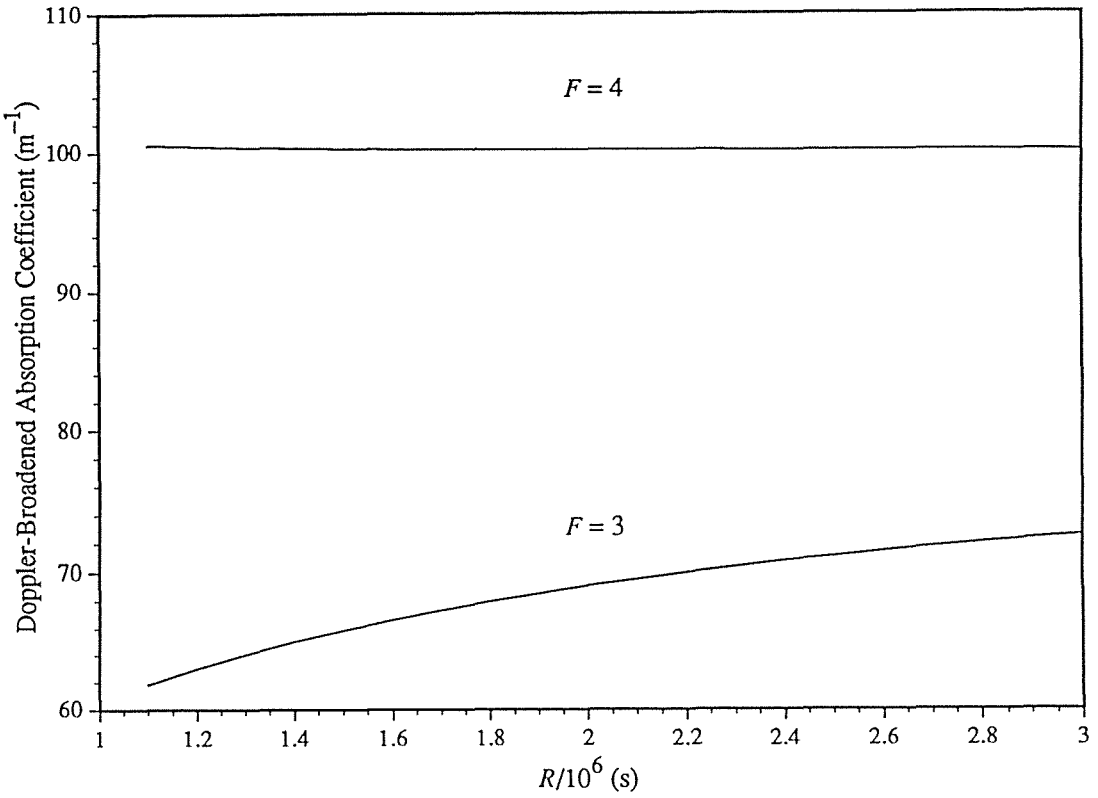

Figure 6.9. Variation of the Doppler-broadened absorption coefficient with the ground state relaxation rate for the transitions with $F = 3$ and $F = 4$ in the ground state. The laser power was 0.040 mW and the cell temperature 30 °C.

difficulty in defining the value of R, it was selected by comparing the ratios of the experimental absorption peaks from the $F = 3$ and $F = 4$ levels at low intensity with those obtained theoretically by varying R. It should be noted that the calculations indicate that the $F = 3$ absorption is far more sensitive to the value of R than that for $F = 4$ (see Figure 6.9). This was expected from the discussion at the end of the previous sub-section. The best-fit value of R was 2×10^6 s^{-1}, a factor of ten higher than that calculated from equation (6.48). The ground state relaxation rate is examined further in Section 6.9.

Finally, the number density was adjusted from that calculated from equation (6.46) using the measured cell temperature, again by comparison with experimental spectra at low intensity. The maximum adjustment necessary was about 25%, which translates to a 1% change in the absolute temperature of the cell. In all cases the corrected temperature was greater than the measured temperature, consistent with the fact that during cooling the interior of the cell would be at a higher temperature than outside.

Some theoretical spectra, overlaid on their experimental counterparts, are shown in Figures 6.10 and 6.11 for different temperatures and intensities. The rectangular approximation was used in the calculations. The experimental spectra were scaled to the measured power at one off-resonance point after the background correction due to other "non-lasing" longitudinal modes was made. The frequency axis was also scaled so that the two absorption peaks coincided with the theoretical peaks. On average, the frequency change per increment on the scan counter was -20.2 ± 0.1 MHz. This corresponds to $\Delta\nu/\Delta I = -3.99 \pm 0.02$ GHz mA^{-1}, in agreement with the result found in Section 4.6.

The theoretical spectra show good agreement with experiment for low power over all temperatures (Figure 6.10). In this case the laser power satisfies the condition given in Section 6.5.1 for the rate equation approximation to be valid for all transitions ($P \ll 1.5$ mW for the weakest transition and $P \ll 0.08$ mW for the strongest). For $P = 0.040$ mW (Figure 6.11) the agreement is still fairly good since the rate equation approximation is satisfied for most of the resonances, and even the 0.25-mW solution shows reasonable agreement. However, at powers higher than 0.25 mW coherence effects become important and the rate equation approach breaks down as anticipated in Section 6.5.1. This is more evident for the $F = 4$ transition because of its larger line strength.

A comparison between spectra calculated using the rectangular approximation and a Gaussian beam profile is shown in Figure 6.12. The solution varied by less than 2% on resonance for powers less than or equal to 0.040 mW, and less than 10% above this. It should be noted that it is not necessary to employ the cell integration technique described in Section 6.5.5 to model the propagation of the beam through the cell because the vapour is optically thin at high intensities so only one iteration is required, while at low intensities the absorption is linear and thus not dependent on intensity.

For these medium-resolution experiments the frequency stability of the diode laser is sufficiently good, and the laser linewidth adequately narrow, to completely resolve the Doppler-broadened transitions from the two ground state hyperfine components of the caesium D_2 line. The rate equation model predicts that the ratio of the Doppler-broadened absorption coefficients for the two transitions varies with the ground state relaxation rate (see Figure 6.9). By varying the beam diameter, thus changing the ground state relaxation rate, one could use the laser to experimentally examine the

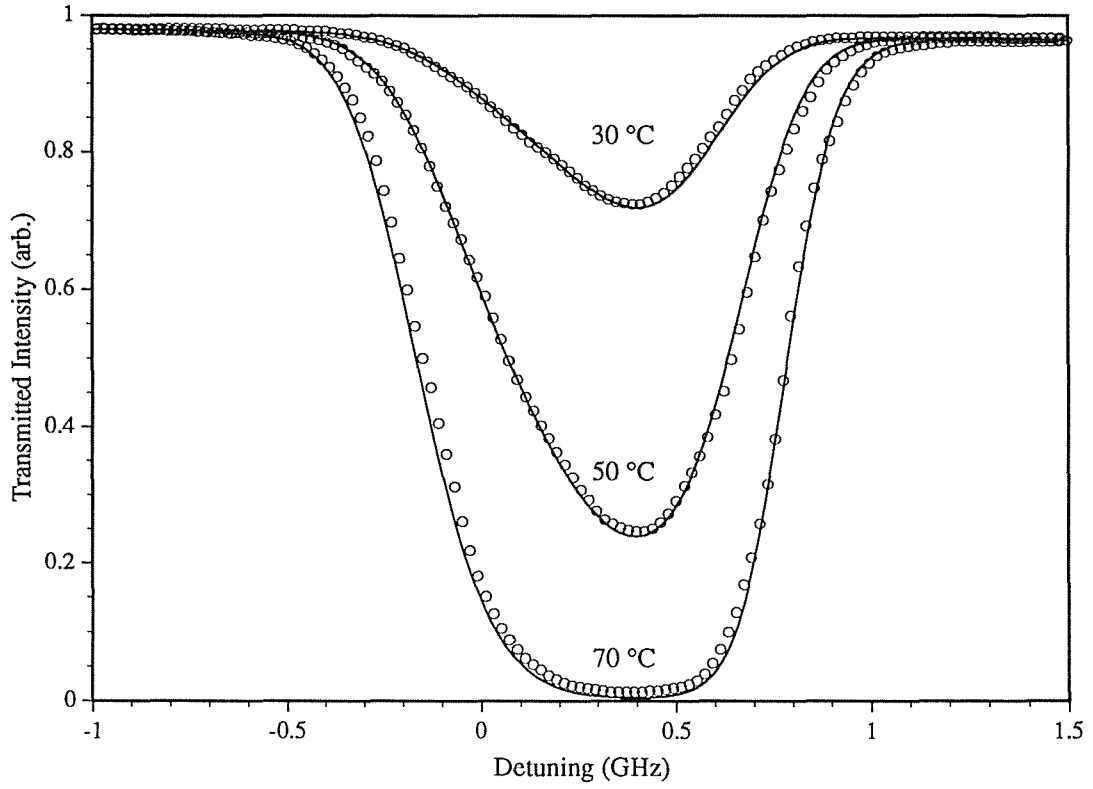

Figure 6.10(*a*). Calculated single-beam spectra (solid lines) overlaid on experimental spectra (open circles) with $F = 4$ in the ground state for $P = 0.0011$ mW over a range of cell temperatures. Each signal has been normalised to unity at a common arbitrary frequency.

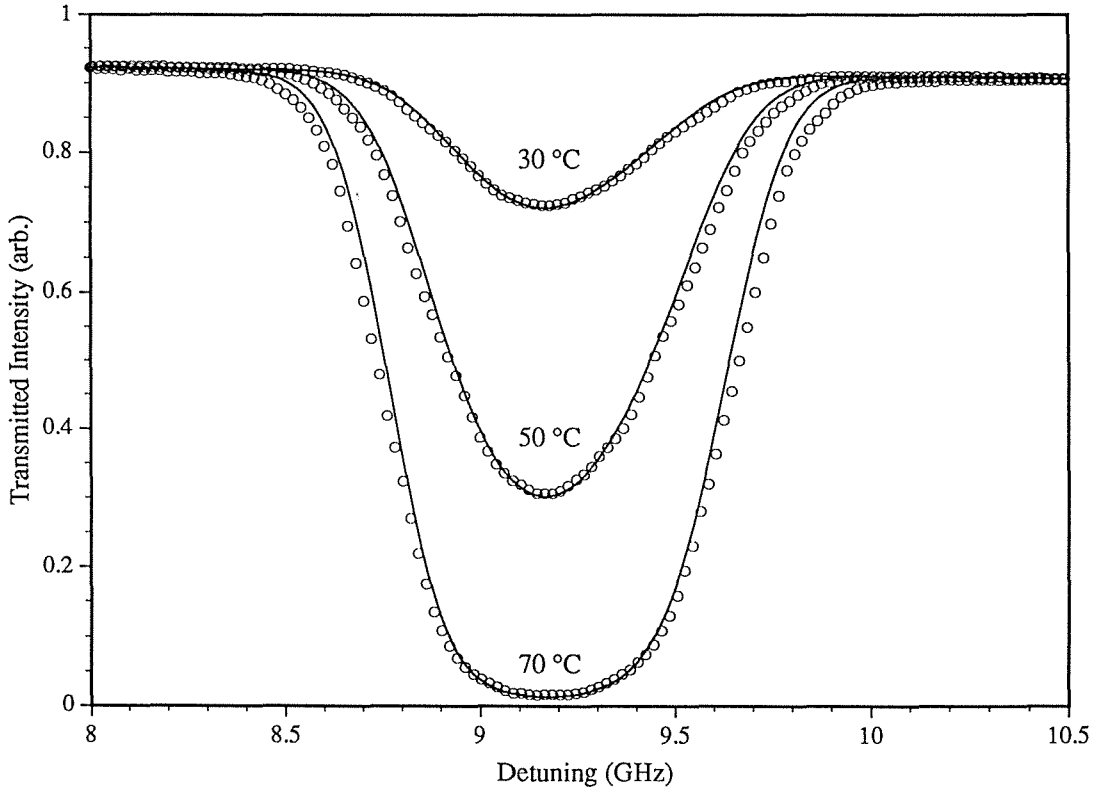

Figure 6.10(*b*). As for (*a*) but with $F = 3$ in the ground state.

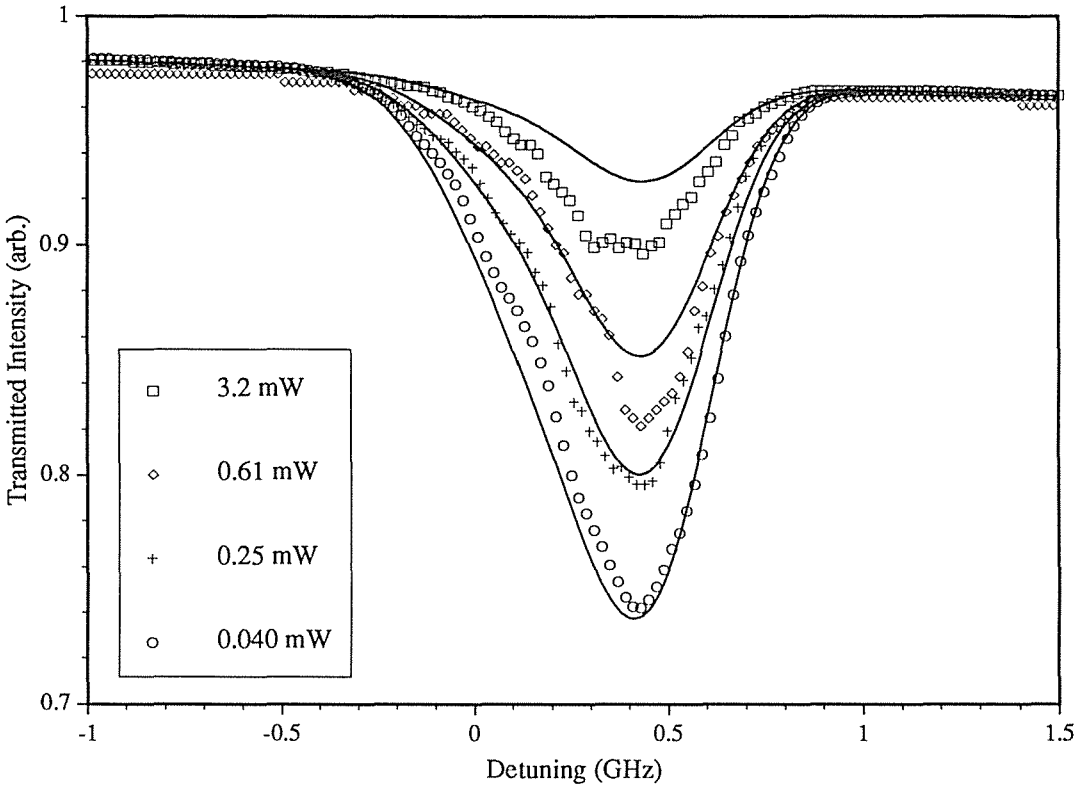

Figure 6.11(*a*). Calculated single-beam spectra (solid lines) overlaid on experimental spectra (symbols) with $F = 4$ in the ground state for $T = 30$ °C over a range of laser powers. Each signal has been normalised to unity at a common arbitrary frequency.

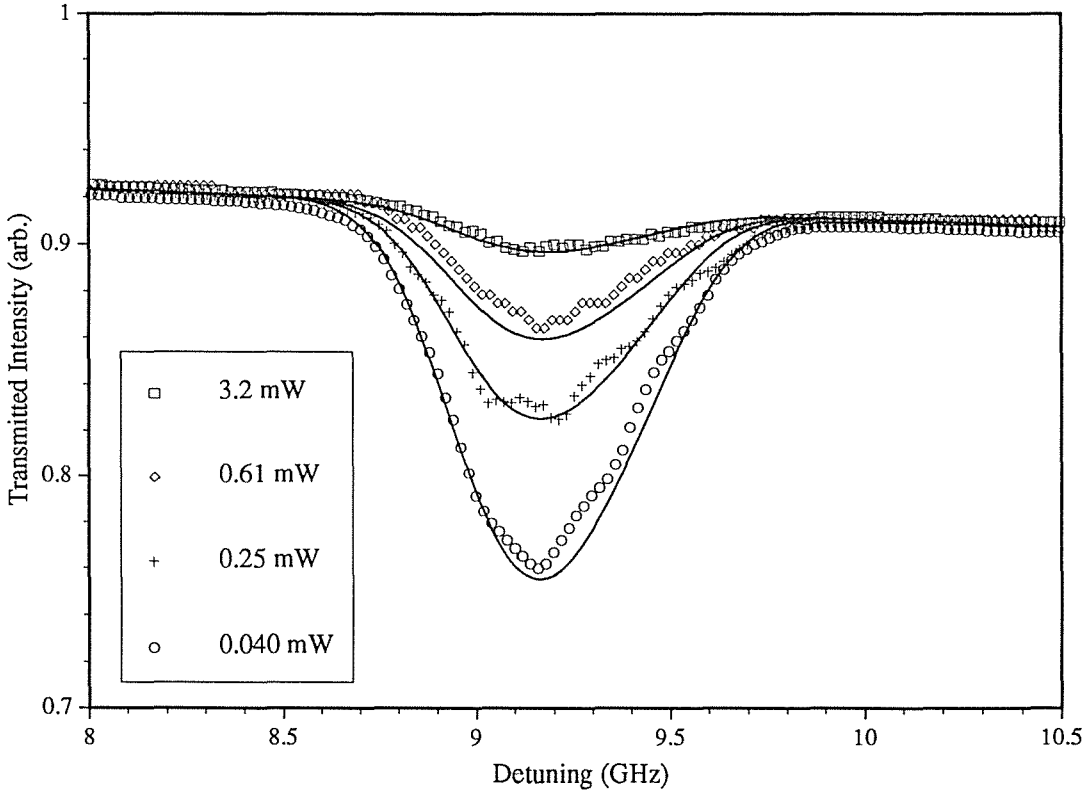

Figure 6.11(*b*). As for (*a*) but with $F = 3$ in the ground state.

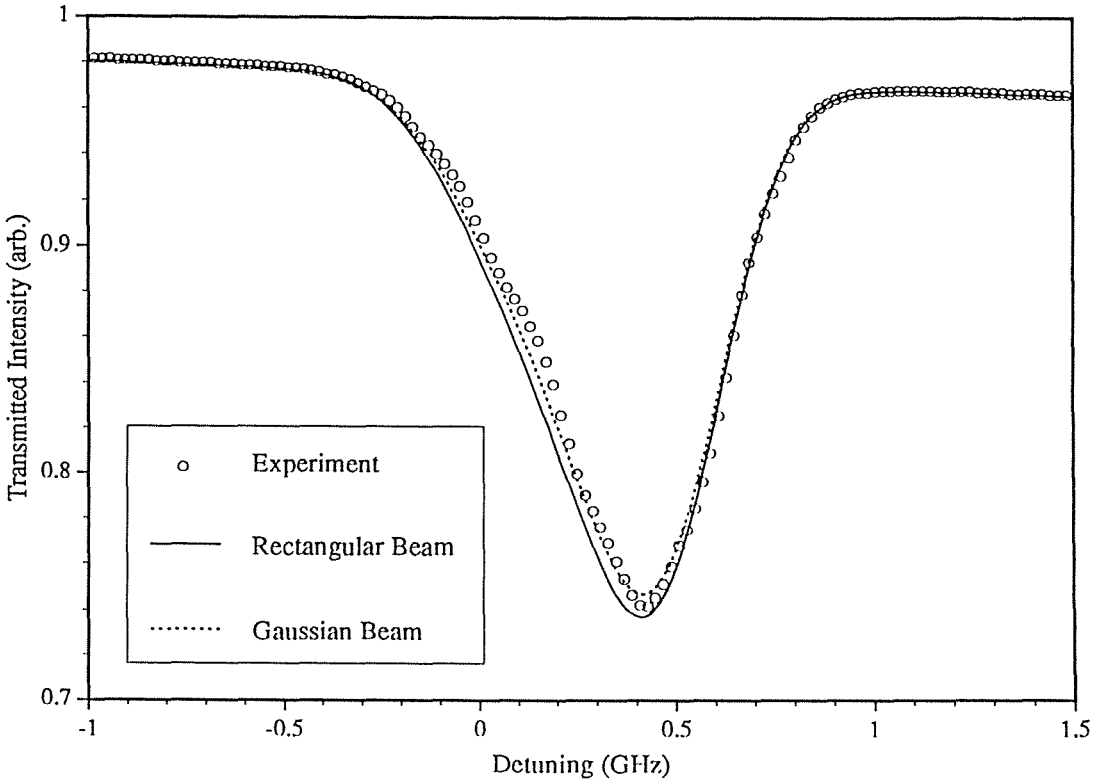

Figure 6.12. Comparison between spectra calculated using a Gaussian beam (dotted line) and a rectangular approximation to a Gaussian beam (solid line) for P = 0.040 mW and T = 30 °C. Each spectrum has been normalised to unity at a common arbitrary frequency.

relationship between the beam transit time and the average thermal speed. As mentioned previously, this relationship does not seem to conform well to the much-accepted equation (6.48).

6.7. Two-Beam Experiments

6.7.1. Introduction

The single-beam experiments described in the previous section are to a large extent insensitive to instabilities in the absolute frequency or linewidth of the laser. This is, of course, due to the fact that Doppler broadening of the absorption signal masks most of the detail of the interaction between the caesium atoms and the laser field. In order to recover more of this detail a sub-Doppler spectroscopic technique is required. The well-known method of saturated absorption spectroscopy using two counter-propagating beams from the same laser[93] was chosen because of its simple arrangement and because only one of the four lasers was capable of output at the caesium D_2 wavelength.

The experimental arrangement is depicted in Figure 6.13. The laser beam was split into a strong pump and a weak probe which overlapped at a small angle inside the absorption cell. To increase the signal-to-noise ratio and to suppress the Doppler background the pump beam was chopped using an acousto-optic modulator and the probe was detected at the chopping frequency.

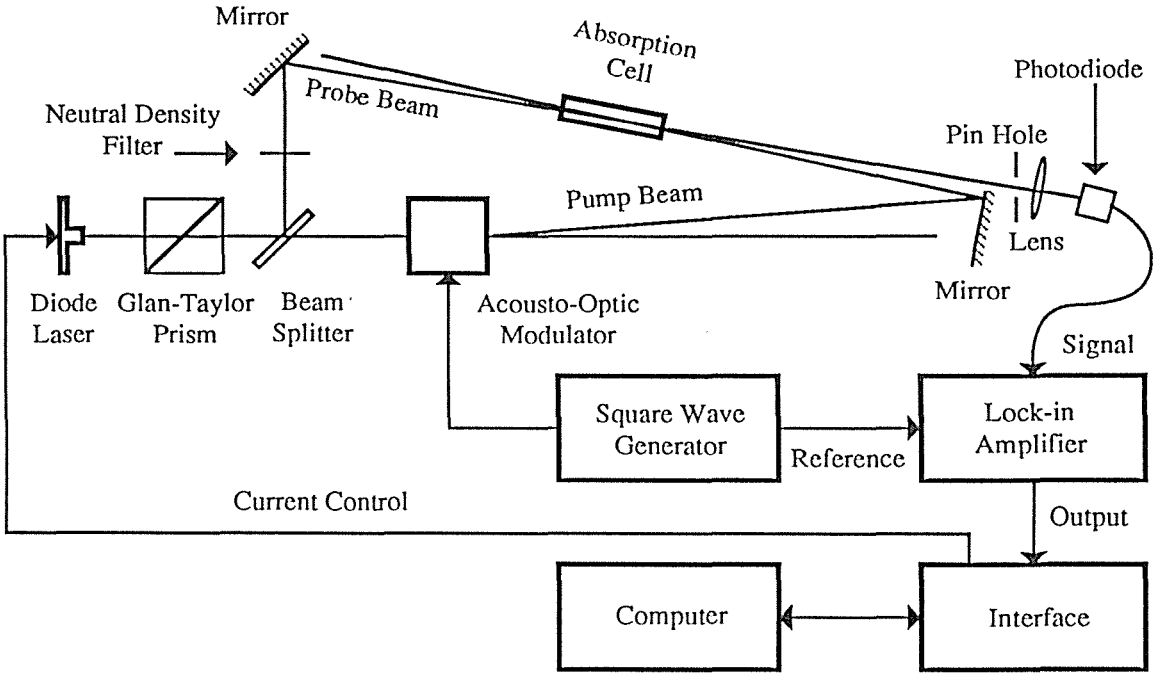

Figure 6.13. Experimental arrangement for two-beam experiments.

6.7.2. Theoretical Treatment

The probe beam is assumed to be a truly classical probe. That is, its intensity is so low that it doesn't significantly alter any of the atomic populations but merely samples the population imbalance created by the pump. The rate equations can be solved then in exactly the same manner as for the single-beam case. Again only the zero-velocity class of atoms is solved, with solutions for the non-zero classes corresponding to appropriately detuned and weighted zero-class solutions. However, since the probe interacts with the velocity class with opposite sign to that with which the pump interacts, the absorption coefficient takes on a different form:

$$\alpha(\Delta_L, T) = \frac{\pi^{3/2} c^2}{v_p \omega^3} \int \sum_{i,k} A_{ik} \left[N_i(\Delta^+) - N_k(\Delta^+) \right] g(\Delta^- - \Delta_{ik}) \times \exp\left\{ -\left[\frac{c(\Delta_L - \Delta^-)}{v_p \omega} \right]^2 \right\} d\Delta^-. \tag{6.66}$$

The detunings appearing in equation (6.66) are defined as follows:

$\Delta_L = \omega_L - \omega_0$ (Laboratory frame laser detuning from lowest-frequency resonance in the atomic rest frame, *i.e.* $F = 4$ to $F' = 3$.)

$\Delta^+ = \Delta_L + kv$ (Rest frame detuning of the pump beam as seen by an atom in velocity class v.)

$\Delta^- = \Delta_L - kv$ (Rest frame detuning of the probe beam as seen by an atom in velocity class v.)

$\Delta_{ik} = \omega_{ik} - \omega_0$ (Rest frame detuning of the $|k\rangle$ to $|i\rangle$ resonance from the lowest-frequency resonance.)

$N_i(\Delta^+)$ represents the population density of state $|i\rangle$ at the pump detuning.

For unequal pump and probe detunings (*i.e.* non-zero-velocity classes) equation (6.66) represents a Doppler-broadened profile, as for the single-beam case, since the probe interacts only with atoms which have not been pumped. When $\Delta^+ = \Delta^-$, corresponding to the zero-velocity class, the absorption coefficient differs from the single-beam case because now the probe examines the population imbalance created by the pump. These atoms produce the familiar Lamb-dip† resonances on the Doppler-broadened profile.

† The term "Lamb-dip" refers, strictly speaking, to the dip in gain which occurs on resonance with the zero-velocity-class atoms in an active medium. However, it will be used throughout this thesis for convenience to refer to the related phenomenon of *passive-cavity* resonances for zero-velocity-class atoms.

Additionally, crossover resonances occur when the laser frequency is exactly midway between two Lamb-dip resonances which share a common level. In this case the velocity class of atoms in resonance with the pump on one transition is probed on the other transition. In terms of the detunings defined above, the crossover resonances occur when

$$\Delta_L = \frac{\Delta_{ik} + \Delta_{ij}}{2} . \tag{6.67}$$

Since $\Delta_L - \Delta^- = (\Delta_{ik} - \Delta_{ij})/2$ the spacing of the k and j levels must be within the Doppler width so that the exponential factor in equation (6.66) does not become vanishingly small. Thus, for the caesium D_2 transition crossover resonances can occur only between levels coupled to the same *lower* level. The probe examines the change in lower level population produced by the pump since the upper levels on the probe transition are undisturbed.

The transmitted probe intensity is calculated as in Section 6.5.5. This Doppler-broadened profile is integrated over the laser spectral lineshape. This was not necessary for the single-beam calculations because the laser profile could be treated as a delta function in comparison with the spectral features of interest. Finally, the Doppler background is subtracted, leaving only the Lamb-dip and crossover resonances, so that a comparison can be made between the theoretical calculations and the experimental spectra.

6.7.3. Experimental Parameters

The two-beam experiments were performed with the cell at room temperature (about 20 °C). The crossing angle between the pump and probe beams (of the same diameter) was measured to be 6 mrad, giving a residual Doppler width of 2 MHz at 20 °C. The probe power was adjusted, using the neutral density filter in Figure 6.13, to a sufficiently low level that the absorption of the probe was in the linear régime as determined from the single-beam results. The probe power could not be set arbitrarily low because of the reduction of the signal-to-noise ratio. The power in the pump beam was adjusted using the analogue input to the acousto-optic modulator. This input controls the amount of power diffracted into the first order beam (see Appendix *G* for a description of the acousto-optic modulator driver). The pump beam was chopped at a frequency of 100 kHz and the probe was detected at this frequency using a lock-in amplifier. It was found that at chopping frequencies below 100 kHz the Doppler

pedestal produced by atoms undergoing velocity-changing collisions[94] during the integration time of the lock-in amplifier could not be removed. The 380-Ω ramp resistor on the current source was selected to give a frequency scan of about 1 GHz, sufficient to scan through either of the group of transitions originating from the $F = 3$ or $F = 4$ ground state levels.

6.7.4. Comparison Between Experiment and Theory

As for the single-beam experiments, the frequency axis for the two-beam experimental spectra needed to be scaled so that a comparison could be made with the theoretical results. Because of the higher resolution of the two-beam experiments, the scaling is more critical in this case. Scaling was performed for each interval between adjacent resonances based on their known positions. This has revealed some inadequacies in the frequency stability of the diode laser for such high-resolution studies. Examination of 30 different spectra for the transitions with $F = 4$ in the ground state gave an average scan rate of 1.05 ± 0.03 MHz/count. However, individual rates ranged from 0.92 to 1.24 MHz/count. This relatively large range is due to the slow (> 1 s) fluctuations in laser temperature, and is consistent with the residuals shown in the linearity plot of Figure 4.10. During a scan the temperature change can cause an additional frequency change either in the same sense as the injection-current-induced scan or opposing it. Thus, the experimental spectra can appear either spread out or bunched up. In addition, the direction of the temperature drift can change during a scan causing, for example, one part of the spectrum to appear spread out and another to be bunched. Not only does this effect shift the positions of the resonances, but it can also broaden or narrow the spectral features. This problem of non-linearity in the frequency scan could be overcome with the use of a fibre-optic Fabry-Perot reference cavity, since this would provide arbitrarily small FSR allowing accurate computer linearisation.

The peak heights of the experimental spectra were scaled to those resulting from the calculations by matching either the $F = 4$ to $F' = 5$ or the $F = 3$ to $F' = 4$ resonances. Thus, the relative heights of the peaks could be compared. The absolute heights of the experimental peaks were not known because of the integration and amplification performed by the lock-in amplifier.

Figures 6.14(*a*) to 6.14(*d*) show comparisons between the scaled experimental spectra and the results of the theoretical calculations for the transitions originating from the

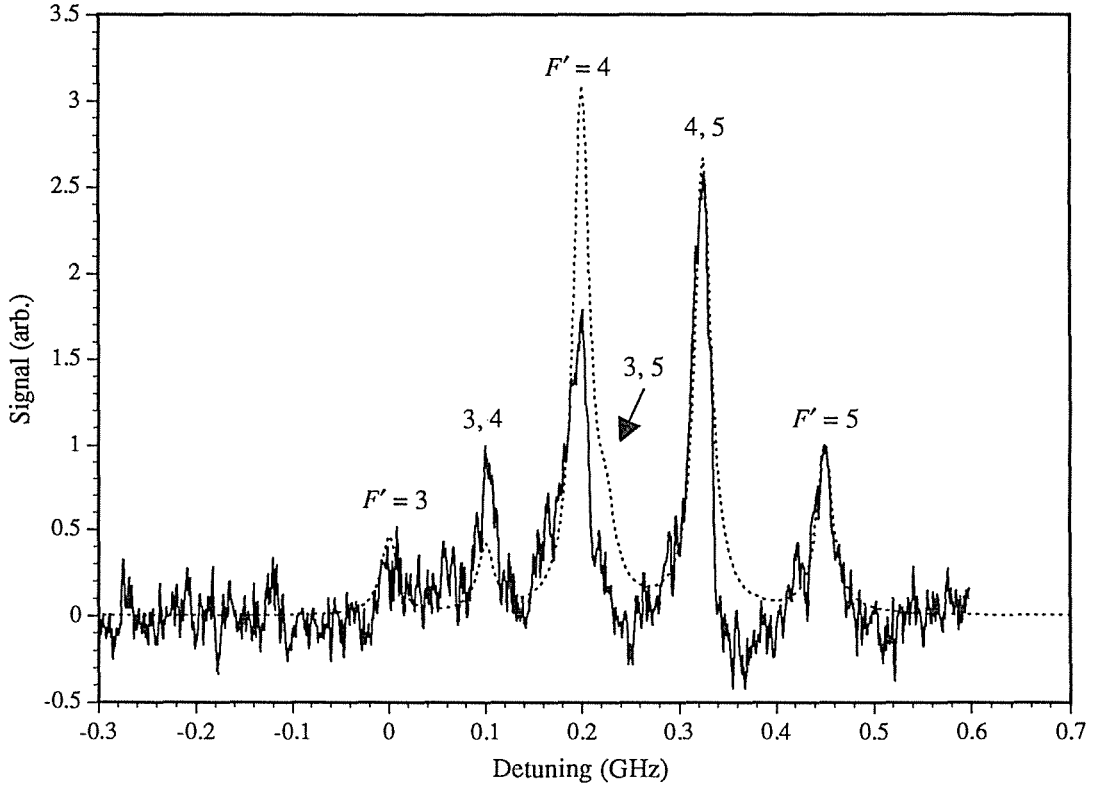

Figure 6.14(*a*). Saturated absorption spectrum (solid line) of the transitions with $F = 4$ in the ground state for a pump power of 0.014 mW and cell temperature of 20 °C. The dotted line is the calculated spectrum. The resonances labelled by an F' number are Lamb-dips while those labelled with two numbers are the corresponding crossover resonances. The vertical axes have been scaled so that the $F' = 5$ resonances match.

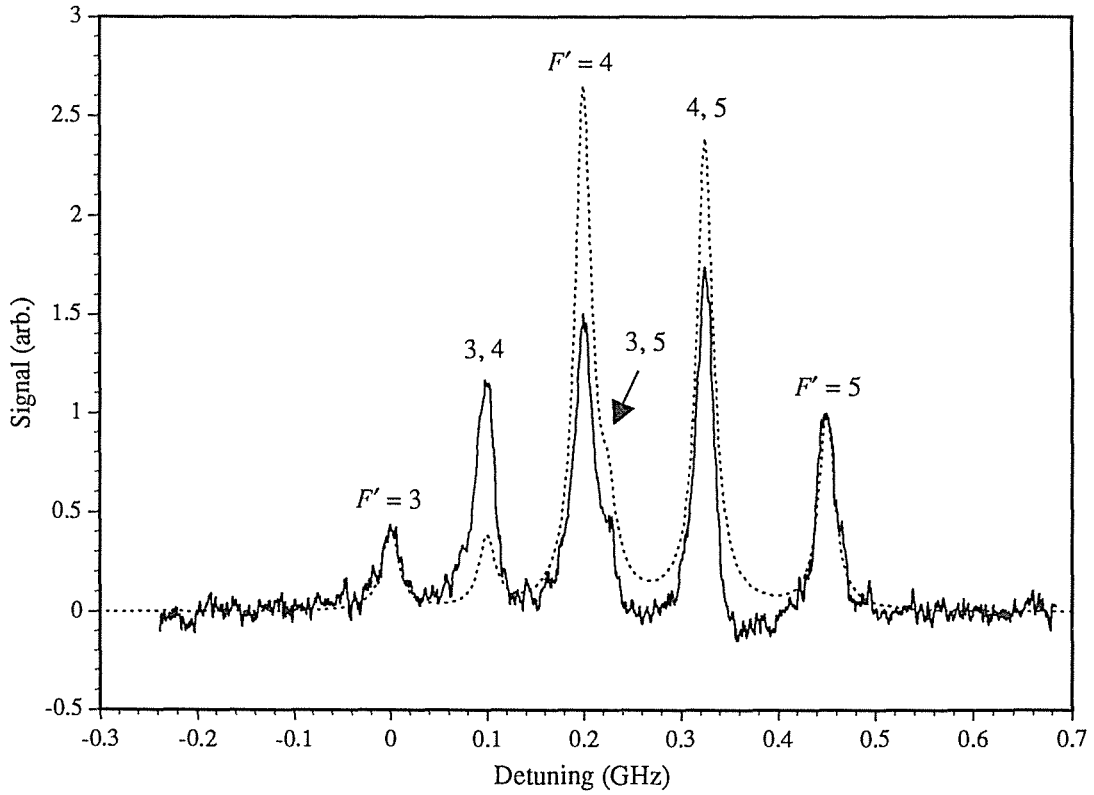

Figure 6.14(*b*). As for (*a*) but with pump power of 0.035 mW.

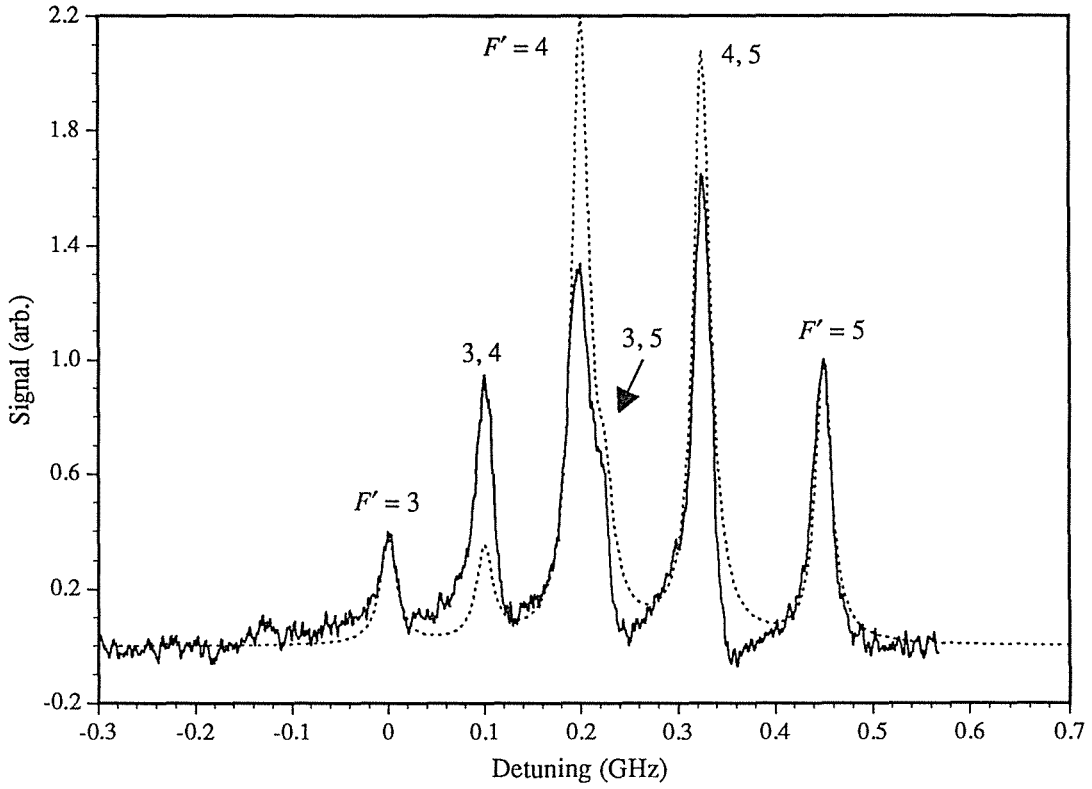

Figure 6.14(*c*). As for (*a*) but with pump power of 0.069 mW.

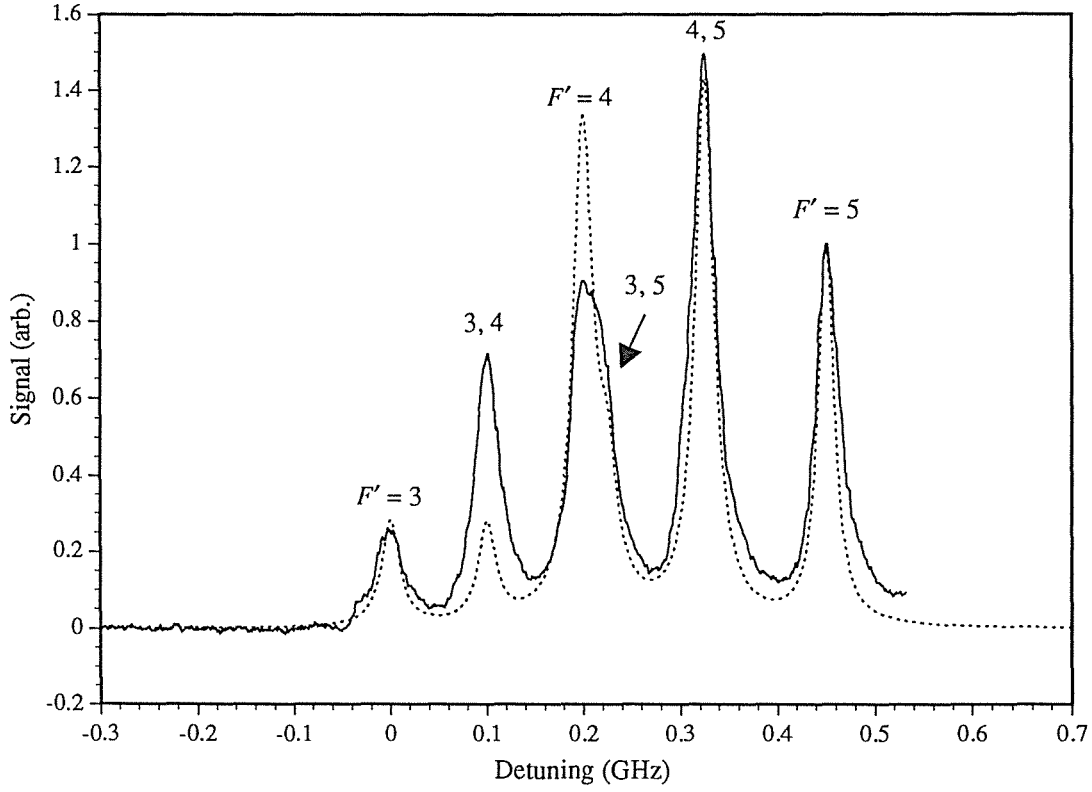

Figure 6.14(*d*). As for (*a*) but with pump power of 0.25 mW.

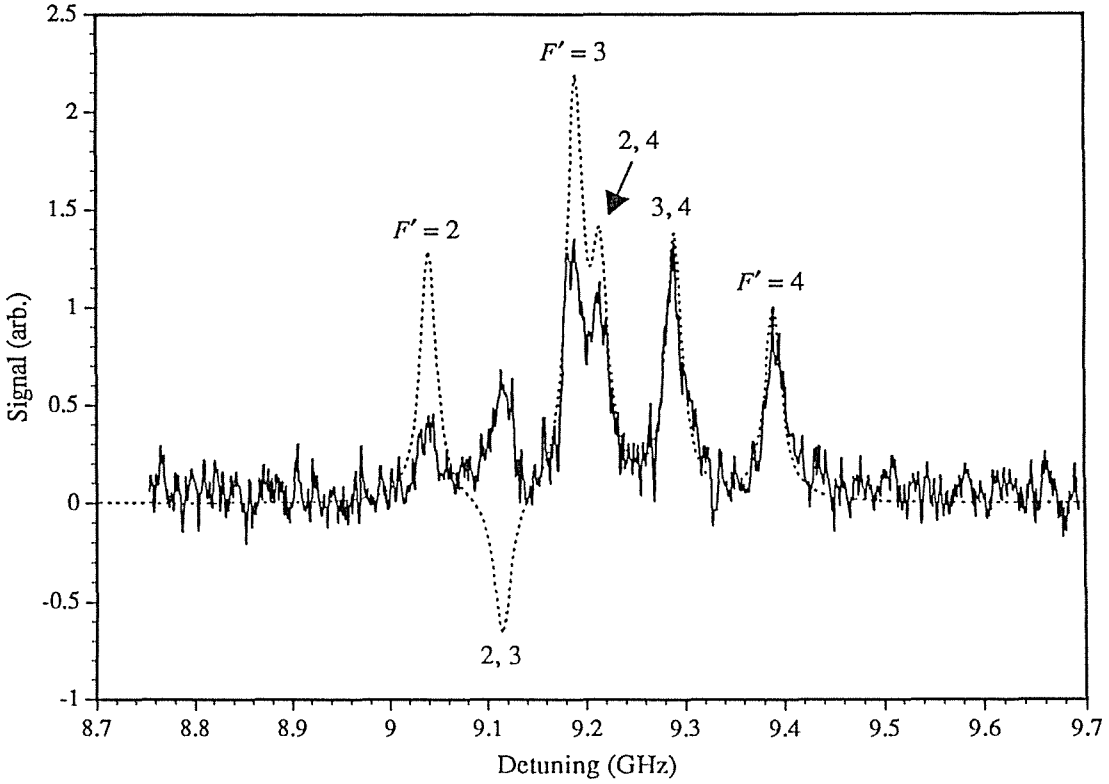

Figure 6.14(*e*). As for (*a*) but with $F = 3$ in the ground state and pump power of 0.0085 mW. The experimental and theoretical spectra have been matched at the $F' = 4$ resonance.

$F = 4$ hyperfine component of the ground state for several values of pump power. Figure 6.14(*e*) shows a comparison for the $F = 3$ transitions for a low pump power. The ground state relaxation rate was taken to be $R = 2 \times 10^6$ s^{-1}. The spectral widths of the resonances agree quite well. In all cases these are to a great extent limited by the laser linewidth (about 10 MHz), although at the higher powers there is evidence of power broadening. There is large discrepancy between the heights of the experimental and theoretical spectra. However, there does appear to be reasonable agreement between the relative heights of the $F = 4$ to $F' = 3$ and $F = 4$ to $F' = 5$ Lamb-dips, and also the $F = 3$ to $F' = 4$ Lamb-dip and the $F = 3$ to $F' = 3$, 4 crossover resonance. These discrepancies are addressed in Section 6.8. A further inconsistency is apparent in Figure 6.14(*e*) where the theory predicts a negative crossover resonance which is not seen experimentally. This is examined in the following sub-section.

6.7.5. Theoretical Effect of Ground State Relaxation Rate

It is interesting to look at the theoretically predicted spectra as a function of the ground state relaxation rate, R. These spectra are shown in Figure 6.15 for several values of R. The signal increases with decreasing R for all resonances except the $F = 4$ to $F' = 5$ Lamb-dip and the crossover resonance between the $F = 3$ to $F' = 2$ and $F = 3$ to $F' = 3$ transitions. This is due to the fact that for smaller R there is more net optical pumping of atoms into the non-resonant ground state hyperfine component. The normalised steady-state populations for the $F = 4$ to $F' = 3$ transition, for example, are shown in Table 6.5. As R increases atoms are returned more quickly to the resonant level resulting in a greater absorption of the probe beam. Noting that for a larger signal there is less absorption of the probe, it can be seen that a larger value of R leads to a smaller signal.

$F = 4$ to $F' = 3$, $R = 0.2 \times 10^6$ s^{-1}

5	0.0000	0.0000	0.0000	0.0000	0.0000	0.0000	0.0000	0.0000	0.0000	0.0000	0.0000
4		0.0000	0.0000	0.0000	0.0000	0.0000	0.0000	0.0000	0.0000	0.0000	
3			0.0003	0.0003	0.0004	0.0004	0.0004	0.0003	0.0003		
2				0.0000	0.0000	0.0000	0.0000	0.0000			
4		0.0700	0.0293	0.0209	0.0179	0.0171	0.0179	0.0209	0.0293	0.0700	
3			0.0967	0.1007	0.1030	0.1037	0.1030	0.1007	0.0967		
	−5	−4	−3	−2	−1	0	1	2	3	4	5

$F = 4$ to $F' = 3$, $R = 3.2 \times 10^6$ s^{-1}

5	0.0000	0.0000	0.0000	0.0000	0.0000	0.0000	0.0000	0.0000	0.0000	0.0000	0.0000
4		0.0000	0.0000	0.0000	0.0000	0.0000	0.0000	0.0000	0.0000	0.0000	
3			0.0005	0.0008	0.0010	0.0010	0.0010	0.0008	0.0005		
2				0.0000	0.0000	0.0000	0.0000	0.0000			
4		0.0634	0.0585	0.0555	0.0539	0.0534	0.0539	0.0555	0.0585	0.0634	
3			0.0667	0.0683	0.0693	0.0696	0.0693	0.0683	0.0667		
	−5	−4	−3	−2	−1	0	1	2	3	4	5

Table 6.5. On-resonance normalised steady-state populations (rounded to four decimal places) for the $F = 4$ to $F' = 3$ transition for two values of the ground state relaxation rate and a pump power of 0.069 mW. Note that the equilibrium values for the ground state are 0.0625 and those for the excited state are zero. The layout is the same as that depicted in Table 6.2.

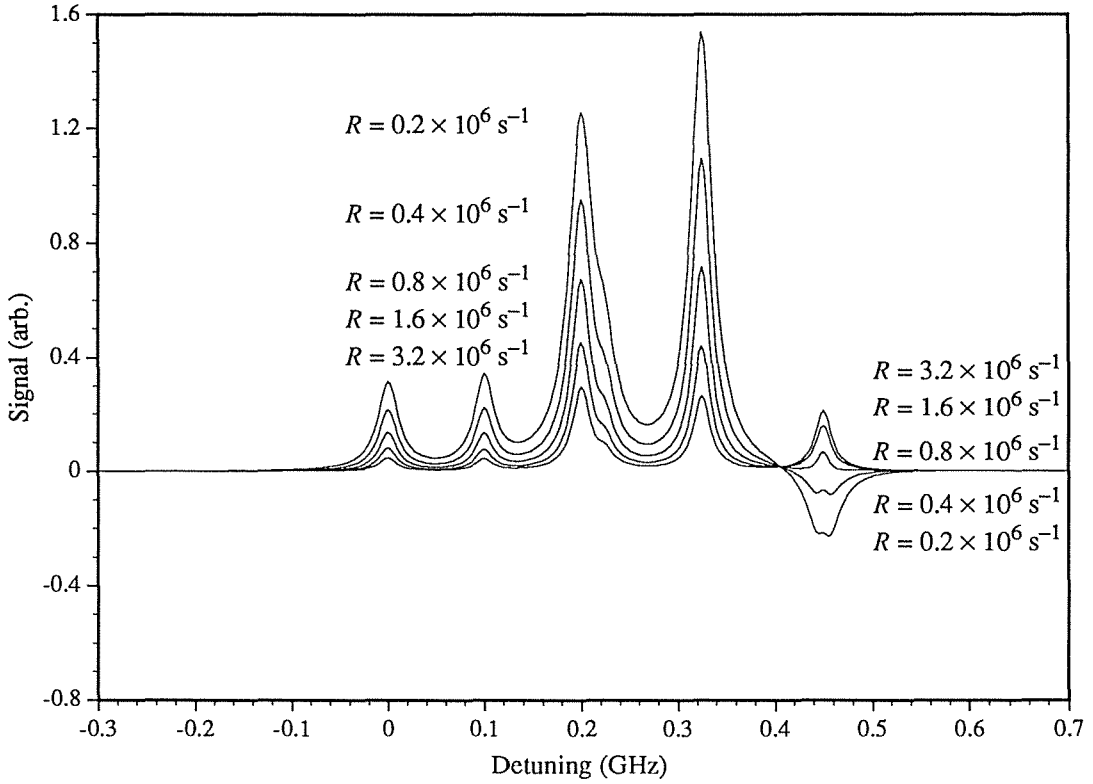

Figure 6.15(*a*). Calculated saturated absorption spectra as a function of the ground state relaxation rate for the transitions with $F = 4$ in the ground state, with pump power of 0.069 mW and cell temperature 20 °C.

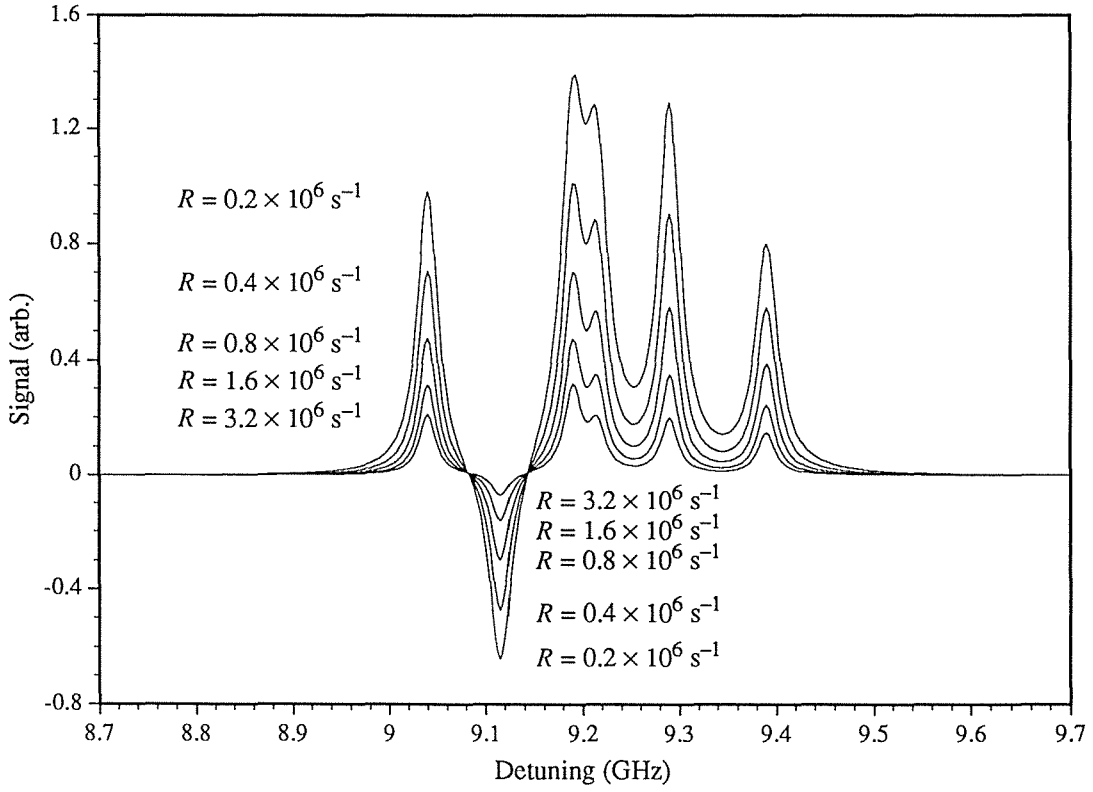

Figure 6.15(*b*). As for (*a*) but for $F = 3$ in the ground state.

$F = 4$ to $F' = 5$, $R = 0.2 \times 10^6$ s^{-1}

5	0.0000	0.0004	0.0014	0.0042	0.0100	0.0136	0.0100	0.0042	0.0014	0.0004	0.0000
4		0.0119	0.0214	0.0503	**0.1052**	**0.1386**	**0.1052**	0.0503	0.0214	0.0119	
3			0.0626	0.0626	0.0626	0.0626	0.0626	0.0626	0.0626		
	–5	–4	–3	–2	–1	0	1	2	3	4	5

$F = 4$ to $F' = 5$, $R = 3.2 \times 10^6$ s^{-1}

5	0.0000	0.0017	0.0033	0.0047	0.0057	0.0061	0.0057	0.0047	0.0033	0.0017	0.0000
4		0.0486	0.0548	0.0607	0.0652	0.0669	0.0652	0.0607	0.0548	0.0486	
3			0.0625	0.0625	0.0625	0.0625	0.0625	0.0625	0.0625		
	–5	–4	–3	–2	–1	0	1	2	3	4	5

Table 6.6. As for Table 6.5 but for the $F = 4$ to $F' = 5$ transition. The populations for the excited-state levels not shown are all zero.

For the $F = 4$ to $F' = 5$ resonance the signal decreases with decreasing R and below a certain value becomes negative. The reason is that this is a cycling transition in which hyperfine pumping to the $F = 3$ level of the ground state is forbidden. Thus, all atoms pumped to the excited $F' = 5$ level return to the ground-state $F = 4$ level (see Table 6.6). Zeeman pumping tends to accumulate atoms in the low-$|M_F|$ sublevels at the expense of the higher-$|M_F|$ sublevels because of the asymmetry in the σ^+ and σ^- transition rates for these latter sublevels (see Figure 6.2). For small values of R the atoms in the $F = 4$ level remain significantly redistributed from equilibrium resulting in the possibility of a higher-than-equilibrium population in the strongly absorbing states (bold in Table 6.6) and thus a negative signal. However, for larger values of R this distribution is returned more quickly to equilibrium and there is less absorption of the probe. An interesting feature of this transition is the small peak that appears for low R values (see Figure 6.15(a)). This occurs because slightly off resonance there is sufficient population in the less-strongly absorbing high-$|M_F|$ sublevels of the $F = 4$ level to produce larger probe absorption than precisely at resonance.

The negative crossover resonance shown in Figure 6.15(b) occurs because of two similar effects. Atoms accumulate in the $M_F = \pm 3$ sublevels of the $F = 3$ ground state level due to Zeeman pumping on the $F = 3$ to $F' = 2$ cycling transition since transitions from these sublevels are forbidden with linearly polarised light (see Table 6.7).

Probing on the $F = 3$ to $F' = 3$ transition produces large absorption from these sublevels thus leading to the negative signal. For increasing values of R the atoms in these sublevels are redistributed at a faster rate reducing the absorption of the probe. The second effect is due to the fact that when pumping on the $F = 3$ to $F' = 3$ resonance the $M_F = 0$ to $M'_F = 0$ transition has zero probability, hence atoms are Zeeman pumped into the $M_F = 0$ sublevel of the $F = 3$ ground-state level (see Table 6.8). Probing on the $F = 3$ to $F' = 2$ transition again produces large absorption. (For extremely large R this crossover resonance becomes positive.) However, as shown in Figure 6.14(*e*),

$F = 3$ to $F' = 2$, $R = 0.2 \times 10^6$ s^{-1}

3			0.0000	0.0000	0.0000	0.0000	0.0000	0.0000	0.0000		
2				0.0010	0.0010	0.0011	0.0010	0.0010			
4		0.0638	0.0629	0.0627	0.0625	0.0625	0.0625	0.0627	0.0629	0.0638	
3			**0.1677**	0.0234	0.0159	0.0144	0.0159	0.0234	**0.1677**		
	−5	−4	−3	−2	−1	0	1	2	3	4	5

$F = 3$ to $F' = 2$, $R = 3.2 \times 10^6$ s^{-1}

3			0.0000	0.0000	0.0000	0.0000	0.0000	0.0000	0.0000		
2				0.0022	0.0031	0.0033	0.0031	0.0022			
4		0.0625	0.0625	0.0625	0.0625	0.0625	0.0625	0.0625	0.0625	0.0625	
3			**0.0777**	0.0580	0.0512	0.0494	0.0512	0.0580	**0.0777**		
	−5	−4	−3	−2	−1	0	1	2	3	4	5

Table 6.7. As for Table 6.5 but for the $F = 3$ to $F' = 2$ transition. The populations for the excited-state levels not shown are all zero.

$F = 3$ to $F' = 3$, $R = 0.2 \times 10^6$ s^{-1}

3			0.0011	0.0008	0.0004	0.0000	0.0004	0.0008	0.0011		
2				0.0000	0.0000	0.0000	0.0000	0.0000			
4		0.0935	0.0894	0.0815	0.0726	0.0683	0.0726	0.0815	0.0894	0.0935	
3			0.0117	0.0188	0.0386	**0.1110**	0.0386	0.0188	0.0117		
	−5	−4	−3	−2	−1	0	1	2	3	4	5

Table 6.8. As for Table 6.5 but for the $F = 3$ to $F' = 3$ transition for a value of $R = 0.2 \times 10^6$ s^{-1}. The populations for the excited-state levels not shown are all zero.

experimentally this crossover was observed to be positive. A possible explanation for this could be that the laser light contained a small degree of elliptical polarisation. Thus, atoms would then be pumped out of the $M_F = \pm 3$ sublevels on the $F = 3$ to $F' = 2$ transition, and out of the $M_F = 0$ sublevel on the $F = 3$ to $F' = 3$ transition, destroying the build-up of atoms in these sublevels. However, due to the presence of the Glan-Taylor prism in the experimental arrangement, it seems unlikely that any elliptically-polarised light would have sufficient intensity to remove significant population from these sublevels. It may be that saturation with a noisy laser is a more subtle phenomenon than is modelled here, and that the laser field fluctuations need to be taken into account, as in the calculation of Tremblay and Jacques[41].

6.7.6. Comparison With Previous Calculations

As discussed in Section 6.5.1, several other workers have performed similar rate equation calculations concerning the caesium D_2 transition. In most of these calculations the ground state relaxation rate due to transit of atoms through the laser beam was not included in the rate equations. It has been shown here that the extent of hyperfine and Zeeman pumping is strongly dependent upon the magnitude of the ground state relaxation rate. Thus, for the purpose of efficiently pumping the "clock transition" for frequency standards[40, 41, 83] it would be necessary to ensure a sufficiently small value of R that significant population is not removed from the sublevels involved in the clock transition during the time required to pump those atoms. Ground state relaxation is also important for lineshape studies as it has been shown that the relative signs and magnitudes of the resonances vary greatly with R. Thus, for example, the predicted change in sign of the $F = 4$ to $F' = 5$ resonance shown in Figure 6.15 was not seen in calculations neglecting R[89]. Also, the narrow peak on this resonance for small values of R is a feature of the present calculation. The calculation by Hirano[87], which includes relaxation of the lower levels, does not consider the differences between the Zeeman sublevels. Thus, the effects of Zeeman pumping discussed in the previous sub-section were not seen in that calculation. It has been shown that Zeeman pumping has important consequences on the relative sizes of the resonances. For example, for linearly polarised light, Zeeman pumping is responsible for the negative crossover resonance between the $F = 3$ to $F' = 2$ and $F = 3$ to $F' = 3$ Lamb-dips.

6.8. Signal Detection

6.8.1. The Lock-in Amplifier

It is necessary to look in more detail at the detection process to be able to explain some of the discrepancies between the experimental and theoretical two-beam spectra. In particular, the function of the lock-in amplifier, which should be pointed out is an essential component for recovering the small sub-Doppler signals from the noise, is examined in this section. A block diagram of the lock-in amplifier is shown in Figure 6.16. An implicit assumption made when calculating the theoretical results is that the input to the lock-in amplifier and the reference signal are equal frequency square waves. If this is so, then the output is proportional to the difference between the two levels of the input square wave, since the lock-in amplifier integrates the signal for the first half-cycle of its reference input (at the chopping frequency) and subtracts the signal integrated for the second half-cycle. To obtain maximum output the phase of the reference must match that of the input signal. Figure 6.17 shows a plot of the output of a lock-in amplifier with an ideal response as a function of phase difference, $\Delta\phi$, between the input and reference square waves. As expected, the graph consists of two straight-line sections with zeroes occurring at phase differences of $\Delta\phi = \pi/2, 3\pi/2$. In general, any periodic input at the reference frequency gives an output S obeying the relationship

$$S(\Delta\phi + \pi) = -S(\Delta\phi). \tag{6.68}$$

If the various rates appearing in the rate equations are of the same order of magnitude as the chopping frequency then one would not expect the absorption signals to be square

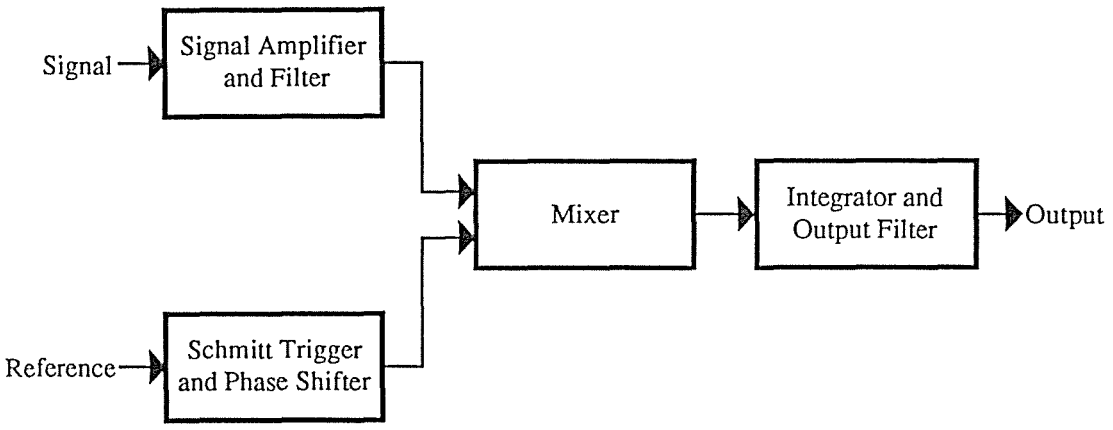

Figure 6.16. Block diagram of the lock-in amplifier.

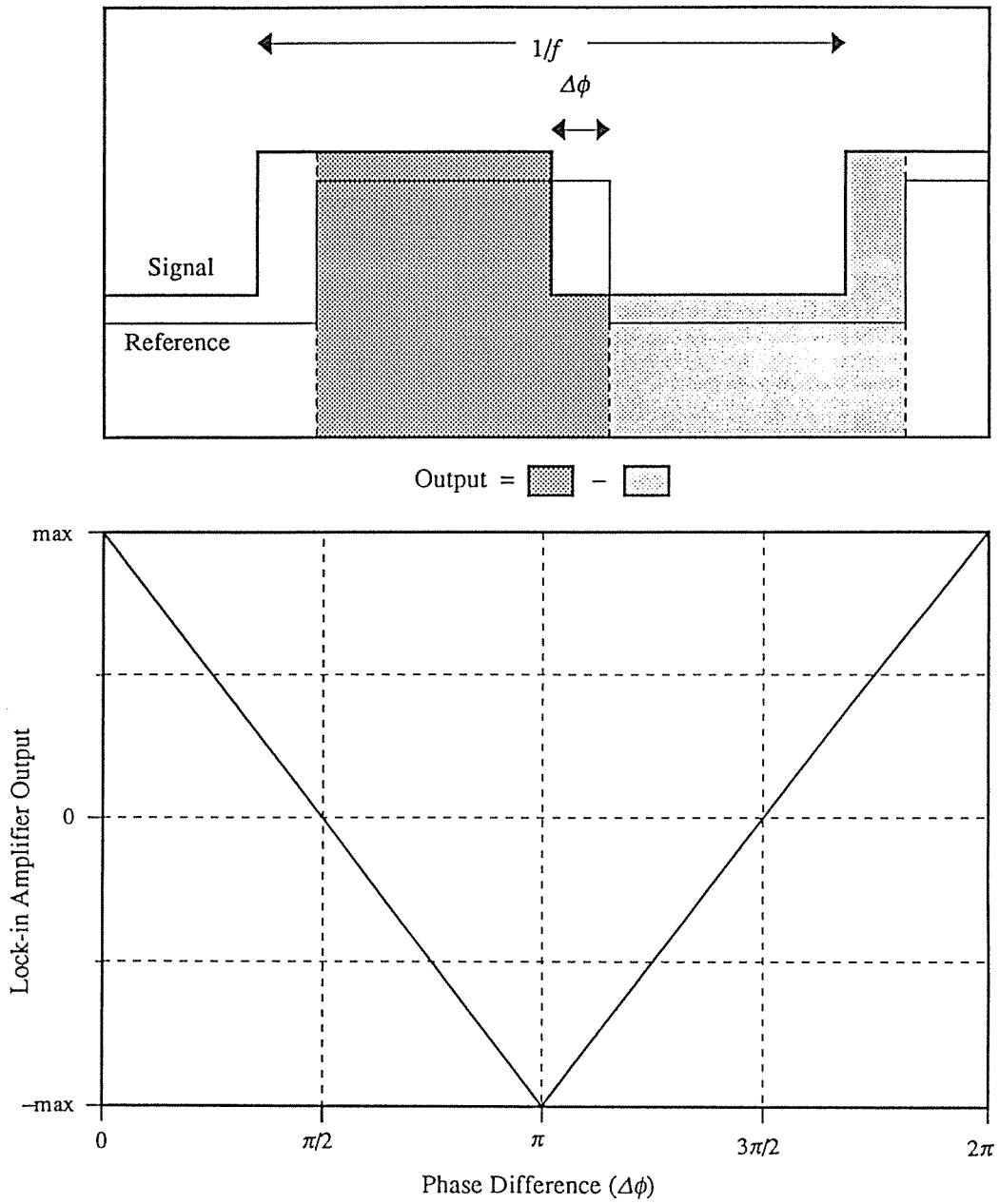

Figure 6.17. Output of an ideal lock-in amplifier for a square-wave input signal.

because of the finite time required for the populations to reach a steady state. In general, it is not possible to measure directly the shape of the input signal to the lock-in amplifier because of its very low signal-to-noise ratio. Indeed, this is the very reason for using a lock-in amplifier. The shape can be obtained theoretically by simply integrating the rate equations for the duration of one chopping cycle. During the first half-cycle the solution evolves with both the pump and probe beams on, while the second half-cycle corresponds to the pump beam having been turned off. The rates at which the solutions approach their steady-state values are primarily determined by the

pumping time (pump intensity) for the first half-cycle, and by the ground state relaxation time for the second half-cycle. If these times are of the same order of magnitude or longer than the chopping period then the detected signal will show significant deviations from squareness.

6.8.2. Signal Evolution

To illustrate the departure from squareness of the detected signal, a solution for the $F = 4$ to $F' = 4$ Lamb-dip resonance evolving over a chopping period of 10 μs is shown in Figure 6.18 for two different pump intensities and two different values of the ground state relaxation rate. As expected, the larger the pump intensity and the larger the ground state relaxation rate, the faster the solution approaches the steady-state values for the pump on and pump off. It will be shown in the following section that this relaxation can be approximated as exponential. A description of these solutions is as follows. During the first half-cycle a number of competing processes operate to achieve a steady-state population distribution. First, atoms are excited from the $F = 4$ level of the ground state by the pump beam after which they decay spontaneously to both the $F = 4$ and $F = 3$ levels. Thus, atoms are hyperfine-pumped from the $F = 4$ to the $F = 3$ level. For a linearly polarised pump beam Zeeman pumping tends to accumulate atoms in the low-$|M_F|$ states of the $F = 4$ level, predominantly the $M_F = 0$ state since this state has zero transition probability, and the high-$|M_F|$ states of the $F = 3$ level (see Figure 6.2). This causes alignment of these levels. During this alignment process ground state relaxation returns atoms from the $F = 3$ to the $F = 4$ level where they can be subsequently re-pumped. When the pump beam is turned off there is an initial rapid build-up of population in both the $F = 3$ and $F = 4$ levels due to spontaneous emission of the atoms in excited states at this time. This causes a slight increase, depending on pump power, in absorption (decrease in transmitted intensity) over the steady-state pump-on case, and leaves an excess of population in the $F = 3$ level over the zero-field equilibrium population. This non-equilibrium distribution of lower-level population then relaxes exponentially towards equilibrium at the ground state relaxation rate.

A simulated lock-in amplifier output for each signal in Figure 6.18 is shown in Figure 6.19. These show deviations from the straight lines of Figure 6.17, with a greater curvature as the solutions in Figure 6.18 depart further from squareness. In addition, Figure 6.19(*a*) demonstrates that in-phase detection does not necessarily give the maximum output.

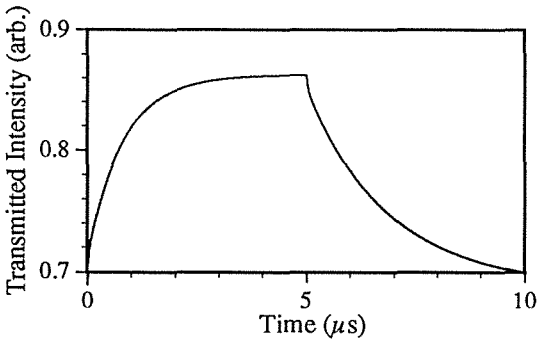

(*a*) $P = 0.06$ mW, $R = 5 \times 10^5$ s^{-1}.

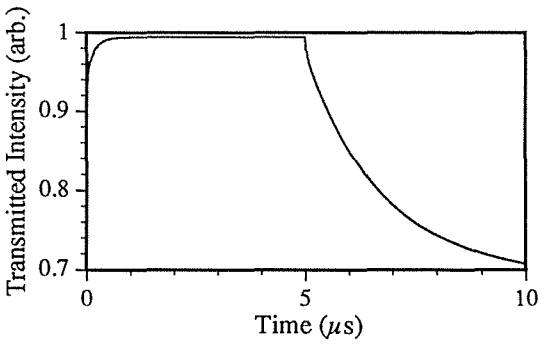

(*b*) $P = 3.2$ mW, $R = 5 \times 10^5$ s^{-1}.

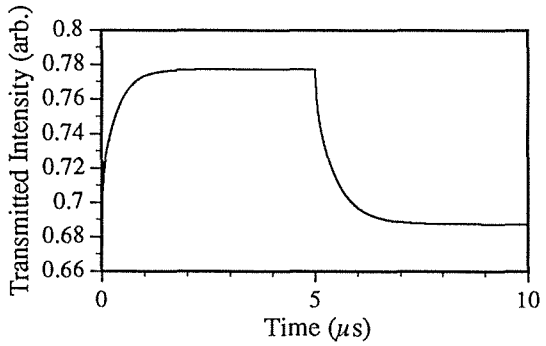

(*c*) $P = 0.06$ mW, $R = 2 \times 10^6$ s^{-1}.

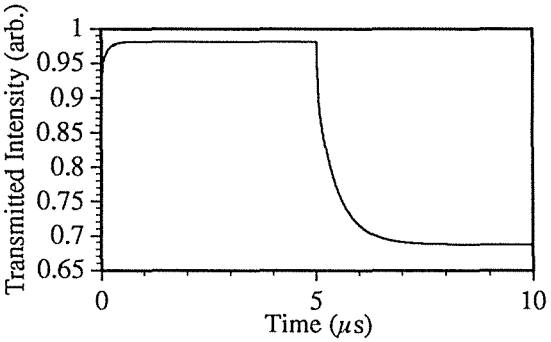

(*d*) $P = 3.2$ mW, $R = 2 \times 10^6$ s^{-1}.

Figure 6.18. Calculated evolution of the transmitted signals for the $F = 4$ to $F' = 4$ transition over a 100-kHz chopping cycle for combinations of pump power, P, and ground state relaxation rate, R.

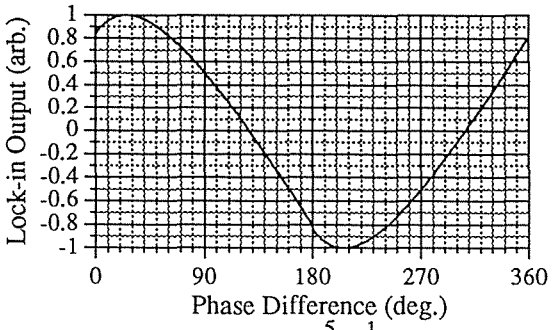

(*a*) $P = 0.06$ mW, $R = 5 \times 10^5$ s^{-1}.

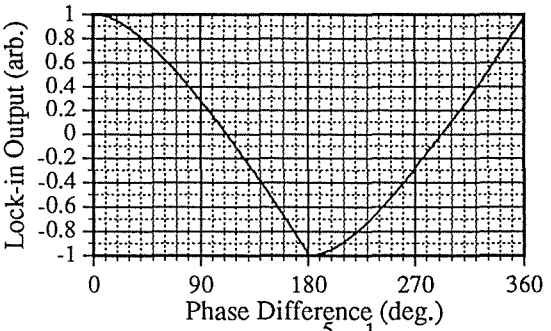

(*b*) $P = 3.2$ mW, $R = 5 \times 10^5$ s^{-1}.

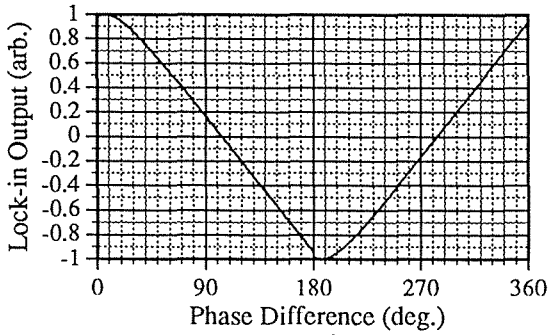

(*c*) $P = 0.06$ mW, $R = 2 \times 10^6$ s^{-1}.

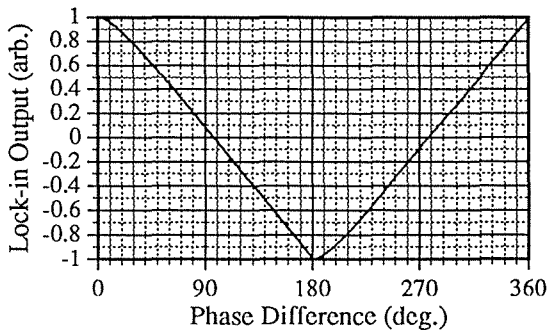

(*d*) $P = 3.2$ mW, $R = 2 \times 10^6$ s^{-1}.

Figure 6.19. Simulated lock-in amplifier outputs as a function of the phase difference between the input and reference signals for the respective input signals of Figure 6.18.

The evolutionary behaviours of the other resonances are all similar to that described for the $F = 4$ to $F' = 4$ transition except for the $F = 4$ to $F' = 5$ cycling transition. This is illustrated in Figure 6.20. Here atoms pumped from the $F = 4$ level are returned solely to this level. Saturation causes a rapid decrease in the absorption coefficient as a balance is maintained between pumping and spontaneous emission. This is followed by a slower increase in absorption as atoms move towards the lower-$|M_F|$ states of the $F = 4$ level due to Zeeman pumping. This increase is ultimately halted by ground state relaxation. When the pump beam is turned off spontaneous emission returns all the remaining excited atoms to the $F = 4$ level, accumulating them in the low-$|M_F|$ states. Thus, the absorption is greater than for the zero-field equilibrium distribution since transitions from these states are more favoured than for the higher-$|M_F|$ states. Hence, the population relaxes back to equilibrium from 'above' rather than from 'below' as for the $F = 4$ to $F' = 4$ transition.

Simulated lock-in amplifier outputs for the curves in Figure 6.20 are shown in Figure 6.21. Comparison of these with the simulated outputs in Figure 6.19 for the other transitions shows that for a given phase difference between the input and reference, the relative sizes of the signals for each type of transition can vary quite significantly.

It is worth noting that the $F = 3$ to $F' = 2$ cycling transition does not display the same evolutionary behaviour as the $F = 4$ to $F' = 5$ transition, but rather evolves as for the $F = 4$ to $F' = 4$ transition described on page 133. The reason for this is that the $M_F = \pm 3$ states of the $F = 3$ level do not participate in the pumping process but still accept spontaneous emission from the $F' = 2$ level. Thus, Zeeman pumping accumulates atoms in these states preventing over-population of the resonant states. The two non-resonant states in this case can be thought of as an independent level.

The results shown in Figures 6.18 and 6.20 indicate that a simple subtraction of the Doppler background to theoretically obtain the two-beam spectra is not appropriate to model the lock-in amplifier response. These provide some qualitative explanation of the discrepancies between the theoretical and experimental two-beam spectra, and suggest that an evolutionary calculation for the entire spectrum should produce better agreement. However, as discussed in the following Section 6.9.2, the lock-in amplifier used in these experiments has a limited frequency response which further complicates the analysis by distorting the evolutionary curves.

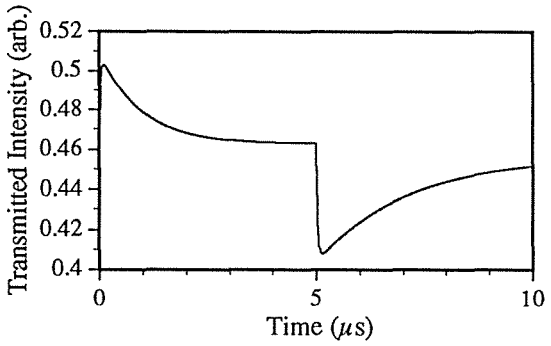

(*a*) $P = 0.06$ mW, $R = 5 \times 10^5$ s^{-1}.

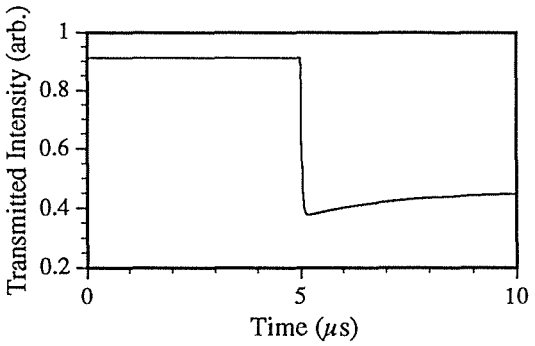

(*b*) $P = 3.2$ mW, $R = 5 \times 10^5$ s^{-1}.

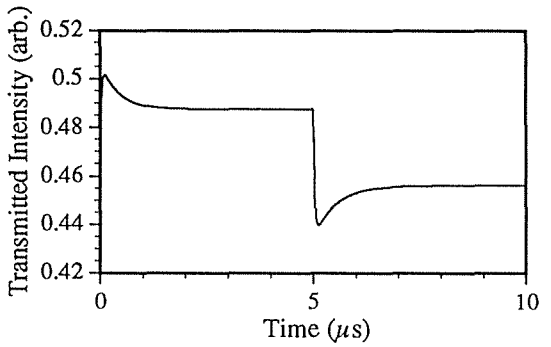

(*c*) $P = 0.06$ mW, $R = 2 \times 10^6$ s^{-1}.

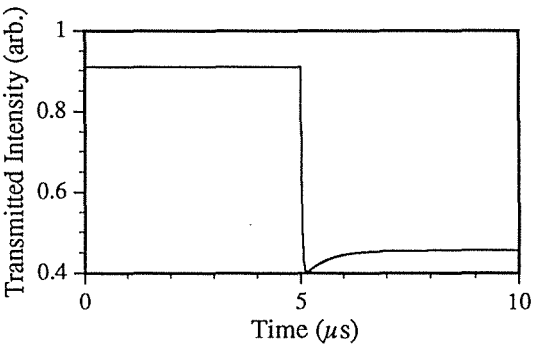

(*d*) $P = 3.2$ mW, $R = 2 \times 10^6$ s^{-1}.

Figure 6.20. Calculated evolution of the transmitted signals for the $F = 4$ to $F' = 5$ transition over a 100-kHz chopping cycle for combinations of pump power, P, and ground state relaxation rate, R.

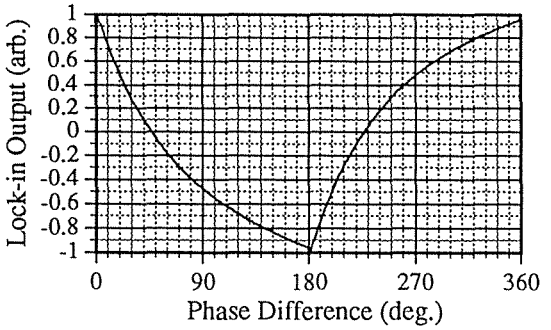

(*a*) $P = 0.06$ mW, $R = 5 \times 10^5$ s^{-1}.

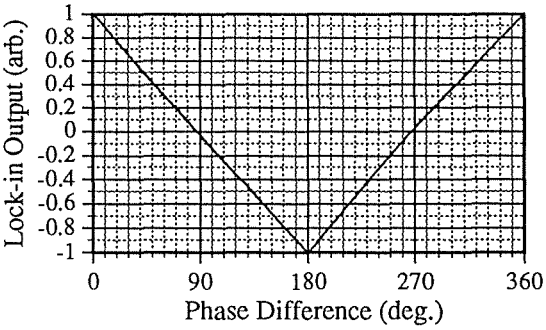

(*b*) $P = 3.2$ mW, $R = 5 \times 10^5$ s^{-1}.

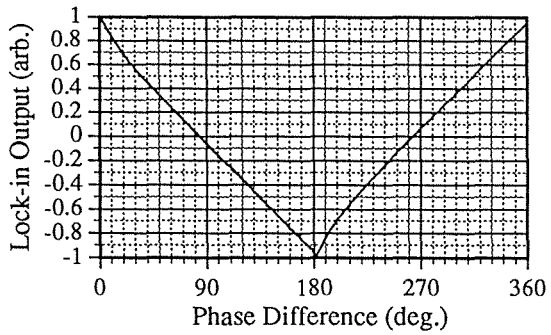

(*c*) $P = 0.06$ mW, $R = 2 \times 10^6$ s^{-1}.

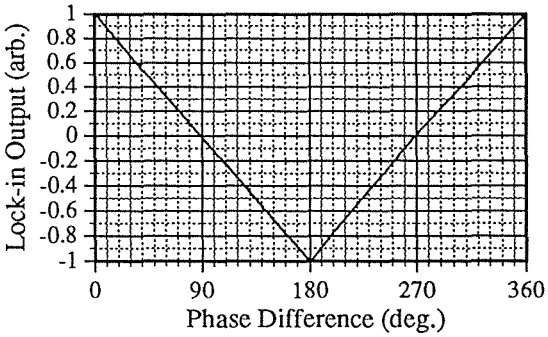

(*d*) $P = 3.2$ mW, $R = 2 \times 10^6$ s^{-1}.

Figure 6.21. Simulated lock-in amplifier outputs as a function of the phase difference between the input and reference signals for the respective input signals of Figure 6.20.

6.9. Determination of Ground State Relaxation Rate

6.9.1. Introduction

Together, the curves in Figures 6.18 and 6.19 suggest a means of determining experimentally an effective ground state relaxation rate. It is possible to calculate an approximate analytic form for the lock-in amplifier output curve where the deviation from a straight line is an explicit function of the ground state relaxation rate, R. Thus, fitting this equation to experimental data will determine R. Several assumptions are made in order to simplify the calculation. First, the pumping rate is assumed to be much larger than the ground state relaxation rate. This will hold for sufficiently high pump intensities, and allows the first half of the chopping cycle to be treated as square. That is, the populations rapidly approach their steady-state values and the absorption coefficient is constant over this half-cycle. Second, the spontaneous decay rate of the upper levels is much larger than the ground state relaxation rate. This condition fails only for exceptionally narrow beam geometries. Thus, during the second half-cycle (pump beam off), after a rapid change in lower-level population due to spontaneous decay of the upper levels, the evolution of the former is determined by the rate R. This evolution is given by the last term in equation (6.47):

$$\frac{\partial \rho_i}{\partial t} = R\left(\tfrac{1}{16} - \rho_i\right). \tag{6.69}$$

The solution to this is

$$\rho_i = \tfrac{1}{16} - \Delta\rho_{i(0)}\, e^{-Rt}, \tag{6.70}$$

where $\Delta\rho_{i(0)}$ is the state i population difference from the zero-field equilibrium value of $\frac{1}{16}$ at time $t = 0$ defined when the pump beam is turned off. For a given state, $\Delta\rho_{i(0)}$ can be either positive or negative as determined by the optical pumping processes which lead to the particular population distribution of the lower levels.

The absorption coefficient at a given frequency is proportional to the sum over allowed transitions of equation (6.70) multiplied by the appropriate Einstein A coefficient:

$$\alpha(t) \propto \frac{1}{16}\sum_{i=1}^{n} A_{ik} - e^{-Rt}\sum_{i=1}^{n} A_{ik}\,\Delta\rho_{i(0)}, \tag{6.71}$$

where n is the number of allowed transitions and k labels the upper state of the i^{th} transition. The two summations give constants over time, thus the absorption

coefficient evolves at the rate R in the same manner as the individual populations in equation (6.70).

For optically thin vapours ($|\alpha z| \ll 1$) the transmitted intensity is proportional to $e^{-\alpha z}$:

$$\begin{aligned} I(t) &\propto \exp\left[-\alpha_0 z + (\alpha_0 - \alpha_1) z e^{-Rt}\right] \\ &= 1 - \alpha_0 z + (\alpha_0 - \alpha_1) z e^{-Rt}. \end{aligned} \tag{6.72}$$

Therefore, $I(t)$ can be written:

$$I(t) = I_0 + (I_1 - I_0) e^{-Rt}, \tag{6.73}$$

where α_0 and I_0 are the steady-state absorption coefficient and transmitted intensity, respectively, with the pump beam off, and α_1 and I_1 are the steady-state values with the pump beam on.

Hence, the input signal to the lock-in amplifier consists of a constant value of magnitude I_1 over the first half of the chopping cycle followed by an exponential decay given by equation (6.73) over the second half-cycle. The lock-in amplifier output for a given phase difference $\Delta\phi$ between the input and reference is calculated by integrating the input over an appropriately-shifted (reference) square wave with the same period T as the input. This gives

$$S(\Delta\phi) = p_1 - p_2 \Delta\phi - p_3 e^{-p_4 \Delta\phi}, \tag{6.74}$$

where

$$p_1 = (I_0 - I_1)\left[\frac{T}{2} + \frac{1}{R} + \frac{1}{R} e^{-TR/2}\right], \tag{6.75a}$$

$$p_2 = \frac{(I_0 - I_1)T}{\pi}, \tag{6.75b}$$

$$p_3 = \frac{2(I_0 - I_1)}{R}, \tag{6.75c}$$

and

$$p_4 = \frac{TR}{2\pi}. \tag{6.75d}$$

When $TR \gg 1$ the last term in equation (6.74) approaches zero and $S(\Delta\phi)$ gives the straight-line graph of Figure 6.17. For $R \sim T$ the last term describes the curvature shown in Figure 6.19. Fitting experimental data to equation (6.74) yields the ground state relaxation rate through parameter p_4.

The above discussion assumes that the lock-in amplifier has an infinite frequency response. In practice there will be an upper cut-off frequency (and possibly a lower cut-off frequency) above (and below) which any frequency components of the input signal will be effectively lost. In this case equation (6.74) will not hold. The next sub-section describes an experimental situation in which only the fundamental of the input signal was detected.

6.9.2. Experiment

The experiment was performed with the same arrangement as shown in Figure 6.13. The phase difference between the reference and input signals was adjusted from 0° to 360° in steps of 10°. For each phase difference a series of 20 spectra were recorded and the average height of each Lamb-dip resonance and crossover resonance was calculated. The cell temperature remained within 18.8 ± 0.2 °C throughout the experiment. The results for the transitions with $F = 4$ in the ground state are shown in Figure 6.22. Rather than the curves fitting equation (6.74), they are all well approximated by sinusoids, with the $F = 4$ to $F' = 5$ cycling transition having a significant phase shift in comparison with the other resonances. This arose because the chopping frequency was 100 kHz, which is the maximum operating frequency of the lock-in amplifier (Princeton Applied Research Model 128A). Mixing of the signal and reference waveforms thus resulted in detection of only the first harmonic of the input signal—hence the sinusoidal curves in Figure 6.22.

The phase shifts of each signal from zero phase difference were due to several factors:

(*i*) There was a phase lag between the reference input and the detected signal resulting from delays due to the acousto-optic modulator.

(*ii*) There was a further phase lag and distortion of the input signal due to preamplification by the lock-in amplifier.

(*iii*) There was a phase lag of the reference signal due to the phase shifter of the lock-in amplifier.

(*iv*) There were further phase lags of both the shifted reference and the amplified signal and distortion of the latter due to the mixer of the lock-in amplifier.

Any remaining phase shift was due to the "first harmonic approximation" to the signal at the mixer. Although it is possible to relate this remaining phase shift to the shape of

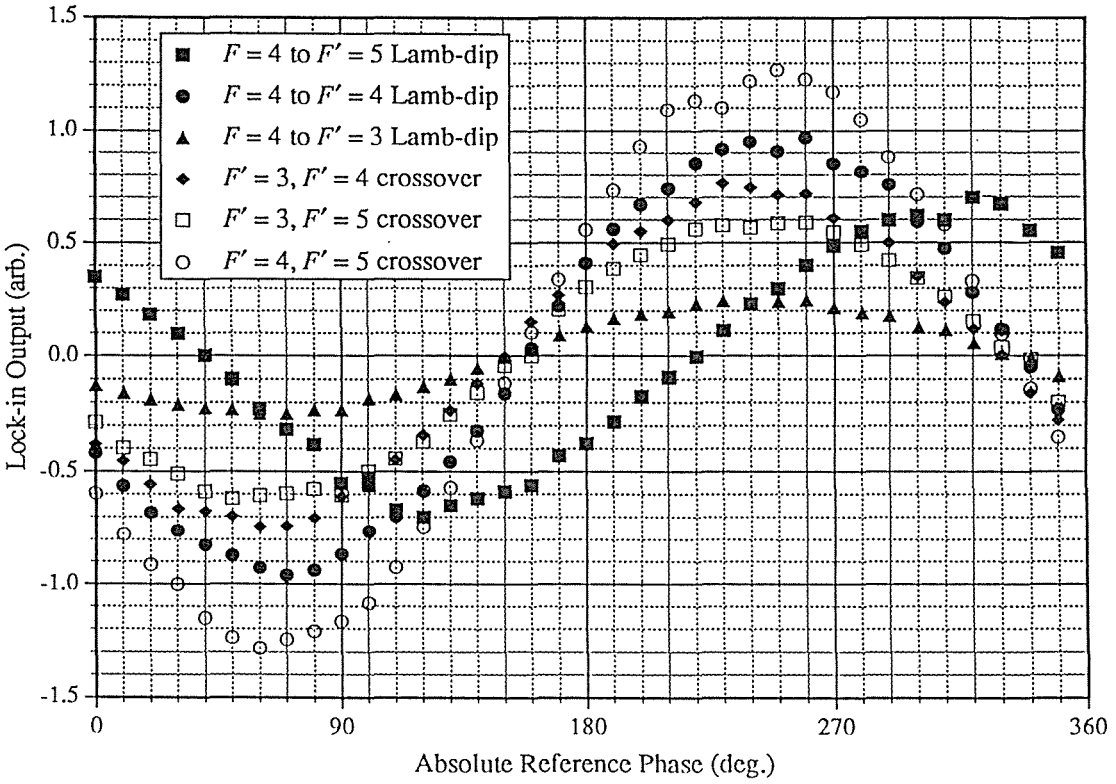

Figure 6.22. Experimental on-resonance lock-in amplifier outputs for the Lamb-dip and crossover resonances with $F = 4$ in the ground state as a function of the absolute phase of the amplifier reference.

the mixer signal through Fourier analysis, it is not in general possible to determine the separate phase shifts listed above or the amount of distortion for an arbitrary input signal. Nevertheless, the curves in Figure 6.22 are consistent with a first harmonic calculation based on the theoretical time evolution signals. That is, the cycling transition gives a sinusoid with a phase lead relative to the chopping cycle while the other transitions produce a lag. This is illustrated in Figure 6.23.

It is possible to gain limited quantitative information from the results in Figure 6.22 if the response time of the detector is sufficiently short. This is a good approximation here since the detector used has a bandwidth of 500 MHz. Thus, since the lock-in amplifier is a linear device (for frequencies within its bandwidth), the first harmonic of the detected signal at its input behaves in the same way for all signals. In particular, the $61 \pm 8°$ difference between the $F = 4$ to $F' = 4$ and the $F = 4$ to $F' = 5$ maxima will be preserved. Calculations yield a value for signal decay rate, consistent with this phase shift, of $R_S = (1.3 \pm 0.2) \times 10^6\ s^{-1}$. This contains contributions from both the atomic response and the instrumental effect of the detector and its cable. The capacitance of the cable and detector was measured to be 250 pF with a resistance of 1000 Ω, resulting in

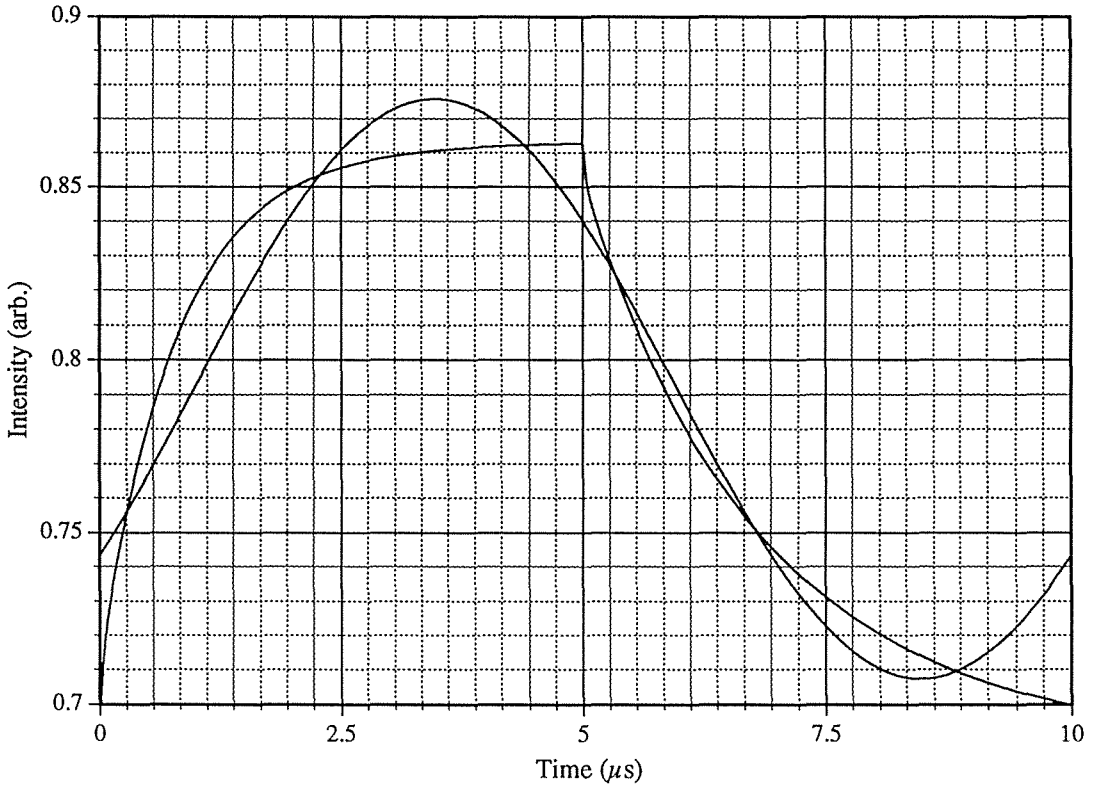

Figure 6.23(a). First harmonic approximation to the $F = 4$ to $F' = 4$ evolution signal, demonstrating a phase lag of the first harmonic signal.

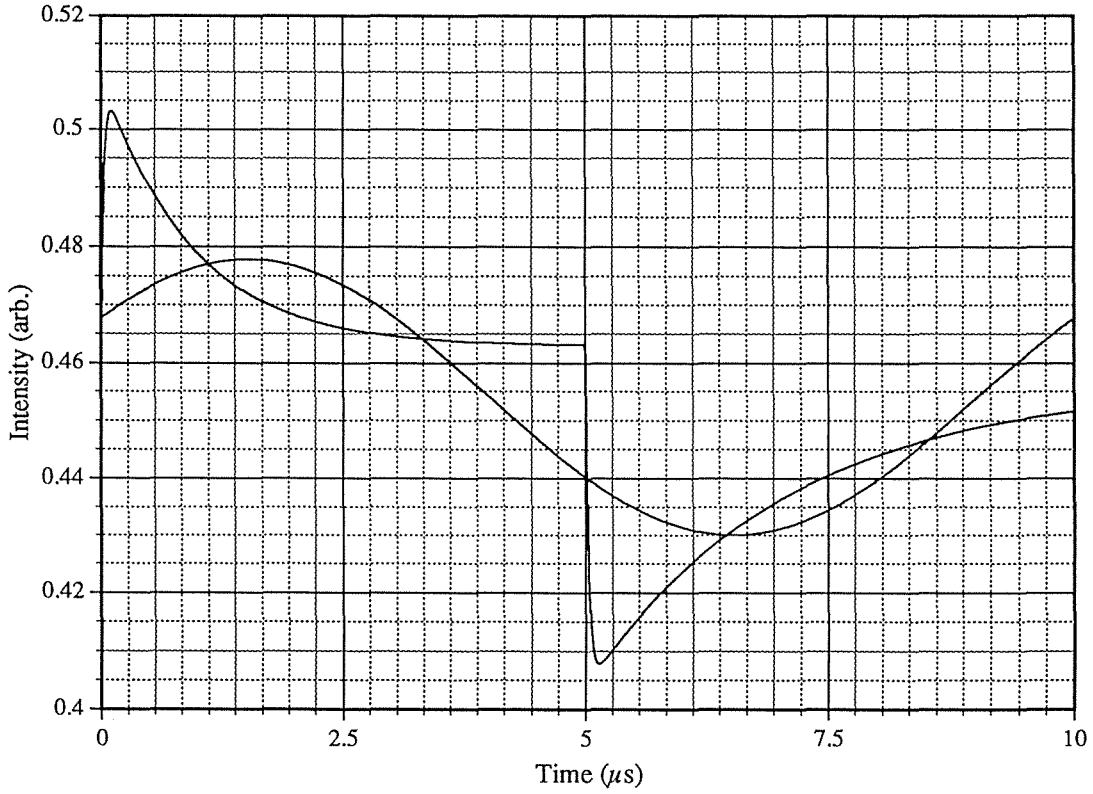

Figure 6.23(b). First harmonic approximation to the $F = 4$ to $F' = 5$ evolution signal, demonstrating a phase lead of the first harmonic signal.

a time constant of 0.25 μs. This is consistent with a direct measurement on an oscilloscope of a large signal chopped at 100 kHz, which gave an exponential decay rate of $(3.7 \pm 0.3) \times 10^6$ s^{-1}, or a time constant of 0.27 μs. Subtracting this from the observed total time constant of $1/R_S = 0.77$ μs yields a value of 0.5 μs for the atomic response alone. Inversion of this gives $R = (2.0 \pm 0.4) \times 10^6$ s^{-1}, in agreement with the fitted result from the single-beam experiments.

It would be more instructive to perform this experiment using a lock-in amplifier with a higher frequency response, such as the Princeton Applied Research Model 5202 which has a response up to 50 MHz. Also, this experiment would be more suitably performed using a diode laser actively stabilised to a resonance signal since this would eliminate the need to scan repeatedly through all the transitions for each phase difference setting.

7. Summary and Conclusion

"...My brain hurt like a warehouse, it had no room to spare
I had to cram so many things to store everything in there..."
David Bowie†.

This thesis has described the manner in which a standard commercial 'off-the-shelf' relatively low-cost AlGaAs diode laser can be used to carry out laser spectroscopy studies with sub-Doppler resolution. An example of such an application is reported for the D_2 transition in atomic caesium, in which measurements have been made of the influence of saturation and optical pumping on the saturated absorption spectrum. Single-beam absorption spectra for the transition have also been recorded.

The key to success in the use of such a laser lies in the very tight control of operating conditions, involving a specially constructed, ultra-stable constant current source, and close temperature control over laser operation. A benefit from such control is that the spectral linewidth is reduced from several hundred MHz down to about 10 MHz. The associated circuitry also allows for accurate control over the setting and scanning of the output frequency of the laser.

An important aspect of the work is that since the circuitry needed for these control functions is relatively simple to construct and operate, there is potential for broad application in small-scale laboratories, with particular value in providing a starting point for researchers new to laser spectroscopy.

However, there are some subtleties with the system. It is well known that 'off-the-shelf' diode lasers exhibit a map of laser wavelength versus injection current and temperature which is only quasi-continuous, with wavelength discontinuities at current/temperature values that vary from laser to laser. It is vital to be able to establish such a map for any particular diode laser so as to ascertain whether a current/temperature régime exists in which the desired continuous operation can be achieved. The thesis has described (Chapter 3) how a purpose-designed data acquisition and control unit gains this information and also facilitates the recording of spectra by controlling the laser frequency scan and automatically storing paired frequency-intensity values directly on a computer.

An important part of the thesis has been devoted to testing the limits of performance of the controlled diode laser. The narrowing of the linewidth has been mentioned. The

† From the album *The rise and fall of Ziggy Stardust and the Spiders from Mars*, 1972.

linewidth was measured, as described in Chapter 4, by heterodyning the outputs of two stabilised lasers, one at a fixed power. The result of this experiment showed the expected linear dependence of linewidth on inverse power for powers greater than 1.25 mW, and also demonstrated the spectral profile of the output beam to be Lorentzian in shape.

An independent determination of the linewidth (Chapter 5) involved operating a Fabry-Perot interferometer using a small free spectral range for which the different orders were not resolved, but in which the fringe visibility was a strong function of linewidth. A theoretical analysis showed the feasibility of the method for determining linewidth given a known lineshape; experiments using the diode laser verified the analysis and enabled a measurement of the linewidth to be obtained. However, it was found that for low powers the presence of additional longitudinal modes in the output spectrum of the laser produced too much distortion of the transmitted fringe pattern for the analysis to hold. The technique is nevertheless a fundamentally valid one, and should be able to be used with success (for example) for cleaved-coupled-cavity lasers where the non-lasing longitudinal modes are greatly suppressed. Finally, the long-term stability of the laser was checked using an absorption cell.

The remainder of the thesis has been concerned with applications of the laser.

In Chapter 6 saturated absorption experiments have been reported for caesium vapour using the D_2 transition in an absorption cell. A theoretical framework was developed to model these experiments. The model is based on rate equations describing the transfer of atomic population density among the 48 sublevels involved in the transition. The calculations were performed for the régime of low vapour pressure and relatively low beam intensity (but large enough for saturation and optical pumping effects to be significant). The model introduces a ground state relaxation rate, R, arising from the transit of atoms through the beam and the subsequent destruction of their polarisation upon impact with the cell wall. Previous models of this transition appearing in the literature do not include this ground state relaxation rate.

The single-beam experiments described in Section 6.6 demonstrated the use of the laser as a medium-resolution source, where the laser linewidth is narrow in comparison with the Doppler width of the measured spectra. The model predicts that, due to the differences in the optical pumping occurring for transitions originating from the $F = 3$ and $F = 4$ hyperfine components of the ground state, the $F = 3$ Doppler-broadened absorption coefficient is more sensitive to the magnitude of R than the $F = 4$ absorption

coefficient. The experimental ratio of these two values was used to select R for the calculations. The resulting value of $R = 2 \times 10^6$ s^{-1} was a factor of ten greater than one would expect from a simple calculation based on beam diameter and thermal atomic speed. A future study of the relationship between these latter parameters and the ground state relaxation rate could be made by performing these experiments over an appropriate range of beam diameters. The calculations produced good agreement with experiment for those spectra for which the laser coherence time was much less than the pumping time (as defined in Section 6.5.1). In this case optical coherences have insufficient time to build up and so the rate equation approximation is valid. For higher powers there was some discrepancy between the calculated and experimental spectra.

In Section 6.7 the two-beam saturated absorption experiments demonstrated the limitations imposed by the laser's frequency fluctuations and drift. Similar spectra taken over a nominal 1 GHz sweep, covering the transitions from either of the ground state hyperfine components, resulted in excursions as large as 20% from the nominal frequency scan rate. This effect, due largely to laser temperature drift, had the apparent consequence of either broadening or narrowing (depending on the sign of the drift) the spectral components. The frequency axes of the measured spectra were linearised to the known hyperfine splittings for comparison with theory. The results of varying the ground state relaxation rate in the calculations were examined and it was discovered that below critical values of R two of the resonances change sign due to the effects of Zeeman pumping coupled with redistribution of population at the rate R.

Discrepancies between the heights of the experimental and theoretical spectra for the two-beam experiments led to an examination of the lock-in detection process used to enhance the low signal-to-noise ratio inherent in the measured signal. It was shown that for values of the ground state relaxation rate of the order of the chopping frequency for the lock-in detection, a simple subtraction of the Doppler-broadened background is not appropriate to model the function of the lock-in amplifier. In this case it is necessary to look at the evolution of the population distribution under the pump beam during the first half of the chopping cycle, followed by relaxation back to equilibrium with the pump removed during the second half-cycle. The shape of this evolution is dependent upon which transition is in resonance due to the different effects of hyperfine and Zeeman pumping occurring for each transition.

Finally, in Section 6.9 a method was outlined to determine the ground state relaxation rate by measuring the resonance signal as a function of lock-in phase at an appropriate chopping frequency. The limited frequency response of the lock-in amplifier used in an

experiment to check this method produced distortion of the measured result from that expected. However, a significant difference was obtained for the $F = 4$ to $F' = 5$ transition in comparison with the other resonances with $F = 4$ in the ground state, in accord with that expected from a consideration of the optical pumping processes involved. A calculation based on this difference produced a value of R in agreement with the result from the single-beam experiments. It is believed that this method for determining ground state relaxation rate in this transition has not been utilised previously, and has significant potential value in unravelling the various contributions to relaxation in the system. The effect was discovered quite late in the research programme, and no attempt has been able to be made to explore the potential of the method systematically; for example, more success could be obtained using a larger-bandwidth lock-in amplifier and a more highly stabilised laser source, such as an external-cavity device.

References

1 M.J. Beesley, *Lasers and Their Applications*, (London: Taylor and Francis Ltd, 1976), pp. 100 – 107.

2 G. Burns and M.I. Nathan, *Proc. IEEE*, **52**, 770, (1964).

3 R.N. Hall, G.E. Fenner, J.D. Kingsley, T.J. Soltys, and R.O. Carlson, *Phys. Rev. Lett.*, **9**, 366, (1962).

4 M.I. Nathan, W.P. Dumke, G. Burns, F.H. Dill, Jr, and G. Lasher, *Appl. Phys. Lett.*, **1**, 62, (1962).

5 T.M. Quist, R.H. Rediker, R.J. Keyes, W.E. Krag, B. Lax, A.L. McWhorter, and H.J. Zeiger, *Appl. Phys. Lett.*, **1**, 91, (1962).

6 N. Holonyak, Jr and S.F. Bevacqua, *Appl. Phys. Lett.*, **1**, 82, (1962).

7 W.E. Howard, F.F. Fang, F.H. Dill, Jr, and M.I. Nathan, *IBM J. Res. & Dev.*, **7**, 74, (1963).

8 M.I. Nathan, *Proc. IEEE*, **54**, 1276, (1966).

9 W.P. Dumke, *Phys. Rev.*, **127**, 1559, (1962).

10 I. Melngailis and A. Mooradian in *Laser Applications to Optics and Spectroscopy*, edited by S.F. Jacobs, M Sargent III, J.F. Scott, and M.O. Scully, (Massachusetts: Addison-Wesley, 1975).

11 I. Hayashi, M.B. Panish, P.W. Foy, and S. Sumski, *Appl. Phys. Lett.*, **17**, 109, (1970).

12 N. Holonyak, Jr, R.M. Kolbas, R.D. Dupuis, and P.D. Dapkus, *IEEE J. Quant. Electron.*, **16**, 170, (1980).

13 W.T. Tsang, N.A. Olsson, and R.A. Logan, *Appl. Phys. Lett.*, **42**, 650, (1983).

14 T. Matsuoka, H. Nagai, Y. Itaya, Y. Noguchi, Y. Suzuki, and T. Ikegami, *Electron. Lett.*, **18**, 27, (1982).

15 Y. Sakakibara, K. Furuya, K. Utaka, Y. Suematsu, *Electron. Lett.*, **16**, 456, (1980).

16 C.E. Wieman and L. Hollberg, *Rev. Sci. Instrum.*, **62**, 1, (1991).

17 J.C. Camparo, *Contemp. Phys.*, **26**, 443, (1985).

18 T.L. Paoli, *IEEE J. Quant. Electron.*, **11**, 489, (1975).

19 Y. Suematsu, *Physics Today*, May 1985, p. 32.

20 Y.P. Varshni, *Physica*, **34**, 149, (1967).

21 C.H. Henry, R.A. Logan, and K.A. Bertness, *J. Appl. Phys.*, **52**, 4457, (1981).

22 D. Chambliss and M. Johnson, *Opt. Commun.*, **48**, 343, (1984).

23 M. Nakamura, K. Aiki, N. Chinone, R. Ito, and J. Umeda, *J. Appl. Phys.*, **49**, 4644, (1978).

24 M.W. Fleming and A. Mooradian, *Appl. Phys. Lett.*, **38**, 511, (1981).

25 J.M. Osterwalder and B.J. Rickett, *Proc. IEEE*, **67**, 1671, (1978).

26 C.H. Henry, *IEEE J. Quant. Electron.*, **19**, 1391, (1983).

27 A.L. Schawlow and C.H. Townes, *Phys. Rev.*, **112**, 1940, (1958).

28 M. Lax, *Phys. Rev.*, **160**, 290, (1967).

29 C.H. Henry, *IEEE J. Quant. Electron.*, **18**, 259, (1982).

30 A. Mooradian, *Physics Today*, May 1985, p. 43.

31 S. Siahatgar and U.E. Hochuli, *IEEE J. Quant. Electron.*, **5**, 295, (1969).

32 I. Hirano, *Opt. Commun.*, **57**, 331, (1986).

33 J.C. Camparo and C.M. Klimcak, *Am. J. Phys.*, **51**, 1077, (1983).

34 K. Fukuoka, M. Ohtsu, and T. Tako, *Jap. J. Appl. Phys.*, **23**, L117, (1984).

35 K. Tachibana, H. Harima, and Y. Urano, *J. Phys. B*, **15**, 3169, (1982).

36 J.H. Hollister, G.R. Apperson, L.L. Lewis, T.P. Emmons, T.G. Vold, and E.N. Fortson, *Phys. Rev. Lett.*, **46**, 643, (1981).

37 G. Singh, P. DiLavore, and C.O. Alley, *IEEE J. Quant. Electron.*, **7**, 196, (1971).

38 M. Arditi and J.L. Picqué, *J. Physique Lettres*, **41**, L-379, (1980).

39 M. Arditi and J.L. Picqué, *J. Phys. B*, **8**, L331, (1975).

40 G. Avila, V. Giordano, V. Candelier, E. de Clercq, G. Theobald, and P. Cerez, *Phys. Rev. A*, **36**, 3719, (1987).

41 P. Tremblay and C. Jacques, *Phys. Rev. A*, **41**, 4989, (1990).

42 C.M. Klimcak and J.C. Camparo, *Phys. Rev. A*, **30**, 1791, (1984).

43 C.E. Tanner and C.E. Wieman, *Phys. Rev. A*, **38**, 1616, (1988).

44 D. Sesko, C.G. Fan, and C.E. Wieman, *J. Opt. Soc. Am. B*, **5**, 1225, (1988).

45 K.E. Gibble and A. Gallagher, *Phys. Rev. A*, **43**, 1366, (1991).

46 T. Yabuzaki, T. Mitsui, and U. Tanaka, *Phys. Rev. Lett.*, **67**, 2453, (1991).

47 C.C. Bradley, J. Chen, and R.G. Hulet, *Rev. Sci. Instrum.*, **61**, 2097, (1990).

48 M.S. Cafferty and E.D. Thompson, *Rev. Sci. Instrum.*, **60**, 2896, (1989).

49 B. Levy and A.J. Greenfield, *Rev. Sci. Instrum.*, **50**, 655, (1979).

50 J. Dratler, Jr, *Rev. Sci. Instrum.*, **45**, 1435, (1974).

51 D. Sarid and D.S. Cannell, *Rev. Sci. Instrum.*, **45**, 1082, (1974).

52 R.D. Esman and D.L. Rode, *Rev. Sci. Instrum.*, **54**, 1368, (1983).

53 M. Ohtsu, Y. Otsuka, and Y. Teramachi, *Appl. Phys. Lett.*, **46**, 108, (1985).

54 M. Ohtsu and Y. Teramachi, *IEEE J. Quant. Electron.*, **25**, 31, (1989).

55 H. Hori, K. Endo, E. Koro, and T. Sakurai, *J. Appl. Phys.*, **60**, 2231, (1986).

56 D. Letalick and I. Renhorn, *Rev. Sci. Instrum.*, **58**, 765, (1987).

57 T.S. Jaseja, A. Javan, and C.H. Townes, *Phys. Rev. Lett.*, **10**, 165, (1963).

58 A.E. Siegman, *Appl. Optics*, **5**, 1588, (1966).

59 M. Ohtsu and S. Kotajima, *IEEE J. Quant. Electron.*, **21**, 1905, (1985).

60 T. Okoshi, K. Kikuchi, and A. Nakayama, *Electron. Lett.*, **16**, 630, (1980).

61 D. Welford and A. Mooradian, *Appl. Phys. Lett.*, **40**, 560, (1982).

62 D. Welford and A. Mooradian, *Appl. Phys. Lett.*, **40**, 865, (1982).

63 A.E. Siegman and D.J. Kuizenga, *Opto-Electronics*, **6**, 43, (1974).

64 J.T. Verdeyen, *Laser Electronics*, (New Jersey: Prentice-Hall, 1981), ch. 9.

65 R.G. de Voe and R.G. Brewer, *Laser Spectroscopy VII*, (Berlin, Heidelberg: Springer-Verlag, 1985), pp. 358 – 361.

66 I. Stakgold, *Boundary Value Problems of Mathematical Physics, Vol I*, (New York: MacMillan, 1967), p. 47.

67 A. Reichel, *Special Functions*, (Sydney: Science Press, 1966), p. 59.

68 *a.* W. Demtröder, *Laser Spectroscopy. Basic Concepts and Instrumentation*, (Berlin, Heidelberg, New York: Springer-Verlag, 1982), pp. 153 – 159.

b. *ibid.*, p. 86.

69 R.S. Longhurst, *Geometrical and Physical Optics*, (London, New York: Longman, 1973), p. 181.

70 M.A. Khashan, *Physica*, **98C**, 93, (1979).

71 *a.* I.S. Gradshteyn and I.M. Ryzhik, *Table of Integrals, Series and Products*, (New York and London: Academic Press, 1965), p. 480.

b. *ibid.*, p. 36.

72 E.W. Smith, J. Cooper, W.R. Chappell, and T. Dillon, *J. Quant. Spectrosc. Radiat. Transfer*, **11**, 1547, (1971).

73 W. Happer, *Rev. Mod. Phys.*, **44**, 169, (1972).

74 *a.* A. Corney, *Atomic and Laser Spectroscopy*, (Oxford: Clarendon Press, 1977), pp. 664 – 667.

b. *ibid.*, p. 291.

c. *ibid.*, p. 293.

75 E. Arimondo, M. Inguscio, P. Violino, *Rev. Mod. Phys.*, **49**, 31, (1977).

76 P. Buck, I.I. Rabi, and B. Senitzky, *Phys. Rev.*, **104**, 553, (1956).

77 S. Svanberg and S. Rydberg, *Z. Phys.*, **227**, 216, (1969).

78 P. Violino, *Can. J. Chem.*, **47**, 2095, (1969).

79 S. Svanberg and G. Belin, *Z. Phys.*, **251**, 1, (1972).

80 *a.* A.R. Edmonds, *Angular Momentum in Quantum Mechanics*, (New Jersey: Princeton University Press, 1974), p. 75.
b. *ibid.*, p. 111.
81 M. Rotenberg, R. Bivins, N. Metropolis, and J.K. Wooten, Jr, *The 3-j and 6-j Symbols*, (Massachusetts Institute of Technology: The Technology Press, 1959), pp. 1 – 18.
82 *a.* I.I. Sobel'man, *Introduction to the Theory of Atomic Spectra*, (Braunschweig: Permagon Press, 1972), p. 308.
b. *ibid.*, pp. 85, 308.
83 E. de Clercq, M. de Labachellerie, G. Avila, P. Cerez, and M. Tetu, *J. Physique*, **45**, 239, (1984).
84 R.W. Schmieder, A. Lurio, W. Happer, and A. Khadjava, *Phys. Rev. A*, **2**, 1216, (1970).
85 C. Cohen-Tannoudji, in *Les Houches 1975, Frontiers in Laser Spectroscopy*, ed. by R. Balian, S. Haroche, and S. Liberman, (Amsterdam: North Holland, 1977), p. 66.
86 H. Massey, *Atomic and Molecular Collisions*, (London: Taylor & Francis Ltd, 1979), p. 9.
87 I. Hirano, *J. Quant. Spectrosc. Radiat. Transfer*, **36**, 459, (1986).
88 S. Nakayama, *Jap. J. Appl. Phys.*, **23**, 879, (1984).
89 S. Nakayama, *Jap. J. Appl. Phys.*, **24**, 1, (1985).
90 C. Audoin and J. Vanier, *J. Phys. E*, **9**, 687, (1976).
91 V.N. Belov, A.G. Gevorkyan, and G.G. Yushina, *Opt. Spectrosc. (USSR)*, **63**, 414, (1987).
92 P.G. Pappas, M.M. Burns, D.D. Hinshelwood, and M.S. Feld, *Phys. Rev. A*, **21**, 1955, (1980).
93 M.D. Levenson, *Introduction to Nonlinear Laser Spectroscopy*, (New York, Academic Press, 1982), p. 84.
94 C.H. Holbrow, A.P. Ghosh, D. Heinzen, X. Zhu, W.W. Quivers, Jr, G. Shimkaveg, P.G. Pappas, J.E. Thomas, and M.S. Feld, *Phys. Rev. A*, **34**, 2477, (1986).
95 D.J. Kuizenga and A.E. Siegman, *IEEE J. Quant. Electron.*, **6**, 709, (1970).
96 G.W. Hong and J.R. Whinnery, *IEEE J. Quant. Electron.*, **5**, 367, (1969).
97 D.M. Kane, S.R. Bramwell, and A.I. Ferguson, *Appl. Phys. B*, **39**, 171, (1986).
98 P.W. Smith, *Proc. IEEE*, **58**, 1342, (1970).
99 A.H. Cook, *Interference of Electromagnetic Waves*, (Oxford: Clarendon Press, 1971), p. 101.

100 W.H. Press, B.P. Flannery, S.A. Teukolsky, and W.T. Vetterling, *Numerical Recipes. The Art of Scientific Computing*, (Cambridge: Cambridge University Press, 1986).

Appendix A. The Bias Counter Circuit

The circuit diagram for the bias counter is shown in Figure A1. The D/A converters of the current source are connected directly to the ouputs of the 4029B IC's.

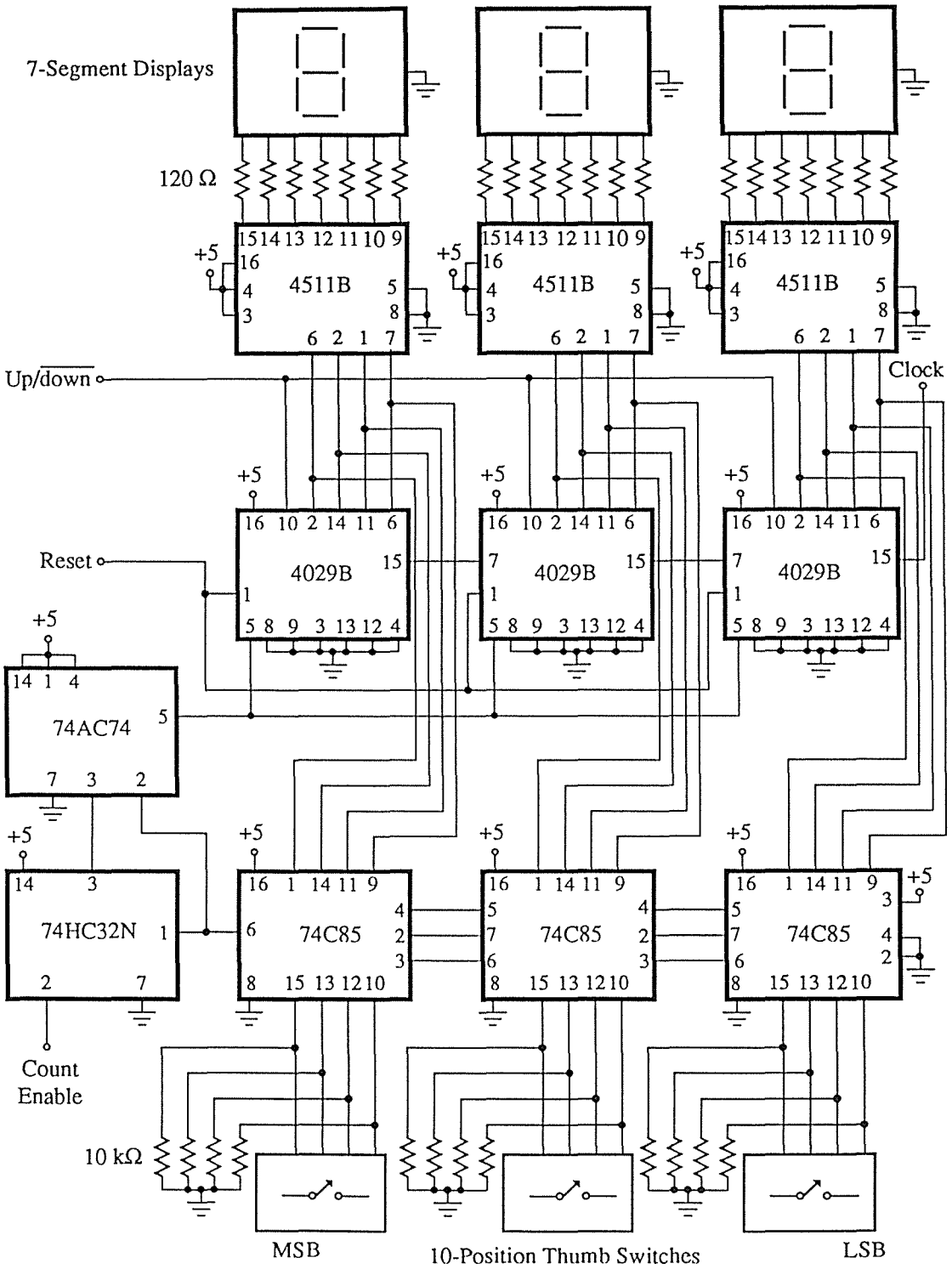

Figure A1. The bias counter circuit. The IC's are as follows—74C85: 4-bit magnitude comparitor; 4029B: synchronous up/down counter; 4511B: BCD-to-7-segment latch/decoder; 74HC32N: quad OR gate; 74AC74: D flip-flop.

Appendix *B*. Commands for the Interface

The following describes the commands required by the interface in order to access the various channels and lines, and the response made by the interface, where appropriate, in each case. The commands each consist of a control character (*A* to *R*) followed by a number of data characters and/or optional characters, and finally a carriage return. Each data byte (character) of the command contains a start bit, eight data bits, and two stop bits (no parity bit). The baud rate is hard-wired at 4800, although this can be easily changed.

(*i*) *Read Analogue Input Channel*

Control characters: $A - H$ (channels 1 – 8, respectively)

Data characters: The control character is followed by three data characters $N_2N_1N_0$, which represent in decimal the number of readings to be returned from the A/D converter via the interface. Each of N_2, N_1 and N_0 is a digit converted into ASCII (*i.e.* the range 0 – 9 in decimal becomes 48 – 57 in ASCII), where N_0 is the least significant digit.

Optional character: *L*

This is a specialised command used for scanning the laser injection current while taking readings from the A/D converter. First a 'high' (5 V) followed by a 'low' (0 V) is written to TTL output line 3 (this resets the ramp counter). Then a 'low' followed by a 'high' is written to TTL output line 4 (this increments the ramp counter) before each reading of the A/D converter is taken. The readings are stored in RAM on the interface. Finally a 'high' followed by a 'low' is again written to TTL output line 3 (this again resets the ramp counter).

If the data characters are followed directly by a carriage return, 1 – 999 conversions (depending on the values of N_2, N_1 and N_0) are performed and stored in RAM.

Response: The readings stored in RAM are sequentially returned to the computer in the order they were taken. Each reading consists of a polarity byte followed by three data bytes. The polarity byte is either ASCII 43 (+) or ASCII 42 (*, representing –). The three data bytes are returned as $D_2D_1D_0$, where D_2 is most significant, and are hexadecimal converted into ASCII (that is, each byte will have an ASCII value from 48 to 63, representing in

hexadecimal 0 to F, respectively). The data bytes can be converted into a real number X with the following formula:

$$X = \frac{256(D_2 - 48) + 16(D_1 - 48) + (D_0 - 48)}{1000}. \qquad (B1)$$

(*ii*) *Write to Analogue Output Channel*

Control character: I

Data characters: The control character is followed by three data characters then a carriage return. The data characters $D_2D_1D_0$, where D_2 is most significant, are hexadecimal numbers converted into ASCII. The real number X, to be output, must lie in the range 0 – 5 V, and can be converted to the appropriate output format by the following algorithm:

$$\begin{aligned} X' &= \mathbf{round}\left(\frac{4095X}{10}\right), \\ X'' &= X' \ \mathbf{mod}\ 256, \\ D_2 &= X' \ \mathbf{div}\ 256 + 48, \\ D_1 &= X'' \ \mathbf{div}\ 16 + 48, \\ D_0 &= X'' \ \mathbf{mod}\ 16 + 48, \end{aligned} \qquad (B2)$$

where for the real number R, **round**(R) gives the nearest integer to R, and for the non-negative integers I_1, I_2, I_3, and I_4, where $\frac{I_1}{I_2} = I_3 + \frac{I_4}{I_2}$ with $I_4 < I_2$, I_1 **div** $I_2 = I_3$, and I_1 **mod** $I_2 = I_4$.

The D/A converter has a double-buffered latch which maintains the output value and prevents the generation of spurious outputs between changes.

(*iii*) *Write to TTL Output Line*

Control characters: $J - M$ (lines 1 – 4, respectively)

Data character: The control character is followed by one data character D then a carriage return. D is either ASCII 48 (0 V) or ASCII 49 (5 V). The TTL lines maintain their values until written to again.

(*iv*) *Read TTL Input Line*

Control characters: $N - P$ (lines $1 - 3$, respectively)

The control character needs only to be followed by a carriage return. All other characters are ignored.

Response: The three lines do not all behave in the same manner. Line 3 will always contain the value on it at any time (that is, 0 or 5 V). Lines 1 and 2 are flag lines. That is, they latch 'high' only if there has been a 'low'-to-'high' transition on their respective inputs since the last time the line was read, and stay 'high' until any other channel or line of any kind is read from or written to. The interface returns one byte, either an ASCII 48 (0 V) or an ASCII 49 (5 V).

(*v*) *Read from RS232 Port*

Control character: *Q*

The control character needs only to be followed by a carriage return. All other characters are ignored.

Response: The interface reads a string of characters from the RS232 port, up to and including either a carriage return (ASCII 13), a BEL (ASCII 7), or a CAN (ASCII 24). This string is returned to the computer, with an extra carriage return for termination on a BEL or a CAN. If for approximately ten seconds no data appears on the RS232 port, the interface will stop listening and return to the computer any data already received, an ASCII 64 (@), and a carriage return.

(*vi*) *Write to RS232 Port*

Control character: *R*

Data characters: The control character can be followed by any characters up to and including a carriage return.

Response: The interface relays the data characters (including the carriage return) to the RS232 port, then executes immediately a *Q* command.

Appendix C. Interface Circuitry

In this appendix a detailed description is given of each of the constituent components of the block diagram of the interface (Figure 3.7).

(i) The Processor Board

The processor board is shown diagrammatically in Figure C1, where only the IC's and logic flow are shown. This is a standard board (designed and built by R.C. O'Driscoll and R. Dykstra, Massey University) and has been used for various research and teaching applications. The EPROM chip stores the software (up to 8 kilobytes) which controls the interface (see Appendix H). This is programmed externally and then physically placed on the board. The most important components shown in Figure C1, with respect to programming the interface, are the ACIA (Motorola MC6850 Asynchronous Communications Interface Adapter) and the two PIA's (Motorola MC6821 Peripheral Interface Adapter).

The ACIA is responsible for serial communications with peripheral devices. Internally it contains four addressable 8-bit registers which the microprocessor can either read

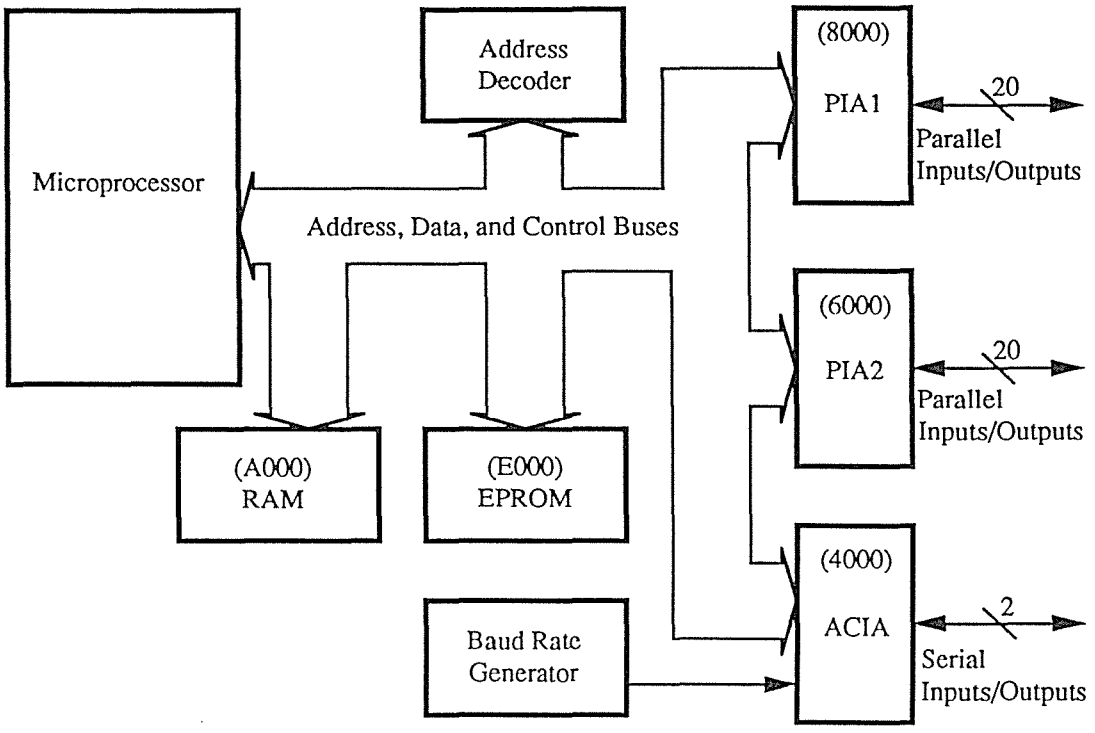

Figure C1. Block diagram of the processor board.

from or write to. Two of these registers, the Receive Data Register and the Status Register, are read-only. Data entering the ACIA from a peripheral device does so serially into a deserialiser (shift register). The data is then passed on to the Receive Data Register where it can be read by the microprocessor via the data bus. The Status Register is read by the microprocessor to obtain information on the status of the ACIA, in particular whether data has been received or transmitted successfully. The two other addressable registers inside the ACIA, the Transmit Data Register and the Control Register, are write-only. Data from the microprocessor is written to the Transmit Data Register, then passed on to a serialiser (shift register) before being sent on to a peripheral device. The Control Register is used to configure the ACIA. It can reset the ACIA, define the byte format (number of data bits and stop bits, and the inclusion of a parity bit), and enable various interrupts.

The two PIA's are responsible for parallel communications with peripheral devices. Each PIA contains six addressable 8-bit registers and four control lines, divided into two independently addressable sections, *A* and *B*. Each section has a Data Register, a Data Direction Register, a Control Register, and two control lines. The Data Direction Register is used to define each bit of the Data Register as an input or an output. Any subsequent read of the Data Register transfers to the microprocessor's data bus those bits which have been configured as inputs, and a write instruction places data onto the lines programmed as outputs. The Control Register contains write-only and read-only bits. The write-only bits are used to define the operation of the two control lines. One of these lines acts as an interrupt input flag, active on either a 'high'-to-'low' or 'low'-to-'high' transition on the line, while the other can be defined as either an interrupt input or a control output. The read-only bits of the Control Register respond to active transitions on the control lines when they are configured as interrupt inputs. In addition, one bit of the Control Register is used to address either the Data Register or the Data Direction Register, as these latter registers have the same memory address.

(ii) D/A Converter and TTL Lines

Each PIA is interfaced to peripheral devices via the following inputs and/or outputs:

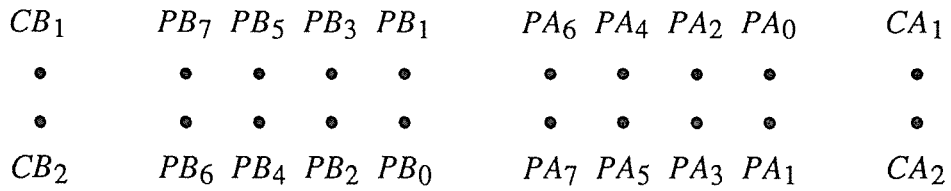

$PA_0 - PA_7$ are the Data Register A bits (PA_7 is most significant), $PB_0 - PB_7$ are the Data Register B bits, $CA_1 - CA_2$ and $CB_1 - CB_2$ are the control lines for sections A and B, respectively.

PIA1 communicates with the D/A converter and the TTL lines (and request-to-send and clear-to-send line for the serial port; however, these lines are not used). The following connections are made to PIA1 (NC stands for no connection):

SI_1	SO_4	SO_3	RTS	S	A_2	A_0	D_2	D_0	NC
•	•	•	•	•	•	•	•	•	•
•	•	•	•	•	•	•	•	•	•
SI_2	SI_3	CTS	SO_2	SO_1	A_3	A_1	D_3	D_1	NC

Outputs $D_0 - D_3$ are the data bits for the D/A converter (D_3 is most significant);
Outputs $A_0 - A_3$ are the address bits for the D/A converter;
Outputs $SO_1 - SO_4$ are the TTL output lines;
Inputs $SI_1 - SI_3$ are the TTL input lines;
Output S is the switching signal for the serial ports;
Output CTS is clear-to-send for the serial port (not used);
Input RTS is the request-to-send for the serial port (not used).

Figure C2 shows the connections of the TTL lines to the PIA. The inverters on the outputs act as buffers to prevent loading of the PIA.

D/A conversion is performed by an Analog Devices AD667JN microprocessor-compatible 12-bit D/A converter, which is configured for unipolar 10 V range output. This device includes a high stability Zener voltage reference and an on-chip output amplifier. The output is monotonic over the full operating temperature range and the maximum linearity error is $\pm\frac{1}{2}$ LSB. The 12 data bits are loaded in three sequential groups of four bits under control of the four address bits (see data sheet for more information). The output is double-buffered to prevent the generation of spurious voltages.

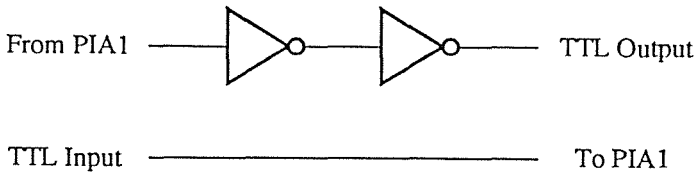

Figure C2. TTL connections to the PIA.

(iii) A/D Converter and Multiplexer

The analogue-to-digital section of the interface consists of an Intersil ICL7109 12-bit microprocessor-compatible A/D converter and a CD4097B analogue multiplexer. The multiplexer provides eight differential input channels, selected by three binary control inputs. These two components are interfaced to the microprocessor through PIA2 according to the following:

OVR	POL	B	B_{11}	B_9	B_6	B_4	B_2	B_0	STA
•	•	•	•	•	•	•	•	•	•
•	•	•	•	•	•	•	•	•	•
NC	C	A	B_{10}	B_8	B_7	B_5	B_3	B_1	R/$\overline{\text{H}}$

Inputs $B_0 - B_{11}$ are the data bits for the A/D converter (B_{11} is most significant);
Outputs $A - C$ are the control bits for the multiplexer;
Output R/$\overline{\text{H}}$ is the Run/ $\overline{\text{Hold}}$ input to the A/D converter;
Input STA is the Status output from the A/D converter;
Input POL is the Polarity output from the A/D converter ('high' if positive);
Input OVR is the Over-range output from the A/D converter ('high' if over-ranged).

A schematic of the A/D converter and multiplexer is illustrated in Figure C3. The inputs to the multiplexer, A, B, and C, control which of the analogue input channels 1 to 8 is selected according to Table C1. These lines are available directly from PIA2.

The R/$\overline{\text{H}}$ (Run/ $\overline{\text{Hold}}$) input and STA (Status) output lines to and from the A/D converter are used to control the time when a conversion takes place. Writing a 'high' to the R/$\overline{\text{H}}$ line causes the converter to initiate the conversion cycle. During the

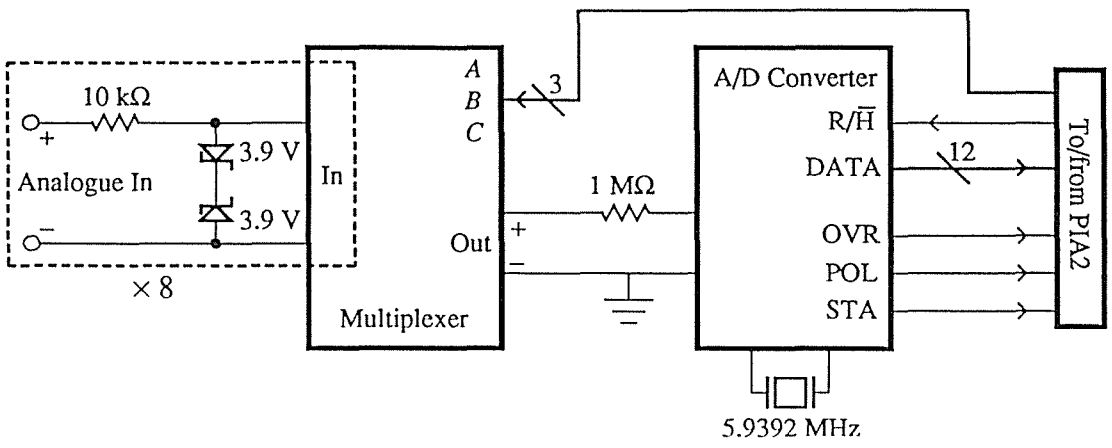

Figure C3. Schematic of the A/D converter (ICL7109) and the multiplexer (CD4097B).

C	*B*	*A*	Channel
0	0	0	1
0	0	1	2
0	1	0	3
0	1	1	4
1	0	0	5
1	0	1	6
1	1	0	7
1	1	1	8

Table *C*1. Truth table for the multiplexer.

integration the STA line is 'high', and goes 'low' when the converted data is latched. Setting the R/$\overline{\text{H}}$ line 'low' at this stage ensures minimum conversion time, and prevents the data from changing so that it can be successfully read from the DATA and POL (Polarity) lines. The OVR (Over-range) output is ignored since the input Zener diodes ensure that the input is never over-range.

The analogue ground and the digital ground were connected in order to avoid large common mode signals. This effectively references all of the analogue input channels to the same point.

(*iv*) Switching Circuit and RS232 Drivers and Receivers

A pair of 'home-made' two-channel digital multiplexers comprise the switching circuit which is used to interface the serial port of the processor board to both the Macintosh computer and the SPEX Compudrive. One of the multiplexers is responsible for the ACIA receive data line and the other for its transmit data line. A typical data frame for both TTL and RS232 levels is shown in Figure *C*4. As mentioned in Appendix *B*, this consists of a start bit, eight data bits, and two stop bits. When no data is being transmitted, the data line idles in the 'high' state. Each bit of the transmitted data frame configures the line either 'high' or 'low' for a fixed length of time determined by the baud rate. The start bit is a 'low' signal indicating to the receiving device that data will follow. The start bit also allows the clock of the receiving device to be synchronised with that of the transmitting device. The data is terminated by two 'high' stop bits,

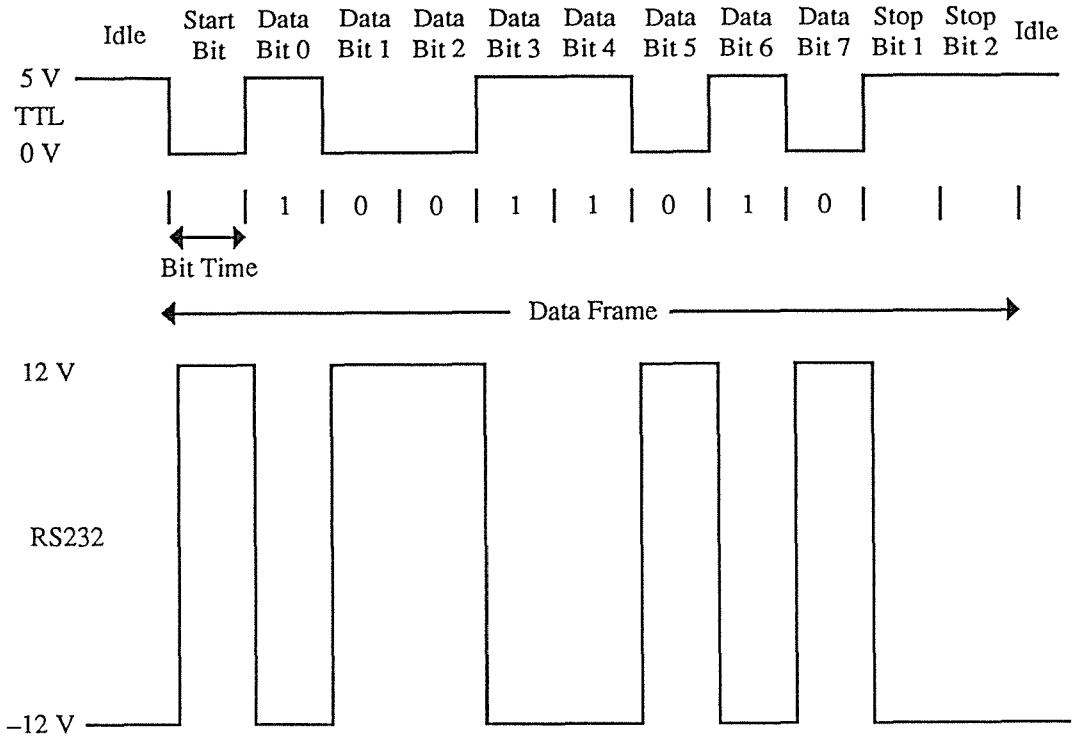

Figure C4. Data frame for the binary character 01011001 (ASCII 'Y') showing both TTL and RS232 signal levels.

after which the data line again idles 'high' until transmission of the next byte (which could immediately follow the stop bits).

The configuration of the switching circuit with respect to the ACIA and the RS232 line drivers (DS1488) and receivers (DS1489) is shown in Figure C5. The *S* input, available directly from PIA1, is used to select either the computer or the SPEX as the device in communication with the ACIA. As shown in Table C2, when *S* is 'high' the signal at point *C* is equal to that at point *A*, and likewise for points *E* and *D*, implying that the ACIA is in communication with the computer. In addition, the signal at point *F* is 'high' regardless of that at point *D*. That is, the SPEX receive data line is in its idle state. Similarly, when *S* is 'low', the ACIA is in communication with the SPEX, and the computer receive data line is in its idle state.

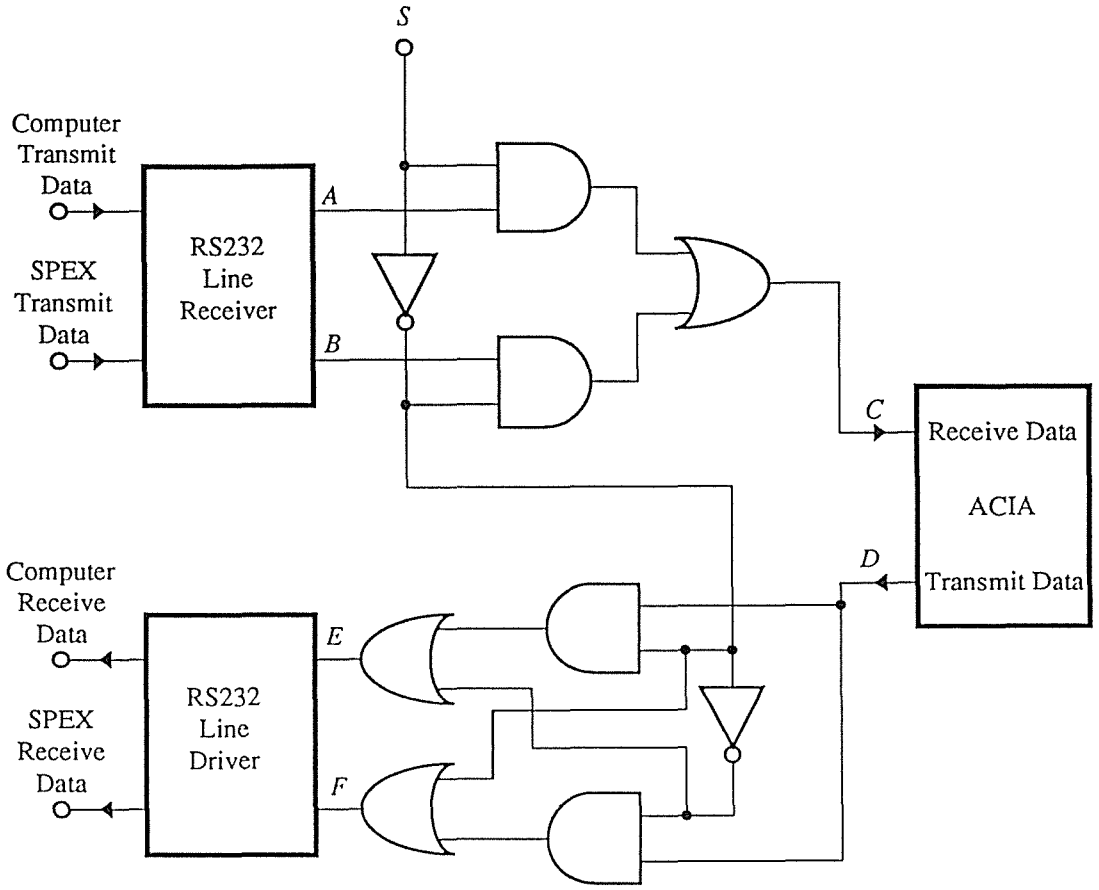

Figure C5. Switching circuit and RS232 line drivers and receivers.

S	A	B	C	D	E	F
0	0	0	0	0	1	0
0	0	1	1	1	1	1
0	1	0	0			
0	1	1	1			
1	0	0	0	0	0	1
1	0	1	0	1	1	1
1	1	0	1			
1	1	1	1			

Table C2. Truth table for the switching circuit in Figure C5.

Appendix *D*. Convolution of Two Lorentzian Profiles

The convolution of two Lorentzian profiles with FWHM's of γ_1 and γ_2, centred about ν_1 and ν_2, respectively, is performed. The result is shown to be a Lorentzian of FWHM $\gamma_1 + \gamma_2$, centred about $\nu_1 + \nu_2$. Without loss of generality, the profiles are normalised to have unit area. They are represented by

$$I_1(\nu) = \frac{1}{2\pi} \frac{\gamma_1}{(\nu - \nu_1)^2 + (\gamma_1/2)^2}, \tag{D1a}$$

and

$$I_2(\nu) = \frac{1}{2\pi} \frac{\gamma_2}{(\nu - \nu_2)^2 + (\gamma_2/2)^2}. \tag{D1b}$$

The convolution of I_1 with I_2 is performed through the following integral:

$$I_1(\nu) * I_2(\nu) = \int_{-\infty}^{\infty} I_1(\nu')\, I_2(\nu - \nu')\, d\nu'. \tag{D2}$$

Several substitutions are appropriate:

$$\gamma_1' = \frac{\gamma_1}{2}, \tag{D3a}$$

$$\gamma_2' = \frac{\gamma_2}{2}, \tag{D3b}$$

$$\nu'' = \nu' - \nu_1, \tag{D3c}$$

and

$$\Delta\nu_{12} = \nu - \nu_1 - \nu_2. \tag{D3d}$$

With these substitutions equation (*D*2) becomes

$$I_1(\nu) * I_2(\nu) = \frac{\gamma_1'\gamma_2'}{\pi^2} \times \int_{-\infty}^{\infty} \frac{1}{\left[(\nu'')^2 + (\gamma_1')^2\right]\left[(\Delta\nu_{12} - \nu'')^2 + (\gamma_2')^2\right]}\, d\nu''. \tag{D4}$$

The integrand in equation (D4) can be expanded in partial fractions to yield:

$$I_1(\nu) * I_2(\nu) = \frac{\gamma_1'\gamma_2'}{\pi^2} \times \int_{-\infty}^{\infty} \left\{ \frac{A\nu'' + B}{\left[(\nu'')^2 + (\gamma_1')^2\right]} + \frac{C(\Delta\nu_{12} - \nu'') + D}{\left[(\Delta\nu_{12} - \nu'')^2 + (\gamma_2')^2\right]} \right\} d\nu'', \quad (D5)$$

where

$$A = C = \frac{2\Delta\nu_{12}}{\left[(\Delta\nu_{12})^2 + (\gamma_2')^2 - (\gamma_1')^2\right]^2 + 4(\Delta\nu_{12})^2(\gamma_1')^2}, \quad (D6a)$$

$$B = \frac{(\Delta\nu_{12})^2 + (\gamma_2')^2 - (\gamma_1')^2}{\left[(\Delta\nu_{12})^2 + (\gamma_2')^2 - (\gamma_1')^2\right]^2 + 4(\Delta\nu_{12})^2(\gamma_1')^2}, \quad (D6b)$$

and

$$D = \frac{(\Delta\nu_{12})^2 - (\gamma_2')^2 + (\gamma_1')^2}{\left[(\Delta\nu_{12})^2 + (\gamma_2')^2 - (\gamma_1')^2\right]^2 + 4(\Delta\nu_{12})^2(\gamma_1')^2}. \quad (D6c)$$

Integration of equation (D5) gives

$$I_1(\nu) * I_2(\nu) = \frac{\gamma_1'\gamma_2'}{\pi^2} \times \left[\frac{A}{2} \ln\left[(\nu'')^2 + (\gamma_1')^2\right] + \frac{B}{\gamma_1'} \tan^{-1}\left(\frac{\nu''}{\gamma_1'}\right) - \frac{A}{2} \ln\left[(\Delta\nu_{12} - \nu'')^2 + (\gamma_2')^2\right] - \frac{D}{\gamma_2'} \tan^{-1}\left(\frac{\Delta\nu_{12} - \nu''}{\gamma_1'}\right) \right]_{-\infty}^{\infty}, \quad (D7)$$

which reduces to

$$I_1(\nu) * I_2(\nu) = \frac{\gamma_1'\gamma_2'}{\pi}\left(\frac{B}{\gamma_1'} + \frac{D}{\gamma_2'}\right). \quad (D8)$$

Substituting back from equations (D3) and (D6), equation (D8) becomes, after some algebraic manipulation,

$$I_1(\nu) * I_2(\nu) = \frac{1}{2\pi} \frac{\gamma_1 + \gamma_2}{(\nu - \nu_1 - \nu_2)^2 + [(\gamma_1 + \gamma_2)/2]^2}, \quad (D9)$$

which is a normalised Lorentzian with FWHM equal to $\gamma_1 + \gamma_2$, centred about $\nu_1 + \nu_2$.

Appendix *E*. Curve Fits of Mode-Locked Laser Spectra

A number of published frequency spectra from mode-locked lasers were digitised by hand and fitted using a non-linear fitting routine to a Gaussian profile. The maximum intensity, FWHM, and the centre frequency were treated as fitting parameters. A sample fit to data from Kuizenga and Siegman[95] is shown in Figure *E*1. Table *E*1 shows a range of results for the residuals obtained by fitting a Gaussian to several experimental spectra[95–98]. For six of the eight spectra analysed, the residuals fall within 7% of the fitted Gaussian. Taking into account the difficulty in predicting the zero level of the spectra when digitising, and the uncertainty caused by the breadth of the oscilloscope trace when the original publication data were enlarged, the fits support the theoretical prediction that the output of a mode-locked laser has a Gaussian profile.

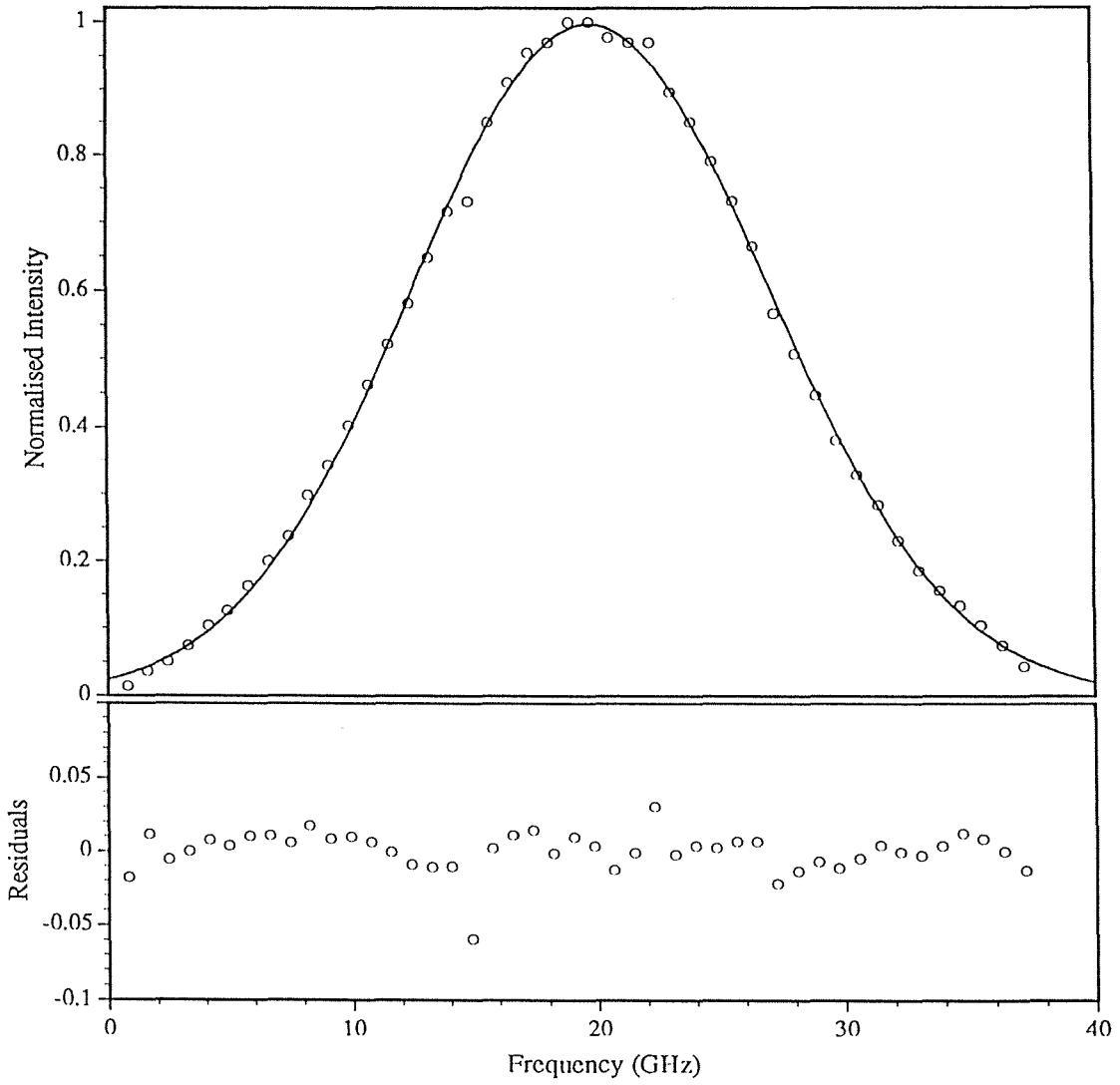

Figure *E*1. Digitised mode envelope (circles in upper plot) for a mode-locked Nd^{+++} YAG laser after Kuizenga and Siegman[95]. The solid line is a Gaussian profile fitted to the data. The lower plot shows the residuals from the fitted profile.

Reference	Range of fit (FWHM)	Range of fit (MHz)	Min. residual	Max. residual	Mean residual	Standard deviation of residuals
[95] Figure 8(*a*)	2.2	36 100	–0.059	0.031	0.00014	0.013
[95] Figure 2(*b*)	2.1	8000	–0.040	0.059	0.0040	0.028
[96] Figure 3(*b*)	2.0	1300	–0.036	0.066	0.00039	0.028
[97] Figure 4(*a*)	1.8	1500	–0.050	0.054	–0.0028	0.031
[97] Figure 4(*b*)	2.4	1400	–0.045	0.067	–0.0027	0.037
[98] Figure 19(*a*)	2.3	†	–0.061	0.129	–0.0070	0.045
[98] Figure 19(*b*)	2.3	†	–0.072	0.067	–0.0092	0.039
[98] Figure 20(*a*)	2.1	†	–0.094	0.134	–0.0072	0.048

Table *E*1. Results of fitting experimental mode-locked laser spectra to Gaussian profiles.
† FWHM and mode spacing not given.

Appendix *F*. Series Representation of the Airy Function

By considering the superposition of multiply-reflected beams emerging from a Fabry-Perot interferometer, it will be shown that the Airy function, equation (5.28), can be expressed as an infinite sum of Lorentzian profiles, each offset by one FSR with respect to the adjacent profile.

A beam with unit amplitude incident normally on two semi-transparent parallel plates emerges with amplitude[99]

$$E(\phi) = t^2 \sum_{n=0}^{\infty} r^{2n} e^{-in\phi}, \qquad (F1)$$

where t and r are the fractions of the amplitude transmitted and reflected, respectively, at each plate, ϕ is the round-trip phase change given by equation (5.29), and n represents the number of round-trips made by each component before emerging. This is a geometric series which can be summed to give

$$E(\phi) = \frac{t^2}{1 - r^2 e^{-i\phi}}. \qquad (F2)$$

The intensity of this Airy function is given by

$$I(\phi) = E(\phi)E^*(\phi) = \frac{T^2}{1 + R^2 - 2R\cos\phi}$$

$$= \frac{T^2}{(1-R)^2} \frac{1}{1 + F\sin^2(\phi/2)}, \qquad (F3)$$

where $T = t^2$ and $R = r^2$ are the intensity transmission and reflection coefficients, respectively, and F is given by equation (5.30). In the absence of absorption $T + R = 1$, and the peak intensity of equation ($F3$) is unity, in which case it is identical to equation (5.28). On the other hand, if the beam undergoes absorption at the plates then $T + R + A = 1$, where A is the intensity absorption coefficient, and the peak intensity becomes $[1 - A/(1 - R)]^2$.

Explicitly equating equations ($F1$) and ($F2$), and equating the real parts of each side of the resulting equation, gives the following expression:

$$\frac{1 - R^2}{(1-R)^2} \frac{1}{1 + F\sin^2(\phi/2)} = 1 + 2\sum_{n=1}^{\infty} R^n \cos(n\phi). \qquad (F4)$$

With the damping factor γ_A defined as in equation (5.31), the factor $(1 - R^2) / (1 - R)^2$ is equal to $\coth(\gamma_A/2)$, and thus equation (*F*4) becomes:

$$I(\phi) = \tanh(\gamma_A/2)\left(1 + 2\sum_{n=1}^{\infty} R^n \cos(n\phi)\right), \qquad (F5)$$

where it is assumed there is no absorption. (In the presence of absorption equation (*F*5) can be renormalised to have the same form.) This is in fact a Fourier expansion of the Airy function. By defining the complex variable χ by[70]

$$\chi = \phi + i\gamma_A, \qquad (F6)$$

equation (*F*5) can be rewritten as

$$I(\phi) = \tanh(\gamma_A/2)\left(1 + \sum_{n=1}^{\infty} e^{in\chi} + \sum_{n=1}^{\infty} e^{-in\chi^*}\right). \qquad (F7)$$

The two series are summed to give

$$\begin{aligned} I(\phi) &= \tanh(\gamma_A/2)\left(1 + \frac{e^{i\chi}}{1 - e^{i\chi}} + \frac{e^{-i\chi^*}}{1 - e^{-i\chi^*}}\right) \\ &= \frac{1}{2i}\tanh(\gamma_A/2)\left[\cot(\chi^*/2) - \cot(\chi/2)\right]. \end{aligned} \qquad (F8)$$

Finally, the cotangents in equation (*F*8) can be expanded into infinite series using the standard expansion[71*b*]:

$$\cot(\pi x) = \frac{1}{\pi x} + \frac{x}{\pi}\sum_{n=-\infty,\, n\neq 0}^{\infty} \frac{1}{n(x - n)}. \qquad (F9)$$

With $\pi x = \chi/2$, equation (*F*8) is expanded to give

$$I(\phi) = \frac{\tanh(\gamma_A/2)}{\gamma_A/2}\sum_{n=-\infty}^{\infty} \frac{\gamma_A^2}{(\phi - 2\pi n)^2 + \gamma_A^2}. \qquad (F10)$$

This is a sum of Lorentzian profiles, each shifted by one FSR (2π in phase terms) from the adjacent one.

Appendix G. Acousto-Optic Modulator Driver

The acousto-optic modulator is an Omnichrome Model 801, which has a fixed carrier frequency of 105 ± 0.5 MHz. It is driven using ECL logic, requiring a power supply of –5.2 V with better than 3% regulation. An ECL-compatible digital input from DC to 10 MHz is used to turn on and off the diffracted beam, while the power in this beam is controlled by a 0-V to 28-V analogue DC input. Figure G1 shows the driving circuit built for the acousto-optic modulator. The input labelled "–*V* in" must have a magnitude greater than 5.2 V.

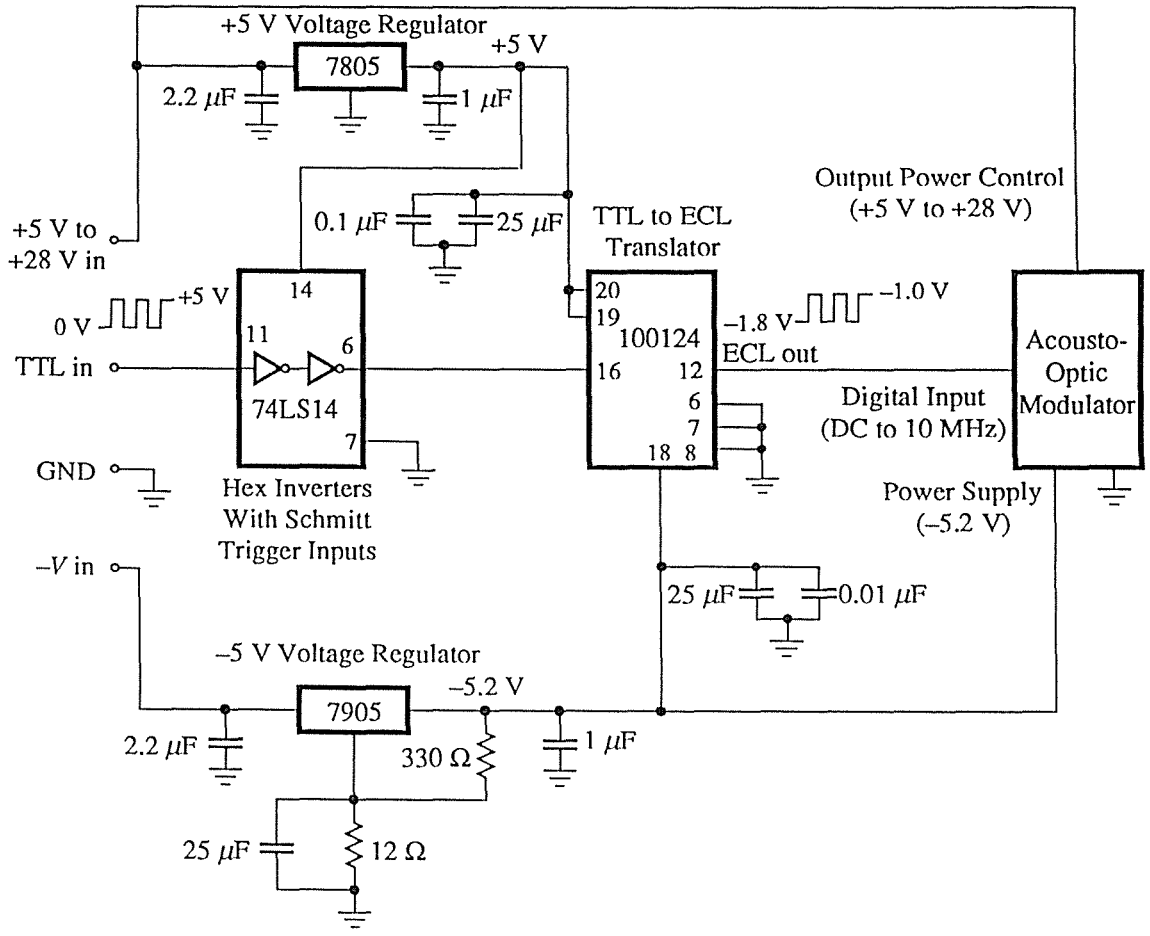

Figure G1. The acousto-optic modulator driver.

Appendix *H.* Software

The listings for the following Pascal programs (*i*) – (*iii*) can be found on disc† inside the back cover. The assembly language program (*iv*) is listed here following its description.

(*i*) Laser Control Program

This program has evolved over a period of time to carry out certain experiments as the need arose. Two main programs ("LaserControl" and "SystemTest") are listed with their accompanying common subroutine implementations. Initially the program was designed solely for the purpose of obtaining the wavelength maps described in Section 4.2. The result of this is the program "LaserControl". During the course of the development of "LaserControl", a more basic form of the program "SystemTest" was written to test each of the subroutines required for "LaserControl". Subsequently, "SystemTest" has been expanded to include other functions as required and, if necessary, can be easily added to in future.

(*ii*) Rate Equations Program

This program solves the rate equations and calculates the single-beam and two-beam spectra as discussed in Chapter 6. The routines LUDCMP and LUBKSB for the matrix inversion and subsequent linear equations' solution are taken directly from *Numerical Recipes*[100].

(*iii*) Curve Fitting Program

This program performs a non-linear fit, using the Levenberg-Marquardt method, of a choice of several different functions to a set of data, as needed for various data analyses. The routines MRQMIN, GAUSSJ, MRQCOF and COVSRT are taken directly from *Numerical Recipes*[100].

† These programs were written using the program THINK Pascal™ for the Macintosh computer. They can be opened and read using any text editor.

(*iv*) Interface Control Program

This 6809 assembly language program controls the internal operation of the interface in response to the set of commands listed in Appendix *B*.

```
*******************************************************************************
*       Program for interface to Macintosh computer.
*******************************************************************************
*
*       System Addresses.
*
ROMBEG      EQU     $F800           Beginning of ROM.
RAMBEG      EQU     $A000           Beginning of RAM.
PIA1        EQU     $8000           PIA1 base address.
P1DRA       EQU     $8000           PIA1 data register A.
P1CRA       EQU     $8001           PIA1 control register A.
P1DRB       EQU     $8002           PIA1 data register B.
P1CRB       EQU     $8003           PIA1 control register B.
PIA2        EQU     $6000           PIA2 base address.
P2DRA       EQU     $6000           PIA2 data register A.
P2CRA       EQU     $6001           PIA2 control register A.
P2DRB       EQU     $6002           PIA2 data register B.
P2CRB       EQU     $6003           PIA2 control register B.
ACIA        EQU     $4000           ACIA base address.
SCR         EQU     $4000           Serial control register (write only).
SSR         EQU     $4000           Serial status register (read only).
STDR        EQU     $4001           Serial transmit data register (write only).
SRDR        EQU     $4001           Serial receive data register (read only).
STACK       EQU     $DF50           System stack.
NUMPTS      EQU     $A7FE           Number of data points for ADC channels.
BDATA       EQU     $A000           Bottom of data.
LSCAN       EQU     $A7FD           Laser scan boolean variable.
*
*******************************************************************************
*
*  System constants.
*
P1CRAD      EQU     $04             Data for port 1 control register A.
P1CRBD      EQU     $1F             Data for port 1 control register B.
P2CRAD      EQU     $35             Data for port 2 control register A.
P2CRBD      EQU     $1F             Data for port 2 control register B.
P1DRAD      EQU     $F0             Data for port 1 data register A.
P1DRBD      EQU     $13             Data for port 1 data register B.
P2DRAD      EQU     $00             Data for port 2 data register A.
P2DRBD      EQU     $00             Data for port 2 data register B.
*
*
*******************************************************************************
*
*  Main Program.
*
            ORG     ROMBEG
*
*  Start.
*
MSTART      LEAS    STACK,PCR       Set stack pointer.
            LBSR    INIT            Initialise ports.
LOOP1       LEAY    ,S              Save the stack pointer.
            LEAS    -200,S          Allocate 200 bytes.
            LEAX    ,S              Make X point to the start of the allocated memory.
INSTLP      LBSR    INCH            Input character.
            STA     ,X+             Store character.
            CMPA    #$0D            Look for a carriage return.
            BNE     INSTLP          Get next character.
*
            LEAX    ,S              X points to start of data.
            LDA     ,X+             Get first character.
            CMPA    #$51            Look for a 'Q'.
            LBEQ    SPIN
            CMPA    #$52            Look for an 'R'.
```

```
                LBEQ    SPOUT
                CMPA    #$41            Look for an 'A'.
                LBEQ    AIN
                CMPA    #$42            Look for a 'B'.
                LBEQ    AIN
                CMPA    #$43            Look for a 'C'.
                LBEQ    AIN
                CMPA    #$44            Look for a 'D'.
                LBEQ    AIN
                CMPA    #$45            Look for an 'E'.
                LBEQ    AIN
                CMPA    #$46            Look for an 'F'.
                LBEQ    AIN
                CMPA    #$47            Look for a 'G'.
                LBEQ    AIN
                CMPA    #$48            Look for an 'H'.
                LBEQ    AIN
                CMPA    #$49            Look for an 'I'.
                LBEQ    AOUT
                CMPA    #$4A            Look for a 'J'.
                LBEQ    ASO
                CMPA    #$4B            Look for a 'K'.
                LBEQ    BSO
                CMPA    #$4C            Look for an 'L'.
                LBEQ    CSO
                CMPA    #$4D            Look for an 'M'.
                LBEQ    DSO
                CMPA    #$4E            Look for an 'N'.
                LBEQ    ASI
                CMPA    #$4F            Look for an 'O'.
                LBEQ    BSI
                CMPA    #$50            Look for a 'P'.
                LBEQ    CSI
                LBRA    LOOP2
*
SPIN            LBSR    SPEXIN          Get information from spectrometer.
                LBRA    LOOP2
SPOUT           LBSR    SPXOUT          Send information to spectrometer.
                LBRA    LOOP2
AIN             LBSR    ANIN            Read one of the analogue input channels.
                LBRA    LOOP2
AOUT            LBSR    ANOUT           Write to analogue out channel.
                LBRA    LOOP2
ASO             LBSR    ASOUT           Write to TTL out channel 1.
                LBRA    LOOP2
BSO             LBSR    BSOUT           Write to TTL out channel 2.
                LBRA    LOOP2
CSO             LBSR    CSOUT           Write to TTL out channel 3.
                LBRA    LOOP2
DSO             LBSR    DSOUT           Write to TTL out channel 4.
                LBRA    LOOP2
ASI             LBSR    ASIN            Read TTL in channel 1.
                LBRA    LOOP2
BSI             LBSR    BSIN            Read TTL in channel 2.
                LBRA    LOOP2
CSI             LBSR    CSIN            Read TTL in channel 3.
*
LOOP2           LEAS    ,Y              De-allocate the 200 bytes.
                LBRA    LOOP1
*
*******************************************************************************
*       Subroutine to initialise the PIA's and Serial Port.
*
*       PIA1 Port A.
*
INIT            CLR     P1CRA           Select data direction register A.
                LDA     #$FF
                STA     P1DRA           Set up as outputs.
                LDA     #P1CRAD
                STA     P1CRA           Set up control register A.
*
*       PIA1 Port B.
*
                CLR     P1CRB           Select data direction register B.
                LDA     #$B7
                STA     P1DRB           Set up inputs/outputs.
                LDA     #P1CRBD
```

```
                STA     P1CRB           Set up control register B.
*
*       PIA2 Port A.
*
                CLR     P2CRA           Select data direction register A.
                CLR     P2DRA           Set up as inputs.
                LDA     #P2CRAD
                STA     P2CRA           Set up control register A.
*
*       PIA2 Port B
*
                CLR     P2CRB           Select data direction register B.
                LDA     #$70
                STA     P2DRB           Set up inputs/outputs.
                LDA     #P2CRBD
                STA     P2CRB           Set up control register B.
*
*       Give initial values to PIA's.
*
                LDA     #P1DRAD
                STA     P1DRA           PIA1 port A.
                LDA     #P1DRBD
                STA     P1DRB           PIA1 port B.
                LDA     #P2DRAD
                STA     P2DRA           PIA2 port A.
                LDA     #P2DRBD
                STA     P2DRB           PIA2 port B.
*
*       Serial Port
*
                LDA     #$03            Initialise ACIA.
                STA     ACIA
                LDA     #$51
                STA     ACIA            Control register.
*
                PULS    PC              Return.
*
*******************************************************************************
*       Subroutine to dump data to either the Macintosh or the spectrometer.
*
DUMP            LEAX    -200,Y          X points to the start of the allocated memory.
                LDA     ,X+             Load the dummy character.
LOOP4           LDA     X+              Load character.
                LBSR    OUTCH           Output character.
                CMPA    #$0D            Look for carriage return.
                BNE     LOOP4           Get next character.
LBL24           PULS    PC              Return.
*
*******************************************************************************
*       Subroutine to get information from the spectrometer.
*
SPEXIN          LDA     P1DRB           Load port 1 data register B.
                ANDA    #$FD            Set bit 1 to zero.
                STA     P1DRB           Connect serial port to spectrometer.
                LEAX    -200,Y          X points to the start of the allocated memory.
                LDA     #$0D            Load dummy character.
                STA     ,X+             Store dummy character.
LOOP3           PSHS    X               Push X onto the stack.
                LDB     #$08            Start value for B (time delay).
LOOP10          LDX     #$FFFF          Start value for X (time delay).
LOOP7           LEAX    -1,X            Subtract 1 from X.
                CMPX    #$0000
                BEQ     LBL21           Branch if no more characters.
                LDA     SSR             Load serial status register.
                ANDA    #$01            Look at bit zero.
                BEQ     LOOP7           Branch if no data yet.
                LDA     SRDR            Load serial receive data register.
                PULS    X               Pull X off the stack.
                STA     ,X+             Store character.
                CMPA    #$0D            Look for a carriage return.
                BEQ     LBL1
                CMPA    #$07            Look for a BEL.
                BEQ     LBL1
                CMPA    #$18            Look for a CAN.
                BEQ     LBL1
                BRA     LOOP3           Get next character.
LBL21           DECB                    Subtract 1 from B.
```

```
                BNE     LOOP10          Continue time delay.
                BRA     LBL17           No more characters.
LBL17           PULS    X               Pull X off the stack.
                LDA     #$40            Character to indicate no more data.
                STA     X+              Store character.
LBL1            LDA     #$0D            Load a carriage return.
                STA     ,X              Store carriage return.
                LDA     P1DRB           Load port 1 data register B.
                ORA     #$02            Set bit 1 to one.
                STA     P1DRB           Connect serial port to Macintosh.
                LBSR    DUMP            Dump data to Macintosh.
                PULS    PC              Return.
*
*******************************************************************************
*       Subroutine to send information to the spectrometer.
*
SPXOUT          LDA     P1DRB           Load port 1 data register B.
                ANDA    #$FD            Set bit 1 to zero.
                STA     P1DRB           Connect serial port to spectrometer.
                LBSR    DUMP            Dump data to spectrometer.
                LBSR    SPEXIN          Get reply from spectrometer.
                PULS    PC              Return.
*
*******************************************************************************
*       Subroutine to read an analogue input channel.
*
ANIN            LEAX    -200,Y          X points to start of data.
                LDA     ,X+             Get channel.
                SUBA    #$41            Convert A to 0, B to 1, etc.
                LSLA
                LSLA
                LSLA
                LSLA
                STA     P2DRB           Choose analogue input channel.
*
* Convert three BCD inputs (no. of data points) into binary.
                LDA     #$00            Clear A.
                PSHS    A               Push A onto stack (carry sum).
                LDB     #$00            Clear B (binary sum).
                LDA     ,X              Get hundreds digit.
                SUBA    #$30            Convert from ASCII.
                STA     ,X              Store converted value.
                BEQ     LBL3            Branch if no hundreds.
LOOP13  ADDB            #$64            Add 100 to B.
                PULS    A               Get carry sum.
                ADCA    #$00            Add to carry sum.
                PSHS    A               Push A back onto stack.
                LDA     ,X              Get hundreds digit again.
                DECA                    Decrement hundreds digit.
                STA     ,X
                BNE     LOOP13          Branch if more hundreds.
LBL3            LEAX    1,X             Increment X.
                LDA     ,X              Get tens digit.
                SUBA    #$30            Convert from ASCII.
                STA     ,X              Store converted value.
                BEQ     LBL5            Branch if no tens.
LOOP14          ADDB    #$0A            Add 10 to B.
                PULS    A               Get carry sum.
                ADCA    #$00            Add to carry sum.
                PSHS    A               Push A back onto stack.
                LDA     ,X              Get tens digit again.
                DECA                    Decrement tens digit.
                STA     ,X
                BNE     LOOP14          Branch if more tens.
LBL5            LEAX    1,X             Increment X.
                LDA     ,X+             Get ones digit.
                SUBA    #$30            Convert from ASCII.
                PSHS    A               Push ones digit onto stack.
                ADDB    0,S             Add ones to B.
                PULS    A               Pull ones off stack.
                PULS    A               Pull carry sum off stack.
                ADCA    #$00            Add to carry sum.
* Double number of data count.
                LSLB
                ROLA
                ORA     #$A0            Add base address to no. pts.
                STD     NUMPTS          Store number of data points to be read.
```

```
*
                LDA     ,X              Get next character (laser scan ch.).
                STA     LSCAN           Store laser scan character.
                LDX     #BDATA          X points to bottom of data location.
*
* Reset laser scan counter if needed.
                LDA     LSCAN           Load laser scan character.
                CMPA    #$0D            Look for carriage return.
                BEQ     LBL6            Branch if not laser scan.
                LDA     #$01            Load A with 1.
                LBSR    LAS1
                LDA     #$00            Load A with 0.
                LBSR    LAS1            Reset laser scan counter.
*
* Clock laser scan counter if needed.
LOOP11          LDA     LSCAN           Load laser scan character.
                CMPA    #$0D            Look for carriage return.
                BEQ     LBL6            Branch if not laser scan.
                LDA     #$00            Load A with 0.
                LBSR    LAS2
                LDA     #$01            Load A with 1.
                LBSR    LAS2            Clock laser scan counter.
*
LBL6            LDA     P2CRA           Load port 2 control register A.
                ORA     #$08
                STA     P2CRA           Set ADC to RUN.
                LDA     P2DRA           Flush IRQA1 flag.
*
* Wait for ADC to latch data.
LOOP5           LDA     P2CRA           Load port 2 control register A.
                ANDA    #$80            Mask out all but bit 7.
                BEQ     LOOP5           Branch if STATUS flag not set.
*
* Read ADC and store value (polarity bit plus 12 data bits).
                LDA     P2CRA           Load port 2 control register A.
                ANDA    #$F7
                STA     P2CRA           Set ADC to HOLD.
                LDB     P2DRB           Read polarity bit of input.
                ANDB    #$80            Mask out all but bit 7.
                LSRB
                LSRB
                LSRB
                LDA     P2DRB           Read 4 MSB's of input.
                ANDA    #$0F            Mask out irrelevant bits.
                PSHS    B               Push B onto stack.
                ORA     0,S             Join to polarity.
                PULS    B
                LDB     P2DRA           Read 8 LSB's of input.
                STD     ,X++            Store reading.
                CMPX    NUMPTS          Enough points read?
                BLO     LOOP11          Branch if not enough points read.
*
* Reset laser scan counter if needed.
                LDA     LSCAN           Load laser scan character.
                CMPA    #$0D            Look for carriage return.
                BEQ     LBL2            Branch if not laser scan.
                LDA     #$01            Load A with 1.
                LBSR    LAS1
                LDA     #$00            Load A with 0.
                LBSR    LAS1            Reset laser scan counter.
*
* Output data to computer.
LBL2            LDX     #BDATA          Reset X to bottom of data.
LOOP12          LDA     ,X              Load polarity and 4 MSB's.
                ANDA    #$F0            Mask out 4 MSB's.
                LSRA
                LSRA
                LSRA
                LSRA
                ADDA    #$2A            Convert to ASCII (polarity, +plus, #minus).
                LBSR    OUTCH           Output polarity.
                LDA     ,X+             Load polarity and 4 MSB's again.
                ANDA    #$0F            Mask out polarity bit.
                ADDA    #$30            Convert to ASCII.
                LBSR    OUTCH           Output 4 MSB's.
                LDA     ,X              Load 8 LSB's.
                ANDA    #$F0            Mask out 4 LSB's.
```

```
            LSRA
            LSRA
            LSRA
            LSRA
            ADDA    #$30            Convert to ASCII.
            LBSR    OUTCH           Output middle 4 bits.
            LDA     ,X+             Load 8 LSB's again.
            ANDA    #$0F            Mask out middle 4 bits.
            ADDA    #$30            Convert to ASCII.
            LBSR    OUTCH           Output 4 LSB's.
            CMPX    NUMPTS          Enough points output?
            BLO     LOOP12          Branch if not enough points output.
            PULS    PC              Return.
*
*******************************************************************************
*       Subroutine to write to the analogue output channel.
*
ANOUT       LDA     ,X+             Get next character.
            CMPA    #$0D            Look for carriage return.
            BEQ     LBL8            Exit subroutine.
            SUBA    #$30            Convert from ASCII.
            ORA     #$B0
            STA     P1DRA           Enable 4 MSB's of first rank of DAC.
            ORA     #$F0
            STA     P1DRA           Latch 4 MSB's.
            LDA     ,X+             Get next character.
            CMPA    #$0D            Look for carriage return.
            BEQ     LBL8            Exit subroutine.
            SUBA    #$30            Convert from ASCII.
            ORA     #$D0
            STA     P1DRA           Enable middle 4 bits of first rank of DAC.
            ORA     #$F0
            STA     P1DRA           Latch middle 4 bits.
            LDA     ,X              Get next character.
            CMPA    #$0D            Look for carriage return.
            BEQ     LBL8            Exit subroutine.
            SUBA    #$30            Convert from ASCII.
            ORA     #$E0
            STA     P1DRA           Enable 4 LSB's of first rank of DAC.
            ORA     #$F0
            STA     P1DRA           Latch 4LSB's.
            LDA     #$70
            STA     P1DRA           Enable second rank.
            LDA     #$F0
            STA     P1DRA           Load second rank and set to no operation.
LBL8        PULS    PC              Return.
*
*******************************************************************************
*       Subroutine to write to TTL output channel 1.
*
ASOUT       LDA     ,X              Get next character.
            ANDA    #$01            Mask out all but bit 0.
            BEQ     LBL9            Branch if zero.
            LDA     P1DRB           Load port 1 data register B.
            ORA     #$01
            STA     P1DRB           Set to 1.
            BRA     LBL10           Exit subroutine.
LBL9        LDA     P1DRB           Load port 1 data register B.
            ANDA    #$FE
            STA     P1DRB           Set to 0.
LBL10       PULS    PC              Return.
*
*******************************************************************************
*       Subroutine to write to TTL output channel 2.
*
BSOUT       LDA     ,X              Get next character.
            ANDA    #$01            Mask out all but bit 0.
            BEQ     LBL11           Branch if zero.
            LDA     P1DRB           Load port 1 data register B.
            ORA     #$04
            STA     P1DRB           Set to 1.
            BRA     LBL12           Exit subroutine.
LBL11       LDA     P1DRB           Load port 1 data register B.
            ANDA    #$FB
            STA     P1DRB           Set to 0.
LBL12       PULS    PC              Return.
*
```

```
*****************************************************************************
*       Subroutine to write to TTL output channel 3.
*
CSOUT   LDA     ,X              Get next character.
LAS1    ANDA    #$01            Mask out all but bit 0.
        BEQ     LBL13           Branch if zero.
        LDA     P1DRB           Load port 1 data register B.
        ORA     #$20
        STA     P1DRB           Set to 1.
        BRA     LBL14           Exit subroutine.
LBL13   LDA     P1DRB           Load port 1 data register B.
        ANDA    #$DF
        STA     P1DRB           Set to 0.
LBL14   PULS    PC              Return.
*
*****************************************************************************
*       Subroutine to write to TTL output channel 4.
*
DSOUT   LDA     ,X              Get next character.
LAS2    ANDA    #$01            Mask out all but bit 0.
        BEQ     LBL15           Branch if zero.
        LDA     P1DRB           Load port 1 data register B.
        ORA     #$80
        STA     P1DRB           Set to 1.
        BRA     LBL16           Exit subroutine.
LBL15   LDA     P1DRB           Load port 1 data register B.
        ANDA    #$7F
        STA     P1DRB           Set to 0.
LBL16   PULS    PC              Return.
*
*****************************************************************************
*       Subroutine to read TTL input channel 1.
*
ASIN    LDA     P1CRB           Load port 1 control register B.
        ANDA    #$80
        ROLA
        ROLA
        ANDA    #$01            Clear any carry bit.
        ADDA    #$30            Convert to ASCII.
        LBSR    OUTCH           Output character.
        LDA     P1DRB           Clear flag.
        PULS    PC              Return.
*
*****************************************************************************
*       Subroutine to read TTL input channel 2.
*
BSIN    LDA     P1CRB           Load port 1 control register B.
        ANDA    #$40
        ROLA
        ROLA
        ROLA
        ANDA    #$01            Clear any carry bit.
        ADDA    #$30            Convert to ASCII.
        LBSR    OUTCH           Output character.
        LDA     P1DRB           Clear flag.
        PULS    PC              Return.
*
*****************************************************************************
*       Subroutine to read TTL input channel 3.
*
CSIN    LDA     P1DRB           Load port 1 data register B.
        ANDA    #$40
        ROLA
        ROLA
        ROLA
        ANDA    #$01            Clear any carry bit.
        ADDA    #$30            Convert to ASCII.
        LBSR    OUTCH           Output character.
        PULS    PC              Return.
*
*****************************************************************************
*       Subroutine to input a character from Macintosh or spectrometer.
*
INCH    LDA     SSR             Load serial status register.
        ANDA    #$01            See whether there's any data to read.
        BEQ     INCH            Branch if no data yet.
        LDA     SRDR            Load data from receive data register.
```

```
                PULS    PC                      Return.
*
*******************************************************************************
*
*       Subroutine to output a character to Macintosh or spectrometer.
*
OUTCH           STA     STDR                    Put data into transmit data register.
LOOP6           LDB     SSR                     Load serial status register.
                ANDB    #$02                    Look at second bit.
                BEQ     LOOP6                   Branch if data not yet sent.
                PULS    PC                      Return.
*
*******************************************************************************
*
*       Interrupt Subroutine  (Default).
*
INTD            RTI                             Return from interrupt.
*
*******************************************************************************
*
*     Vectors
*
VSTART          ORG     $FFF0                   Start of hardware vectors.
                FDB     INTD                    Reserved.
                FDB     INTD                    Software interrupt 3.
                FDB     INTD                    Software interrupt 2.
                FDB     INTD                    Fast interrupt request.
                FDB     INTD                    Interrupt request.
                FDB     INTD                    Software interrupt.
                FDB     INTD                    Non maskable interrupt.
                FDB     MSTART                  Reset.
*
*******************************************************************************
*
                END
*
*******************************************************************************
```

Appendix *I*. Publications

(*i*) Refereed Articles

P. Saunders and D.M. Kane, *J. Mod. Opt.*, **35**, 1801, (1988).
Calculation of spectral linewidths from measured fringe visibility using a Fabry-Perot interferometer.

P. Saunders and D.M. Kane, *Rev. Sci. Instrum.*, **63**, 2141, (1992).
A driver for stable-frequency operation of laser diodes.

(*ii*) Poster Presentations

P. Saunders, D.M. Kane, and R. Dykstra, *An automated system for wavelength characterisation of an AlGaAs diode laser*, presented at the Australian Conference on Lasers, Optics and Spectroscopy, Adelaide, Australia, 1989.

P. Saunders and D.M. Kane, *Heterodyne experiment to determine the frequency stability of an injection current- and temperature-stabilised diode laser*, presented at the Australian Conference on Lasers, Optics and Spectroscopy, Adelaide, Australia, 1989.

P. Saunders and D.M. Kane, *Calculation of spectral linewidths from measured fringe visibility using a Fabry-Perot interferometer*, presented at the Australian Conference on Lasers, Optics and Spectroscopy, Adelaide, Australia, 1989.

D.M. Kane, P. Saunders, and D.M. Warrington, *Application of a fiber optic Fabry-Perot interferometer to frequency calibration and stabilisation of a single frequency dye laser*, presented at the Australian Conference on Lasers, Optics and Spectroscopy, Adelaide, Australia, 1989.

P. Saunders and D.M. Kane, *Frequency stabilisation of an AlGaAs diode laser for use as a spectroscopic source*, presented at the New Zealand Institute of Physics Conference, Palmerston North, 1990.

P. Saunders, *Determination of caesium* $6^2S_{1/2}$ *ground state relaxation rate*, presented at the New Zealand Institute of Physics Conference, Auckland, 1992.

JOURNAL OF MODERN OPTICS, 1988, VOL. 35, NO. 11, 1801–1812

Calculation of spectral linewidths from measured fringe visibility using a Fabry–Perot interferometer

P. SAUNDERS and D. M. KANE

Department of Physics and Biophysics, Massey University, Palmerston North, New Zealand

(*Received 1 March 1988; revision received 10 June 1988*)

Abstract. An analysis is presented which allows the spectral linewidth of a light source with a pure Gaussian or a pure Lorentzian spectral profile to be calculated from the measured visibility of the transmission fringes of a scanning Fabry–Perot interferometer. The linewidth is expressed in terms of the free spectral range of the interferometer and hence the result is general and may be applied to any interferometer. The relationship between fringe visibility and spectral linewidth has an analytic form for complete profiles. In addition, the method is applied to truncated spectral profiles, which may provide a more appropriate model for the spectral profile of some lasers, and the differences are characterized. Linewidths up to 2 times the free spectral range for Lorentzian and 1·3 times for Gaussian envelopes are measurable using these techniques.

1. Introduction

A large amount of research has been carried out on the use of the Fabry–Perot interferometer (FPI) to resolve atomic emission line spectra for such applications as isotope shift and hyperfine splitting measurements, and the investigation of line broadening processes. This in general involves deconvolution of the instrumental line (Airy) function to obtain the Voigt profile of the line under study. In some cases, it is possible to approximate the Voigt profile by a Gaussian, if Doppler broadening is the dominant broadening process, or a Lorentzian, if natural/pressure broadening is dominant. In all these cases, it is important that the spacing of the FPI is such that its free spectral range (FSR) is significantly larger than the linewidth of the spectral line. In the present analysis, which has been motivated by the use of a FPI to measure laser linewidths which are of the order of the FSR of the interferometer, it is shown that the linewidth of a Gaussian or Lorentzian profile can be calculated from the measured fringe visibility when the profile is not fully resolved.

The fringe visibility is defined as

$$V=\frac{I_{\max}-I_{\min}}{I_{\max}+I_{\min}}, \tag{1}$$

where $I_{\max}$ and $I_{\min}$ are the maximum and minimum intensities transmitted by the FPI, respectively. The transmitted intensity of the FPI is monitored, using a linear photodetector, as the interferometer is piezo-electrically or pressure scanned. This intensity is a superposition of an infinite number of transmission peaks (fringes), each shifted by one FSR with respect to the adjacent fringe. If we assume a high

finesse for the interferometer, the lineshape of the transmission fringes will be determined, to good accuracy, by the spectral distribution of the light source and the degree of overlap of adjacent fringes [1]. Interferometers with a finesse in excess of 20 000 are available [2].

The analysis is applicable to spectral emission lines which are well approximated by a single Gaussian or Lorentzian lineshape and to some lasers. For example, the intensities of the modes of a mode-locked laser are predicted to have a Gaussian frequency distribution [3]. This is well supported by fitting the mode intensities of practical mode-locked lasers to a Gaussian (Appendix). For the analysis to apply to such mode-locked lasers, it is also necessary that the longitudinal modes are numerous and closely spaced in frequency relative to the FSR of the interferometer, so that they provide an essentially continuous frequency distribution. Single mode lasers may be approximated by a Lorentzian lineshape, as may, to a first approximation, some multi-mode homogeneously broadened lasers which also satisfy the condition for number and spacing of longitudinal modes previously stated for mode-locked lasers [4].

In the analysis, it is the intensity of light transmitted in each order, for a given FPI spacing, that is summed. This is justified in the following discussion. Adjacent orders transmit light that is different in frequency by one FSR. If the light is incoherent, there is no interference between the different frequencies and the total transmitted intensity is obtained by adding the individual intensities. If the light is coherent then interference fringes at the mean of any two frequencies modulated by beating at half the difference frequency will occur and, therefore, it is the amplitudes which must be added. When many frequencies are present, the interference and beating effects will tend to be averaged out. Also, as all the frequencies are derived from a single light source, the light is only partially coherent and only partial interference will be observed. When the transmitted light of the FPI is being monitored, a photodetector with a response time which is very long compared with the beat period and interference period is used. Thus, it is the average intensity which is measured. The average intensity is the sum of the individual intensities.

The first part of the analysis calculates the fringe visibility as a function of the linewidth of a complete Lorentzian or a complete Gaussian profile. The linewidth is expressed as a multiple of the FSR of the interferometer used and, therefore, is applicable to any interferometer.

When measuring the linewidth of a laser light source, it may be observed that the mode envelope is better modelled by a truncated Lorentzian or Gaussian because of the finite number of modes that lase, corresponding to the laser cavity modes. For this reason, the analysis is repeated for truncated profiles. There are significant and unexpected differences in the results, which will allow truncated profiles to be easily identified in practical lasers if they occur.

The curves of fringe visibility as a function of linewidth obtained from the analysis allow linewidths up to 2 times the FSR of the interferometer to be measured for a Lorentzian profile and up to 1·3 times the FSR for a Gaussian profile. For the complete profiles, I_{max} always occurs at the position of a transmission peak of the interferometer and I_{min} is always at the midpoint between adjacent transmission peaks. The fringe pattern for the truncated profiles is rather more complicated, but follows a systematic progression. The visibility curves show unexpected regions of increasing visibility with linewidth beyond the limits stated when truncated profiles are used.

2.1. *Lorentzian envelope*

The frequency dependence of a Lorentzian envelope is given by

$$L(\Delta\nu)=\frac{\gamma^2/4}{(\Delta\nu)^2+(\gamma^2/4)}, \tag{2}$$

where γ is the full width at half maximum (f.w.h.m.) and $\Delta\nu$ is the frequency offset from the line centre. We now write the linewidth γ as a multiple of the FSR

$$\gamma=p\times\mathrm{FSR}, \tag{3}$$

where p is a positive real number. The maximum fringe intensity $I_{\max}$ is a sum of expressions like (2) with each $\Delta\nu$ an integer multiple of the FSR

$$I_{\max}=\sum_{k=-\infty}^{\infty}\frac{p^2/4}{k^2+(p^2/4)}=\sum_{k\,\mathrm{even}}\frac{p^2}{k^2+p^2}. \tag{4}$$

This is independent of the FSR of the interferometer and hence is valid for any interferometer. Likewise, $I_{\min}$ is obtained from (2) with each $\Delta\nu$ a half odd integer multiple of the FSR

$$I_{\min}=\sum_{k=-\infty}^{\infty}\frac{p^2/4}{(k-\frac{1}{2})^2+(p^2/4)}=\sum_{k\,\mathrm{odd}}\frac{p^2}{k^2+p^2}. \tag{5}$$

The infinite series

$$\sum_{k=-\infty}^{\infty}\frac{p^2}{k^2+p^2} \tag{6}$$

may be summed with the aid of Poisson's summation formula [5] which relates the sum of a function ϕ to the sum of its Fourier transform $\hat{\phi}$

$$\sum_{k=-\infty}^{\infty}\phi(k\lambda)=\frac{1}{|\lambda|}\sum_{n=-\infty}^{\infty}\hat{\phi}\left(\frac{2\pi n}{\lambda}\right). \tag{7}$$

If we consider the function

$$\phi(k\lambda)=\frac{1}{1+(k\lambda)^2}, \tag{8}$$

and put $\lambda=1/p$, then the series on the left-hand side of (7) becomes the series (6), and the series on the right-hand side is a geometric series. This gives

$$\sum_{k=-\infty}^{\infty}\frac{p^2}{k^2+p^2}=\pi p\coth(\pi p) \tag{9}$$

and hence

$$I_{\max}=\frac{\pi p}{2}\coth\left(\frac{\pi p}{2}\right). \tag{10}$$

$I_{\min}$ is obtained from the fact that

$$\sum_{k=-\infty}^{\infty}\frac{p^2}{k^2+p^2}=\sum_{k\,\mathrm{even}}\frac{p^2}{k^2+p^2}+\sum_{k\,\mathrm{odd}}\frac{p^2}{k^2+p^2}. \tag{11}$$

Thus

$$I_{\min}=\pi p\coth(\pi p)-\frac{\pi p}{2}\coth\left(\frac{\pi p}{2}\right) \tag{12}$$

and, hence,

$$V=\frac{I_{\max}-I_{\min}}{I_{\max}+I_{\min}}=\frac{2x}{1+x^2}, \tag{13}$$

where $x=\exp(-\pi p)$ (or $x=\exp(\pi p)$ since V is an even function).

2.2. *Gaussian envelope*

A Gaussian profile has the form

$$G(\Delta\nu)=\exp\left\{\frac{-4\ln 2\,(\Delta\nu)^2}{\Delta\nu_D^2}\right\}=2^{-4(\Delta\nu)^2/\Delta\nu_D^2}, \tag{14}$$

where $\Delta\nu_D$ is the f.w.h.m., which we write as $\Delta\nu_D=p\times\mathrm{FSR}$.

From equation (14) we obtain

$$I_{\max}=\sum_{k=-\infty}^{\infty}\exp[-4\ln 2\,(k^2/p^2)]=1+2\sum_{k=1}^{\infty}2^{-4k^2/p^2} \tag{15}$$

and

$$I_{\min}=\sum_{k=-\infty}^{\infty}\exp[-4\ln 2(k-\tfrac{1}{2})^2/p^2]=2\sum_{k=1}^{\infty}2^{-4(k-1/2)^2/p^2}. \tag{16}$$

These two infinite series cannot be expressed analytically. However, they occur frequently enough in mathematics to form part of a set of special functions called theta functions. There are four such functions each of which is defined as a function of a variable z and a parameter q, where $|q|<1$ [6]. The two theta functions of interest here are

$$\theta_2(z,q)=\sum_{n=-\infty}^{\infty}q^{(n+1/2)^2}\exp[(2n+1)\mathrm{i}z] \tag{17}$$

and

$$\theta_3(z,q)=\sum_{n=-\infty}^{\infty}q^{n^2}\exp(2n\mathrm{i}z). \tag{18}$$

From these, we obtain

$$I_{\max}=\theta_3(0,q) \tag{19}$$

and

$$I_{\min}=\theta_2(0,q), \tag{20}$$

where

$$q=2^{-4/p^2}. \tag{21}$$

Therefore

$$V=\frac{I_{max}-I_{min}}{I_{min}+I_{min}}$$
$$=\frac{\theta_3-\theta_2}{\theta_3+\theta_2}$$
$$=\frac{1-2(y-y^4+y^9-y^{16}+y^{25}-\ldots)}{1+2(y+y^4+y^9+y^{16}+y^{25}+\ldots)}, \quad (22)$$

where

$$y=2^{-1/p^2}. \quad (23)$$

Note, however, that the 2^{-n^2} terms cause the numerator and denominator of (22) to converge very rapidly, so that taking terms up to y^{16} gives the visibility accurate to three decimal places for the whole range of p values between 0 and 1·5. (The smaller values of p in this range have an accuracy of up to nine decimal places.)

2.3. *Visibility curves*

Figure 1 gives a plot of fringe visibility against p for both the Lorentzian and Gaussian cases. When the visibility is unity, the linewidth may be measured directly from the interferometer transmission fringe-width. For smaller visibilities, the

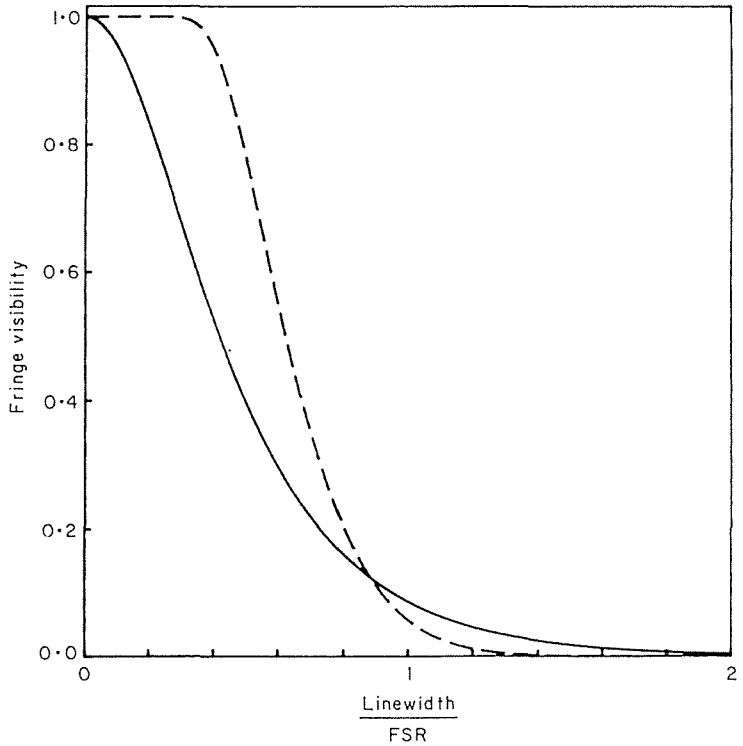

Figure 1. Fringe visibility as a function of the linewidth expressed in multiples of the FSR of an interferometer for a Lorentzian (solid line) and Gaussian (dashed line) profile.

curves in figure 1 can be used to obtain the linewidth as a multiple of the interferometer FSR, using the measured fringe-visibility. The range of linewidths for which the uncertainty in p is less than that in the visibility can be found by calculating dV/dp. For the Lorentzian case, the uncertainty in p will be less than or equal to that of V for values of p in the range 0·1 to 0·6, while for the Gaussian case this range is 0·4 to 0·85.

3. Truncated Lorentzian and Gaussian envelopes

If the Lorentzian or Gaussian envelopes are cut off at a truncation value, the resulting linewidth is reduced as shown in figure 2. A more significant effect, however, is that the infinite series previously obtained for the fringes now become finite series. A direct mathematical analysis of these finite series is very complex since the number of terms in each series varies with p and the truncation value t. A simpler approach is to generate these series on a computer for different values of p and t. The following analysis is carried out using the full Lorentzian and Gaussian linewidths. The reduced linewidths are then calculated from these.

The fringe pattern for both the Lorentzian and Gaussian cases is similar and follows a definite pattern as p increases. For small values of p, the fringes are of a similar shape to those for the untruncated case (figure 3 (*a*)), thus reflecting the line-shape exactly, since this is the region where no overlap of fringes occurs. (Note, the intensity scales of the curves in figure 3 have been normalized to give only the 'a.c.' components of the fringe pattern.) As p increases, the fringes begin to overlap in the wings, and thus the bases of the resulting fringe pattern increase leaving the peaks

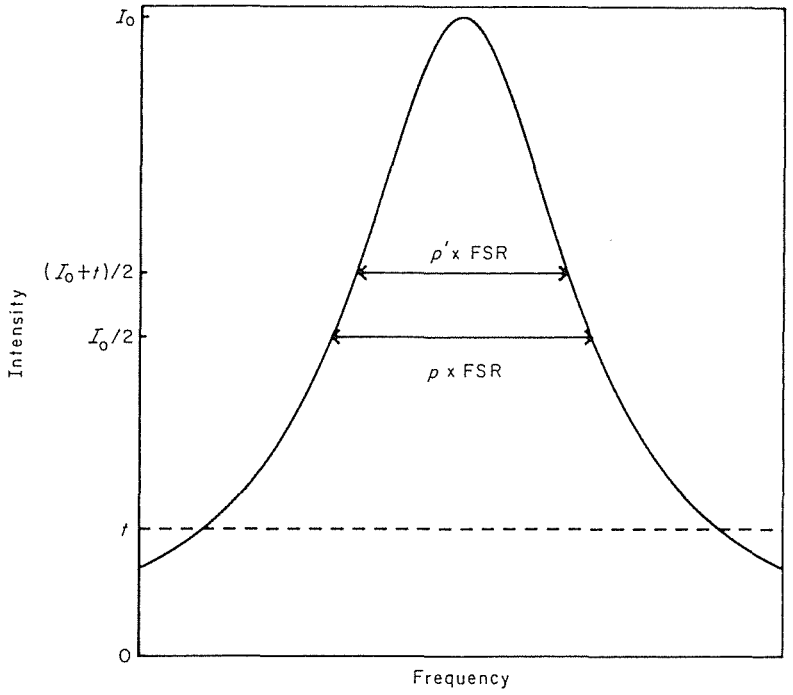

Figure 2. Lorentzian or Gaussian profile showing the full linewidth $p \times$ FSR and the reduced linewidth $p' \times$ FSR for a truncation value of t.

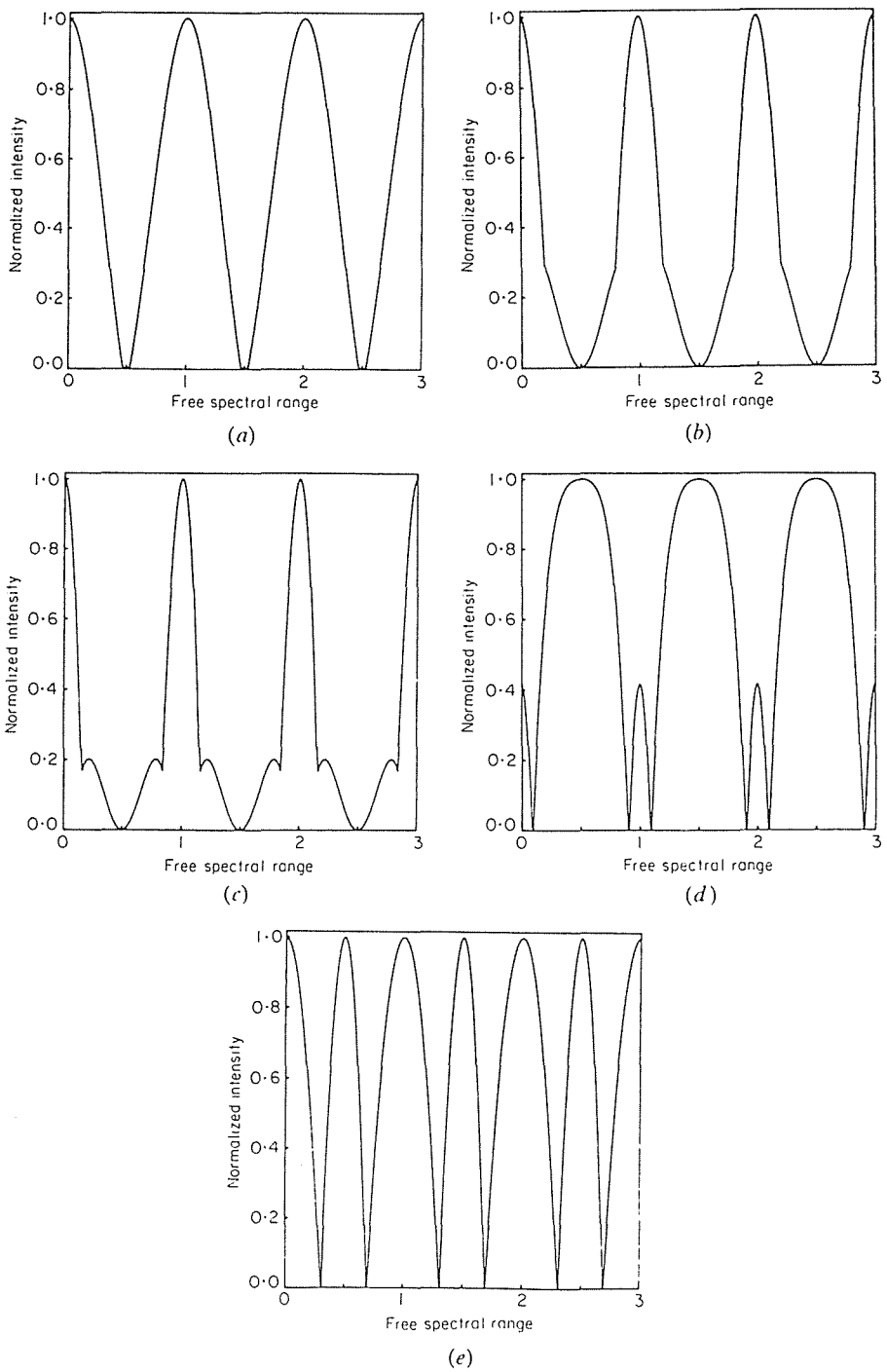

Figure 3. 'a.c.' components of the fringe pattern calculated for a Gaussian profile with a truncation value of 0·2. The reduced linewidths are $p' = 0{\cdot}6$, 0·9, 0·95, 1·02, 1·4755, respectively. The plots represent the output of an interferometer scanned over three FSRs. The intensity is normalized so that $I_{max} - I_{min} = 1$. (I_{max}, I_{min}) are: (*a*) (0·8, 0·08); (*b*) (0·8, 0·66); (*c*) (0·8, 0·73); (*d*) (0·82, 0·78); and (*e*) (1·18, 1·15).

undisturbed. This causes the slope of the lower part of the pattern to decrease as shown in figure 3 (*b*).

The fringes first overlap at

$$p=\left(\frac{t}{1-t}\right)^{1/2} \tag{24}$$

for Lorentzian line-shapes, and

$$p=\left(\frac{-\ln 2}{\ln t}\right)^{1/2} \tag{25}$$

for Gaussian line-shapes.

As p increases further, the number of line-shapes contributing to the fringe pattern differs across one FSR. At any point, this number will increase by one as the successive line-shape orders become non-zero at that point. However, at the peaks corresponding to the transmission-maxima of the interferometer, and midway between these peaks, the number of contributing line-shapes periodically increases by two due to the symmetry of these points. The resulting fringe pattern reflects this non-uniformity by a correspondingly non-uniform growth. Two peaks develop on the sides of the main peak, at about $p=1{\cdot}9$ for the Lorentzian case and about $p=1{\cdot}1$ for the Gaussian, for a truncation value of $t=0{\cdot}2$ (figure 3 (*c*)). These peaks increase in intensity relative to the main peak and also shift closer together. The relative amplitude of these two new peaks in comparison with the 'transmission-maxima' peaks is greater for Lorentzian than Gaussian envelopes. However, the absolute amplitude, in both cases, is very small and it would be difficult to observe these peaks when the interferometer is scanned. The appearance of these additional peaks is due solely to the way in which the truncated line-shapes superpose. Increasing p further causes these two peaks to appear to merge, leaving a single peak midway between each successive pair of 'transmission-maxima' peaks (figure 3 (*d*)). From this point on, as p increases, the 'transmission-maxima' and 'transmission-minima' peaks oscillate in amplitude, 180° 'out of phase' relative to each other. This oscillation occurs due to the increase of the two contributing line-shapes, as mentioned above. This increase takes place alternately between 'transmission-maxima' and 'transmission-minima' positions, and, because of the different symmetry of the two positions, one always has one more contributing line-shape than the other, hence the oscillation. The preceding 'anomalous' behaviour is more prominent for higher values of t. When the two peaks are of equal intensity, one could mistakenly identify the intermediate peak as a transmission-maximum of the interferometer and conclude that the linewidth is larger, by a factor of two, than it actually is. However, figure 3 (*e*) shows that in this case the widths of the two peaks are not equal.

For a truncation value of t, the reduced linewidth p' for a Gaussian envelope, as a function of the FSR, is

$$p'=p\left(\frac{-\ln[(1+t)/2]}{\ln 2}\right)^{1/2}. \tag{26}$$

The visibility curve for any value of t is similar to the untruncated curve up to a linewidth of one FSR. For larger linewidths, small bumps appear at about $t\geqslant 0{\cdot}02$ due to the oscillating 'transmission-maxima' peaks. The solid line in figure 4 (*a*) is the fringe visibility with I_{max} taken to be the intensity of the peaks corresponding to the

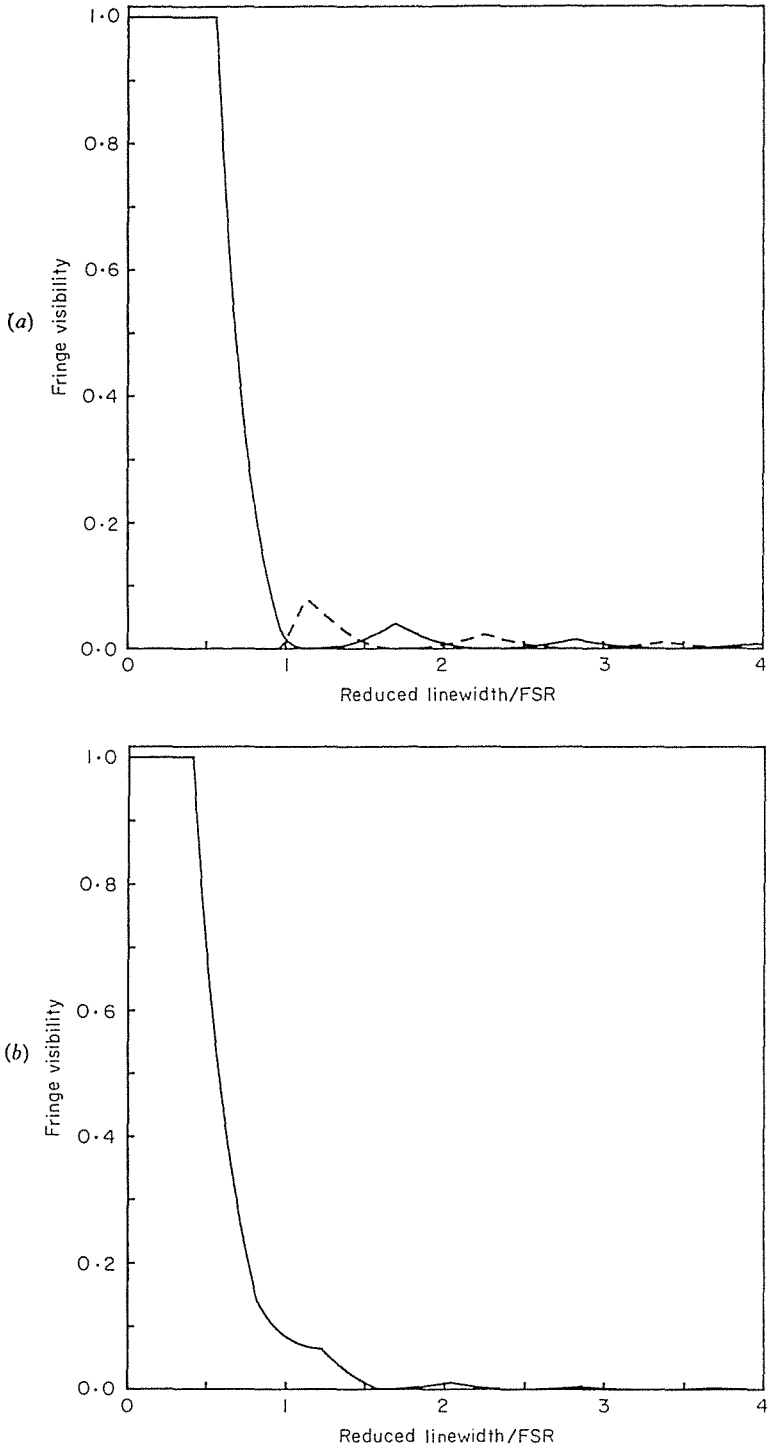

Figure 4. Fringe visibility, with a truncation value of 0·2, as a function of the reduced linewidth expressed in multiples of the FSR of an interferometer for (*a*) a Gaussian and (*b*) a Lorentzian profile. The solid line in (*a*) gives the 'transmission-maximum' visibility, while the dashed line gives the 'transmission-minimum' visibility.

positions of the transmission maxima of the interferometer. This value is not necessarily the maximum intensity, as is indicated in figure 3. The 'transmission minimum' fringe visibility, where I_{max} is the intensity of the intermediate peak, is given by the dashed line in figure 4 (*a*). The two curves demonstrate the oscillatory nature of the fringes.

The reduced Lorentzian linewidth is given by

$$p' = p\left(\frac{1-t}{1+t}\right)^{1/2}. \tag{27}$$

The visibility curves show, as expected, a flat portion for small linewidths (figure 4 (*b*)), since a truncated Lorentzian resembles the form of a Gaussian. The curves drop to zero at approximately the same linewidth as the curves for the complete profiles, but at a faster rate for larger truncation values. The visibility begins to oscillate at about $t = 0{\cdot}1$. The 'transmission minimum' fringe visibility in this case is effectively zero over the entire range of linewidths shown in figure 4 (*b*) and is therefore insignificant.

4. Conclusion

It has been shown that measurements of fringe visibility using a scanning FPI can be used to determine the linewidth of a Lorentzian or Gaussian atomic emission profile or a laser mode envelope. The linewidth is expressed as a multiple of the FSR of the interferometer. When a complete profile is modelled, visibility can be written explicitly as a function of spectral linewidth. However, the inverse function would require an algorithmic approach and numerical solution. The information is available in a graphical form, but the accuracy is determined by how well one can measure the fringe visibility. An accuracy of 5% is typical.

When the visibility of the fringes is unity, the spectral width can be measured directly as the f.w.h.m. of the transmitted intensity profile. For a Gaussian profile, this occurs for spectral widths up to 0·33 times the FSR and for a Lorentzian only up to about 0·04 times the FSR. Thus, for the Lorentzian case, the linewidth can only be obtained directly, without correction, when the linewidth is very small compared with the FSR. This fact reinforces the usefulness of the analysis presented here.

In modelling a truncated Lorentzian or Gaussian profile, a graph of fringe visibility against linewidth was produced by computer calculation. This results in the prediction of unexpected peaks in the transmission of the FPI which occur at the usual 'transmission-minimum' frequencies. These 'transmission-minima' peaks increase in visibility as the usual 'transmission-maxima' peaks decrease. An oscillatory behaviour for these two visibilities is predicted. At the same time, the structure of the fringe pattern goes through a systematic series of changes. These features provide a means of testing for truncation of the line profile when a laser linewidth is being measured. We will be in a position, in the near future, to test the predictions of this analysis experimentally.

Appendix

A number of published frequency spectra from mode-locked lasers have been digitized by hand and fitted using a nonlinear fitting routine to a Gaussian line profile. The maximum intensity, full width at half maximum (f.w.h.m.) and the

centre frequency are treated as fitting parameters. A sample fit to data from Kuizenga and Siegman (figure 8 (*a*) in [7]) is shown in figure 5. The table shows a range of results for the residuals obtained by fitting a Gaussian to several experimental spectra [7–10]. For six of the eight spectra analysed, the residuals fall within 7% of the fitted Gaussian. Taking into account the difficulty in predicting the zero level of

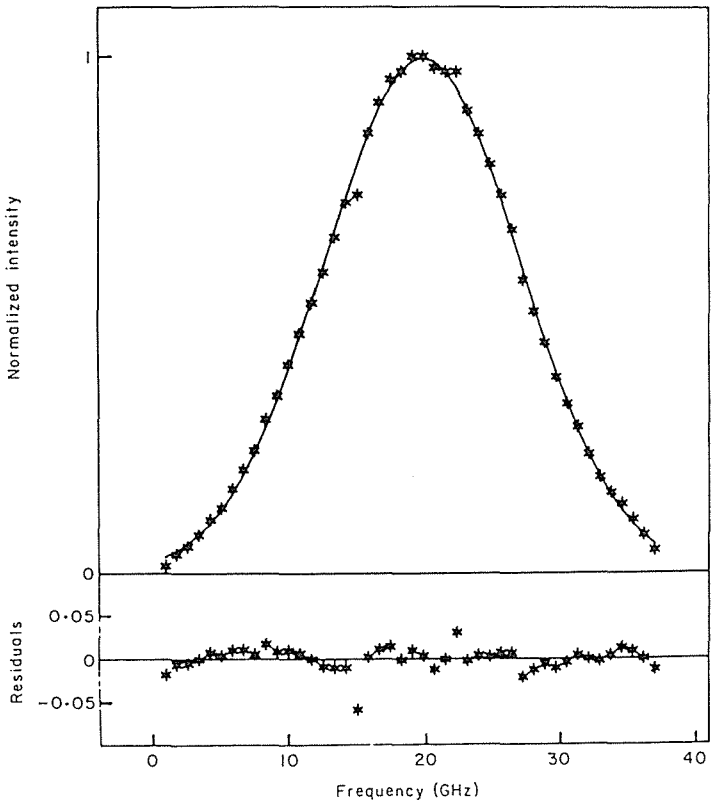

Figure 5. Digitized mode envelope for a mode-locked Nd^{+++} YAG laser (*) after Kuizenga and Siegman [7] and the fitted Gaussian. The residuals are shown in the lower portion of the figure.

Results of fitting experimental mode-locked laser spectra to a Gaussian line profile.

Reference	Range of fit (f.w.h.m.)	Range of fit (MHz)	Minimum residual	Maximum residual	Mean residual	Standard deviation of residuals
Figure 8 (*a*) [7]	2·2	36 100	−0·059	0·031	$1{\cdot}4 \times 10^{-4}$	0·013
Figure 2 (*b*) [7]	2·1	8000	−0·040	0·059	$4{\cdot}0 \times 10^{-3}$	0·028
Figure 3 (*b*) [8]	2·0	1300	−0·036	0·066	$3{\cdot}9 \times 10^{-4}$	0·028
Figure 4 (*a*) [9]	1·8	1500	−0·050	0·054	$-2{\cdot}8 \times 10^{-3}$	0·031
Figure 4 (*b*) [9]	2·4	1400	−0·045	0·067	$-2{\cdot}7 \times 10^{-3}$	0·037
Figure 19 (*a*) [10]	2·3	†	−0·061	0·129	$-7{\cdot}0 \times 10^{-3}$	0·045
Figure 19 (*b*) [10]	2·3	†	−0·072	0·067	$-9{\cdot}2 \times 10^{-3}$	0·039
Figure 20 (*a*) [10]	2·1	†	−0·094	0·134	$-7{\cdot}2 \times 10^{-3}$	0·048

† FWHM and mode spacing not given.

the spectra when digitizing, and the uncertainty caused by the breadth of the oscilloscope trace when the original publication data are enlarged, the fits support the theoretical prediction that the output of a mode-locked laser has a Gaussian line profile.

Acknowledgment

We wish to thank Professor G. C. Wake, Department of Mathematics and Statistics, Massey University for helpful discussions on infinite series and for pointing out the relevant material contained in references [5] and [6].

References

[1] KANE, D. M., 1988 (unpublished results).
[2] DE VOE, R. G., and BREWER, R. G., 1985, *Laser Spectroscopy VII* (Berlin, Heidelberg: Springer-Verlag), pp. 358–361.
[3] SIEGMAN, A. E., and KUIZENGA, D. J., 1974, *Opto-Electronics*, **6**, 43.
[4] VERDEYEN, J. T., 1981, *Laser Electronics* (New Jersey: Prentice-Hall), ch. 9.
[5] STAKGOLD, I., 1967, *Boundary Value Problems of Mathematical Physics, Vol. I* (New York: MacMillan), p. 47.
[6] REICHEL, A., 1966, *Special Functions* (Sydney: Science Press), p. 59.
[7] KUIZENGA, D. J., and SIEGMAN, A. E., 1970, *IEEE J. quant. Electron*, **6**, 709.
[8] HONG, G. W., and WHINNERY, J. R., 1969, *IEEE J. quant. Electron*, **5**, 367.
[9] KANE, D. M., BRAMWELL, S. R., and FERGUSON, A. I., 1986, *Appl. Phys.* B, **39**, 171.
[10] SMITH, P. W., 1970, *Proc. IEEE*, **58**, 1342.

A driver for stable-frequency operation of laser diodes

P. Saunders and D. M. Kane[a)]
Department of Physics and Biophysics, Massey University, Palmerston North, New Zealand

(Received 28 May 1991; accepted for publication 3 January 1992)

A driver for the stable-frequency operation of an AlGaAs laser diode is described. This consists of a constant current source with short-term fluctuations of ± 8 μA and a drift of less than 2 μA in 10 h, in conjunction with a ± 1 mdeg temperature controller. The current can be set to values up to 100 mA and a ramp current up to 20 mA can be added to this to allow frequency scanning of the laser. The laser linewidth is measured by heterodyning two such stabilized lasers and recording the beat note. This has a width of 27 ± 7 MHz. The frequency drift is monitored by exciting the D_2 transition of cesium and recording the change in absorbed power when a laser is tuned to the side of an absorption peak. The drift is measured to be 10 kHz/s over 5 h, and is attributed largely to temperature drift. In addition, the current circuit can be readily interfaced to a microcomputer for automatic control of the laser current without sacrificing stability.

I. INTRODUCTION

Laser diodes are now an important tool for both commercial and research applications. Commercially they are used, for example, in optical communications, laser gyroscopes, and optical disk systems. The research applications include infrared atomic and molecular spectroscopy, precise metrology, optical pumping for time and frequency standards, trapping and cooling of atoms, and they are used as a pumping source for other laser systems. The features that laser diodes have for these applications are: (i) They are inexpensive. (ii) They are portable and have a low power consumption, and hence can be conveniently operated "in the field" using battery power. The low output power of laser diodes with good mode quality is, however, not always a desirable feature. (iii) They are tunable over a region of tens of nanometers within which continuous tuning ranges of tens of gigahertz are punctuated by mode hops. The continuous tuning ranges can be increased considerably, typically to between 50 and 250 nm, by operating the laser diode with a long external cavity (~ 10 cm long) and a feedback grating[1] or with a short external cavity (~ 200 μm long) with a reflecting facet.[2,3] (iv) They can lase in an essentially single longitudinal mode within a few megahertz of the desired wavelength as soon as they are turned on.[4] Although the spectral emission is well characterized by a pure Lorentzian, there are in reality many much less intense (about 100 times less intense) spectral components several hundred gigahertz away from the main mode.[5] (v) They are capable of rapid modulation. (vi) They operate in the infrared where many molecular transitions occur, and where fibers used for optical communications have least loss and dispersion. The above and other applications require a narrow frequency bandwidth and frequency-stable source.

The tunability of laser diodes is due to the temperature dependence of the active region refractive index and band gap. As well as by gross control of the laser diode's temperature, frequency tuning is achieved by adjusting the injection current which affects the temperature through Joule heating.[5] For AlGaAs laser diodes the typical frequency changes are -20 to -30 GHz/°C and -3 to -7 GHz/mA for temperature and injection current changes, respectively. Stabilization of the injection current is also important when considering laser linewidth. A contribution to broadening of the spectral linewidth arises from the change in active region refractive index with carrier density.[6] Hence fluctuations in injection current should be minimized to limit this broadening.

At the present time there is considerable interest in instrumentation for driving laser diodes which meets certain stability and experimental requirements. This article discusses the construction and performance of a laser diode frequency stabilization system, consisting of a stable current source and a temperature control unit. This was motivated by the need for a relatively inexpensive, easy to construct, laser diode system for high-resolution atomic spectroscopy. As well as for obtaining good frequency stability, the current source was designed to be easily interfaced to a microcomputer, without loss of stability, for external control. For this purpose, digital to analog converters were incorporated into the design. The current can be swept over several ranges to provide frequency scans of differing magnitudes. The linewidth obtained using this system was measured by heterodying two such stabilized Hitachi HL8314E AlGaAs laser diodes, operating near 850 nm, and recording their beat signal. The width of this signal was 27 ± 7 MHz. Also, to measure the frequency drift, a single stabilized laser was used to excite the D_2 transition of cesium vapor in a 10-cm pyrex cell at room temperature. From the absorption signal the laser frequency was found to be stable to within ± 20 MHz over short periods and to drift by about 10 kHz/s over 5 h.

Improved frequency stability has been obtained by several authors (e.g., Refs. 1,7–14) by employing active stabilization whereby changes in frequency are detected and compensated for by changing either the injection current

a)Present address: School of Mathematics, Physics, Computing, and Electronics, Macquarie University, NSW 2109, Australia.

 0034-6748/92/042141-05$02.00

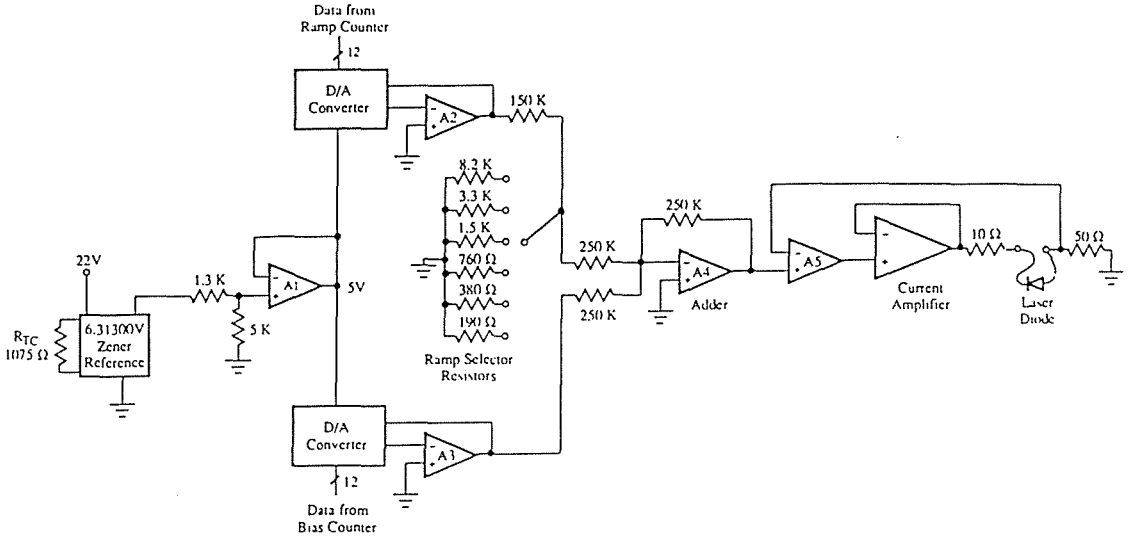

FIG. 1. Current source for laser diode, capable of supplying up to 100-mA constant current plus up to 20-mA ramped current. The 12 digital inputs to the D/A converters come from counter circuits which can be internally clocked at variable speeds or clocked by computer. The components are as follows—Op. amps A1–A5: AD510; D/A converters: AD563; Current amplifier: AD3554; Zener reference: ZVR-50o; laser diode: Hitachi HLS314E; resistors: Vishay metal foil.

or laser temperature, or by altering the length of an external cavity coupled to the laser. These systems use a stable frequency reference, such as an atomic or molecular absorption line, or a stabilized Fabry–Perot interferometer, with which to compare the laser frequency and determine an error signal which is fed back to the laser completing a servoloop. However, frequency stabilization to this degree can only be achieved once the sort of injection current and temperature stability described here has been obtained.

II. CURRENT SOURCE

The current source was designed with the following criteria in mind. It needed to be a high precision source capable of supplying up to 100 mA dc (bias current), with an additional current (ramp current), up to 20 mA, added to the bias current in the form of a current ramp. The bias current was required in order to select a particular laser diode wavelength, with the ramp current providing a frequency scan through the desired atomic transition. As with any laser diode current source, it was necessary to avoid any voltage spikes and transients which could easily destroy the device. Finally, a means of interfacing the current source to a computer was required.

Figure 1 shows the circuit used. It is based on a constant current supply for a superconducting quantum interference device (SQUID)[15] which has been modified to fulfill the above criteria. The operational amplifiers labeled A1–A5 were chosen for their low offset voltage drifts ($<0.5\ \mu V/°C$) and low noise. The resistors are metal foil resistors which have a temperature coefficient of 0.3 ppm/°C and a tolerance of ±0.005%. The current amplifier has an offset voltage temperature coefficient of 8 $\mu V/°C$ and has a larger noise figure than the amplifiers A1–A5, but although it is wideband it was the most appropriate amplifier available at the time of construction. Two digital counters are used to control the current through the laser, one for slowly setting the bias current and the other to produce a current ramp in addition. Under normal operation the counter ICs (4029 synchronous up/down counter) are clocked by an internal variable speed clock. For remote operation this internal clock is disabled and the clock pulses are sent directly from a computer. The digital outputs from the counter circuits are converted into analog via the 12-bit D/A converters in Fig. 1. These have true 12-bit accuracy with a maximum error of ±0.5 LSB at 25 °C, and have a maximum zero drift of 2 ppm of full scale per °C. The reference voltage for the D/A converters is taken from a Zener reference with a rated output voltage of 6.313 00 V, which is divided down to 5 V and buffered. The 50-Ω resistor between the laser and ground limits the bias current to 100 mA for a full scale setting on the bias D/A converter. The ramp voltage is divided down with the ramp selector resistors to obtain the desired tunability range, and is added to the bias voltage before being converted into a constant current. The current amplifier is configured as a unity voltage gain buffer and, together with the laser, is enclosed in a constant current feedback loop.

In order to determine the current flowing through the laser, the digital values on the D/A converters are shown on digital displays connected directly to the counter circuits. Once calibrated, this provides a direct current reading without disruption of the actual laser current and with no effect on its stability.

The bias current is ramped up slowly when initially

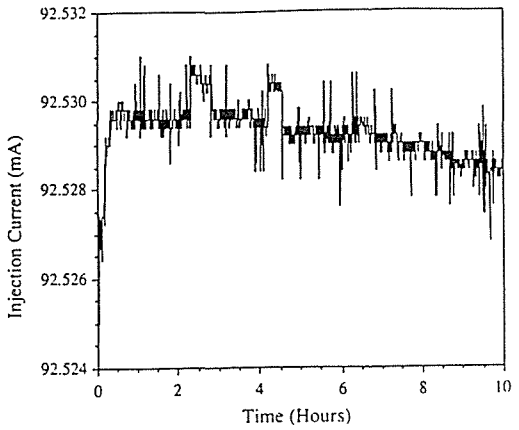

FIG. 2. Injection current variation over a 10-h period. An initial drift occurs during warm up, then the current is stable to within ± 1 μA with a drift of 1.2 μA in over 10 h. Note that these values are limited by the multimeter's accuracy.

turned on, and is reduced to zero before disconnecting the mains power supply to avoid sudden changes in injection current. Decoupling capacitors on the power supply lines to the operational amplifiers are the only safety features included to eliminate voltage spikes and transients. (We are able to make the claim of not destroying a laser in three and a half years of experimentation!)

The current can be ramped over ranges of 0.12 up to 20 mA, each range consisting of 999 steps. This corresponds to frequency scan ranges of about 0.5 up to 80 GHz for the AlGaAs lasers used. These ranges can be readily varied by changing the selector resistors. However, the sizes of the continuous tuning ranges are influenced by mode hopping, the occurrence of which depends on the particular laser diode being used. Uninterrupted scans of more than 20 GHz have been achieved with the lasers used here. We have used computer control of the frequency scan to record atomic absorption spectra since this allows the scan to by synchronized with the detected signal which is recorded by the same computer. We have also remotely controlled the bias current and the laser temperature in order to obtain complete wavelength maps of several laser diodes.

Figure 2 shows a measure of the current stability. The voltage across the 50-Ω resistor was monitored using a Philips PM2535 System Multimeter while the laser was operating at 92 mA. The multimeter's A/D converter averages over 20 ms. Following a 20-min warm up period, during which the current increased by 5 μA, the current remained stable to within ± 1 μA and drifted by only 1.2 μA in over 10 h. The accuracy of the multimeter is ± 0.1 mV, giving a current accuracy of ± 2 μA. Hence the values plotted in Fig. 2 are limited by the accuracy of the meter. The short-term stability (less than 20 ms), measured using an oscilloscope, was found to be about 8 μA peak to peak. The maximum error of the 12-bit D/A converters (± 0.5 LSB) implies a maximum contribution to this current noise of ± 12 μA. This could be reduced to less than ± 1 μA by using 16-bit D/A converters, but at increased cost. Any remaining noise is due to the current amplifier, and could possibly be reduced by replacing this component by a less noisy one, such as a single transistor, should such a component become available.

Recently Bradley *et al.*[16] and Cafferty and Thompson[17] have also reported stable current supplies for laser diodes of ± 1 μA at 150 mA and ± 40 μA at 1.3 A, respectively. The latter supply is designed for high current operation of lead-salt laser diodes and features cutoff protection circuitry for a range of undesirable conditions, but has no provision for ramping the current. The supply of Bradley *et al.* contains three analog voltage inputs which are added together to set the output current. Two of these, the coarse and fine adjustments, are derived from an internal precision voltage reference using potentiometers. The third voltage input, the sweep input, is obtained from an external source upon which its stability depends. In comparison, we have built digital circuitry into the current source described here in order to meet the requirements discussed above. In particular, the stability of the voltage inputs (bias and ramp) is determined only by that of the D/A converters as there are no potentiometers, and no additional circuitry is required to ramp the current. The digital inputs also allow the current supply to be interfaced to a computer without loss of stability. By sending clock pulses to the counter circuits, the computer can both set the bias current and perform a current scan at a desired rate.

III. STANDARD HEATER/COOLER CIRCUIT

A standard heater/cooler circuit, as described in many laser diode manufacturers' handbooks, is used as a temperature controller. This uses a thermistor to sense the laser's temperature and a peltier element to heat or cool the laser in response to a change in temperature. The unit is capable of a short-term stability, with the laser operating, of ± 1 mdeg (Fig. 3), although over a long time period the temperature drifts in accordance with room-temperature changes (see inset). Over a 10-h period the laser temperature was observed to change by 10 mdeg at 32 °C while the room temperature varied by 1.5 °C. Other, more complicated, circuits have been constructed[16,18–20] which can achieve stabilities of ± 10, 15, 100, and 300 μdeg, respectively.

IV. FREQUENCY STABILITY

In order to measure the overall effect of both temperature and current variations on the performance of an 850-nm AlGaAs laser diode two different techniques were employed. The first was to build two identical temperature controllers and current sources, and observe the beat signal between two heterodyned stabilized laser diodes. The second was to tune a single laser diode onto the side of one component of the cesium D_2 transition, observed by passing the beam through a cell containing cesium vapor, and to monitor the drift up and down the side of the peak.

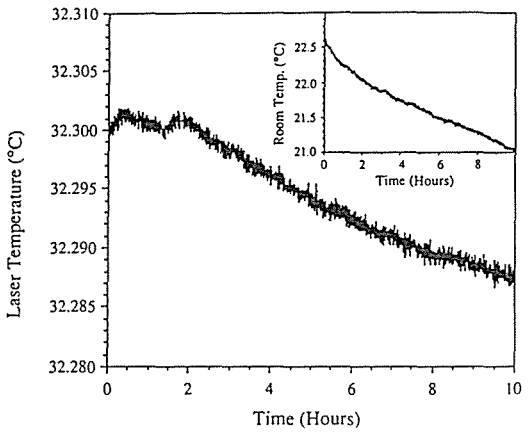

FIG. 3. Variation in laser temperature over a 10-h period. Short-term fluctuations are within ±1 mdeg and the long-term drift of 10 mdeg is due to a drift in ambient temperature of 1.5 °C as shown in the inset.

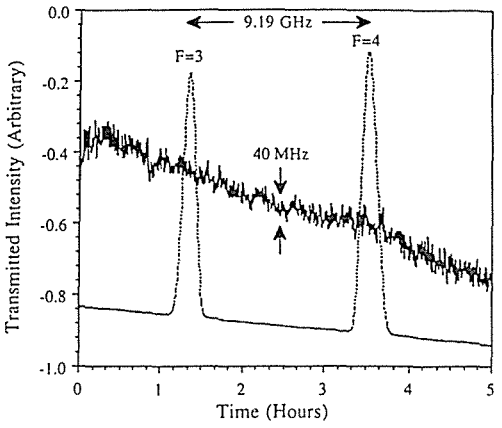

FIG. 5. Frequency stability of an AlGaAs laser diode. The dotted curve shows the absorption of the beam by Cs vapor. The horizontal axis for this curve is in frequency units and the scale is indicated near the top. The two peaks correspond to hyperfine transitions from the $F=3$ and $F=4$ levels in the ground state. The background slope is due to the change in output power as the laser current is ramped. The solid curve gives the change in intensity, hence frequency as indicated by the vertical arrows, for the laser tuned to the inside of the $F=4$ peak over a period of 5 h.

The heterodyne technique was used because the width of the beat note can be used as a measure of the laser linewidth. The beams from two different lasers were arranged to fall collinearly on to a detector. This signal was detected using a high-speed Hewlett Packard 5082-4220 PIN photodiode (rise and fall times <1 ns) and recorded on a Tektronix 2710 spectrum analyzer. The signal displayed on the spectrum analyzer is proportional to the convolution[21] of the two independent laser line shapes and occurs at the difference frequency of the two laser frequencies. The individual line shapes are Lorentzian, hence the beat signal is also Lorentzian with a FWHM equal to the sum of the original FWHMs. Figure 4 shows a photograph of a beat note recorded with a 5-MHz resolution bandwidth. The top trace is the signal and the lower trace the noise floor. The horizontal scale is 20 MHz per division and the vertical scale is logarithmic. Several measurements of the beat note were taken at various difference frequencies. The average FWHM of these is 27±7 MHz. Figure 4 is a representative sample arbitrarily centered around 270 MHz. As a comparison, a single laser diode was driven by a general purpose Hewlett Packard 6218B power supply in conjunction with a slow-starter circuit. Here the peak to peak current fluctuations were measured to be 200±20 μA and the laser linewidth was measured using a Fabry–Perot interferometer to be 410±20 MHz. Hence a significant reduction in linewidth is achieved through stabilization of the injection current.

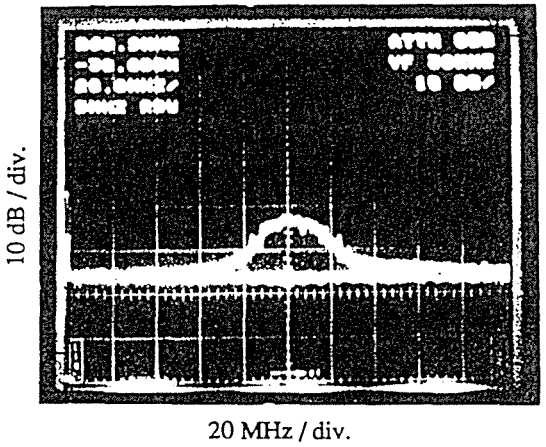

FIG. 4. Beat note between two stabilized AlGaAs laser diodes. The top trace is the signal and the lower trace the noise floor. The horizontal scale is 20 MHz per division and the vertical scale is logarithmic. The resolution bandwidth is 5 MHz and the FWHM of the signal is 27±7 MHz.

To measure the drift of the laser frequency, the beam was passed through a pyrex cell, 10 cm in length, containing cesium vapor, exciting the cesium D_2 transition at 852.1 nm. The absorption of the beam was monitored by a photodiode. The cell was placed inside an insulated enclosure and left at room temperature. The slope of the absorption signal was used to relate a change in the output of the photodiode to a change in laser frequency. The hyperfine transition with $F=4$ in the ground state was used rather than $F=3$ because of the greater absorption on the former (Fig. 5). The laser was tuned to the lower wavelength side of the $F=4$ peak and the photodiode signal was monitored for a period exceeding 5 h. This signal is dependent not only on changes in laser frequency, but also on intensity fluctuations of the laser output itself, and on changes in the cesium number density which is determined by the cell temperature. Laser intensity fluctuations were measured to be smaller than ±1% of the initial intensity with no significant drift over the time scale of Fig. 5. These fluctuations account for 4% of the total fluctuations. The temper-

ature of the cesium cell drifted by no more than 0.5 °C, giving an intensity drift of 4% of the initial intensity over 5 h, that is only 7% of the total drift in Fig. 5. The remaining intensity fluctuations and drift are due to laser frequency changes. Frequency fluctuations were within ±20 MHz and there was an overall drift of about 10 kHz per second.

By varying the temperature and injection current, and using a spectrometer to measure the laser wavelength, the tunability of the laser was previously determined to be

$$\Delta\nu/\Delta I = -3.93 \pm 0.08 \text{ GHz/mA}, \quad (1)$$

and

$$\Delta\nu/\Delta T = -24 \pm 2 \text{ GHz/°C} \quad (2)$$

where $\Delta\nu$, ΔI, and ΔT stand for changes in laser frequency, injection current, and temperature, respectively. The injection current and temperature drifts were 3.3×10^{-5} μA/s (Fig. 2) and 4.2×10^{-7} °C/s (Fig. 3), respectively. From Eqs. (1) and (2), these values imply frequency drifts of 0.1 and 10 kHz/s, respectively. Hence the long-term stability of the temperature controller would need to be improved in order to reduce the long-term frequency drift. This could be achieved by placing the circuit in a constant temperature enclosure, although the extra effort and cost involved may not be warranted since the frequency drift over the duration of a scan (<1 min) would not be improved. Short-term temperature variations could be improved by using a more sophisticated circuit, such as that in Ref. 16, which uses PID gain stages and optimized time constants.

Further improvements to the short-term injection current fluctuations, as discussed in Sec. II, would need to be made in order to reduce the linewidth to the theoretical limit, without optical feedback, as derived by Henry.[6] This is based on the modified Schawlow–Townes formula with an additional broadening due to the strong coupling between amplitude and phase fluctuations of the optical field. For the AlGaAs lasers used here this linewidth limit is of the order of 1 MHz, hence an order of magnitude improvement is possible. With the present system we have been able to observe the hyperfine splittings in the $6^2P_{3/2}$ level of cesium (~100 MHz splitting) using sub-Doppler saturated absorption spectroscopy, although the natural linewidth (~5 MHz) is dominated by the laser linewidth. With improvements to the short-term current fluctuations this width should be fully resolved.

Detailed information concerning the circuitry is available from the authors.

ACKNOWLEDGMENTS

We wish to thank R. Dykstra, Massey University, for his valuable advice concerning the electronics. We also thank R. Gledhill, University of Otago, Dunedin, for constructing the cesium absorption cell. This work was supported by the New Zealand University Grants Committee and the Massey University Research Fund.

[1] S. Sampei, H. Tsuchida, M. Ohtsu, and T. Tako, Jpn. J. Appl. Phys. 22, L258 (1983).
[2] O. Yamamoto, H. Hayashi, N. Miyauchi, S. Maei, H. Kawanishi, T. Morimoto, S. Yamamoto, S. Yano, and T. Hijikata, J. Appl. Phys. 61, 870 (1987).
[3] H. Kawanishi, H. Hayashi, O. Yamamoto, N. Miyauchi, S. Maei, S. Yamamoto, and T. Hijikata, Jpn. J. Appl. Phys. 26, L590 (1987).
[4] C. E. Wieman and L. Hollberg, Rev. Sci. Instrum. 62, 1 (1991).
[5] J. C. Camparo, Contemp. Phys. 26, 443 (1985).
[6] C. H. Henry, IEEE J. Quantum Electron. QE-18, 259 (1982).
[7] T. Tako and H. Tsuchida, JARECT 11, Optical Devices and Fibers (1984).
[8] J. L. Picqué and S. Roisen, Appl. Phys. Lett. 27, 340 (1975).
[9] F. X. Desforges, Y. André, and P. Cérez, J. Phys. E 19, 731 (1986).
[10] S. Okude, F. Matsushima, and T. Shimizu, Jpn. J. Appl. Phys. 26, L1277 (1987).
[11] H. Tsuchida, M. Ohtsu, T. Tako, N. Kuramochi, and N. Oura, Jpn. J. Appl. Phys. 21, L561 (1982).
[12] T. Yabuzaki, A. Ibaragi, H. Hori, M. Kitano, and T. Ogawa, Jpn. J. Appl. Phys. 20, L451 (1981).
[13] H. Tsuchida, M. Ohtsu, and T. Tako, Jpn. J. Appl. Phys. 21, L1 (1982).
[14] S. Yamaguchi and M. Suzuki, IEEE J. Quantum Electron. QE-19, 1514 (1983).
[15] B. Levy and A. J. Greenfield, Rev. Sci. Instrum. 50, 655 (1979).
[16] C. C. Bradley, J. Chen, and R. G. Hulet, Rev. Sci. Instrum. 61, 2097 (1990).
[17] M. S. Cafferty and E. D. Thompson, Rev. Sci. Instrum. 60, 2896 (1989).
[18] J. Dratler, Rev. Sci. Instrum. 45, 1435 (1974).
[19] D. Sarid and D. S. Cannell, Rev. Sci. Instrum. 45, 1082 (1974).
[20] R. D. Esman and D. L. Rode, Rev. Sci. Instrum. 54, 1368 (1983).
[21] M. Françon, *Optical Interferometry* (Academic, New York, 1966).